CRANFIELD UNIVERSITY

A WRIGHT

TYRE / SOIL INTERACTION MODELLING WITHIN A VIRTUAL PROVING GROUND ENVIRONMENT

SCHOOL OF APPLIED SCIENCES

PhD THESIS

Academic Year: 2009 - 2012

Supervisor : Dr. James Brighton

January 2012

CRANFIELD UNIVERSITY

SCHOOL OF APPLIED SCIENCES

PhD THESIS

Academic Year: 2009 - 2012

A WRIGHT

Tyre / soil interaction modelling within a virtual proving ground environment

Supervisor : Dr James Brighton

January 2012

This thesis is submitted in fulfilment of the requirements for the degree of Doctor of Philosophy

Abstract

Off-road mobility defines the ability of land-based vehicles to accelerate, pull loads and climb gradients. Historically, much of the work completed to relate mobility to vehicle and terrain characteristics has been empirical in nature, and has therefore been susceptible to errors caused by the inherent variability of naturally occurring soils. This thesis addresses the off-road mobility of wheeled vehicles, and in particular the use of a finite element (FE) based approach to predict performance metrics such as rolling resistance, drawbar pull and tractive efficiency. Tools to predict these measures of performance have a wide range of applications, including military, agricultural and leisure vehicles, aircraft operating from temporary airfields and planetary landing craft.

The current study extends the virtual proving ground (VPG) concept, where a single vehicle model can be subjected to a series of virtual test conditions, to include the assessment of off-road mobility. Throughout, modelling has been carried out using LS-DYNA, a commercially available non-linear dynamic analysis code. Unlike previous studies using FE techniques to investigate wheel / soil interaction, an Eulerian representation of the soil has been employed, which permits a consistent approach to be applied to both purely cohesive and purely frictional soils, as well as those displaying a combination of cohesive and frictional behaviour. At each stage of the research, the validity of the FE-based modelling approach has been assessed using data from controlled experimental testing at Cranfield University's off-road dynamics facility.

A key finding of the work completed is that rate sensitivity in moisture containing soils can significantly affect the accuracy of (empirical, analytical and numerical) model predictions, even at low translational speeds (less than 0.1m/s). This finding highights the adverse impact of simplifications in many previous experimental and modelling studies, which have assumed that rate effects may be ignored providing the translational speed of the vehicle is low.

Dedication

This thesis is dedicated to the memory of David Archibald Wright, who inspired me to pursue a career in science and engineering. Thanks, Dad.

Acknowledgements

I would like to extend my thanks to both QinetiQ and the UK Ministry of Defence (MOD) for providing financial support to the research, particularly MOD for their funding of the project on which this thesis is largely based.

I would also like to thank my supervisor, Dr James Brighton, Dr Kim Blackburn, Dr Andrew Walton, and all of the staff at Cranfield's School of Applied Sciences who supported much of the experimental work and provided guidance along the way.

Finally, and most of all, I would like to offer my heartfelt thanks to my wife, Stacy, for all of her support and understanding over the many evenings and weekends that I have spent staring at a computer screen.

Contents

List of figures

List of tables

List of symbols and abbreviations

A	Contact patch area
a_0	Shear failure surface constant, LS-DYNA Mat 5 and Mat 16
a_1	Shear failure surface constant, LS-DYNA Mat 5 and Mat 16
a_2	Shear failure surface constant, LS-DYNA Mat 5 and Mat 16
ALE	Arbitrary Lagrange Eulerian
b	Wheel width
B_n	Mobility number, Brixius
c	Cohesion
CF	Ground clearance factor, Mobility Index
CI	Cone index
C_n	Wheel numeric
CPF	Contact pressure factor, Mobility Index
C_{RR}	Rolling resistance coefficient
D	Wheel diameter
DEM	Discrete element method
E	Young's modulus
EF	Engine factor, Mobility Index
F	Towing force
FE	Finite element
G	Shear modulus
G_{CI}	Cone index gradient
GF	Grouser factor, Mobility Index
h	Tyre section height
j	Horizontal soil deformation, Janosi and Hanamoto
K	Bulk modulus
K	Empirical constant, Freitag
K	Shear deformation modulus, Janosi and Hanamoto
K_c	Soil bearing capacity factor
K_{un}	Unloading modulus
K_γ	Soil bearing capacity factor

k	Empirical constant, mean maximum pressure
k	Sinkage modulus, Bernstein
k'_1	Soil stiffness constant, Reece sinkage equation
k'_2	Soil stiffness constant, Reece sinkage equation
m	Number of axles, mean maximum pressure
MI	Mobility index
n	Sinkage exponent, Bernstein
n	Strain rate constant, LS-DYNA Mat 147
N_q	Bearing capacity factor, Terzaghi
P	Drawbar pull
p	Pressure / mean stress
R	Rolling resistance
r	Wheel radius
S	Proportionality constant, mean maximum pressure
S	Wheel slip
SD	Deviator stress
SPH	Smooth particle hydrodynamics
T	Traction force
T	Tread factor, mean maximum pressure
t	Time
TEF	Traction element factor, Mobility Index
TF	Transmission factor, Mobility Index
v	Translational speed
VCI	Vehicle cone index
VPG	Virtual proving ground
W	Wheel load
WF	Vehicle mass factor, Mobility Index
WLF	Wheel load factor, Mobility Index
z_0	Sinkage, Bekker
γ	Specific weight
γ	Strain rate constant

δ	Tyre deflection
$\dot{\varepsilon}$	Strain rate
ε_v	Volumetric strain
η	Tractive efficiency
θ	Contact angle
υ	Poisson's ratio
ρ	Density
τ	Shear stress
τ	Torque
ϕ	Friction angle
ω	Rotational speed

Chapter 1: Introduction

This thesis will address the prediction of off-road vehicle mobility within a virtual proving ground (VPG) environment using a finite element (FE) based approach. This chapter describes the on-going requirement for improved mobility prediction tools that can be applied to wheeled vehicles operating on soft soils.

1.1 Motivation

Historically, the mobility of wheeled vehicles operating on soft soils has primarily been assessed through full-scale physical testing. In naturally occurring soils, however, where spatial and temporal variations in soil properties are to be expected for a given test site, differences in performance between competing designs may be masked by the inherent variability of the terrain. In an effort to address this, and to reduce the reliance on full-scale testing, a number of modelling approaches have been developed, with the aim of predicting vehicle mobility based on known vehicle and terrain characteristics.

Various performance metrics have been proposed to allow the off-road performance of competing designs to be compared, with the assessment criteria used and the weighting applied to them dependant on the intended application. Contemporary military operations, for example, require vehicles that offer a balance between occupant protection (with an associated increase in vehicle mass) and off-road mobility. The off-road mobility of military vehicles has a significant impact on the results of operational analysis (OA), including terrain accessibility (go / no go), mission tempo and fuel consumption. During vehicle procurement projects, a number of competing prototype vehicle designs are typically assessed for down selection through full scale experimental trials. The cost of these down selection trials can be significant, and is generally passed on to the customer in one way or another. For off-road sports and leisure vehicles, a similar balance must be struck between limiting soil conditions and fuel efficiency, although the implications of immobilisation are clearly less severe. Finally, for agricultural vehicles, the effect of vehicle passes

on the condition of the soil must be considered in terms of the impact on crop yield, in addition to concerns regarding efficiency and absolute mobility.

For aircraft operating from unpaved airfields, the implications of operating on a deformable surface are slightly different. As well as dictating whether or not the aircraft can operate from a given airfield (a similar concept to go / no go for land vehicles), the interaction of the aircraft's tyres with the soil will govern the length of runway that must be prepared to ensure that the aircraft can operate safely. As the resistance to motion increases, the distance required to achieve the speed needed for take-off increases but, conversely, the aircraft's landing roll – the distance travelled before coming to rest – is reduced. Multiple take-off and landing operations may degrade the airfield to the extent that repair is necessary, and the effect of tyre / soil interaction on the soil will dictate the frequency of airfield maintenance required for safe operation.

For both land vehicles and aircraft, the primary driver for the development of predictive mobility tools has been to reduce the number of expensive and time-consuming experimental trials required. For planetary landing craft, the development of modelling tools is a more fundamental issue, as the options for physical testing are limited. Due to a lack of bulk soil for testing, physical assessment of planetary landers typically relies on small scale test beds using surrogate soils (Nakashima, 2010). A potentially more significant issue is the fact that soil strength is often pressure dependent, and that the apparent strength of the soil will therefore be influenced by gravity, which cannot be readily controlled during experimental mobility trials (Wong, 2011).

1.2 Research rationale

In the applications described above, the ability to predict the effect of soil properties and vehicle characteristics on mobility and tractive efficiency is highly desirable. As well as the difficulties associated with the spatial and temporal variability of a given test site, the limited control available over soil properties in full-scale experimental testing means that it is not always possible to test on the desired range of soils. This is particularly true in the case of cohesive clays,

where soil preparation prior to each experimental run requires much more time and effort than is necessary for a dry sand. Modelling tools that can accurately represent the physical processes involved in wheel / soil interaction, while permitting full control over soil properties, therefore represent an important component in the study of off-road mobility.

Due to the variable nature of many soils, predictive modelling tools for use in 'real world' applications must be viewed as complimentary to experimental assessment methods, rather than a direct replacement for them. While full-scale experimental testing is still necessary for final acceptance trials, the degree of control available in a simulation environment and the ability to interrogate the model in detail enables an improved understanding of the processes involved and the influence of soil and vehicle characteristics, leading to improved designs.

1.2.1 Available modelling methods

The modelling tools which are currently available can generally be divided into three categories: empirical models, which seek to describe experimental observations; analytical models, which seek to describe the physical processes involved using simplified sub-systems; and numerical modelling techniques, which seek to describe the physical processes involved using a numerical simplification scheme. In both analytical and numerical models, some degree of resolution is lost in the simplification of the problem to yield a tractable solution. With numerical techniques, however, this loss of resolution can be offset by increases in computing power, which have permitted the use of more detailed models as research in this area has progressed. Numerical mobility models, using FE analysis codes, also offer a greater level of control over soil properties than empirical or analytical methods, as spatial variations in soil properties can be included if required. Numerical mobility models are potentially more widely applicable than empirical or analytical methods, although their accuracy is still dependent on the input data provided by the user.

1.2.2 The virtual proving ground

Of the above modelling methods, analytical and numerical approaches are the most directly applicable within the framework of a virtual proving ground (VPG), where the expected performance of a vehicle design can be assessed prior to the availability of a physical prototype through a number of simulated tests. For passenger, commercial or agricultural vehicles, the VPG will typically include components addressing vehicle dynamics, structural integrity, durability / fatigue, noise, vibration and harshness (NVH), and crash safety (impact / rollover). For military vehicles, the scope of the VPG may be increased to assess the vehicle's resistance to both mine and free air blast loads. For vehicle manufacturers, the primary advantage of a VPG approach is the ability to undertake an initial assessment of new vehicle designs without the capital expenditure associated with the manufacture of prototype vehicles.

While the basic concept of a VPG has remained constant over time, the approach to data management within the VPG environment has changed with the aim of streamlining the analysis process (Choi and Min, 2000). At its simplest, a VPG is essentially a collection of vehicle analysis models, all using the same geometry, but with differing analysis techniques applied to address different aspects of the vehicle's performance: as an example, rigid body dynamics may be used for vehicle dynamics and NVH simulations, static FE analysis for structural integrity, and dynamic FE analysis for crash safety. With the development of software packages such as ANSYS Workbench (www.ansys.com, accessed 2nd December 2011), recent developments have focussed on reducing the manpower effort required to generate a suite of analysis models by using a single vehicle mesh for as many components as possible.

The typical structure of a VPG, as applied to a new military vehicle design, is illustrated in Figure 1.1. One area where the VPG approach requires considerable development is in assessing performance at the wheel / soil interface. In addition to determining a vehicle's expected off-road capability, an accurate representation of the interaction between wheel and terrain would

provide valuable input data for a number of other VPG components, in the form of road loads for linear static, fatigue, vehicle dynamics and NVH simulations. For the reasons discussed above, the research presented in this thesis has focussed on the use of an FE-based approach to predict the off-road mobility of wheeled vehicles operating on naturally occurring soils. Figure 1.2 presents an overview of the research interest, and illustrates the primary components of any predictive mobility modelling tool.

1.3 Background

The exact origin of the wheel is unclear, with the earliest known depictions of wheeled vehicles occurring in the middle of the fourth millennium BC (Anthony, 2007). It is thought that the widespread use of the wheel was delayed due to the lack of smooth roads, which suggests that the off-road mobility of wheeled vehicles was a concern even in the Bronze Age. The controlling factor for the earliest wheeled vehicles, which limited their use off-road, was the lack of power available to overcome the resistance to motion presented by obstacles and the deformable terrain itself. With the development of the internal combustion engine and the motor vehicle, the power available to propel wheeled vehicles increased steadily, to the extent that failure of the soil body or the tyre / soil interface became the limiting factor for off-road mobility (Gill, 1965). Wheel and soil properties are therefore the controlling factors in the mobility of off-road vehicles, and the key to increased mobility is in making better use of the engine power that is available.

Tyre / soil interaction is a complex problem, involving the dynamic interaction of two deformable bodies. The response of the soil to applied loading is typically non-linear, with extensive plastic deformation of the soil occurring, particularly at high levels of wheel slip. In addition, the three-phase structure of soil, consisting of air, water and solid soil particles means that the mechanical response of the soil may be dependent on the rate of applied loading.

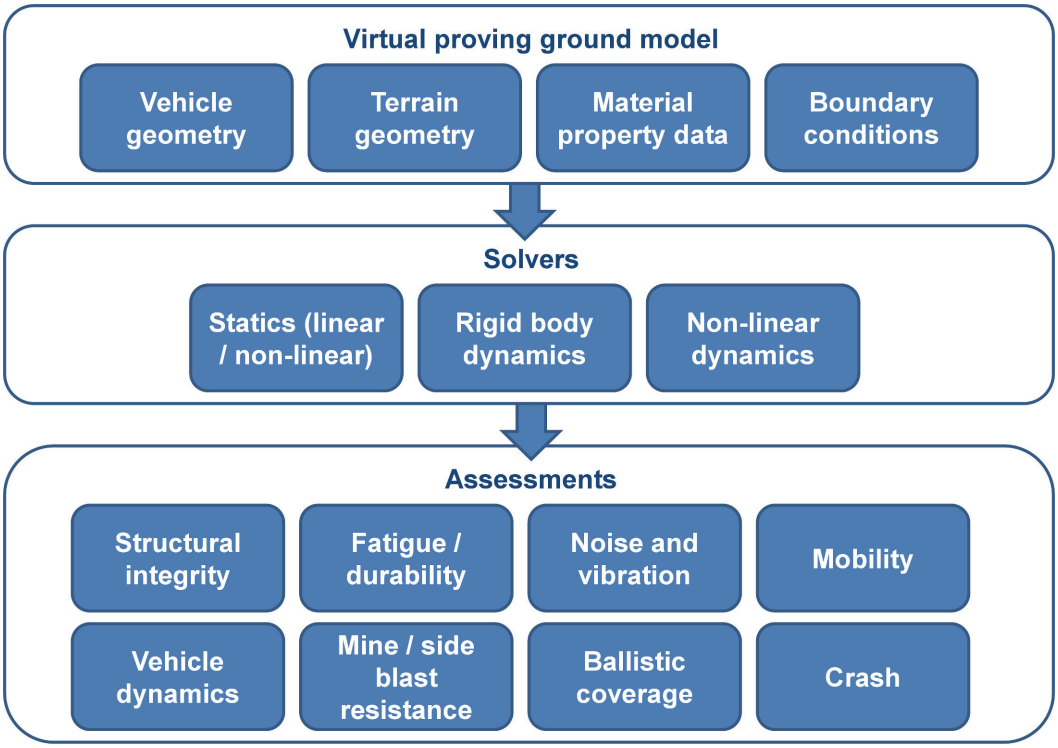

Figure 1.1: Example of a virtual proving ground for a military ground vehicle

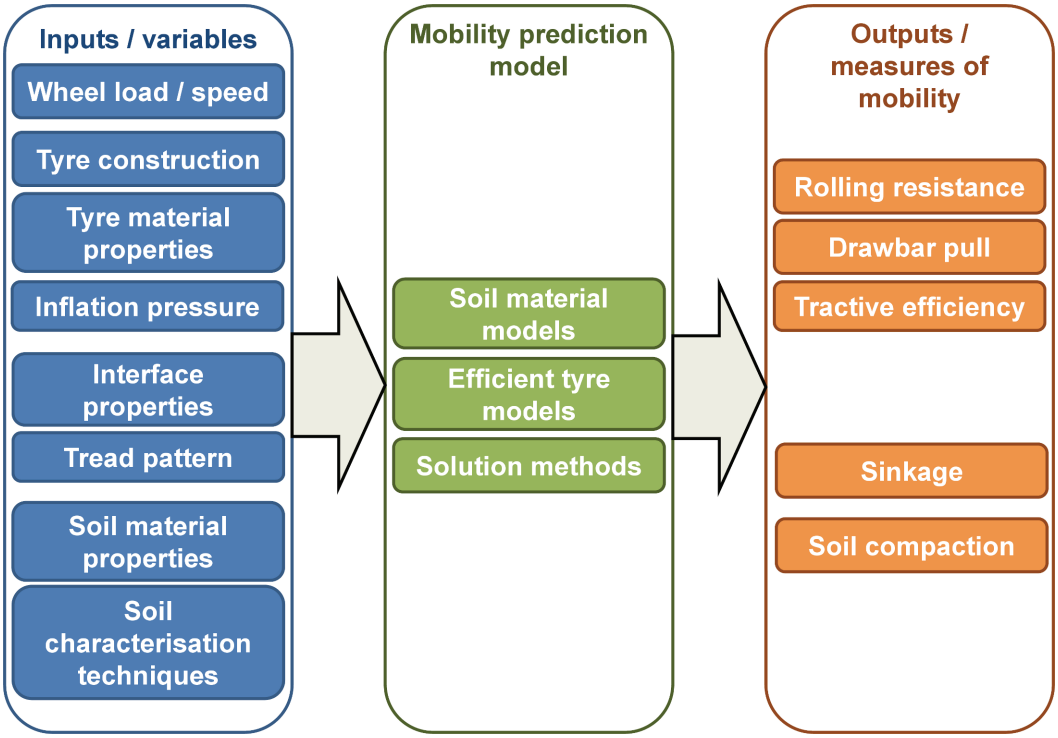

Figure 1.2: Overview of research interest

1.4 Research specification

The aim of the current study was to develop a numerical modelling approach that could be used to predict key measures of mobility such as rolling resistance, drawbar pull and tractive efficiency. The modelling approach, implemented in LS-DYNA Version 971, was intended to accurately capture the main aspects of the interaction between a pneumatic tyre and a deformable soil, allowing the influence of soil properties, tyre geometry, inflation pressure and vehicle translational speed to be predicted.

The accuracy of the results obtained from the proposed modelling approach was assessed against experimental data. Comparison against experimental data was undertaken at multiple stages during the research, covering each component of the tyre / soil interaction model to ensure that the main aspects of the process were represented.

One of the key aspects of the work completed was to ensure that a consistent modelling approach could be applied, regardless of the soil type under investigation. Existing empirical and numerical modelling methods for mobility prediction often suffer from the fact that different relationships (in the case of empirical models) or solvers (in the case of numerical models) must be employed, depending on whether the soil under consideration is cohesive, frictional or displays a combination of cohesive and frictional behaviour.

The main objectives of the research were as follows:

- Development of soil material models to represent the in-situ response of dry sand and sandy loam, including any sensitivity to the rate of applied loading;
- Development of a generic tyre modelling approach, which can be used to represent pneumatic tyres of varying geometry and construction, including the effect of inflation pressure on tyre deflection and contact patch area as a function of wheel load;
- Fully dynamic modelling of the interaction between pneumatic tyres and soft soils to determine rolling resistance and drawbar pull for a range of slip values;

- Assessment of an Eulerian solution method for the soil body, as a means of representing both cohesive and cohesionless soils using a consistent approach;
- Validation of modelling outputs against experimental data for the effects of tyre geometry, inflation pressure, soil properties and vehicle speed.

1.5 Methodology

As described previously, the focus of the research was to develop a finite element based tyre / soil interaction model to predict the off-road mobility of wheeled vehicles, taking into account the effects of tyre geometry, tyre inflation pressure, soil properties and translational speed. The research could therefore be broken down into three main strands: (1) small scale experimental work, including the characterisation of soils to generate input data for the model, validation of tyre models, and investigating the deformation of soil beneath a towed rigid wheel; (2) full scale testing to generate validation data for predictions of vehicle mobility, and (3) numerical modelling studies addressing both individual components (soil samples, pneumatic tyres) and their interactions.

The research began with a review of relevant literature to gain a clear understanding of previous work in this area and, crucially, to identify where gaps existed. This allowed the detailed methodlogy for the research to be developed, which is described in the following sections.

1.5.1 Soil characterisation

In any modelling study, assuming the modelling framework accurately represents the physical processes involved, the accuracy of the predictions made is critically dependent on the quality of the input data provided by the user. As a main objective to the work was to describe the effect of soil properties on off-road mobility, a necessary first step was the generation of material model input data to describe two representative soils (a dry sand and a

moisture-containing sandy loam) through small scale laboratory testing. The influence of the characterisation test procedure used was also assessed.

Testing was undertaken on reconstituted soil samples, which meant that the structure of the soils may have changed from the in-situ condition. Verification and validation of the resulting soil material models therefore addressed two different measures of the soils' response to applied loads. Verification of the material models developed for the dry sand and sandy loam soils was first completed using single element simulations, replicating the loading conditions that were applied during the characterisation tests to confirm that the outputs obtained accurately described the input data supplied by the user. This single element verification was followed by validation using a more complex loading loading regime, representing plate sinkage tests undertaken on in-situ soils. The aim of this work was to assess the ability of the soil material models to predict the response of the in-situ soils, and addressed the influence of the laboratory characterisation methods used.

1.5.2 Tyre characterisation

Prior to their use in large interaction models, the tyre models developed as part of the numerical modelling work were validated against experimental test data for the two tyres considered (445 / 65 R 22.5 and 7.5 R 16 tyres manufactured by Michelin and Goodyear, respectively). The tyres were subjected to static load-deflection and load-contact area characterisation tests on a rigid surface, with this data used to validate the tyre models. The influence of tyre inflation pressure on both deflection and contact area was addressed.

1.5.3 Rigid wheel interaction study

One of the advantages of numerical modelling is that it can permit the physical processes involved in highly dynamic events to be investigated in detail without the need for complex instrumentation. The ability of the numerical modelling approach to represent the physical processes involved in wheel / soil interaction

has been assessed in the current study by examining the deformation of dry sand beneath a towed rigid wheel.

In the small scale experimental work, a rigid wheel was towed across a small scale soil bin, with the wheel in contact with a glass viewing window. This permitted the deformation of the sand to be directly observed in real time and recorded using a series of digital photographs. Post test analysis of these photographs allowed the deformation of the sand beneath the wheel to be quantified, addressing the effects of wheel diameter and translational speed.

1.5.4 Full scale experimental testing

To obtain validation data for the tyre soil interaction models, which were the main focus of the research, full scale experimental tests were undertaken. Rolling resistance and drawbar pull tests were completed to address the behaviour of both towed and driven wheels, including the effects of tyre inflation pressure, translational velocity and soil type on vehicle mobility. Experimental tests were undertaken using a combination of single wheel, single axle and full vehicle tests conducted in Cranfield University's off-road dynamics test facility.

1.5.5 Numerical modelling

The purpose of the small and full scale experimental work described in the preceding sections was to support the development of predictive numerical models for off-road mobility analysis. The numerical modelling work addressed soil model verification and validation, tyre model validation on a rigid surface, soil deformation beneath a rigid wheel and the prediction of rolling resistance and drawbar pull for pneumatic tyres operating off-road. At each stage, numerical modelling outputs were compared against the experimental data generated during the research to provide an assessment of model accuracy.

All numerical modelling work was undertaken in LS-DYNA Version 971. The release of LS-DYNA V971 used to run a particular model was dependent on the date, ranging from release 3.2.1 at the beginning of the project to 5.0 at the time

of thesis submission; in line with LSTC's recommendation, the most up to date release of the software used throughout. All simulations were undertaken on a Sony VAIO laptop with a Core 2 Duo T6600 processor, 4 GB RAM, 320 GB HDD running Windows 7 Home Premium.

1.6 Work disseminations

Aspects of the research reported here have been presented in the following conferences and customer presentations:

- Wright A., 2012. *Tyre soil interaction modelling within a virtual proving ground environment*. Tyre Technology Conference 2012, Cologne, Germany.
- French, M., and Wright, A., 2009. *Research for enhanced AFV performance*. IMechE conference on platform technology for military vehicles, Bristol.
- Wright, A., 2010. *Tyre and soft soil interaction modelling*. MOD customer report, QinetiQ/TS/FPPS/CR1001440.

1.7 Thesis outline

The remainder of this thesis can be summarised as follows:

- Chapter 2: literature survey

  Previous work in the area of wheel / soil interaction is reviewed, discussing the existing methods used to assess and predict off-road mobility for wheeled vehicles.

- Chapter 3: soil characterisation

  The structure of soils, their classification and their response to applied loads are discussed, alongside the laboratory-based test methods used to determine mechanical properties for FE analysis.

- Chapter 4: modelling of in-situ soils

  The difficulties of relating in-situ soil behaviour to laboratory-based characterisation tests are highlighted through a comparison of predicted and experimentally determined plate sinkage profiles for two representative soils. The relative performance of Lagrangian and Eulerian solvers is assessed for a dry sand and a sandy loam.

  The effect of loading rate on the soil's resistance to penetration is discussed, including the sources of rate effects in soil, the implications for mobility prediction using an FE-based approach, and the difficulties associated with the characterisation of soils at intermediate and high strain rates.

- Chapter 5: rigid wheel interaction

  The ability of the Eulerian FE approach to predict the soil displacements occurring beneath a rolling wheel is assessed, using a simplified problem that considers a rigid wheel operating on dry sand under plane strain conditions. A comparison is provided with experimentally determined soil displacements and a more conventional Langrangian representation of the soil. The relative performance of the Lagrange and Euler solution methods is discussed, with an Eulerian approach selected for subsequent work.

- Chapter 6: tyre modelling

  Chapter 6 discusses the construction of pneumatic tyres and details the development and validation of two tyre models for the prediction of off-road mobility. Rather than using a highly detailed description of a particular physical tyre, a generic tyre model was employed to provide a balance between acceptable accuracy and efficiency. Tyre models of this type have previously been used by researchers such as Reid, Boesch and Beilenberg (2006) and Orengo, Ray and Plaxico (2003) in automotive crash simulations. The work reported here builds on these previous studies by addressing the effect of inflation pressure on both

load-deflection response and contact area, with validation against experimental tyre characterisation data.

- Chapter 7: tyre / soil interaction modelling

  The soil and tyre models discussed in Chapters 3, 4 and 5 are used in larger scale tyre / soil interaction models to predict rolling resistance and drawbar pull. The predicted effects of soil type, tyre geometry, inflation pressure and vehicle translational speed are investigated and compared against the results of both single wheel and full-vehicle experimental trials.

- Chapter 8: discussion

  The main features of the proposed modelling process are summarised. The findings of the research are discussed, with particular emphasis on applications and how the numerical modelling approach can contribute to the design of future vehicle platforms.

- Chapter 9: conclusions and future directions

  Finally, the main research contributions and outcomes are summarised. Current limitations of the modelling approach and suggested areas for future development are also discussed.

Chapter 2: Literature survey

The topic of off-road mobility has been under investigation for a number of decades, using a wide range of approaches to quantify and predict the mobility of both wheeled and tracked land vehicles. This chapter reviews previous work in this area, addressing the existing methods used to quantify and predict off-road vehicle mobility.

2.1 Quantifying mobility

The methods used to quantify off-road mobility depend to a large extent on the purpose for which the vehicle is used: for military vehicles, the ability to traverse particular terrains and the speed with which this can be achieved are the most important aspects of performance while, for agricultural vehicles, the efficiency with which a task can be completed or the impact of the operation on the terrain may be of greater significance. The shift in emphasis between vehicle and terrain characteristics is often reflected in the terminology used: trafficability, for example, is defined as "*the ability of a section of terrain to support mobility*" (Muro and O'Brien, 2004), whereas mobility describes the efficiency with which a given vehicle can travel from one point to another across a given section of terrain.

2.1.1 Rolling resistance

For simple transport devices where the wheels are free to rotate, mobility is entirely defined in terms of the force required to tow the wheel across a given terrain. The resistance to motion associated with the wheel is referred to as rolling resistance and, for wheels operating on deformable terrain, is the sum of the resistance to motion from vertical soil compaction, horizontal soil compaction and any deformation of the wheel itself. For pneumatic tyres operating at low inflation pressure on relatively strong soils, rolling resistance is primarily due to the deformation of the tyre and the hysteresis energy losses associated with it. For pneumatic tyres operating at higher inflation pressures

on very soft soils, rolling resistance is almost entirely due to soil compaction (Wong, 2001).

Rolling resistance can be measured experimentally using a single wheel, single axle or a full vehicle. The wheel, axle or vehicle is towed across the terrain of interest at a constant translational speed and the force required measured. Since the level of tyre deformation and soil compaction will be influenced by the applied wheel load, rolling resistance is often expressed in terms of the rolling resistance coefficient, which is defined as the rolling resistance per unit wheel load.

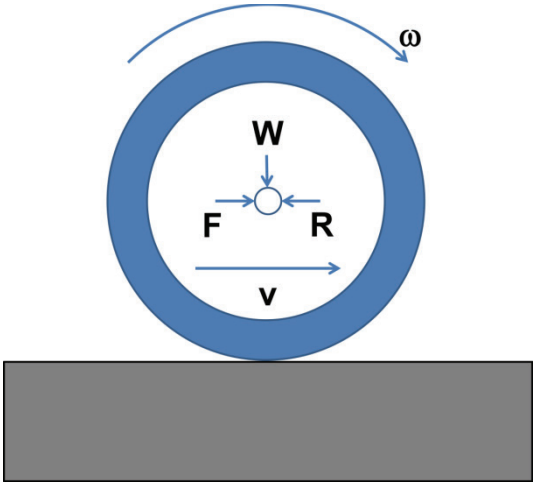

Figure 2.1: Diagram illustrating towing of a rigid wheel

Initial empirical studies into rolling resistance on deformable surfaces focussed on rigid wheels, with the aim of establishing a relationship to describe the effect of vehicle parameters (wheel geometry, load and velocity) and soil properties on the resistance to motion. For flexible wheels, stiffness can also be varied; in the case of pneumatic tyres, this can be achieved by changes to the inflation pressure or tyre construction.

Freitag (1962), as cited by Hetherington and Littleton (1978), investigated the effect of wheel load, diameter and width on rolling resistance using experimental methods, later extending the analysis to include the effects of tyre deflection. Freitag reported that the rolling resistance for a rigid wheel, or a

flexible wheel operating at constant deflection, could be related to wheel diameter, width and load as follows:

$$\frac{RD}{b} = K\left(\frac{W}{b}\right)^{3/2} \qquad \textit{Equation 2.1}$$

2.1.2 Gross tractive force

For transport devices with driven wheels, mobility can be quantified in terms of the thrust that is generated as a result of the applied torque and the resulting interaction between the wheel and soil. For an idealised case where a rigid wheel operates on a non-deformable surface and in the absence of any failure of the interface between the wheel and the terrain, the peripheral velocity of the wheel will equal the translational velocity.

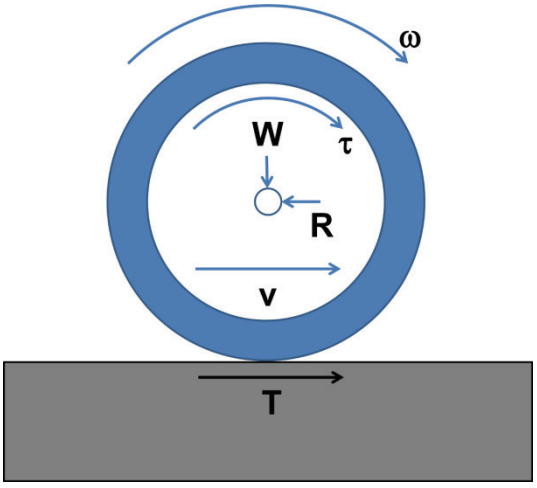

Figure 2.2: Diagram illustrating the generation of tractive force through the interaction of a rigid wheel with a non-deformable surface

One of the earliest mobility prediction models was that developed by Micklethwaite (1944), which assumes that the soil beneath the wheel or track behaves as a rigid body and that mobility is limited by failure within the soil. Micklethwaite's model aims to predict the maximum achievable thrust for a

given vehicle based on the well-known Mohr-Coulomb model for soil shear strength (Equation 2.2), where the influence of vehicle characteristics is accounted for by multiplying both sides of the Mohr-Coulomb equation by the vehicle's ground contact area to determine the maximum traction force, T_{max}, as a function of contact area and vehicle weight (Equation 2.3).

$$\tau = c + p\tan\phi \qquad \textit{Equation 2.2}$$

$$T_{\max} = cA + W\tan\phi \qquad \textit{Equation 2.3}$$

For deformable terrains or where interface failure occurs, however, some degree of relative motion will occur, resulting in a difference between the peripheral and translational velocities of the wheel. This difference in velocity is generally quantified in terms of slip, which is described in terms of a percentage of the difference between the wheel's peripheral and translational velocities (Equation 2.4).

$$S = \frac{\omega r - v}{v} \qquad \textit{Equation 2.4}$$

While Micklethwaite's analysis provided a simple means of assessing a vehicle's maximum traction capability, it did not take account of the soil's deformation characteristics. Janosi and Hanamoto (1961) therefore proposed a modification to Micklethwaite's model, taking into account the effect of the soil's deformation (Equation 2.5) on gross tractive force. The implication of Janosi and Hanamoto's modification to Micklethwaite's model is that gross thrust will increase to the maximum value predicted by Micklethwaite's analysis as a function of soil displacement, as illustrated in Figure 2.3.

$$T = \left(cA + W\tan\phi\right) * \left(1 - e^{-\frac{j}{K}}\right) \qquad \textit{Equation 2.5}$$

Where the the soil's deformation modulus, K, is obtained from small scale soil characterisation tests (Figure 2.4). Gross tractive force provides a measure of the total thrust that is available to overcome resistance to motion and perform useful work. As some resistance to motion will always be present in any experimental assessment of vehicle mobility, gross tractive force cannot be

directly measured, and greater emphasis is often placed on net tractive force or drawbar pull.

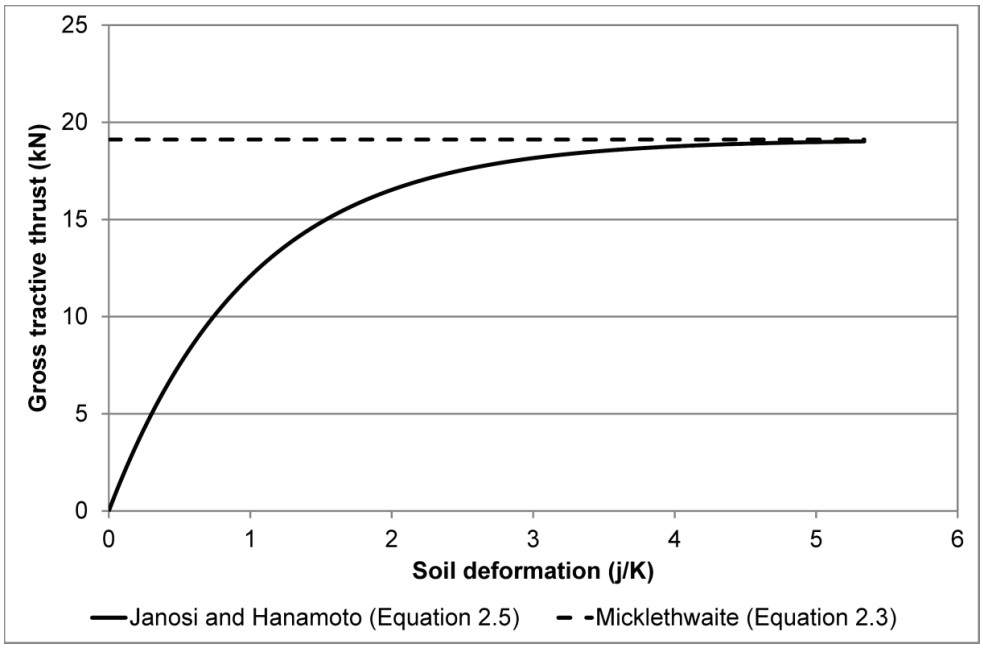

Figure 2.3: Comparison of Janosi and Hanamoto's model for off-road vehicle mobility against Micklethwaite model, illustrating the effect of soil deformation on the gross thrust achievable

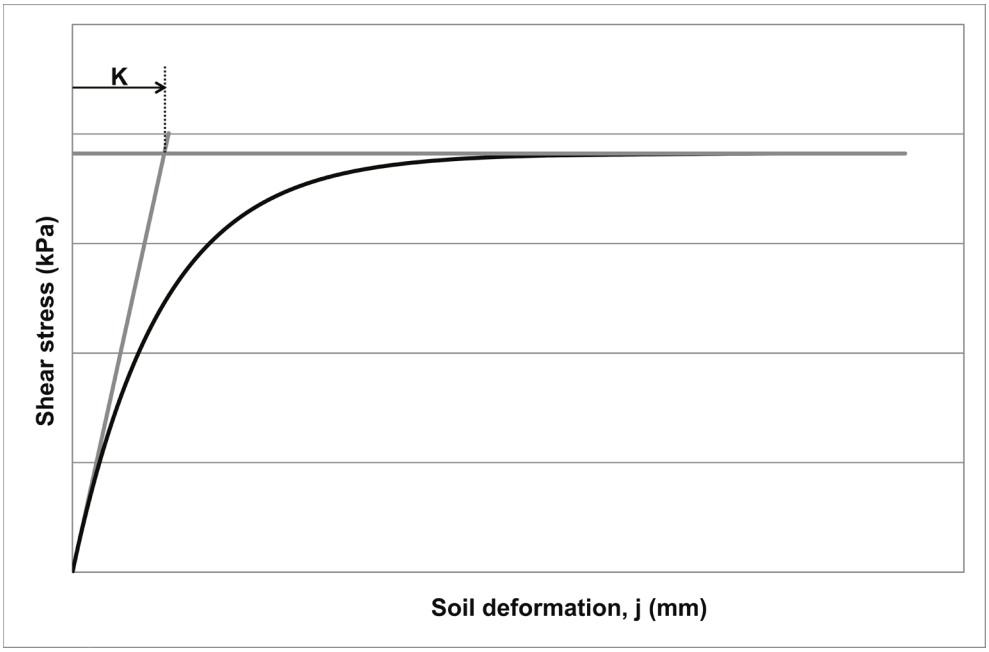

Figure 2.4: Determination of soil deformation modulus, K, for use in Janosi and Hanamoto model for gross tractive force (Equation 2.5)

2.1.3 Net tractive force (drawbar pull)

Net tractive force or drawbar pull represents the 'useful' force that is available to vehicle operators to perform work, which can be used to accelerate, climb gradients and pull loads. As such, it is defined as the difference between the gross tractive force generated by the wheel and the rolling resistance (Equation 2.6).

$$P = T - R \qquad \textit{Equation 2.6}$$

Drawbar pull can be measured experimentally by attaching the vehicle under test to some form of restraint, such as an intelligent winch system (designed to slow the vehicle in a controlled manner) or a second vehicle on which the wheels are locked. The test vehicle is then driven across a given terrain and the resulting drawbar pull measured using a force transducer located between the test vehicle and the restraint (Figure 2.5).

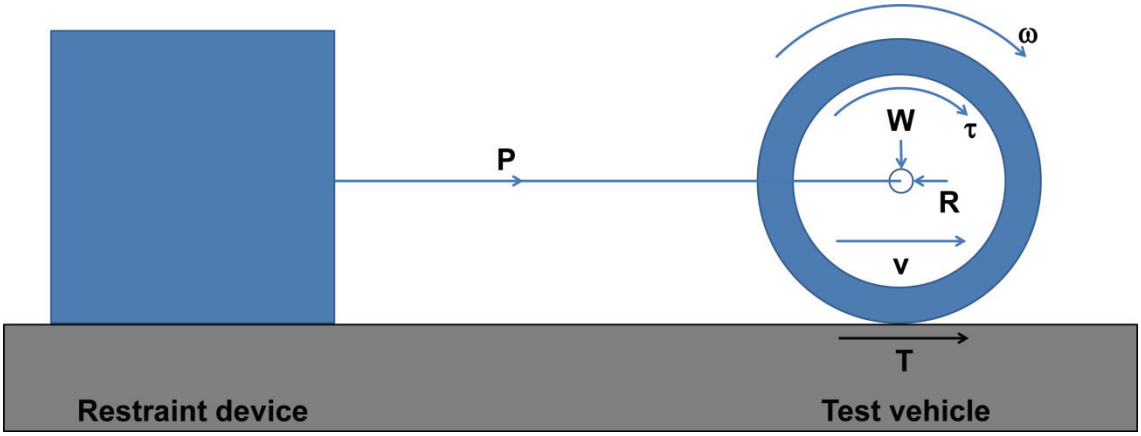

Figure 2.5: Schematic illustration of drawbar pull measurement

2.1.4 Net tractive (drawbar) efficiency

Both gross and net tractive forces vary as a function of soil displacement or slip, with the tractive force increasing to a maximum value with greater soil displacement. As work input is required to deform the soil, an optimum slip condition therefore exists, with additional energy input resulting in greater soil

deformation, but no discernible increase in tractive force. This optimum slip condition can be defined in terms of the peak drawbar efficiency for the wheel / soil system, which can be calculated as the ratio of drawbar power produced to the power input to the wheel (Equation 2.7).

$$\eta = \frac{P v}{\tau \omega} \qquad \textit{Equation 2.7}$$

2.1.5 Performance metrics

In addition to the direct measures of vehicle mobility presented above, a number of performance metrics have been developed over the years to allow the relative mobility of different vehicles to be compared. A number of these metrics also form part of the mobility prediction models discussed in Section 2.2.

2.1.5.1 Vehicle cone index

Vehicle cone index (VCI) was developed by the United States Army's Engineer Research and Development Center (ERDC) at the Waterways Experiment Station (WES) to quantify vehicle mobility in terms of the number of vehicle passes that can be completed over a given piece of terrain before it becomes impassable. The International Society for Terrain Vehicle Systems' (ISTVS) definition of VCI is the "*minimum soil strength in the critical soil layer, in terms of rating cone index for fine grained soils or in cone index for coarse grained soils, required for a specific number of passes of a vehicle*" (Meyer et al., 1977).

To determine VCI, a test vehicle is driven over a soil of known strength several times until immobilisation occurs. The soil strength and number of passes achieved before vehicle immobilisation are recorded, with the number of passes serving as a measure of the vehicle's mobility on that terrain. This test procedure is then repeated for a range of different soil strengths, allowing a plot of the number of vehicle passes against soil strength to be produced for a given vehicle. Once a relationship between soil strength and vehicle passes has

been established, extrapolation allows the limiting soil strength required for a single vehicle pass to be determined. The limiting soil strength for a particular number of passes (typically 50) may also be determined using this method.

For VCI and a number of other metrics, soil strength is quantified in terms of the cone index (CI), where a cone shaped penetrator is forced into the soil. The force required to penetrate the soil using the cone penetrometer provides a measure of the soil's strength. The above ISTVS definition of VCI refers to a critical soil layer, which is the layer of soil which has the greatest influence on vehicle mobility: the depth of this critical layer, however, is dependent on wheel load and contact patch dimensions for wheeled vehicles. According to a review of the VCI performance metric by Priddy and Willoughby (2006), the critical layer is the region between 150 and 300mm below the soil's surface for most vehicles, with the CI value used to describe a given soil being the average of a series of values measured at a number of specified depths.

Due to the relative simplicity of the test, and the fact that measurements of soil strength can be undertaken in-situ, cone index has been widely used as a measure of soil strength and vehicle mobility, since a map of soil trafficability can readily be constructed by comparing the VCI value for a vehicle against in-situ measurements of soil strength. This is particularly true in the case of military operations, where VCI forms the basis of the NATO reference mobility model (NRMM) for predicting the mobility of military vehicles.

While VCI and the cone index test are relatively straightforward methods of quantifying vehicle mobility, the approach relies on the assumption that soil strength reduces with multiple vehicle passes. Maclaurin (2007) conducted a review of traction models for military vehicles, concluding that "*VCI tests and [drawbar pull] tests produce markedly different values of limiting go / no go soil strength*", and that other methods of quantifying vehicle mobility may be more realistic though less easy to perform.

2.1.5.2 Mobility Index

Mobility Index (MI) forms part of a set of empirical models developed by WES to predict the performance of wheeled and tracked vehicles. The mobility index for a given vehicle is based on a series of factors considering contact pressure (CPF), vehicle mass (WF), wheel load (WLF), wheel geometry and tread pattern (TEF and GF), ground clearance (CF), engine power (EF) and a transmission factor (TF) depending on whether the vehicle's transmission is manual or automatic (Equation 2.8).

$$MI = \left(\frac{CPF * WF}{TEF * GF} + WLF + CF \right) * EF * TF \qquad \textit{Equation 2.8}$$

2.1.5.3 Mean maximum pressure

The mean maximum pressure (MMP) metric for quantifying off-road vehicle mobility was developed by the UK Ministry of Defence (MOD), and takes the vertical pressure exerted by the vehicle on the soil as the most significant factor in determining vehicle mobility, with MMP defined as the mean of the peak vertical pressures that occur in the soil under each wheel. MMP is used as a primary assessment criterion in Defence Standard (Def. Stan.) 23-06, with vehicles divided into a series of mobility classes (high mobility, medium mobility etc.) depending on the ground pressure they exert.

As with the mobility index, MMP can subsequently be used to predict VCI based on empirical relationships between the two metrics. The first stage is to calculate MMP for the vehicle in question, based on the wheel load, the number of axles and the wheel's width, diameter and deflection. The formula for the calculation of MMP has been the subject of several revisions since its original derivation by Rowland (1972): the modified formula derived by Larminie (1992) for wheeled vehicles operating on fine grained soils (clay, cohesive soils) is given in Equation 2.9, while that for wheeled vehicles operating on coarse grained soils (sand, frictional soils) is provided in Equation 2.10. The primary modification introduced by Larminie was to extend the applicability of the MMP model to include low profile tyres; this was achieved by using the ratio of the

tyre deflection to the tyre diameter rather than the ratio of tyre deflection to section height, which could lead to the under-prediction of MMP for low profile tyres.

$$MMP = \frac{kW}{2mb^{0.85}D^{1.15}\left(\frac{\delta}{D}\right)^{0.5}} \qquad \textit{Equation 2.9}$$

Table 2.1: Definition of factor, k, in calculation of mean maximum pressure (Equation 2.9) for wheeled vehicles on fine grained soils

Number of axles	Proportion of axles driven						
	1	3/4	2/3	3/5	1/2	1/3	1/4
2	1.83	-	-	-	2.2	-	-
3	1.95	-	2.17	-	-	2.62	-
4	2.05	2.22	-	-	2.48	-	3.02
5	2.16	-	-	2.48	-	-	-
6	2.30	-	2.57	-	2.77	3.10	-

$$MMP = \frac{STW^{1.3}}{2mb^{1.5}D^{1.5}\left(\frac{\delta}{D}\right)} \qquad \textit{Equation 2.10}$$

Table 2.2: Definition of proportionality constant, S, and tyre tread factor, T, in calculation of mean maximum pressure for wheeled vehicles operating on coarse grained soils (Equation 2.10)

Vehicle type	Proportionality constant, S	Tyre type	Tyre tread factor, T
All-wheel drive	0.31	Smooth	1
4 x 2	0.37	Road	1.4
6 x 4	0.35	Road / cross	2.8
8 x 6	0.34	Earth mover	3.3
8 x 4	0.38	-	-

As discussed by Priddy and Willoughby (2006), MMP is an indirect measure of off-road vehicle mobility, relating solely vehicle characteristics to the expected level of performance. Both mobility index and mean maximum pressure are purely vehicle related performance metrics, with the influence of specific soil properties on vehicle mobility only considered once the vehicle limiting soil condition (VCI) has been established.

2.1.5.4 Wheel numerics

An alternative approach to the solely vehicle-based metrics was employed by Freitag (1965), who used dimensional analysis of previous experimental trials on sand to develop a performance metric incorporating both wheel and soil parameters. Within the resulting 'sand number' (Equation 2.11), soil strength is represented by the gradient of the cone index with depth, rather than a characteristic cone index value.

$$\text{Sand Number} = \frac{G_{CI}(bD)^{3/2}}{W} \qquad \textit{Equation 2.11}$$

Wismer and Luth (1974) later used a similar approach to define a wheel numeric for rigid wheels operating on cohesive / frictional soils (Equation 2.12), which was related to soil cone index, wheel geometry and load.

$$C_n = \frac{CIbD}{W} \qquad \textit{Equation 2.12}$$

One drawback of the wheel numeric approach is the use of different expressions depending on the type of soil being considered. Using wheel numerics to model vehicle mobility across a wide range soils, therefore, results in three overlapping curves. As will be discussed in more detail in Chapter 3, naturally occurring soils represent a continuous spectrum, with no clearly defined boundaries between cohesive soils, frictional soils and those displaying a mixture of cohesive and frictional behaviour.

2.1.5.5 Mobility number

As discussed by Crossley et al. (2001), the approach used by Freitag to relate rolling resistance to wheel load, diameter and width was later developed by Turnage (1972) to define a performance metric for flexible wheels operating on soft soils (Equation 2.13). The influence of soil strength was described in terms of the cone index, while the flexibility of the wheel was described by the ratio between the tyre's deflection and section height. This mobility number, M, was then empirically related to rolling resistance by authors such as Gee-Clough (1980) and McAllister (1983).

$$M = \frac{CIbD}{W}\sqrt{\frac{\delta}{h}}\left(\frac{1}{1+{}^{b}\!/_{2D}}\right) \qquad \textit{Equation 2.13}$$

Brixius (1987) suggested an alternative expression for assessing the relative off-road mobility of wheeled vehicles. As with the wheel numeric methods presented above, Brixius's model was based around both vehicle and soil parameters: Brixius's mobility number essentially modified the wheel numeric, originally derived by Wismer and Luth (Equation 2.12), introducing terms to describe tyre deflection and the tyre's width to diameter ratio (Equation 2.14).

$$B_n = \frac{CIbD}{W}\left(\frac{1+{}^{5\delta}\!/_{h}}{1+{}^{3b}\!/_{D}}\right) \qquad \textit{Equation 2.14}$$

2.2 Mobility prediction models

The above section discusses some of the approaches used to quantify the mobility of wheeled vehicles operating on soft soils. While the performance metrics presented go some way to describing the influence of vehicle and, in some cases, soil parameters on vehicle mobility, they only attempt to predict the relative performance of candidate vehicles, rather than predicting a specific level of rolling resistance, drawbar pull or efficiency. For vehicle designers and tyre manufacturers, trial and error represents a very costly and time consuming approach to optimising off-road vehicle mobility. For this reason, the ability to

predict off-road mobility from a range vehicle and terrain parameters has been the focus of many researchers.

The methods used to predict mobility are many and varied, but can generally be grouped into one of three categories:

- empirical methods, which seek to describe observations made during physical tests;
- semi-empirical and analytical methods, which seek to at least partially describe the physical processes involved in tyre / soil interaction;
- numerical methods, which also seek to describe the physical processes involved, but rely on numerical simplification methods to obtain a solution.

2.2.1 Empirical mobility models

Empirical mobility models seek to relate vehicle and terrain characteristics to experimental observations. In general, the empirical models that have been used to predict off-road vehicle mobility are predicated on some form of performance metric, determined from some combination of soil properties and vehicle characteristics, which is then related to rolling resistance and drawbar pull through one or more empirical equations.

For the performance metrics based on vehicle parameters, such as the mobility index and mean maximum pressure, vehicle cone index is first calculated using an empirical relationship such as that presented in Equation 2.15 (Wong, 2001). The resulting vehicle cone index can then be used to predict maximum drawbar pull and rolling resistance, based on the difference between the vehicle cone index value and the cone index of the soil to be traversed. For example, Equation 2.16 describes the relationship between the excess rating cone index (RCI_x) and drawbar pull coefficient reported by Ciobotaru (2009) for tyres with a ground pressure of greater than 28kPa operating on silty sand, while Equation 2.17 describes the relationship for clayey soils.

$$VCI_1 = \left(7.0 + 0.2 * MI - \left(\frac{39.2}{MI + 5.6}\right)\right) * \left(\frac{0.15}{\delta/h}\right)^{1/4} \qquad \textit{Equation 2.15}$$

$$\frac{P}{W} = 0.5200142 - \frac{4.5585}{RCI_x + 8.117059} + 0.374746007 \qquad \textit{Equation 2.16}$$

$$\frac{P}{W} = 0.6152356 - \frac{6.183363}{RCI_x + 9.258565} + 0.05261765 \qquad \textit{Equation 2.17}$$

Empirical mobility models based on performance metrics which include both vehicle and soil parameters do not typically use vehicle cone index as an intermediate stage to predict rolling resistance or tractive force. Wismer and Luth, for example, related their wheel numeric to the coefficients of rolling resistance and gross tractive force through Equations 2.18 and 2.19. Importantly, the wheel numeric method derived by Wismer and Luth also attempts to include the effect of wheel slip on gross tractive force (Equation 2.19), using a similar relationship to that derived by Janosi and Hanamoto.

$$\frac{R}{W} = \frac{1.2}{C_n} + 0.04 \qquad \textit{Equation 2.18}$$

$$\frac{T}{W} = 0.75 * \left(1 - e^{-0.3 C_n S}\right) \qquad \textit{Equation 2.19}$$

Equation 2.20 describes the relationship established by Brixius between mobility number, B_n, and the drawbar pull coefficient, where the first term represents the gross traction generated by the tyre and the second represents the rolling resistance coefficient. One significant difference between the relationships established by Brixius and Wismer and Luth, is the inclusion of slip in the second term of Equation 2.20, such that rolling resistance is also defined as a function of slip. As noted by Onafeko (1969), the common assumption that rolling resistance is constant and equal to that measured using a towed wheel is erroneous.

$$\frac{P}{W} = \left[0.88 * \left(1 - e^{-0.1 * B_n}\right) * \left(1 - e^{-7.5 * S}\right)\right] - \left(\frac{1}{B_n} + \frac{0.5S}{\sqrt{B_n}}\right) \qquad \textit{Equation 2.20}$$

The models discussed thus far employ a single parameter, the cone index, to describe soil strength. More recent empirical studies, undertaken by Upadhyaya et al. (1989, 1993 and 1997) have reported that cone index alone is insufficient to describe the influence of soil properties on vehicle mobility. Cone index may be regarded as a composite material property, which is dependent upon both the compressive and shear properties of the soil. Upadhyaya and Wulfsohn (1993) therefore developed a set of semi-empirical equations to predict net tractive force, based on the soil's plate sinkage profile, cohesion, friction angle and shear modulus.

Of the empirical models identified above, the influence of vehicle translational speed on off-road mobility is not directly addressed. Coutermarsh (2007) completed a primarily experimental study to assess the effect of translational speed on rolling resistance for pneumatic tyres operating on dry sand, which included a comparison with models developed at the US Army's Waterways Experiment Station (WES) and the Engineer Research and Development Center (ERDC) Cold Regions Research and Engineering Laboratory (CRREL) for aircraft tyres operating on soft surfaces. The WES model is based around a modified version of the sand mobility number, which is first used to calculate wheel sinkage and then rolling resistance as a function of translational speed. In the dynamic sand mobility number, the standard mobility number expression (Equation 2.11) is multiplied by a dynamic factor, D, accounting for loading rate effects in terms of the 'pulse time', which is defined as the length of the wheel / soil contact interface divided by the vehicle's translational speed. The dynamic rolling resistance is quantified using two terms, the first representing the low speed rolling resistance and the second the additional 'slush' drag caused by horizontal displacement of the soil around the tyre.

The fundamental drawback of all empirical models is that they are inherently ill-suited to mobility *prediction*: their development relies on costly and time consuming experimental trials, while their application is generally limited to

conditions similar to those studied during their derivation. This is exemplified by the number of studies reported in the literature (for example, Elwaleed et al., 2006, and Tiwari, Pandey and Pranav, 2010) where researchers have compared empirical model predictions of rolling resistance or drawbar pull against experimental results and proposed alternative coefficients for existing models or entirely new empirical relationships. As discussed by Larminie in his review of the MMP model, the accuracy of empirical models can also be severely limited by the quality of the experimental data used to derive them. Closely controlled experiments are therefore required to reduce scatter and allow trends to be clearly identified.

2.2.2 Semi-empirical mobility models

Semi-empirical mobility models seek to improve on the limited predictive capability of empirical models by representing some of the physical processes involved in tyre / soil interaction. One of the most commonly referenced researchers in this area is Bekker (1956), who developed a semi-empirical expression for rolling resistance based on the analogy that a rigid wheel could be represented by a rectangular plate of equal width. As such, soil properties were described using a form of Bernstein's pressure sinkage equation for a rigid footing:

$$p = kz^n \qquad \textit{Equation 2.21}$$

Since the soil sinkage modulus, k, depends on the width of the plate used, Bekker proposed the following modification to account for variations in width, b:

$$k = \frac{k_c}{b} + k_\phi \qquad \textit{Equation 2.22}$$

Bekker's rolling resistance analysis was two-dimensional and based upon the assumption that the soil's reaction to wheel loading is purely radial, such that the rolling resistance is equal to the work done in vertically compacting the soil to a depth, z_0 (Equation 2.23). In order to determine rolling resistance,

therefore, wheel sinkage (z_0) must first be determined as a function of wheel load (Equation 2.24).

$$R_c = \int_0^{z_0} bp\partial z = \frac{bkz_0^{n+1}}{(n+1)} \qquad \textit{Equation 2.23}$$

$$Z_0^{n+1/2} = \frac{3W}{bk\sqrt{D}(3-n)} \qquad \textit{Equation 2.24}$$

Substituting this expression for sinkage into Equation 2.23 then leads to the following equation for rolling resistance as a function of wheel load, diameter, width and soil properties:

$$R_c = \frac{bk}{(n+1)}\left[\frac{3W}{bk\sqrt{D}(3-n)}\right]^{\frac{2n+2}{2n+1}} \qquad \textit{Equation 2.25}$$

Grahn (1991) later extended Bekker's semi-analytical approach to account for dynamic soil loading by undertaking a series of plate sinkage tests in a sandy loam soil at speeds of between 20 and 800mm/s. Given the dependence of the resulting plate sinkage profiles on the rate of penetration, Grahn proposed the following modification to the Bernstein / Bekker's sinkage model to account for loading rate effects:

$$p = kz^n \dot{z}^m \qquad \textit{Equation 2.26}$$

Having related the soil's resistance to penetration to the rate of loading, Grahn went on to relate rolling resistance to translational speed for a rigid wheel. No comparison is provided with experimental rolling resistance data, which limits user confidence in its predictions. The accuracy of the original Bekker model was assessed as part of a review of rolling resistance theories for rigid wheels undertaken by Willis, Barrett and Shaw (1965). The review concludes that the Bekker model significantly underestimates rolling resistance for rigid wheels operating on deformable terrain, and that other factors such as horizontal soil compaction and bow wave formation (Figure 2.6) must also be considered.

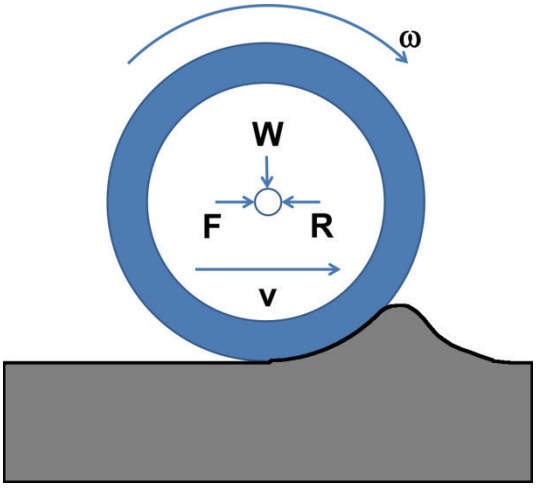

Figure 2.6: Bow wave formation in front of a towed rigid wheel

As cited by both Gee-Clough (1979) and Plackett (1985), Bekker (1976) later expanded the two dimensional analysis discussed above to include the contribution of bulldozing to rolling resistance. The bulldozing component of rolling resistance resistance, R_b, represents the resistance to wheel motion caused by horizontal soil displacement. Bekker proposed two different expressions for bulldozing resistance, with the contribution from the soil's cohesion depending on the extent of shear failure within the soil. For general shear failure:

$$R_b = b\left(z_0 c K_c + 0.5 z_0^{\,2} \gamma K_\gamma\right) \qquad \textit{Equation 2.27}$$

While for local shear failure, the contribution from soil cohesion is reduced by one third:

$$R_b = b\left(0.667 z_0 c K_c + 0.5 z_0^{\,2} \gamma K_\gamma\right) \qquad \textit{Equation 2.28}$$

In both cases, the resistance to motion due to horizontal soil displacement is directly related to the wheel's width, b. From Equation 2.25, the relationship between the rolling resistance due to vertical soil compaction and wheel width is more complex, with the soil's sinkage modulus, k, also varying as a function of wheel width. The relative contributions of bulldozing and vertical soil compaction to the total rolling resistance will depend on the wheel's width to diameter ratio, with the resistance due to bulldozing increasing rapidly as wheel width is increased. Gee-Clough investigated the effect of the wheel's width to

diameter ratio experimentally and reported that, for a constant sinkage, the effect of width on bulldozing resistance was more pronounced than that suggested by equations 2.27 and 2.28. One of the key findings of Gee-Clough's experimental work was that in sandy soils, multiple narrow wheels produce a much lower level of rolling resistance than a single wide wheel.

Hetherington and Littleton (1978) proposed an alternative expression for rigid wheels operating on purely frictional soils (Equation 2.29), based on Terzaghi's expression for bearing capacity (Equation 2.30). The authors report that this approach is more readily applicable than Bekker's method because the soil constants used – bulk density and friction angle – are more widely available than those associated with Bekker's plate sinkage tests. Again, however, rolling resistance is equated to the work done in vertically compacting the soil to form a rut. As noted by Wong and Reece (1967), the plate sinkage analogy that underpins the approach used by Bekker, and later by Hetherington and Littleton, requires that the maximum stress within the soil body is located directly beneath the centre of the wheel. Experimental work reported by Onafeko and Reece (1967), however, concluded that the stress distribution along the contact patch has a peak forward of the wheel's centre, and that the location of maximum radial stress moves further forward as slip is increased.

$$R = \left(\frac{2W^4}{bD^2 \rho N_q} \right) \qquad \textit{Equation 2.29}$$

$$N_q = \frac{e^{\left(\frac{3\pi}{2} - \phi\right)\tan\phi}}{2\cos^2\left(\frac{\pi}{4} + \frac{\phi}{2}\right)} \qquad \textit{Equation 2.30}$$

2.2.3 Analytical mobility models

Like the semi-empirical models described above, analytical mobility models seek to improve on the predictive capability of empirical methods by including the physical processes involved in tyre / soil interaction. Unlike empirical or semi-empirical methods, analytical models seek to represent the radial and

tangential stress distributions that exist at the tyre / soil interface, from which rolling resistance, drawbar pull and traction efficiency can then be determined (Senatore and Sandu, 2011). Due to the complexity of the tyre / soil interaction problem, which includes dynamic contact between two deformable bodies, non-linear materials and large deformations, analytical models generally employ some form of simplification to yield a tractable solution.

For most of the analytical methods reported in literature, the radial soil reaction is calculated based on the pressure sinkage relationship proposed by Bekker (Equation 2.31), while the tangential stress distribution is described by a relationship similar to that proposed by Janosi and Hanamoto (Equation 2.32). Providing the distribution of radial and tangential stresses can be described as functions of angular position, the total vertical and horizontal forces acting on the wheel can be determined.

$$p = \left(k_1 + k_2\right) * \left(\frac{z}{b}\right)^n \qquad \textit{Equation 2.31}$$

$$\tau = \left(c + p\tan\phi\right) * \left(1 - e^{-j/K}\right) \qquad \textit{Equation 2.32}$$

Fundamental to the development of analytical mobility prediction models is the ability to describe the shape of the wheel / soil interface. One of the most common simplifications used, therefore, is to assume that either the tyre or terrain may be regarded as rigid, as this greatly simplifies the geometry of the contact patch. An analytical framework for the prediction of rolling resistance, gross tractive force and drawbar pull is outlined by Muro and O'Brien (2004) for rigid wheel systems. The approach outlined may be summarised as follows:

1. Wheel load, radius, width and either the peripheral or translational velocity are provided as vehicle input parameters, along with a set of fifteen additional input parameters to describe the soil;
2. Entry and exit angles, defining the position and length of the contact patch and the amount of wheel sinkage, are determined using an iterative calculation procedure, ensuring that vertical equilibrium is satisfied;

3. Final normal and shear stress distributions are established, which can be integrated to determine the tractive force and rolling resistance for the wheel as a whole.

A similar approach may be used for flexible wheels and tyres, although the shape of the interface between the wheel and soil is no longer known in advance. As cited by Muro and O'Brien, Karafiath and Nowartzki (1978) proposed that the contact patch could be represented by a central inclined straight line segment with logarithmic spiral lines located at either end. Wong (1989) suggested a simpler contact patch geometry, with a central straight line bounded by circular arc segments. Okello (1992) later developed an analytical model to predict tyre / soil interface forces based on work reported by Qun et al. (1987), which suggested that the contact interface could be represented by a horizontal line with a logarithmic spiral at the leading end, providing the soil was relatively hard and sinkage was limited.

Rather than assuming an initial interface shape, researchers such as Baladi and Rohani (1984) have developed alternative analytical models where the tyre and soil are represented as radial springs arranged in series. The shape of the tyre / soil interface can then be calculated, based on the applied boundary conditions, and the radial and tangential stresses integrated as before to predict rolling resistance and drawbar pull.

Van Es (1998), cited by Coutermarsh, developed an analytical model addressing the influence of translational speed on rolling resistance for pneumatic tyres operating on snow. In a similar manner to the empirical dynamic sand mobility number approach, Van Es's dynamic rolling resistance model is made up of two components, addressing the work required to compact the snow and the work required to accelerate and displace the snow around the wheel. In attempting to apply the Van Es model to a pneumatic tyre operating on dry sand, Coutermarsh notes that both the predicted wheel sinkage and the compaction component of the total rolling resistance are independent of translational speed, with rate dependence coming solely from inertial effects. The lack of loading rate effects in the prediction of wheel sinkage contradicts

the findings of Grahn's experimental / semi-analytical study on sandy loam and the results of Coutermarsh's experimental work on dry sand.

Dagan and Tulin (1969) used an analytical approach to study the behaviour of soils beneath moving wheels. Inertial effects were ignored within the analysis, with the authors stating that their inclusion would complicate the mathematical problem considerably, although it was acknowledged that inertial effects may be significant for certain combinations of soil strength, soil density and translational speed. The authors proposed the use of a dimensionless number, H, to indicate the relative importance of inertial effects in cohesive soils:

$$H = \frac{\rho v^2}{c} \qquad \textit{Equation 2.33}$$

For very small values of H, Dagan and Tulin suggested that inertial effects may be ignored. While the limiting H value at which inertial effects become significant is not clearly defined, a value of unity is used as an example of a case where inertial effects could no longer be neglected. Assuming a soil density of 1,820kg/m^3, cohesion of 10kPa and setting H equal to 1, Equation 2.33 suggests that inertial effects must be taken into account for a translational speed of 2.34m/s (5.15mph).

One of the benefits of an analytical approach, compared with the simpler empirical and semi-empirical methods discussed previously, is the ability to calculate normal and shear stress distributions beneath the wheel, providing a better understanding of soil deformation and compaction. The vast majority of the existing analytical models, however, are based on a two-dimensional analysis, only accounting for the in-plane soil displacements and neglecting the out-of-plane soil flow associated with narrow wheels.

2.2.4 Finite and discrete element models

A promising alternative to the analytical methods described above is the use of FE analysis, in which the complex problem of tyre / soil interaction is broken down into a finite number of small segments. The segments or elements within

a given component are interconnected at nodes, allowing the response of the continuum to applied loads to be determined by approximating the behaviour of individual elements. Using constitutive models to represent the material linking the nodes within the simulation, equilibrium equations are developed, which can then be solved to yield nodal displacements.

Early FE mobility prediction models, such as those developed by Perumpral et al. (1971), Chung and Lee (1975) and Yong and Fattah (1976) made use of similar simplifications to those employed in the analytical models discussed above, representing a rigid wheel interacting with a deformable terrain. The development of these early two-dimensional FE models relied heavily on the experimental work undertaken by authors such as Onafeko and Reece, however, with the wheel described in terms of either a force (Perumpral et al.) or displacement (Yong and Fattah) boundary condition. As such, their predictive capability was limited, although the FE method did permit the use of more complex soil models, such as the viscoelastoplastic model employed by Chung and Lee to investigate the effect of dynamic loading on wheel sinkage.

Later work by Yong et al. (1978) sought to increase the applicability of the FE method by the introduction of a flexible wheel. As with the rigid wheel study by Yong and Fattah, drawbar pull was calculated based on an energy balance approach, where tyre deformation represents an additional mechanism for dissipation of input energy, alongside soil deformation and interfacial energy. As with the analysis reported by Perumperal et al., the flexible wheel is described using a nodal force boundary condition applied to the two-dimensional soil mesh. The length of the contact patch is determined using an iterative procedure based on the Hertz theory of contact between two elastic bodies.

More recent models, such as that reported by Fervers (2004), have addressed the two-dimensional interaction of a non-linear elastic tyre with a deformable terrain using an explicit representation of the tyre. Contact algorithms within the FE code were then used to calculate the relative deformations of the tyre and soil in response to the applied boundary conditions, improving the predictive

capability of FE mobility prediction models. As a consequence of the two-dimensional analysis approach used, the tyre was effectively represented as a series of non-linear springs connecting the tyre tread to the wheel centre. The rolling tyre was represented in the analysis using a series of static simulations, neglecting the effects of dynamic wheel loading, with a piecewise linear translation applied to the wheel.

As the speed of engineering workstations and personal computers have increased, three-dimensional representations of tyre / soil interaction have become more feasible. Chiroux et al. (2005) reported a three-dimensional soil compaction model using ABAQUS/Explicit, which was used to study the interaction between a rigid wheel of finite width interacting with a deformable soil. Modelling results were compared with experimental data in terms of rut depth and the peak normal and shear stresses occurring beneath a rigid wheel. Good agreement is reported with experimental results for peak normal stress and rut depth, although it is noted that the rut depths predicted by the model may be significantly affected by the degree of soil recovery. The authors report that soil recovery after passage of the wheel is significantly over-predicted by the model, implying that the predicted dynamic sinkage of the wheel is greater than that observed during experimental tests.

Hambleton (2006) conducted a study of test rolling in clay using a three-dimensional FE model in ABAQUS/Explicit. The study focussed on modelling of rigid wheels towed through clay using an elastic / perfectly-plastic material model for the soil. Experimental validation was undertaken for the rigid wheel condition, while a small number of additional modelling runs were undertaken using a simplified pneumatic tyre model with linear elastic material properties.

The vast majority of FE mobility prediction models reported to date in the literature employ a Lagrangian representation of the soil body, where the FE mesh deforms with the soil. Due to the relatively low strength and stiffness of soils, and the occurrence of large and highly localised deformations, the application of Lagrangian solution methods is generally limited, particularly at high values of slip, around lugs and where ‘cohesionless’ soils are under

investigation. In recent years, therefore, a number of studies have investigated the use of alternative solution methods, with particular emphasis placed on mesh-free representations of the soil body, such as discrete element modelling (DEM).

An example of this approach is provided by Nakashima and Oida (2004), who considered the case of an agricultural tyre's lug coming into contact with a large body of soil. In this case, the tyre's lug acts as a singular point of stress on the soil, and the soil does not accurately deform around the lug when using a Lagrangian formulation. Nakashima reports on the use of a discrete element (DE) approach to representing the soil, where the soil is represented by an array of individual particles. The approach is demonstrated using a 2D FE / DE simulation of a smooth tyre vertically sinking into a body of linear elastic soil and, as such, the potential benefits of mesh free analysis methods are not fully demonstrated.

Nakashima et al. (2010) have more recently undertaken a combined modelling and experimental study to assess the single wheel performance of a small lunar rover on sloped terrain. In their study, a range of rigid, lugged wheels were assessed using a discrete element approach to represent an inclined soil bin; a simplified two-dimensional analysis was undertaken, acknowledging that previous attempts to develop a three-dimensional mobility prediction model have proved difficult. Within the simulation, the interaction between soil particles is controlled using spring constants, which are derived using a trial and error approach, with the selection of particular values justified by comparison with experimental results.

The lack of a defined procedure for developing material models based on experimental soil characterisation evidently limits the predictive capability of the model. In particular, it is noted that, while the soil under investigation displays some cohesion (2.5kPa), the DEM implementation used does not account for tensile forces between particles. This simplification is also used by Oberymayr et al. (2011) to represent tool / soil interaction using DEM. While there are clearly parallels between a DEM approach and the particulate nature of many

soils, computational cost currently prevents the size of the discrete elements from being comparable to that of the soil particles under investigation (Shmulevich, 2010). There are also likely to be significant differences between macro and micro scale modelling methods, in terms of the material models required to describe the soil's behaviour.

Table 2.3: Summary of selected FE mobility prediction models reported in literature

Reference	Tyre	Soil model	Symmetry	Contact
Perumpral et al. (1971)	Rigid	Lagrange: piecewise linear elastic	Axisymmetric / Plane strain	Nodal force boundary
Chung and Lee (1975)	Rigid	Lagrange: viscoelastic-plastic	Plane strain	Nodal force boundary
Yong and Fattah (1976)	Rigid	Lagrange: piecewise linear elastic	Plane strain	Nodal displacement boundary
Yong et al. (1978)	Linear elastic	Lagrange: piecewise linear elastic	Plane strain	Nodal force boundary
Foster et al. (1995)	Rigid	Lagrange: non-linear elastic	Plane strain	Nodal displacement boundary
Liu and Wong (1996)	Rigid	Lagrange: critical state	Plane strain	Contact algorithm

Table 2.3 (continued): Summary of FE mobility prediction models reported in literature

Reference	Tyre	Soil model	Symmetry	Contact
Fervers (2004)	Non-linear elastic	Lagrange: Drucker Prager / cap plasticity	Plane strain	Contact algorithm
Chiroux et al. (2005)	Rigid	Lagrange: Drucker Prager / cap plasticity	Three dimensional	Contact algorithm
Hambleton (2006)	Rigid / flexible	Arbitrary Lagrangian Eulerian: elastoplastic	Three dimensional	Contact algorithm
Nakashima et al. (2010)	Rigid, lugged	Discrete element: frictional	Plane strain	Contact algorithm
Grujicic et al. (2009)	Flexible	Lagrange: visco-plastic	Three dimensional	Contact algorithm

With the exception of studies by Chung and Lee (1975) and Grujicic et al. (2009), the FE mobility models developed to date have not directly addressed the effect of vehicle translational velocity on off-road mobility. Like the analytical mobility models discussed above, a common assumption in FE studies is that the vehicle's translational speed is sufficiently low that rate effects may be neglected without adversely affecting the accuracy of the results obtained. While this assumption simplifies the analysis and material characterisation requirements, it also limits the applicability of an FE approach to the low speed region. For problems involving higher translational speeds,

such as aircraft operating on unpaved airfields or off-road robotic vehicles, loading rate effects can no longer be neglected.

2.3 Summary

The main findings of the literature review can be summarised as follows:

- A wide range of methods are available to quantify off-road mobility. For military vehicles, indirect measures of mobility, such as VLCI and MMP are frequently used to specify performance requirements. Direct performance measurements such as rolling resistance and drawbar pull are potentially more useful for vehicle users and procurers when assessing how a vehicle is likely to perform on the expected range of terrains.
- Historically, assessment of off-road vehicle mobility has relied heavily on experimental testing. The variability of naturally occurring soils can lead to a significant level of scatter in experimental results, which may mask the influence of the variables under investigation. This is particularly true in the case of full scale trials, where control over soil properties is more limited than in single wheel or small scale testing.
- Early mobility models were primarily empirical in nature, and described the observations from experimental trials. As such, the accuracy of these models was dependent on the quality of the experimental results used to derive them, and their predictive capability was limited beyond the studied range of vehicle and terrain variables.
- Analytical mobility models provide greater predictive capability, since they are based on a representation of the physical processes involved, but often rely on simplifying solutions to make the problem of tyre / soil interaction tractable. By simplifying the problem in this manner, some level of resolution is lost, which may affect the accuracy of the results obtained.

- Numerical models based on FE analysis have been developed more recently. Early models of this type used similar simplifications to the analytical models, or relied on analytical models or experimental observations as inputs and, as such, were subject to many of the same limitations. As computing power has increased, and FE analysis codes have become more advanced, numerical models have been able to retain a higher level of fidelity.
- The current state of the art in off-road mobility prediction is represented by three dimensional numerical models with explicit time integration, using a non-linear representation of the pneumatic tyre in contact with a soil model capable of large localised deformations. While much progress has been made using DEM to represent soils in the virtual environment, the computationally intensive nature of a DEM solution and the physical size of the soil particles being represented has prevented its use to predict the mobility of full scale passenger vehicles.
- As such, the majority of recent modelling studies have retained a Lagrangian representation of the terrain, where the computational mesh deforms with the soil. Due to the large, localised soil deformtions that are often observed during tyre soil interactions, particularly in frictional soils such as dry sand, these Lagrange methods are not generally applicable, and a more consistent approach for the modelling of large volumes of soil is required.
- Given the inherently dynamic nature of the interaction between wheel and soil, mobility prediction tools should seek to capture any rate dependent behaviour in an effort to ensure the accuracy of the predictive tool across the full range of expected operational speeds. To date, a relatively limited amount of work has been completed in this area, with the majority of studies limited to the low speed region (0.1 – 5.5m/s).

Chapter 3: Soil modelling

As discussed, the aim of an off-road mobility prediction model is to describe, either directly or indirectly, the influence of vehicle and terrain characteristics on a vehicle's ability to traverse a deformable terrain. Many of the existing empirical and semi-empirical mobility models use cone index as a means of describing the soil's influence on vehicle mobility, but this has been called into question by authors including Bekker (1956) and Upadhyaya (1993), both of whom proposed that more complex descriptions of soil behaviour are required for the accurate prediction of mobility. This view is supported by the fact that the cone index or plate sinkage profile obtained for a given soil may be regarded as a composite property, reflecting both cohesive and frictional effects within the soil. As such, it can be difficult to separate out the contributions to the soil's strength from cohesion and friction between soil particles, with implications for the ability to represent the effect of parameters such as wheel load on vehicle mobility. Analytical and numerical models, which attempt to describe the physical processes involved, have therefore tended to focus on a more detailed description of the soil's response to compressive and shear loads.

One of the primary advantages of an FE-based mobility prediction approach is the ability to specify soil properties, such that vehicle performance can be directly compared by eliminating the environmental variability associated with full-scale field testing. Whether the specified soil properties are uniform throughout a volume of soil or varied as a function of location (for example, to represent layered soils or variations in moisture content across an area of soil), the ability to precisely control soil properties ensures repeatability between runs. To assess the influence of terrain characteristics on vehicle mobility, material models are required which accurately describe the response of typical soils to applied loads.

This chapter discusses the structure, mechanical behaviour and experimental characterisation of soils. The development and validation of representative material models for dry sand and sandy loam soils is also described.

3.1 Soil characterisation

Two soil types were considered as part of the study to assess the effect of soil properties on predicted vehicle mobility. The soils addressed were a dry sand and a sandy loam, and characterisation during the research programme used a series of laboratory-based and in-situ tests:

- Density measurement
- Moisture content measurement
- Hydrostatic compaction
- Triaxial compaction
- Direct shear box
- Plate sinkage

Of these tests, density measurement, hydrostatic compaction, triaxial compaction and direct shear box tests were used to provide the primary inputs to the soil material models within LS-DYNA, with plate sinkage tests (Chapter 4) used to validate the soil model's response to applied loading for in-situ soils.

3.2 Soil classification

Soils can be described as multi-phase materials, consisting of an arrangement of solid soil particles, water and air, as illustrated in Figure 3.1. The response of the soil to applied loading is controlled by the movement and deformation of these constituent phases, and will therefore depend on the size and shape of soil particles, porosity (void content) and amount of moisture present within these voids.

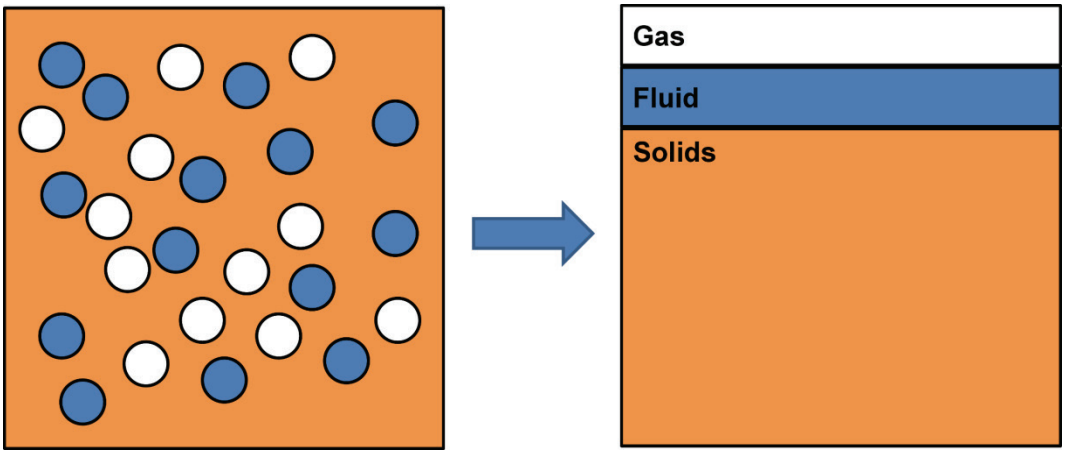

Figure 3.1: Schematic illustration showing idealised structure of soil (left) and relative proportions of gas fluid and solid phases (right)

Soils are primarily classified in terms of their particle size distribution, which defines the relative proportions of clay, silt and sand present within the solid phase. The relative proportions of these three constituent solid parts can then be used to identify one of a number of generic soil types. The twelve generic soil textures identified by the United States Department of Agriculture are illustrated in Figure 3.2, where the soil types considered under this research project are highlighted. Particle size distribution for a given soil is determined by sieving, with the cumulative percentage mass of particles passing through each sieve used to construct a grading curve for the soil, as shown in Figure 3.3 for the soils addressed under the current study. Sedimentation can also be used to establish particle size distribution for soils containing smaller particles such as clays (<0.002mm) and silts (between 0.002 and 0.06mm).

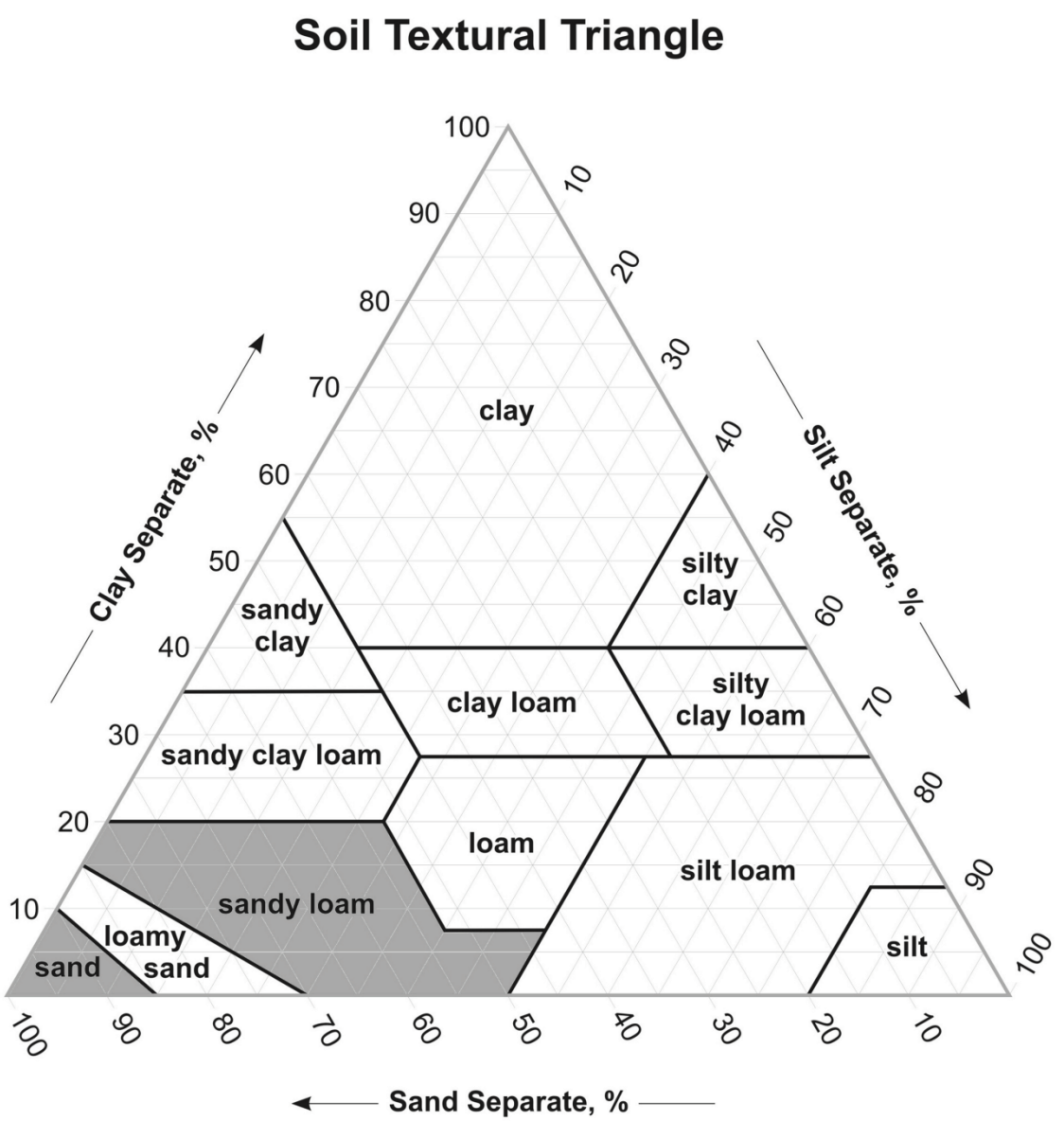

Figure 3.2: Soil texture triangle used to identify soil type based on the proportions of clay, silt and sand particles present (source: soils.usda.gov/education/resources/lessons/texture/, accessed 15th November 2011)

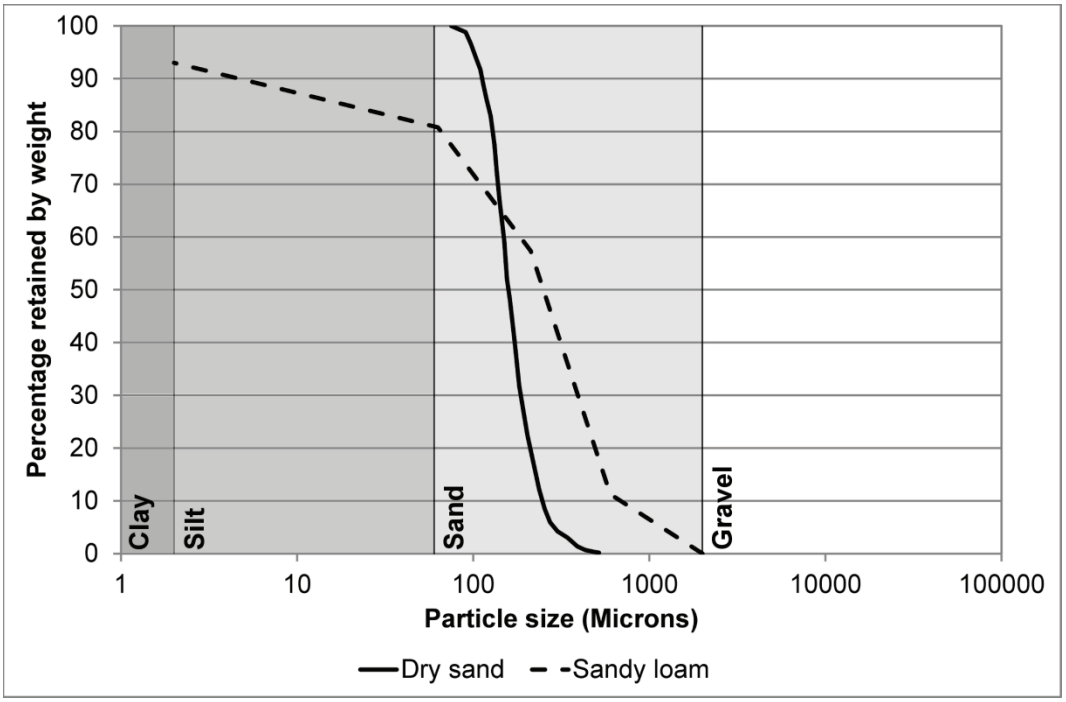

Figure 3.3: Particle size distribution for dry sand and sandy loam soils investigated under current study

In addition to the particle size distribution, soils can be further categorised in terms of their moisture content and level of compaction, which quantify the relative proportions of solid, liquid and gas within the soil. Unlike many other materials, soils are often highly compressible, with permanent plastic deformations occurring when subjected to hydrostatic pressure. As a soil is compacted and its density increased, the contribution of friction between soil particles to the soil's strength increases, leading to an increase in shear strength. The characterisation of soils in terms of their response to hydrostatic and shear loading will be discussed below.

The presence of moisture within the soil leads to changes in the soil's response to applied loading, and the basic nature of cohesive, fine grained soils as a function of moisture content can be described in terms of the Atterberg limits as solid, semi-solid, plastic or liquid (Kedzi, 1974). As moisture is added to a soil in the solid or semi-solid state, the response of the soil changes from brittle to plastic, with an increase in the level of adhesion between soil particles and an

associated increase in the level of stress that can be supported by the soil before yield. As moisture is increased further, the soil moves from the plastic state to the liquid state, with the additional moisture producing a reduction in the contribution to soil strength from inter-particle friction. For 'cohesionless' soils, which rely on friction between soil particles for their strength, the observed mechanical properties of the soil are primarily a function of their density.

3.2.1 Hydrostatic loading

The response of soils to hydrostatic loading can be described in terms of four idealised stages as follows:

- Initial elastic response (Figure 3.4, Section 1) – load paths within the solid soil skeleton, which occur at points of contact between soil particles, initially resist the applied load due to inter-particle friction;
- Pore collapse (Figure 3.4, Section 2) – as the frictional resistance between particles is exceeded, relative movement of the soil, water and air occurs, serving to increase the packing density of soil particles and expel air and water from the soil body;
- Fully compacted response (Figure 3.4, Section 3) – once the maximum packing density of soil particles has been attained through pore collapse, further loading of the soil results in deformation of the soil particles themselves;
- Unloading (Figure 3.4, Section 4) – after the hydrostatic load is removed from the soil, a limited degree of recovery takes place, resulting in a permanent (plastic) volumetric strain in the soil sample.

For physical soil samples, the pressure-volume curve described above can be obtained by applying a hydrostatic load to the sample using a pressurised water vessel and monitoring the associated change in volume. Hydrostatic testing of reconstituted soil samples was completed in this manner for the dry sand and sandy loam soils, the results of which are presented in Figure 3.5 and Figure 3.6, respectively. As shown, a series of interrupted hydrostatic tests were

undertaken on each soil, allowing the influence of soil compaction on the bulk unloading modulus to be assessed.

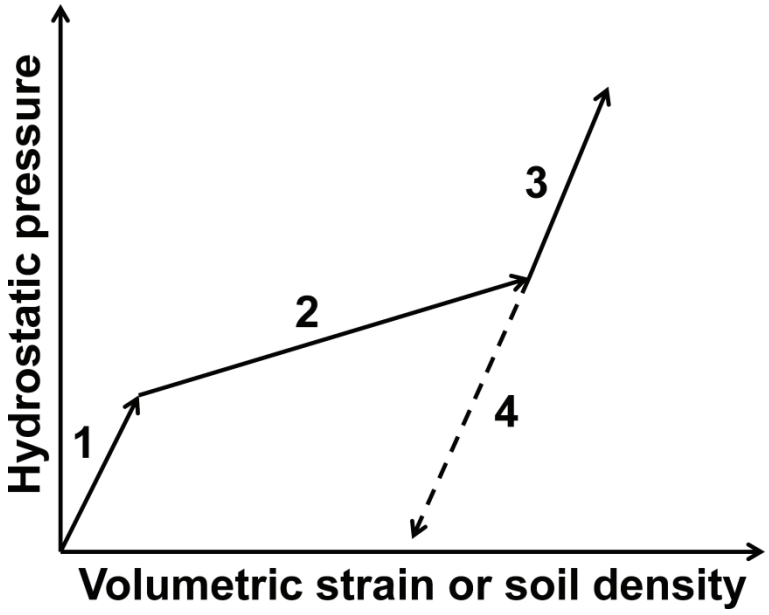

Figure 3.4: Schematic pressure – volume curve for a soil subjected to hydrostatic loading

The results of the hydrostatic tests indicate that the sand is less compressible than the sandy loam, with a substantially lower level of volumetric strain occurring in response to a given level of applied load. This can be explained by the particle size distributions of the two soils; the sand possesses a narrower range of particle sizes, which limits the maximum packing density that can be attained. By contrast, the presence of smaller silt and clay particles within the sandy loam enables a higher packing density, and results in a greater volumetric strain for a given level of hydrostatic pressure.

As demonstrated by the experimental results, the boundaries between the different hydrostatic loading phases for real soils are much less defined than suggested by the idealised curve presented in Figure 3.4. The final unloading portion of the pressure-volume curve can also be highly non-linear, resulting in significant levels of soil recovery once the applied loading is removed.

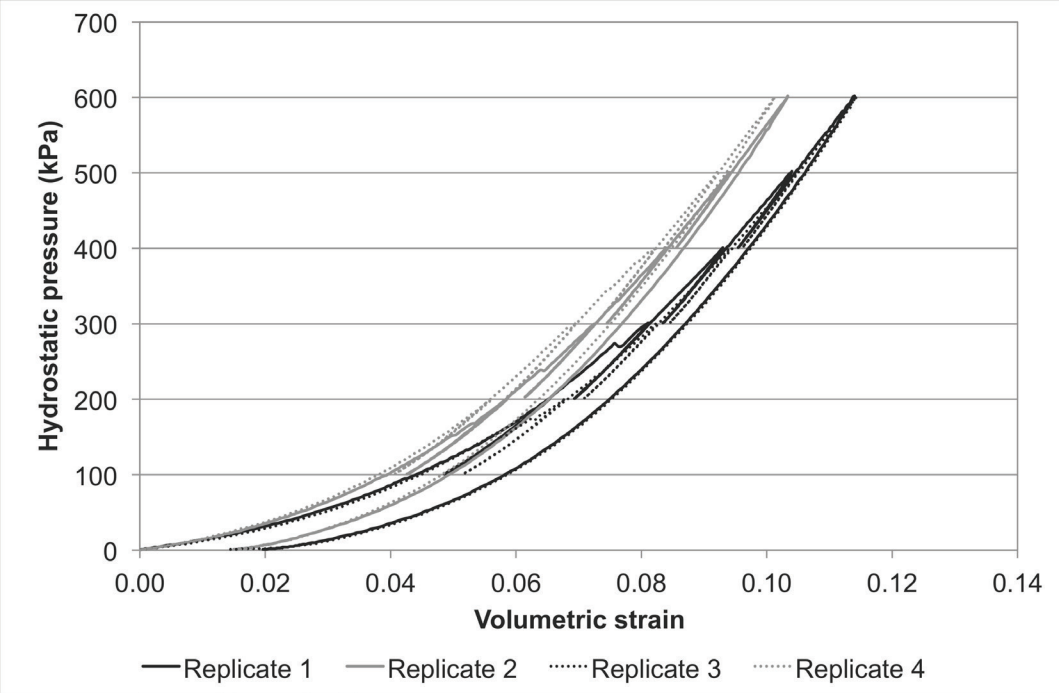

Figure 3.5: Experimental results of hydrostatic testing on reconstituted samples of dry sand

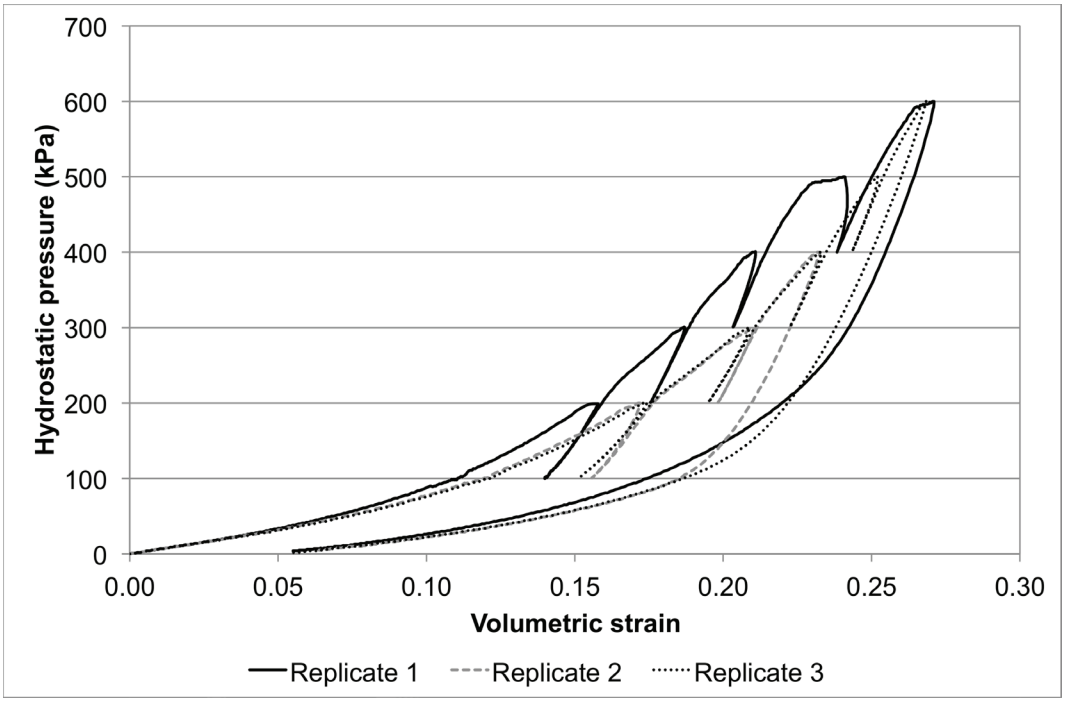

Figure 3.6: Experimental results of hydrostatic testing on reconstituted samples of sandy loam

3.2.2 Shear loading

As discussed in relation to existing analytical models, the prediction of rolling resistance and gross tractive thrust using traction mechanics relies on the ability to describe the distribution of shear stresses across the contact interface. The shear stresses generated at the interface between the wheel and soil will be a function of the relative displacement between the two components (slip), and limited by the shear strength of the soil. It is therefore critical that the shear strength of the soil is accurately described.

Under shear loading, the strength of particulate materials such as soil is a result of the resistance to motion due to chemical and frictional forces between soil particles. The contribution of any frictional forces between particles to shear strength is a function of the degree to which the soil is confined, while the chemical interaction between neighbouring soil particles represents the basic strength of the soil in the absence of any external confinement. The strength of a soil body is controlled by the arrangement of and contact between soil particles, and the observed strength is therefore dependent on the soil's prior loading history. The relative contribution of chemical and frictional forces will also depend on particle size and shape, as the smaller, plate-like particles found in clay soils possess a greater specific surface area (surface area per unit mass) than the larger grains associated with sands, and this leads to a greater contribution to the soil's strength from electrochemical forces between particles. Soils are frequently classified in terms of the relationship between shear strength and confinement, as illustrated in Figure 3.7.

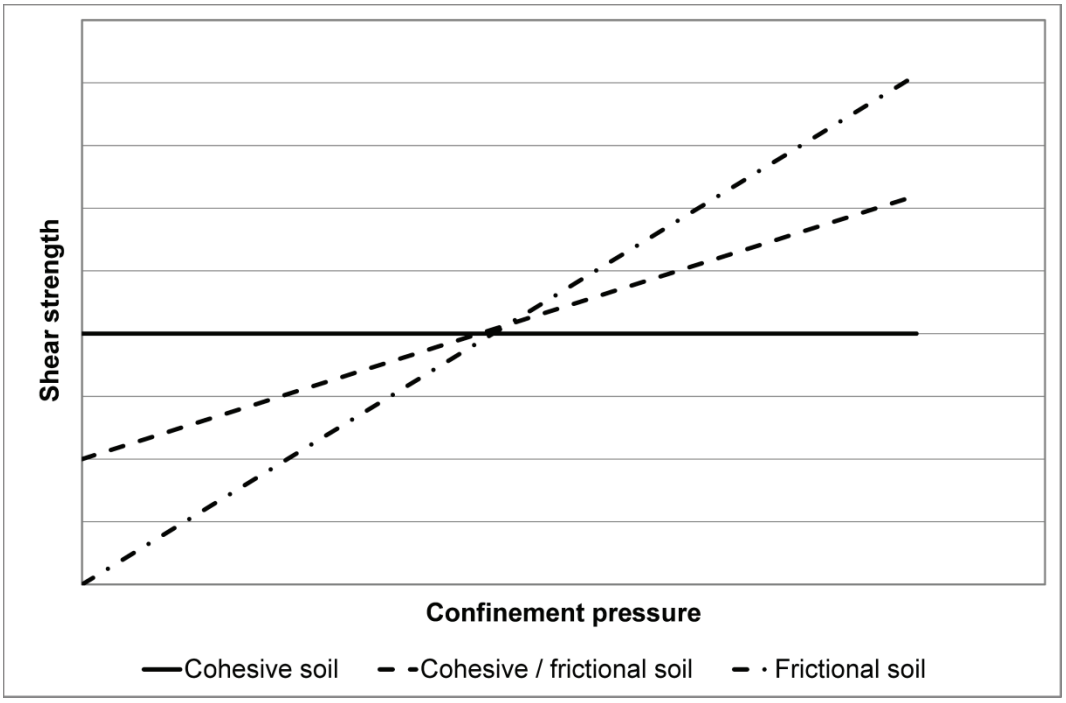

Figure 3.7: Characterisation of soils in terms of idealised relationships between shear strength and degree of confinement for three generic soil types

The linear relationship between shear strength and normal stress illustrated in Figure 3.7 represents an idealised failure surface for the soil, where the slope of the line is dependent on inter-particle friction effects, and the intercept with the y-axis defines the strength of the soil in the absence of any confinement. The volumetric and deviatoric stresses present within the soil determine the position of the overall stress state in relation to the failure surface: stress states lying within the failure surface are elastic, with failure occurring when the stress state contacts the failure surface.

The shear strength of soils and the influence of external confinement can be determined in the laboratory using either direct shear or triaxial test procedures. In direct shear box testing, the soil sample is constrained within two rigid rectangular or circular containers, one above the other, as illustrated in Figure 1.8; the containers are disconnected, such that relative lateral movement can occur, which results in shearing of the soil sample. Varying weights can be

applied to the top surface of the shear box to confine the soil, allowing the effect of confinement on shear strength to be determined.

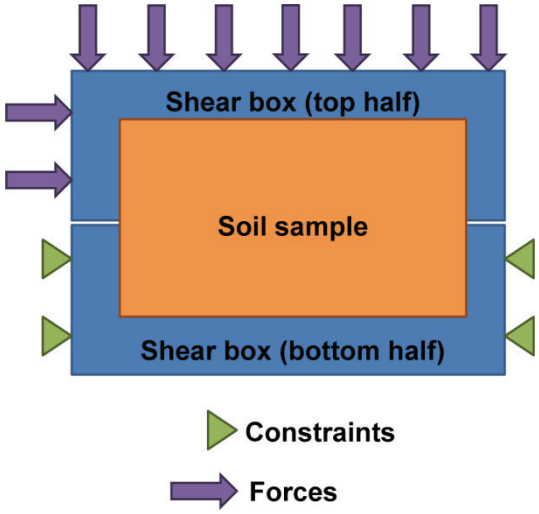

Figure 3.8: Direct shear box test apparatus

Triaxial compression testing employs a cylindrical soil sample, to which a hydrostatic pressure is applied to confine the soil. Once the hydrostatic confining pressure (σ_3) has been established, the stress in the axial direction (σ_1) is steadily increased until shear failure occurs within the soil sample. The stress state within the soil sample, for a range of confining pressures, can then be described using a series of Mohr's circles, where a line tangent to the circles defines the failure surface for the soil in a similar manner to that of the direct shear testing results.

Both the direct shear box and triaxial test procedures were applied to the sand and sandy loam soils under consideration, the results of which are summarised in Table 3.1 and Table 3.2. The two test procedures produce markedly different results, with the direct shear box test suggesting that the two soils are similar in their response to shear loads, while the triaxial test results reporting significant differences in the shape of the failure surface.

Table 3.1: Results of direct shear box tests on reconstituted samples of dry sand and sandy loam soils

Confining Stress (kPa)	Maximum shear stress (kPa)							
	Dry sand				Sandy loam			
	Rep 1	Rep 2	Rep 3	Mean	Rep 1	Rep 2	Rep 3	Mean
40	26	29	29	**28**	27	30	28	**28**
67	44	48	47	**46**	47	46	44	**46**
94	61	62	62	**62**	64	60	60	**61**
121	81	82	81	**81**	84	82	79	**82**

Table 3.2: Results of triaxial compression tests on reconstituted samples of dry sand and sandy loam soils

Confining stress, σ_3 (kPa)	Maximum shear stress (kPa)							
	Dry sand				Sandy loam			
	Rep 1	Rep 2	Rep 3	Mean	Rep 1	Rep 2	Rep 3	Mean
1	22	20	22	**21**	6	6	6	**6**
100	136	160	142	**146**	24	20	20	**22**
200	-	-	-	**-**	70	56	49	**58**
400	484	517	508	**503**	135	113	128	**125**
600	656	776	702	**711**	188	180	205	**191**

3.3 Soil modelling in LS-DYNA

Having determined the mechanical response of the sand and sandy loam soils under consideration, the material models available within LS-DYNA v971 were reviewed with a view to identifying those that may be used to predict the effect of soil properties on wheeled vehicle mobility. A total of 198 material models were available in LS-DYNA v971 Release 5.1.1, with a smaller sub-set that could potentially be applied to represent soils in dynamic FE analysis. The

material models that were initially identified as applicable to soils are summarised in Table 3.3 – further details of the material models available within LS-DYNA are available in Appendix B and the LS-DYNA user's manual (LSTC, 2011).

Following the initial review of LS-DYNA material models, which identified those listed as applicable to soil modelling, it was necessary to define and apply selection criteria to down-select the most promising material models for further investigation. The first down-selection criterion to be applied was implementation for both Lagrange and ALE solvers in LS-DYNA, as a key strand of the research was the ability to compare the results from Lagrange and ALE / Eulerian simulations. This primary down-selection identified the following material models as being applicable to soils using both the Lagrange and ALE solvers:

- *MAT_SOIL_AND_FOAM / *MAT_SOIL_AND_FOAM_FAILURE
- *MAT_PSEUDO_TENSOR
- *MAT_SOIL_CONCRETE
- *MAT_HYSTERETIC_SOIL
- *MAT_FHWA

Of the identified material models, *MAT_SOIL_AND_FOAM was initially selected for use on the basis that it had been implemented and validated by LSTC for use with the ALE solver and, as one of the earliest material models provided in LS-DYNA, there is a relatively large body of user experience to draw upon (Schwer, 2001). Further discussion of the remaining material models is provided in Chapter 4, following comparison of numerical modelling results against the experimental plate sinkage profiles obtained for dry sand and sandy loam soils.

Table 3.3: Material models available within LS-DYNA identified within the LS-DYNA user manual as applicable to soils

ID	Name	Lagrange	ALE	SPH
5	SOIL_AND_FOAM	Implemented and validated by LSTC	Implemented and validated by LSTC	Implemented and validated by LSTC
14	SOIL_AND_FOAM_FAILURE	Implemented and validated by LSTC	Implemented but not validated by LSTC	Implemented and validated by LSTC
16	PSEUDO_TENSOR	Implemented and validated by LSTC	Implemented but not validated by LSTC	Implemented and validated by LSTC
25	GEOLOGIC_CAP	Implemented and validated by LSTC	Not implemented for ALE	Implemented and validated by LSTC
72	CONCRETE_DAMAGE	Implemented and validated by LSTC	Not implemented for ALE	Not implemented for SPH
78	SOIL_CONCRETE	Implemented and validated by LSTC	Implemented but not validated by LSTC	Implemented and validated by LSTC
79	HYSTERETIC_SOIL	Implemented and validated by LSTC	Implemented but not validated by LSTC	Implemented and validated by LSTC
145	SCHWER_MURRAY_CAP	Implemented and validated by LSTC	Not implemented for ALE	Implemented and validated by LSTC
147	FHWA	Implemented and validated by LSTC	Implemented but not validated by LSTC	Implemented and validated by LSTC
173	MOHR_COULOMB	Implemented and validated by LSTC	Not implemented for ALE	Not implemented for SPH
192	SOIL_BRICK	Implemented and validated by LSTC	Not implemented for ALE	Not implemented for SPH
193	DRUCKER_PRAGER	Implemented and validated by LSTC	Not implemented for ALE	Not implemented for SPH

3.3.1 Material model development

The following sections discuss the derivation of material model parameters from laboratory-based soil test data for dry sand and sandy loam soils.

3.3.1.1 Dry sand

Hydrostatic test results for dry sand (moisture content 0.86 %) were presented in Figure 3.5. The soil's response to hydrostatic loading is described within the *MAT_SOIL_AND_FOAM material model using tabulated pressure and volumetric strain data, with a linear unloading function based on a separately defined bulk unloading modulus. Since the hydrostatic loading and unloading behaviour of the soil are treated separately in the material model, the experimental hydrostatic test data was first simplified by considering only the loading portion of the experimental curves. The arithmetic means of the experimental pressure values were then taken for specific values of volumetric strain (Appendix C, Table C.1) to obtain a curve representing an averaged response of the dry sand to hydrostatic loading (Figure 3.9).

The unloading portion of the hydrostatic pressure-volume curve within the MAT_SOIL_AND_FOAM material model is assumed to be linear in nature, based on a single unloading modulus value. To determine the most appropriate value for the bulk unloading modulus, an experimental mean curve was calculated based on the arithmetic mean of the individual test results (Appendix C, Table C.2). A least squares approach was then used to minimise the error between the experimental mean values and those calculated using the following expression:

$$p = p_{\max} + K_{un}\left(\varepsilon_v - \varepsilon_{v\max}\right) \qquad \textit{Equation 3.1}$$

Using this approach minimises the error between the experimental mean values and those calculated by the model, but can introduce energy errors if the resulting bulk unloading modulus is less than the maximum slope of the loading portion of the curve. To address this, the error between the calculated and

experimental unloading curves was minimised subject to the constraint that the bulk unloading modulus must be greater than or equal to the maximum slope of the experimental mean loading curve. For the dry sand, this results in a bulk unloading modulus of 9,463 kPa. Using Equation 3.1 to calculate the permanent volumetric strain by setting *p* equal to zero leads to a predicted permanent volumetric strain of 0.046, compared with an experimental value of approximately 0.010, with the resulting pressure-volume envelope for the MAT_SOIL_AND_FOAM material model compared against experimental mean data in Figure 3.10. The adoption of a linear bulk unloading response has potential implications for the use of the MAT_SOIL_AND_FOAM material model to predict mobility for multiple passes, as the level of soil recovery predicted by the model will be lower than that observed in reality.

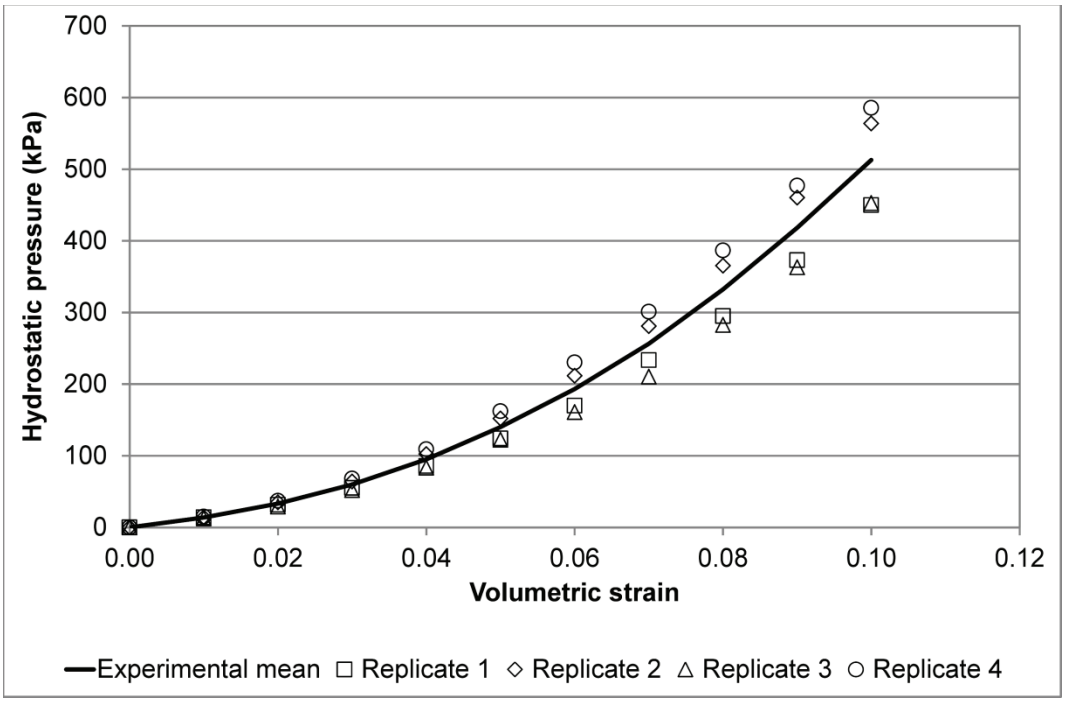

Figure 3.9: Pressure-volume curve used to describe averaged response of dry sand to hydrostatic loading

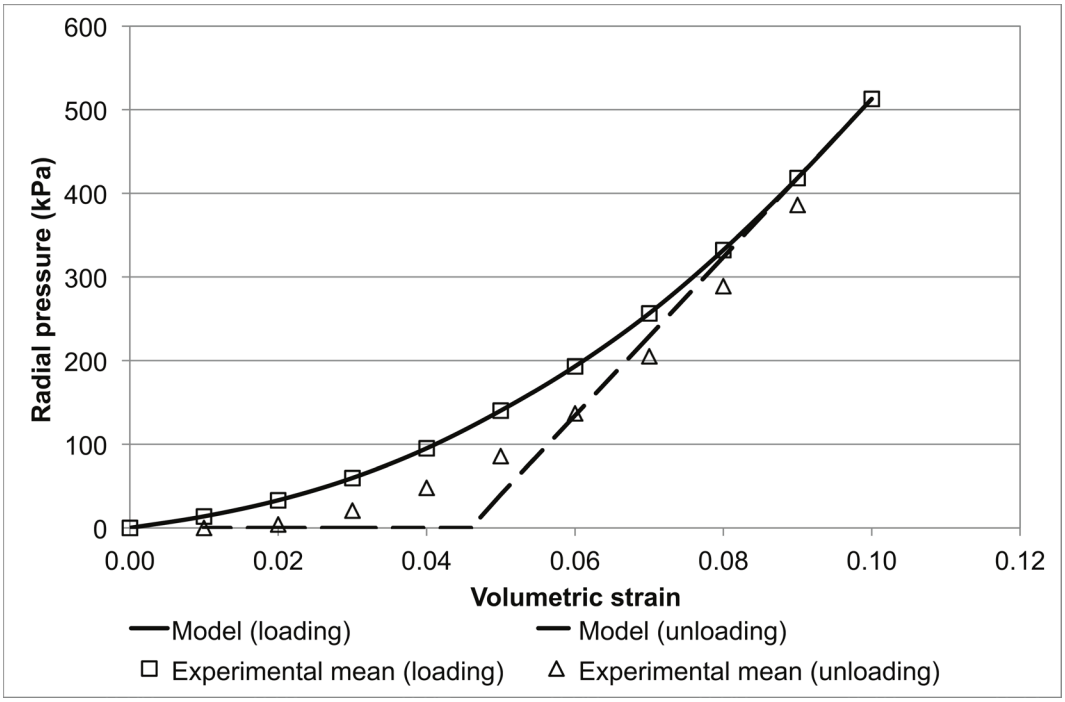

Figure 3.10: Comparison of single element hydrostatic model results against experimental pressure-volume curve for dry sand

The effect of external confinement on soil's shear strength is described within the *MAT_SOIL_AND_FOAM material model using a yield function of the form:

$$\sigma_y = \sqrt{3\left(a_0 + a_1 p + a_2 p^2\right)} \qquad \textit{Equation 3.2}$$

Where σ_y represents the deviator stress ($\sigma_1 - \sigma_3$) at yield. For triaxial testing, the process of fitting the above shear failure model to experimental data is straightforward, as the principal stresses (σ_1 and σ_3) are well defined under triaxial loading conditions. The principal stresses acting on the soil sample during a direct shear box test are more difficult to establish, however, and it becomes necessary to calculate the principal stresses based on the Mohr-Coulomb yield surface and Mohr's circle geometry, as illustrated in Figure 3.11. Since this two-step approach is dependent on the cohesion and friction angle values of the Mohr-Coulomb yield surface, the quality of fit obtained will be dependent on the degree of linearity displayed by the shear box test results. While this clearly represents a simplification compared to the more direct

process used to fit the MAT_SOIL_AND_FOAM yield surface to triaxial test data, where non-linearity is preserved to a greater extent, the limited non-linearity observed in the direct shear box test results suggests that, for the soils under investigation, the effect of this simplification was minimal over the range of confinement pressures used.

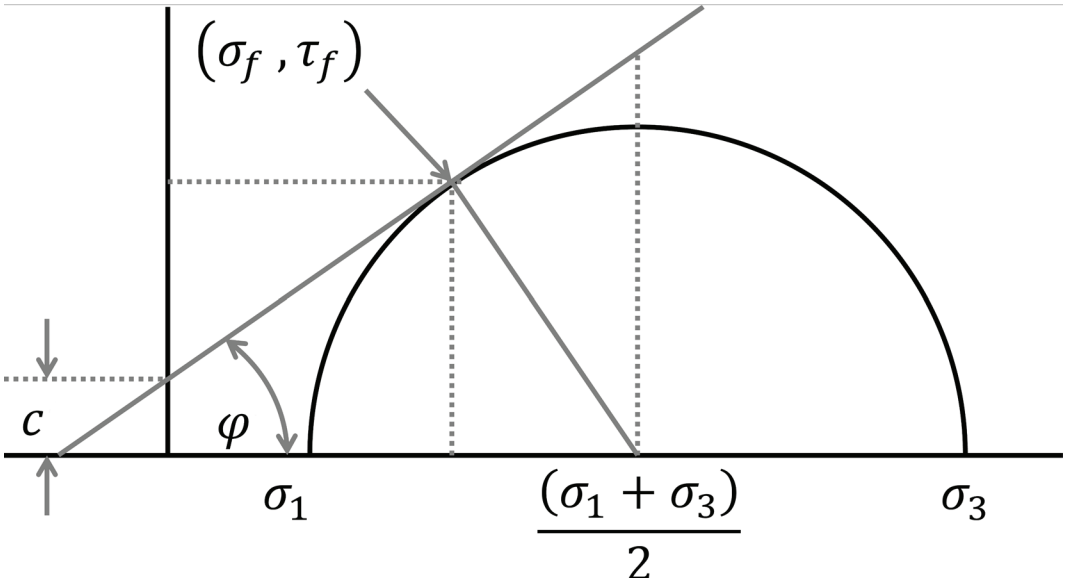

*Figure 3.11: Illustration of Mohr's circle geometry used to determine yield surface parameters for use in *MAT_SOIL_AND_FOAM material from results of direct shear box tests*

Applying the above curve fitting process to both triaxial and direct shear box test data resulted in two possible yield surfaces for the dry sand. Due to similarities in the values obtained for a_0 and a_2, the primary difference between the two yield surfaces exists at low confinement pressures; this difference was noted to be a potential source of error for the modelling of in-situ sand, discussed later in this chapter, since the surface of an in-situ soil is generally unconstrained.

Since the shear failure surface used by MAT_SOIL_AND_FOAM describes the deviator stress at failure as a function of the mean stress in the soil, it is possible to relate the shear failure surface parameters (a_0, a_1 and a_2) to the

Mohr-Coulomb model parameters, c and ϕ. An approach of this type has previously been suggested by Fasanella et al. (2009), but the relationships derived to relate a_0, a_1 and a_2 to c and ϕ were incorrect due to the erroneous statement that the Mohr-Coulomb model describes the deviator stress at failure (σ_1-σ_3), rather than the shear stress. Using a similar approach, but taking into account the difference between the deviator stress (used by LS-DYNA) and the shear stress, the shear stress at failure can be described in terms of the cohesion and friction angle using the Mohr-Coulomb model:

$$\tau = c + p tan\emptyset \qquad \text{Equation 3.3}$$

In the MAT_SOIL_AND_FOAM model, the shear failure surface is described in terms of three *a* parameters, which are used to calculate the deviator stress at failure as a function of mean stress, *p*:

$$\sigma_1 - \sigma_3 = \sqrt{3 * (a_0 + a_1 p + a_2 p^2)} \qquad \text{Equation 3.4}$$

Shear stress at failure can therefore be calculated as follows:

$$\tau = \frac{\sigma_1 - \sigma_3}{2} = \frac{1}{2}\sqrt{3 * (a_0 + a_1 p + a_2 p^2)} \qquad \text{Equation 3.5}$$

Substituting the Mohr-Coulomb model, in terms of cohesion and friction angle and rearranging:

$$c + p tan\emptyset = \frac{1}{2}\sqrt{3 * (a_0 + a_1 p + a_2 p^2)} \qquad \text{Equation 3.6}$$

$$\frac{[2(c + p tan\emptyset)]^2}{3} = (a_0 + a_1 p + a_2 p^2) \qquad \text{Equation 3.7}$$

$$\frac{4c^2}{3} + \frac{8c * tan\emptyset}{3} p + \frac{4tan^2\emptyset}{3} p^2 = (a_0 + a_1 p + a_2 p^2) \qquad \text{Equation 3.8}$$

$$\frac{4c^2}{3} + \frac{8c * tan\emptyset}{3} p + \frac{4tan^2\emptyset}{3} p^2 = (a_0 + a_1 p + a_2 p^2) \qquad \text{Equation 3.9}$$

Equating the coefficients in the above expression allows values for a_0, a_1 and a_2 to be calculated directly from Mohr-Coulomb parameters:

$$a_0 = \frac{4c^2}{3} \qquad \text{Equation 3.10}$$

$$a_1 = \frac{8c * tan\emptyset}{3}$$ Equation 3.11

$$a_2 = \frac{4tan^2\emptyset}{3}$$ Equation 3.12

It is commonly assumed that dry sand is cohesionless, with the soil's resistance to applied loads resulting solely from surcharge effects. Using the above expressions for a_0, a_1 and a_2 in terms of the Mohr-Coulomb model parameters, a_0 and a_1 should both be set to zero to represent a purely frictional soil, while a_1 and a_2 should be set to zero for a purely cohesive soil.

Table 3.4 provides a comparison of the yield surface parameters obtained through curve fitting and direct calculation, with a visual comparison between the resulting yield surfaces provided in Figure 3.12. As shown, the direct calculation of yield surface parameters from cohesion and friction angle values removes any non-linearity, exacerbating the differences in yield strength observed at low confinement pressures. The linear nature of the directly calculated yield surface is to be expected, given the linearity of the Mohr-Coulomb failure surface.

Density and Poisson's ratio[1] values for the dry sand were reported as 1.39 g/cm^3 and 0.35, respectively. Finally, the elastic shear modulus was calculated from the initial bulk loading modulus and Poisson's ratio as follows:

$$G = \frac{3K(1-2\nu)}{2(1+\nu)}$$ *Equation 3.13*

[1] Poisson's ratio values were calculated from triaxial shear test data

Table 3.4: Dry sand yield function constants for MAT_SOIL_AND_FOAM material model obtained using curve fitting and direct calculation methods

Test method	**Triaxial compaction**		**Direct shear box**	
Cohesion	15 kPa		2.5 kPa	
Friction angle	32.35°		32.35°	
Yield function constants	**Curve fitting**	**Direct calculation**	**Curve fitting**	**Direct calculation**
a_0	1.65×10^{-11}	3.00×10^{-10}	1.62×10^{-11}	8.33×10^{-12}
a_1	3.03×10^{-5}	2.53×10^{-5}	3.45×10^{-6}	4.22×10^{-6}
a_2	5.76×10^{-1}	5.35×10^{-1}	5.96×10^{-1}	5.35×10^{-1}

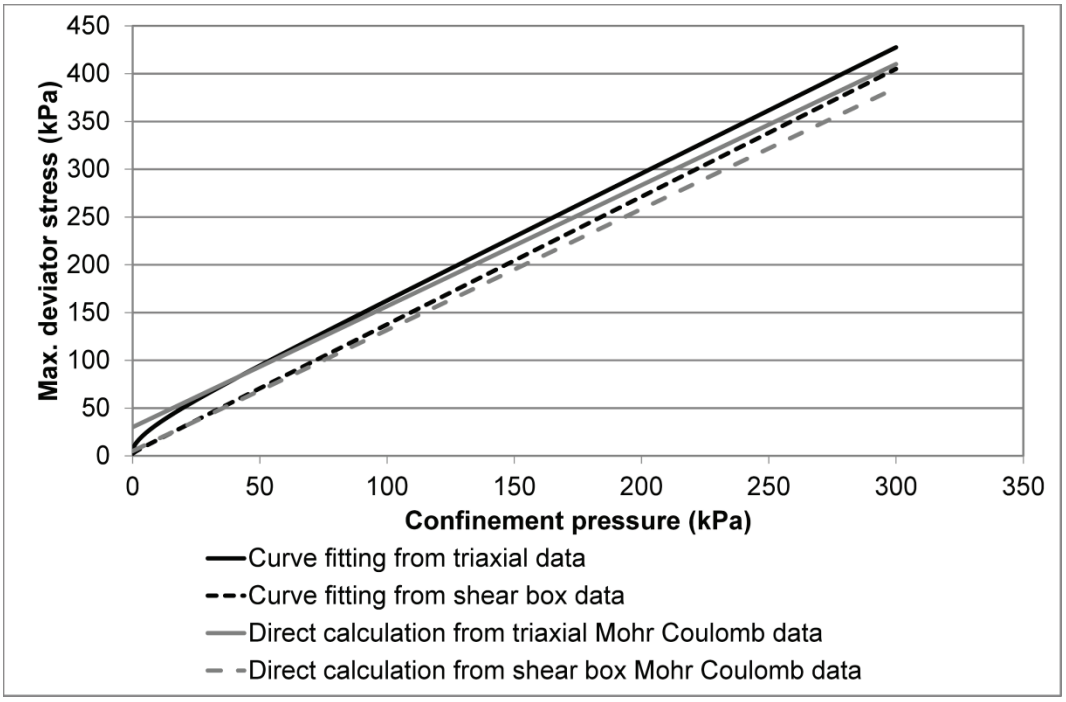

Figure 3.12: Comparison of shear failure surfaces obtained for dry sand using curve fitting to experimental data and direct calculation from Mohr-Coulomb constants

The resulting material model input deck for dry sand, with yield surface parameters taken from Table 3.4 is presented below.

```
*MAT_SOIL_AND_FOAM_TITLE
$ Dry Sand (QinetiQ Model)
$ Units: kg, ms, mm
$#     mid        ro         g      bulk        a0        a1        a2        pc
         1 1.3900E-6  2.620E-3  9.463E-3       [----SEE TABLE 3.4----]
$#     vcr       ref
     0.000     0.000
$#    eps1      eps2      eps3      eps4      eps5      eps6      eps7      eps8
     0.000 -0.010050 -0.020200 -0.030460 -0.040820 -0.051290 -0.061880 -0.072570
$#    eps9     eps10
 -0.083880 -0.105400
$#      p1        p2        p3        p4        p5        p6        p7        p8
     0.000 1.3880E-5 3.3130E-5 5.9750E-5 9.5080E-5 1.4020E-4 1.9320E-4 2.5650E-4
$#      p9       p10
 3.3230E-4 5.1300E-4
```

To verify that the MAT_SOIL_AND_FOAM material model was capable of describing the soil's response to hydrostatic and triaxial loading, a series of single element simulations were undertaken, with hydrostatic and triaxial displacement boundary conditions applied to one point constant stress solid elements (Type 1 solids). The yield surface parameters obtained from curve fitting to the triaxial and shear box test data were used to permit direct comparison of numerical and experimental data. The results of the single element FE models for both hydrostatic and triaxial loading conditions are compared against experimental mean and calculated results in Table 3.5 and Figure 3.13, respectively.

Table 3.5: Comparison of experimental mean, calculated and single element FE model results for hydrostatic loading of dry sand

	Vol. Strain	Radial pressure (kPa)			
		Experimental		Calculated	Single Element Model
		Mean	St. Dev.		
Loading	0.00	0	0.0	-	0
	0.02	33	3.6	-	34
	0.04	95	12.5	-	96
	0.06	193	33.1	-	194
	0.08	332	51.3	-	330
	0.10	513	71.9	-	513
Unloading	0.08	289	59.3	324	308
	0.06	137	35.1	134	103
	0.04	48	16.1	0	0
	0.02	4	3.1	0	0
	0.00	0	0	0	0

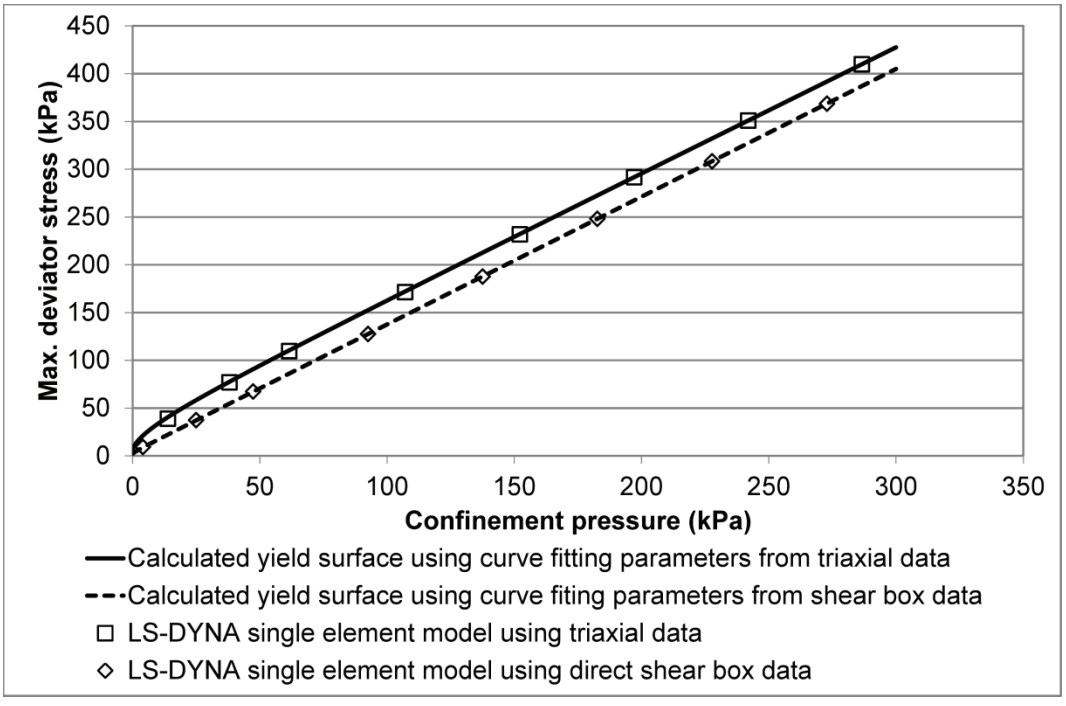

Figure 3.13: Comparison of calculated and single element shear failure surfaces for triaxial loading of dry sand

3.3.1.2 Sandy loam

A material model to represent sandy loam soil with a moisture content of 14.2% was derived in a similar manner to that described above for the dry sand, resulting in the material model input card shown below.

```
*MAT_SOIL_AND_FOAM_TITLE
$ Sandy Loam Model
$ Units: kg, ms, mm
$#     mid        ro          g      bulk        a0        a1        a2        pc
         1 1.4700E-6  1.120E-3  4.444E-3       [----SEE TABLE 3.6----]
$#     vcr       ref
     0.000     0.000
$#    eps1      eps2      eps3      eps4      eps5      eps6      eps7      eps8
 0.000E+00-2.020E-02-4.082E-02-6.188E-02-8.338E-02-1.054E-01-1.508E-01-1.985E-01
$     EPS9     EPS10
-2.485E-01-6.300E-01
$#      p1        p2        p3        p4        p5        p6        p7        p8
 0.000E+00 1.217E-05 2.517E-05 4.033E-05 5.800E-05 8.050E-05 1.437E-04 2.363E-04
$#      p9       p10
 3.794E-04 2.831E-03
```

As for the dry sand, the shape of the yield surface was found to depend on the test method used, with yield surface constants from triaxial and direct shear box tests compared in Table 3.6, using both the curve fitting and direct calculation methods outlined above. The influence of the test method used on the shape of the yield surface for the sandy loam soil was found to be greater than for the dry sand, with marked differences in the values obtained for all three yield surface parameters.

Table 3.6: Sandy loam yield surface parameters for MAT_SOIL_AND_FOAM material model

Test method	**Triaxial compaction**		**Direct shear box**	
Cohesion	1.33 kPa		2.67 kPa	
Friction angle	13.13°		32.35°	
Yield function constants	**Curve fitting**	**Direct calculation**	**Curve fitting**	**Direct calculation**
a_0	9.19×10^{-11}	2.37×10^{-12}	2.52×10^{-11}	9.48×10^{-12}
a_1	-7.23×10^{-6}	8.30×10^{-7}	-2.27×10^{-6}	4.50×10^{-6}
a_2	1.04×10^{-1}	7.26×10^{-2}	6.31×10^{-1}	5.35×10^{-1}

A visual comparison of the resulting shear failure surfaces for sandy loam is provided in Figure 3.14 – as shown, the fact that a_1 is negative for both curve fitting surfaces leads to an initial reduction in shear strength at low confinement pressures. For the yield surface derived by curve fitting to triaxial test data, the more strongly negative value for a_1 results in an error at pressures between 16 and 53kPa, with LS-DYNA attempting to find the square root of a negative number in Equation 3.2. The yield surfaces obtained through curve fitting to laboratory test data and direct calculation from Mohr-Coulomb model constants are compared visually in Figure 3.14.

Given the linear nature of the Mohr-Coulomb failure surface, direct calculation of yield surface parameters for MAT_SOIL_AND_FOAM from cohesion and friction angle values avoids the negative root error at confining pressures of between 16 and 53kPa. As with the dry sand, single element simulations were used to verify that the MAT_SOIL_AND_FOAM material model was correctly interpreting user input data. Due to the potential for “not a number” (NaN) errors when using yield surface parameters obtained from curve fitting to triaxial test data, additional simulations were run at low confinement pressures to investigate how LS-DYNA would respond. The results of the single element hydrostatic simulation are compared against experimental data in Figure 3.15,

while the results of the triaxial simulations are compared against calculated shear failure surfaces in Figure 3.15. No error messages were generated by LS-DYNA during the low confinement single element simulations run using the triaxial yield surface. Analysis of the results obtained for low confinement pressures suggests that, when presented with a negative second invariant, the strength of the soil model defaults to zero.

Table 3.7: Comparison of experimental mean, calculated and single element FE model results for hydrostatic loading of sandy loam

	Vol. Strain	Radial pressure (kPa)			
		Experimental		Calculated	Single Element Model
		Mean	St. Dev.		
Loading	0.00	0	0.0	-	0
	0.04	25	0.8	-	26
	0.08	58	3.6	-	58
	0.12	107	11.7	-	112
	0.16	185	17.9	-	189
	0.20	303	47.5	-	307
	0.24	467	45.8	-	467
	0.27	594	6.5	-	594
Unloading	0.24	301	20.2	461	410
	0.20	140	13.3	283	185
	0.16	72	7.5	105	0
	0.12	36	4.0	0	0
	0.06	5	1.9	0	0

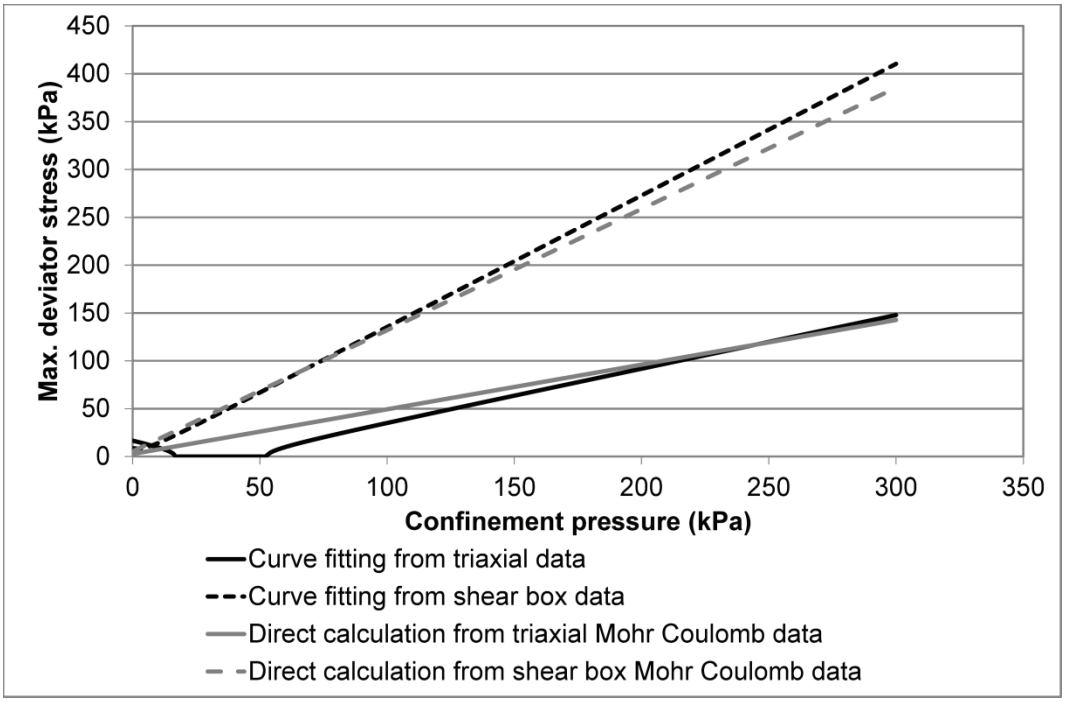

Figure 3.14: Comparison of shear failure surfaces obtained for sandy loam using curve fitting to experimental data and direct calculation from Mohr-Coulomb constants

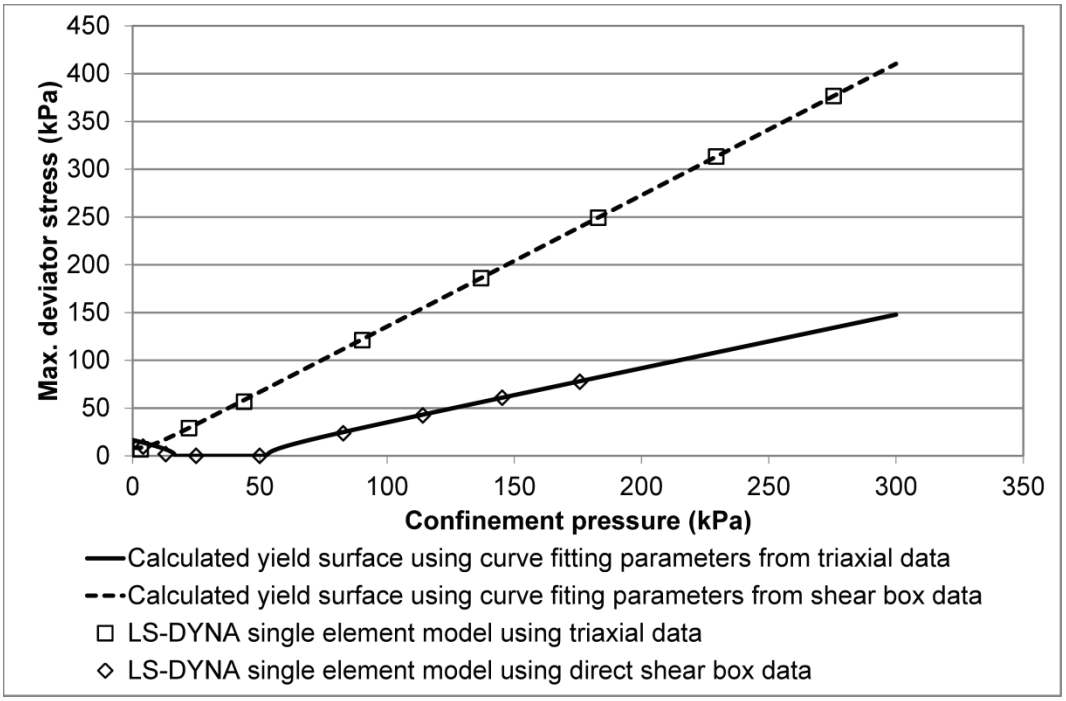

Figure 3.15: Comparison of calculated and single element shear failure surfaces for triaxial loading of sandy loam

3.4 Summary

This chapter has addressed the structure, categorisation and characterisation of naturally occurring soils using laboratory-based techniques. The generic response of soils to hydrostatic and shear loading has been discussed, which has helped to identify applicable constitutive models within LS-DYNA, a commercial FE code. Hydrostatic, triaxial and direct shear box tests have been completed, using reconstituted soil samples, to generate material model input data for two types of soil (dry sand and sandy loam).

In characterising the response of these soils to applied shear loads, the triaxial and direct shear box tests were found to produce different shear failure surfaces. For the dry sand, the difference between the two failure surfaces was mostly confined to the low confinement pressure region, whereas large differences in the shape and location of the shear failure surfaces were observed for the sandy loam across a wide range of confinement pressures. While there are clearly differences between the two test procedures (drained vs. undrained, for example), which could lead to different results, the key question at this stage is: which of the possible failure surfaces best represents the actual response of the in-situ soil to shear loading?

The answer to this question could well be that neither failure surface fully describes the behaviour of the in-situ soil. Since the mechanical properties of a given soil are dictated by its structure, and the process of removing and reconstituting soil samples for laboratory characterisation will inevitably change that structure, shear failure surface parameters may not be representative of the soil that is seen during off-road operation. The relationships between laboratory-based soil characterisation techniques, the results obtained, and the in-situ response of soils to applied loads are therefore investigated in the next chapter.

Chapter 4: Modelling of in-situ soil response

Having verified the response of the developed material models against laboratory test data and observed the different yield surfaces resulting from triaxial and direct shear box tests, it was necessary to determine which yield surface most accurately described the in-situ behaviour of the soils. As discussed in the Chapter 2, in-situ plate sinkage tests are frequently used within semi-empirical and analytical mobility prediction models to describe the compaction of the soil in response to applied wheel loading. The plate sinkage profile can be regarded as a composite material property, with the soil's resistance to penetration being dependent on both the hydrostatic and shear components of the soil's strength. As such, plate sinkage results cannot be used to directly populate material models for FE analysis, but can serve as a useful check that the material models derived from laboratory-based characterisation tests are representative of the in-situ soil.

Plate sinkage tests were undertaken on both the dry sand and sandy loam soils, with a 75.2mm diameter solid steel cylinder forced into the soils under the action of a series of increasing static loads. The sinkage of the cylinder after each load increment was measured to obtain a plate sinkage profile, describing the load required to penetrate the soil to a given depth. The resulting plate sinkage profiles, for both the dry sand and sandy loam soils, are illustrated in Figure 4.1.

As clearly shown in Figure 4.1, the plate sinkage profiles for the dry sand display a larger degree of variability than the sandy loam when viewed in absolute terms, with a variation in sinkage depth of as much as ±31mm for the highest plate loading of 299kPa. In contrast, the plate sinkage profiles for the sandy loam soil show a lower absolute variation in sinkage depth, with a maximum variability of ±5mm at 210kPa. However, looking at the variability of the plate sinkage profiles in relative, rather than absolute, terms the level of variability in the two soils is closer in magnitude (Table D.1).

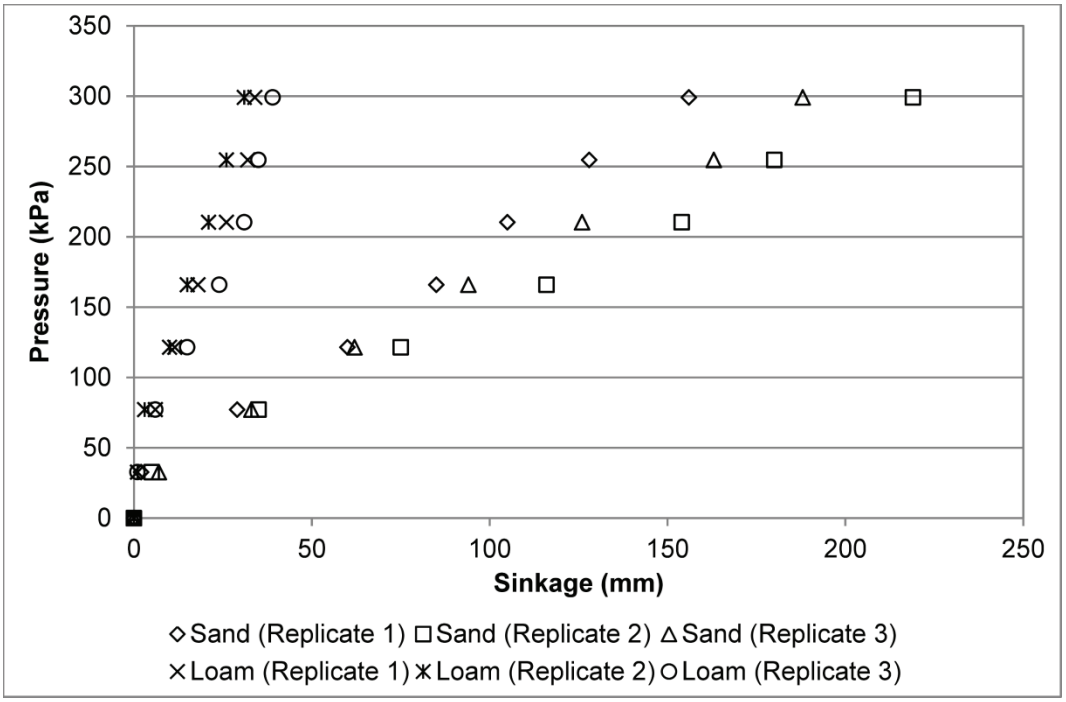

Figure 4.1: Experimental plate sinkage profiles obtained for dry sand and sandy loam soil

The size of penetrator plate used not only affects the resulting plate sinkage profile, but, as discussed by Rashidi, Keyhani and Tabatabaeefar (2006), also influences the level variability observed within a series of tests. Rashidi et al. state that large rectangular plates with a width greater than 300mm can be used to reduce the level of variability seen between individual tests. It is important to note, however, that the natural variability of the soil will not change as the size of the sinkage plate is increased, but a larger volume of soil will be sampled, which reduces the *observed* level of variability. One potential advantage of using a larger sinkage plate is that a smaller number of tests may be used to characterise a given terrain, but this must be balanced against the fact that higher loads will be required to achieve the same vertical pressure.

Given the size of the plate used in the current study and the relatively small number of replicates completed, the variability of the experimental test results must be borne in mind when comparing numerical modelling results against physical test data.

4.1 Quasi-static plate sinkage models

To assess the influence of yield surface parameters on the plate sinkage profiles predicted by LS-DYNA, quarter symmetry models of the plate sinkage test were created. The influence of solution method was investigated, with Lagrangian and Eulerian models run for a series of soil and shear failure surface combinations. As far as possible, differences between the Lagrange and MM-ALE simulations were minimised, with the aim of allowing the results produced by the two solvers to be directly compared.

Symmetry boundary conditions were applied to the relevant surfaces, while the outer surface of the soil body was constrained in the x and y directions to represent a 752mm diameter soil sample within a rigid container. Due to the large difference in stiffness between the steel plate and the soil sample in the physical test, the plate was represented as a rigid material in the simulation, with the Young's modulus of the plate specified as twice the shear modulus of the soil and a Poisson's ratio of zero. In LS-DYNA's *MAT_RIGID card, the specified elastic properties are used solely to calculate contact forces, and artificially reducing the contact stiffness of the plate therefore serves to reduce the likelihood of contact instabilities.

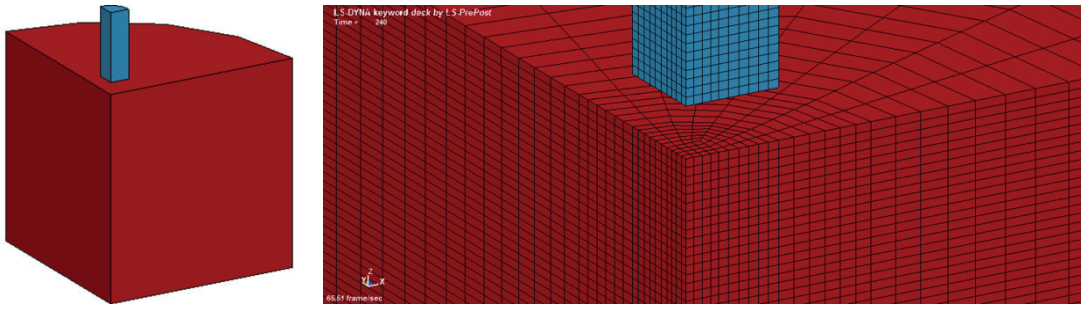

Figure 4.2: Overview (left) and detail (right) of quarter symmetry plate sinkage model using Type 1 selectively reduced solid elements

A prescribed velocity boundary condition was applied to the plate, vertically displacing at a constant rate after an initial acceleration to the desired penetration speed. A prescribed velocity boundary condition was selected over a prescribed displacement condition because application of a displacement boundary condition was found to produce an instantaneous increase in plate velocity at the start of the simulation, leading to large energy errors. In the case of the Lagrangian model, an automatic surface to surface contact algorithm was specified between the soil and plate, using segment-based contact. Segment-based contact considers segment to segment contact rather than the more conventional penalty formulation, which scans for contacts between nodes and segments, resulting in a reduced incidence of undetected penetrations. Contact forces between the plate and soil were recorded throughout the simulation to provide a measure of the force required to penetrate the soil sample, with the boundary force required to maintain the prescribed plate velocity also recorded as an additional check.

For the Eulerian soil model, contact between the Lagrangian plate and Eulerian soil sample was represented using a fluid structure interaction (FSI) approach. As for the Lagrangian simulation, the contact force between the plate and soil could be monitored throughout the simulation to generate a predicted plate sinkage profile. The variables considered during the plate sinkage study can be summarised as follows:

- two soil types (numerical and experimental);
- two solution methods (numerical only);
- yield surface parameters (numerical only);
- mesh resolution (numerical only);
- plate velocity (numerical and experimental).

In addition to the above variables, early simulations using the Lagrange solver with a relatively coarse mesh (five 7.52mm elements across the interface between plate and soil) indicated that some form of hourglass control would be necessary to address non-physical, zero energy hourglass deformations within

the soil mesh, which resulted in mesh tangling, negative element volumes and error terminations. Hourglassing can be reduced in under-integrated elements by mesh refinement, the introduction of hourglass control algorithms, or can be entirely eliminated by the use of selectively reduced or fully-integrated elements, which are not subject to hourglass modes.

All of the available solutions to hourglassing have some potential disadvantages: the introduction of an hourglass control algorithm is generally the least computationally expensive approach, but for soft materials such as soils, the damping of hourglass modes can result in an overly-stiff response; fully-integrated elements, while entirely eliminating hourglass modes, can suffer from severe instabilities in response to large deformations; finally, mesh refinement, while potentially increasing accuracy, results in a significant increase in computational cost due to an increase in the number of elements within the simulation (the number of calculations required per cycle) and a reduction in the allowable timestep size (the number of cycles required to simulate an event of a given duration).

In an effort to remove the hourglass control algorithm as a variable and a potential source of error, baseline Lagrange simulations were initially run using selectively reduced solid elements to represent the soil. Despite successfully addressing the hourglass modes associated with one point constant stress elements, the selectively reduced solids used for the initial Lagrange simulations suffered from severe instability due to the large, localised deformations occurring within the soil sample. It was therefore necessary to revert to one point constant stress elements with an hourglass control algorithm for the Lagrange simulations.

Due to the quasi-static nature of the plate sinkage test, a stiffness-based hourglass control algorithm (Type 4) was selected, with the default hourglass control coefficient scaled back to balance the need for damping of hourglass modes against the stiffening effect of hourglass control on very soft materials. A short parametric study indicated that an hourglass coefficient of 5.5×10^{-3} was required to stabilise the simulation, with lower values resulting in error

termination. Further details of the parametric hourglass study are provided in Appendix F.

Coarse, intermediate and fine models were built for both the Lagrange and Eulerian models, with the coarsest model employing five elements across the radius of the plate, resulting in a mesh size of 7.52mm at the contact interface. The intermediate and fine mesh models employed 3.76mm and 1.88mm elements across the contact interface, respectively, with the element size at all three resolutions gradually increasing away from the plate / soil contact interface. These initial simulations used an arbitrary sinkage rate of 100mm/s to reduce runtime while the effects of yield surface parameters, solution method and mesh resolution were assessed.

4.1.1 Quasi-static simulation results

To assess the accuracy of the FE modelling results, the predicted levels of sinkage for specific vertical pressure values were compared against the mean of the experimental tests, as presented in Appendix D.

The results of the quasi-static plate sinkage simulations are graphically compared against experimental means in Figures 4.3 to 4.10. Quantitative assessments of model accuracy, in terms of the mean percentage error, are provided in Appendix D; modelling results for sandy loam using yield surface parameters from triaxial tests are not included in the quantitative assessment, as numerical errors meant that the minimum vertical pressure for quantitative assessment (33kPa) was never reached. The initial simulations indicated that, for both soils, the yield surface parameters derived from direct shear box testing produced a better level of agreement with the quasi-static experimental data than those derived from the triaxial tests.

For the dry sand, a quantitative comparison was possible. While the yield surface parameters derived from shear box results consistently produced a lower mean percentage error, regardless of the mesh resolution used, the accuracy of the model was still relatively poor when using the coarsest mesh,

with a mean percentage error of 56 to 74% (compared with 86 to 94% using the triaxial yield surface), depending on the solver used. The accuracy of the shear box yield surface results increased as a function of mesh resolution, however, with the mean percentage error dropping markedly as element size was reduced (from 56 - 74% with the coarse mesh to 5 - 7% with the fine mesh). The results obtained using the triaxial yield surface parameters were less sensitive to mesh resolution, but vastly over-estimated the resistance of the dry sand to penetration, even at the highest mesh resolution.

Comparing the results of the Lagrange and Euler simulations for both soils, but restricting the assessment to the shear box yield surface parameters alone, the Euler solver offers greater accuracy at the coarsest mesh resolution. Looking at the results obtained for the dry sand (Figure 4.4 and Figure 4.6), the Lagrange solver predicts a much stronger and noisier response than the Euler approach. This is most likely related to the need to use a higher hourglass control coefficient with the Lagrange solver, as discussed in Appendix F. As mesh resolution is increased, the apparent strength of the Lagrange soil mesh is reduced, reflecting the effect of mesh refinement itself as a method of hourglass control. In the case of the sandy loam, the differences between the Lagrange and Euler solvers are less pronounced due to the higher strength of the sandy loam.

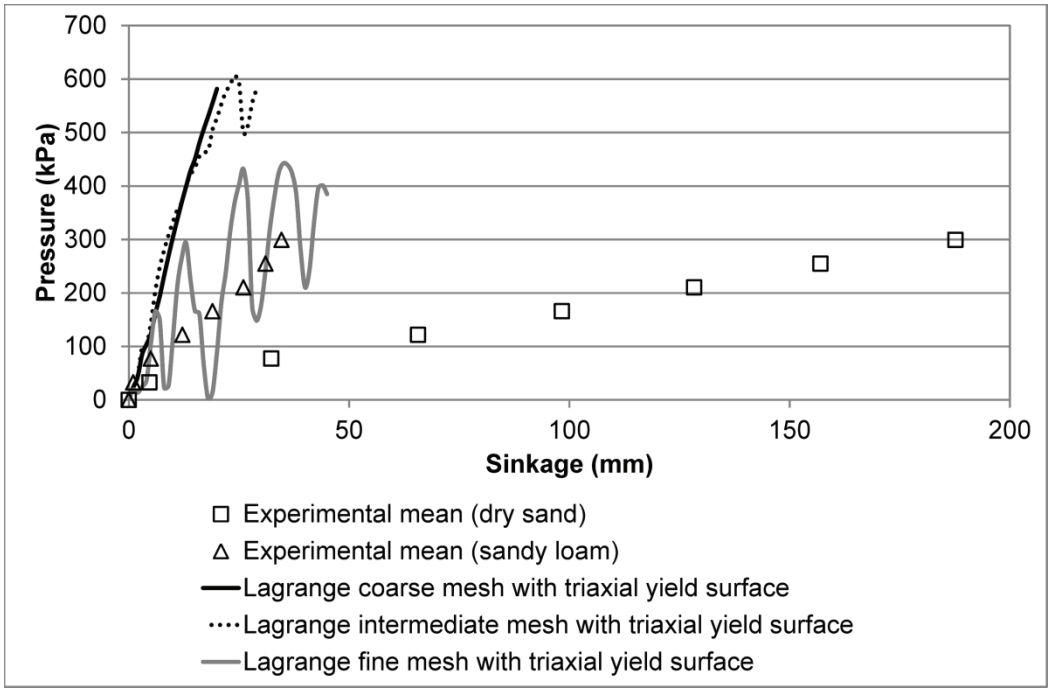

Figure 4.3: Comparison of plate sinkage profiles predicted for dry sand, using Lagrangian FE models with yield surface parameters from triaxial tests, against experimental data

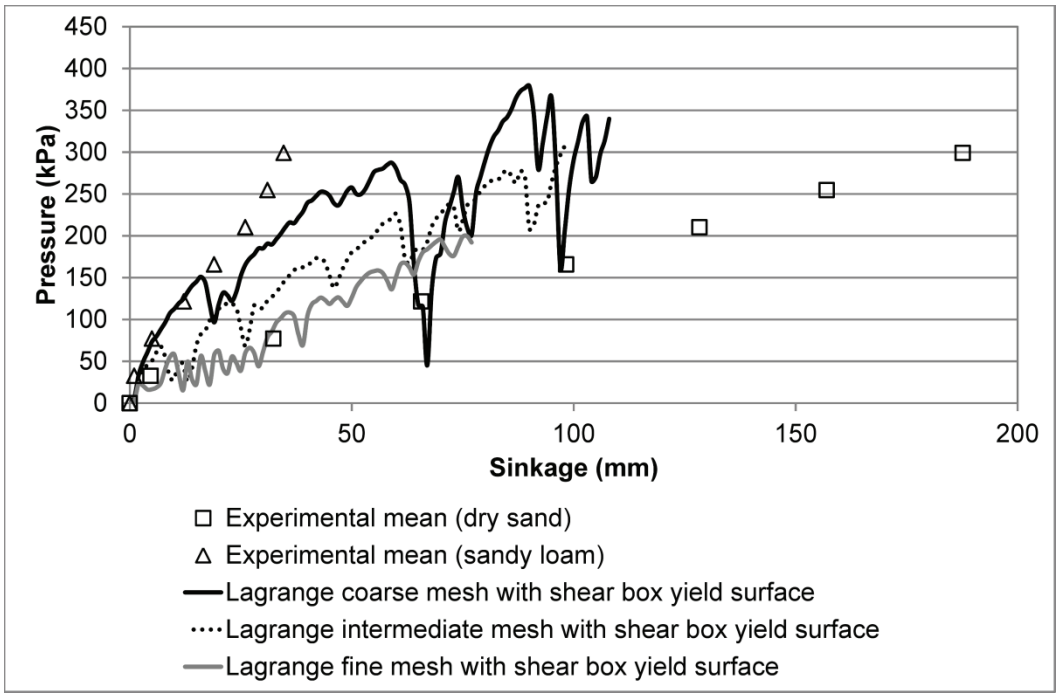

Figure 4.4: Comparison of plate sinkage profiles predicted for dry sand, using Lagrangian FE models with yield surface parameters from shear box tests, against experimental data

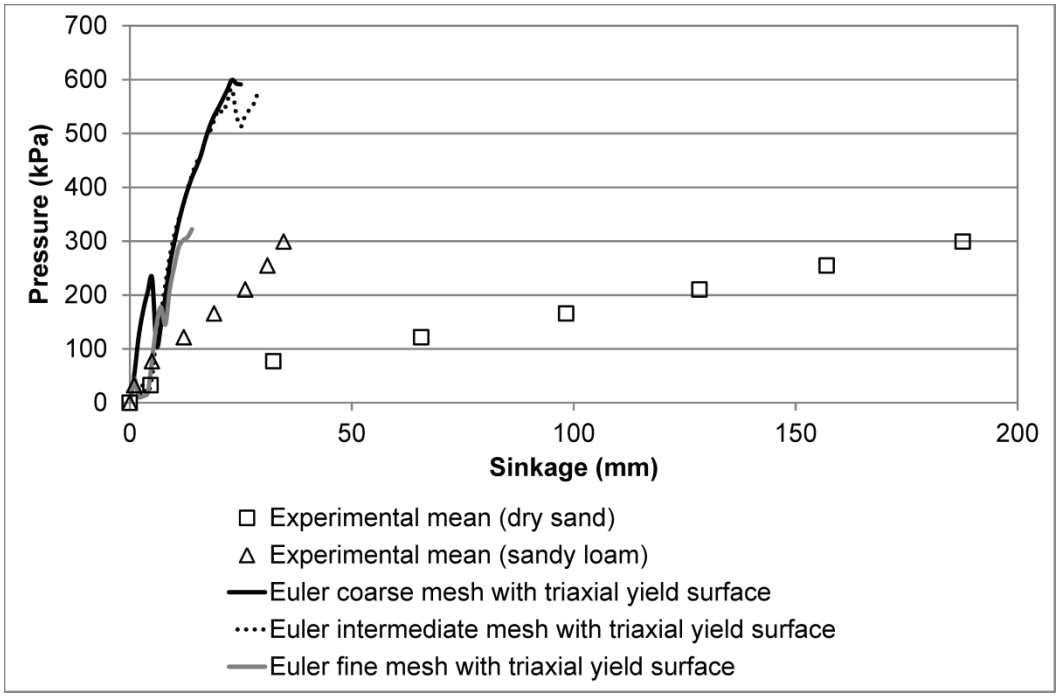

Figure 4.5: Comparison of plate sinkage profiles predicted for dry sand, using Eulerian FE models with yield surface parameters from triaxial tests, against experimental data

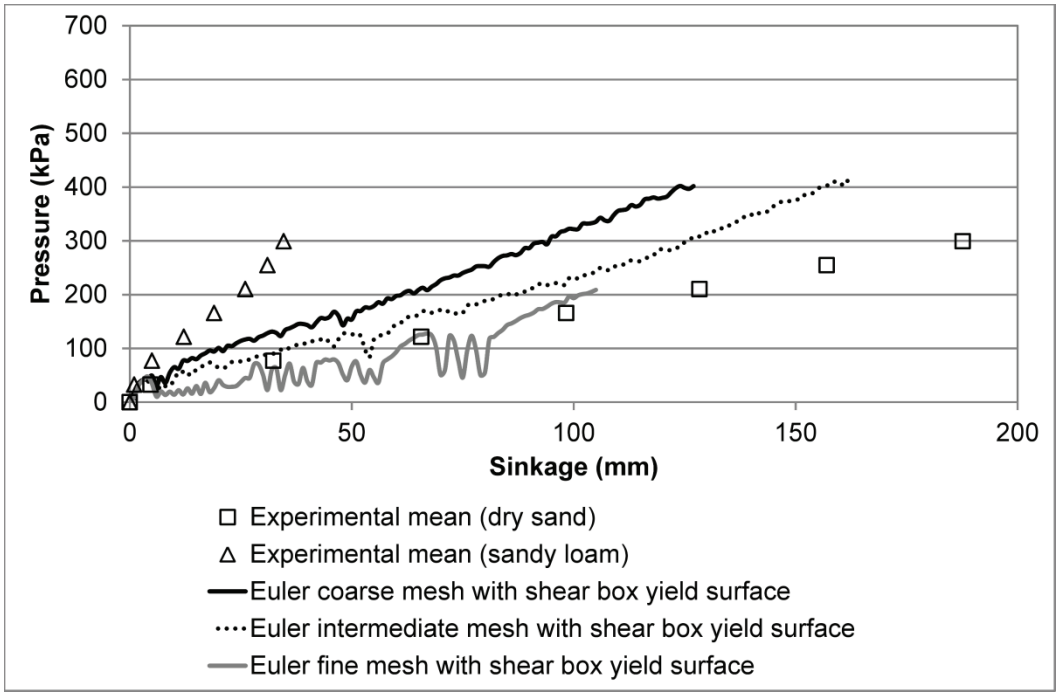

Figure 4.6: Comparison of plate sinkage profiles predicted for dry sand, using Eulerian FE models with yield surface parameters from shear box tests, against experimental data

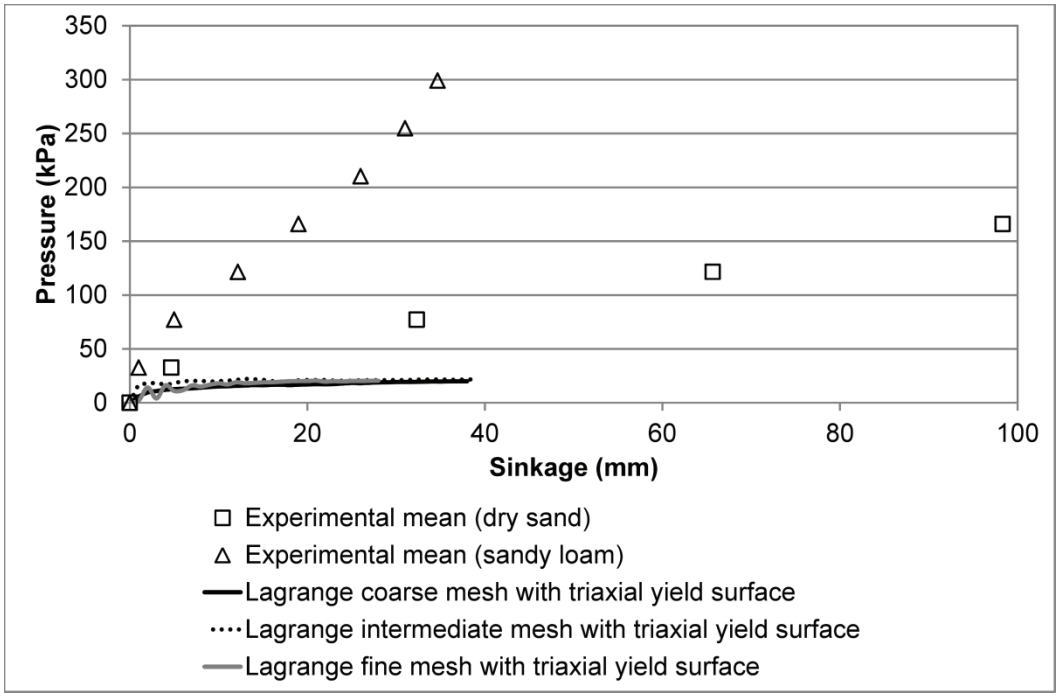

Figure 4.7: Comparison of plate sinkage profiles predicted for sandy loam, using Lagrangian FE models with yield surface parameters from triaxial tests, against experimental data

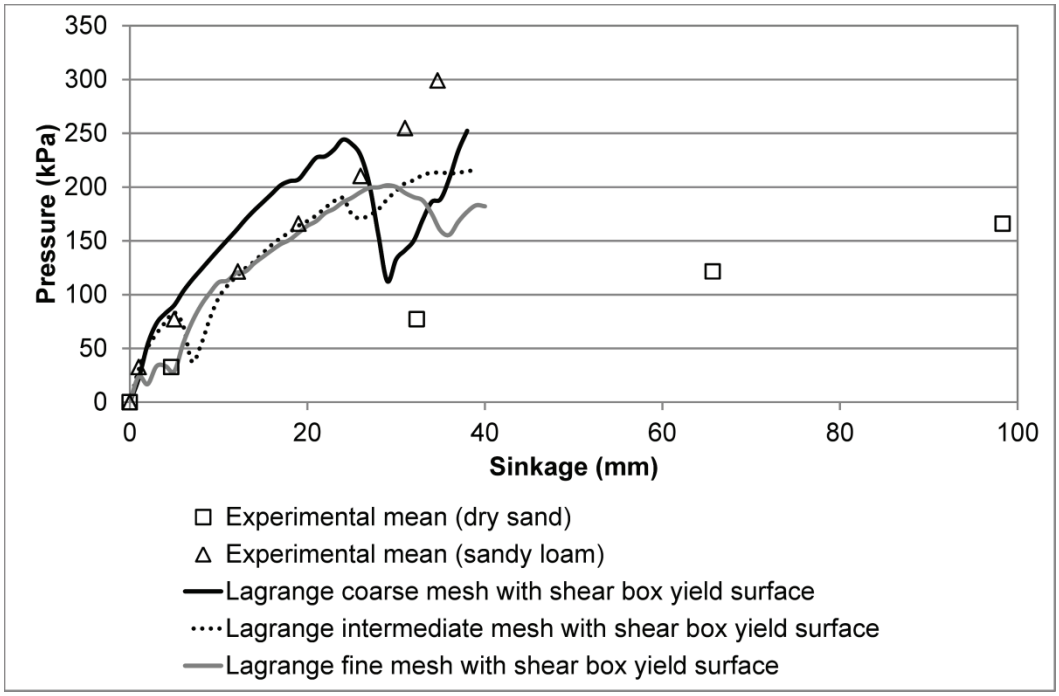

Figure 4.8: Comparison of plate sinkage profiles predicted for sandy loam, using Lagrangian FE models with yield surface parameters from shear box tests, against experimental data

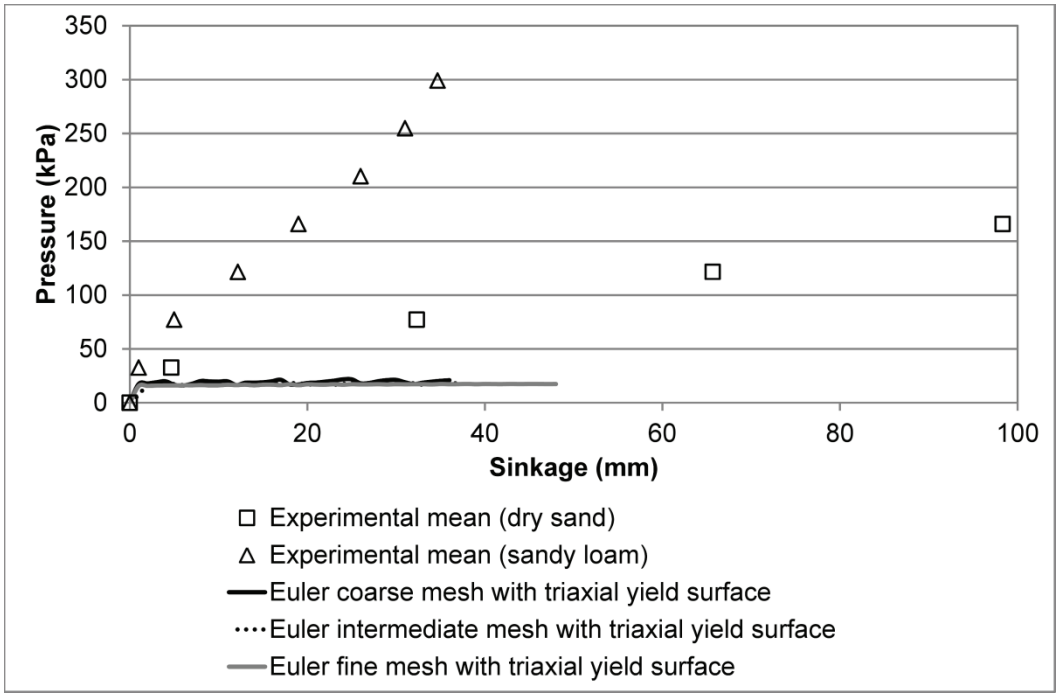

Figure 4.9: Comparison of plate sinkage profiles predicted for sandy loam, using Eulerian FE models with yield surface parameters from triaxial tests, against experimental data

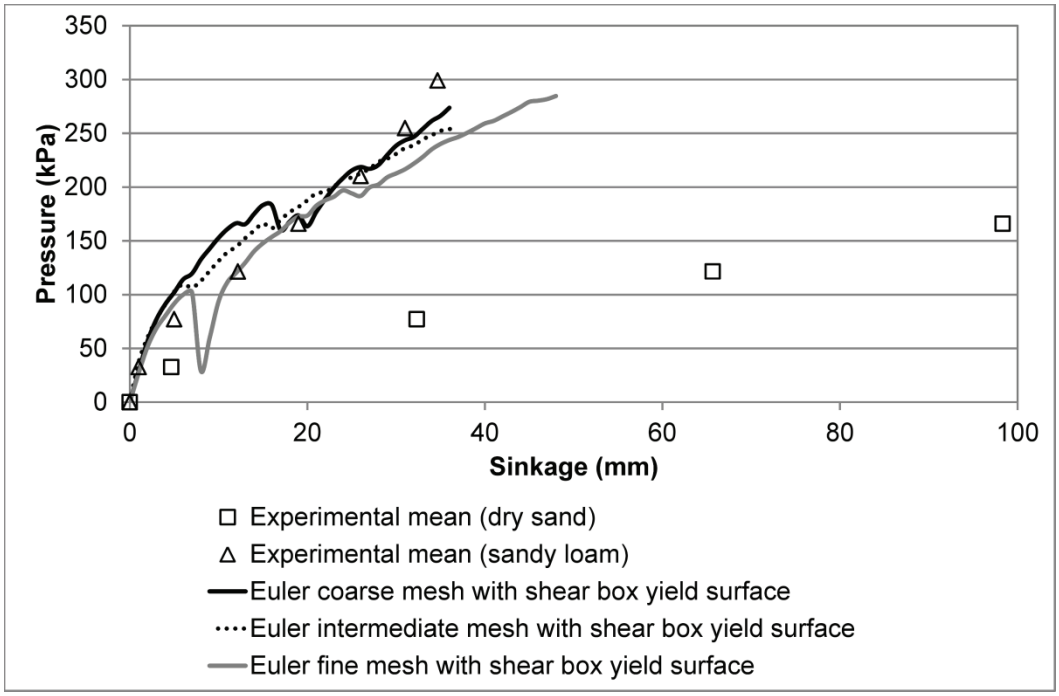

Figure 4.10: Comparison of plate sinkage profiles predicted for sandy loam, using Eulerian FE models with yield surface parameters from shear box tests, against experimental data

4.2 Loading rate study

The plate sinkage tests discussed above were performed statically, with a specified load applied to the plate and the corresponding sinkage measured once equilibrium had been established. Since off-road mobility is an inherently dynamic problem, there is a need to consider the effect of dynamic loading on the soil's resistance to penetration. Dynamic plate sinkage tests were undertaken on both dry sand and sandy loam soils using the Cranfield University single wheel tester (SWT), with a 30mm diameter steel rod forced into the soil. The force required to penetrate the soil was recorded throughout each test as a function of plate displacement, allowing plate sinkage profiles to be constructed for a range of penetration speeds. A minimum of three replicates were completed at each penetration speed, with the arithmetic mean of the individual test results taken at specific levels of sinkage to aid the identification of any relationship between plate penetration speed and the force required for penetration.

4.2.1 Experimental results

The results of the dynamic plate sinkage tests undertaken on dry sand are presented in Figure 4.11, alongside data from the static plate sinkage tests. For ease of visualisation, dynamic plate sinkage profiles are presented separately for speeds of 1 to 100mm/s and 100mm/s to 500mm/s, with the 100mm/s profile serving as a common data set to aid comparison between the two plots.

From the plate sinkage profiles obtained, the relationship between the rate of sinkage and the pressure required is not immediately obvious for the dry sand. At low sinkage levels, below 60mm, there appears to be very little difference in the pressure required to penetrate the soil as the rate of sinkage increases. As the level of sinkage increases beyond 60mm, however, an observable difference develops between the lowest rate dynamic test (1mm/s) and the remaining profiles (10 – 500mm/s), with the 1mm/s profile indicating a greater pressure is required to penetrate the soil at this speed. For the 10 – 500mm/s

profiles, no clearly discernible differences exist in the pressure required for perforation until the sinkage depth exceeds approximately 125mm.

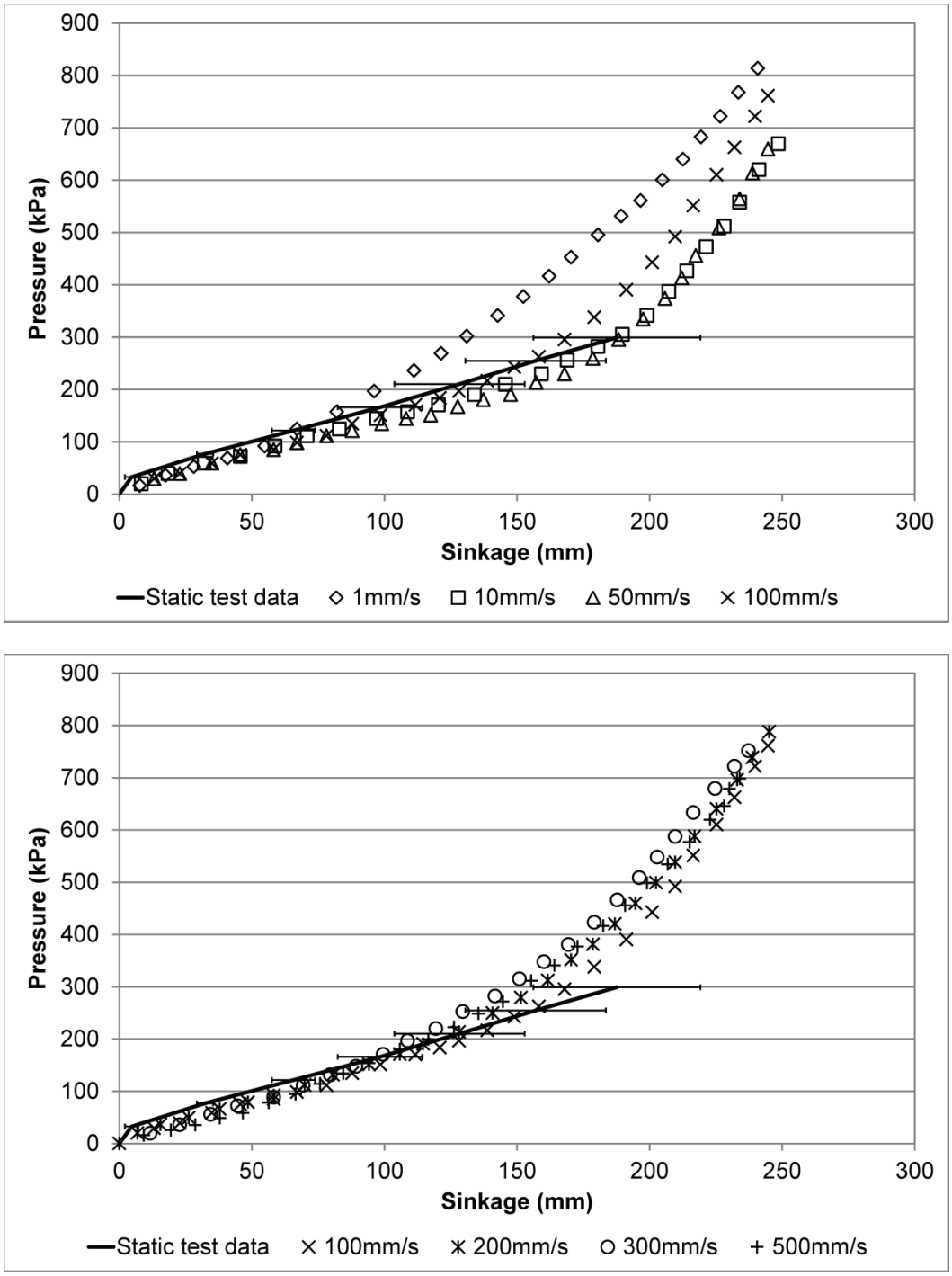

Figure 4.11: Experimental data for dry sand, illustrating effect of plate velocity on resulting plate sinkage profile (error bars indicate standard deviation of static test data)

For sinkage levels greater than 125mm, the effect of loading rate on the pressure required to penetrate the soil is clearer, but is not straightforward. Between 1 and 50mm/s, an increase in penetration rate is accompanied by an apparent reduction in soil strength, with a lower pressure required to achieve a given level of sinkage. At penetration speeds above 50mm/s, however, the apparent strength of the sand partially recovers.

For off-road mobility applications, it may be more appropriate to consider the variation in sinkage with plate penetration speed for a fixed ground pressure, as shown in Figure 4.12. When viewed in this manner, the relationship between loading rate and the resulting level of sinkage is more clearly discernible, with an initial increase in sinkage as the speed of penetration increases from 1mm/s to 50mm/s. As the speed of penetration increases further, there is a gradual reduction in the level of sinkage observed, until a plateau is reached at a penetration speed of approximately 300mm/s. The relationship between the rate of sinkage and the level of sinkage observed, with an apparent softening of the soil between 1 and 50mm/s, was found to be consistent regardless of the ground pressure used for comparison. Pressures of 150 to 550kPa were selected on the basis that these ground pressures reflect the MMP criteria for High Mobility (HMLC), Improved Medium Mobility (IMMLC) and Medium Mobility (MMLC) load carriers in Def. Stan 23-06 Issue 3 (2000).

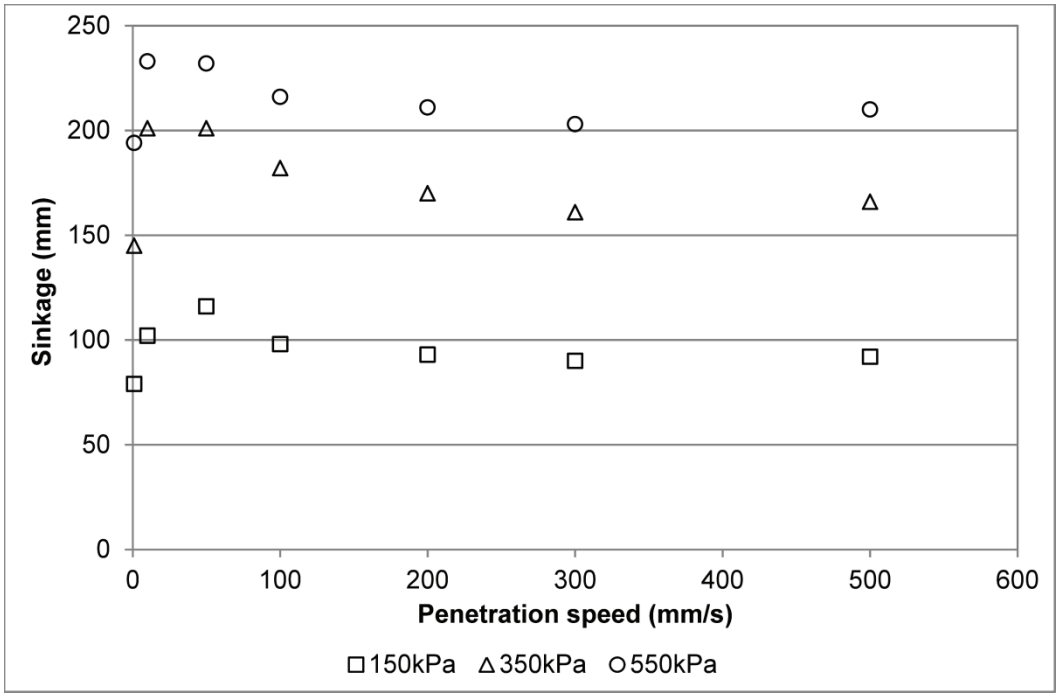

Figure 4.12: Effect of plate penetration speed on depth of sinkage for a given ground pressure

While Figure 4.12 demonstrates that there is a clear and consistent relationship between the rate and depth of sinkage for a given pressure level, Figure 4.11 suggests that, for pressures of 300kPa or less, the variation in sinkage with the rate of loading is generally within the scatter of the data obtained from a series of static plate sinkage tests on the dry sand. This is highlighted in Figure 4.13, which compares the dynamic sinkage values for pressures of 150 and 250kPa against the minimum, maximum and mean sinkage values recorded during static plate sinkage tests.

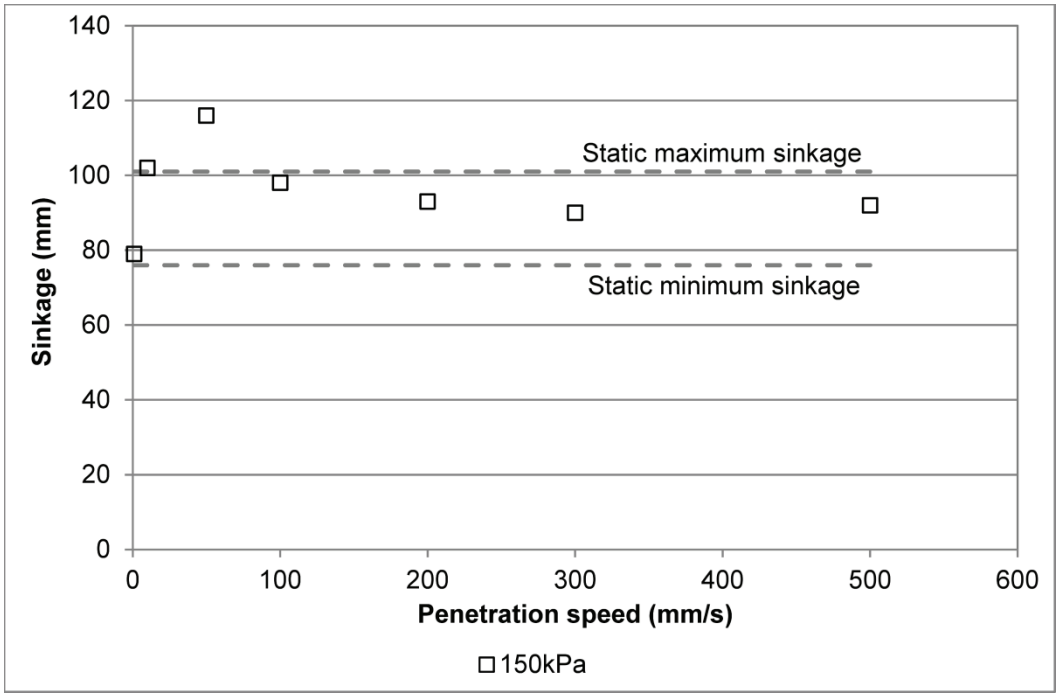

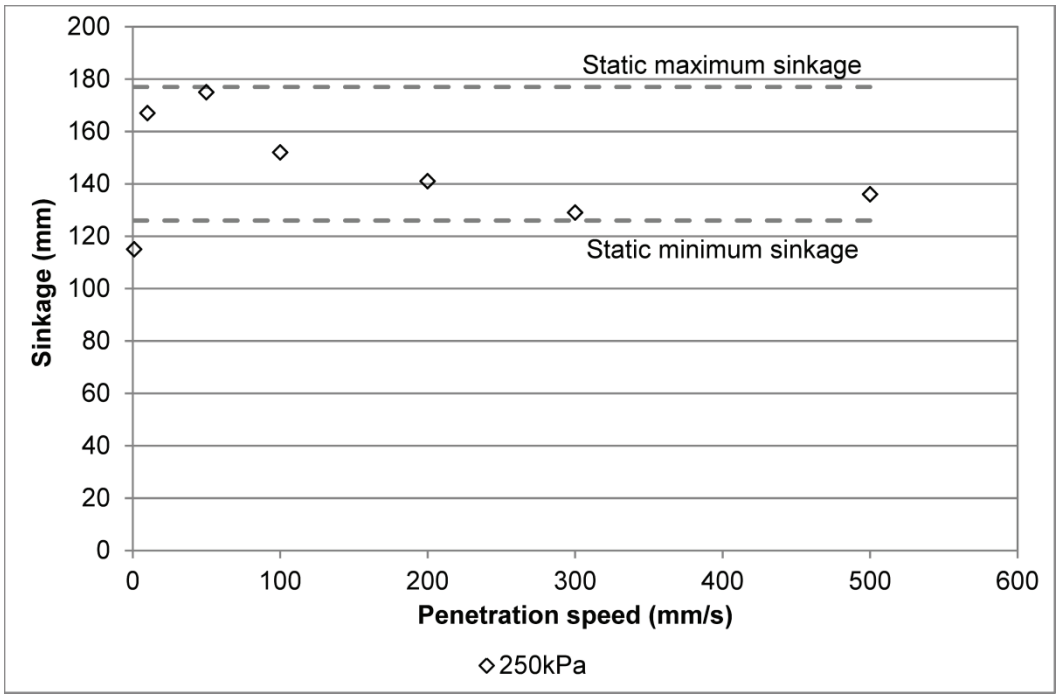

Figure 4.13: Comparison of dynamic plate sinkage data against static test results for applied pressures of 150kPa (top) and 250kPa (bottom) in dry sand

The results of the dynamic plate sinkage tests undertaken on sandy loam soil are presented in Figure 4.14 for sinkage depths of up to 160mm. The pressures required to penetrate the soil to this depth (3,000 – 5,000kPa) significantly exceed the level of ground pressure expected for even low mobility load carriers (LMLC, with MMP greater than 700kPa); for this reason, Figure 4.15 provides a more detailed view of the low sinkage region of the profiles, for sinkage depths of up to 50mm. As for the dry sand, sinkage rates of 1 – 100mm/s and 100 – 500mm/s are presented separately for ease of visualisation.

From the results obtained, the influence of loading rate on the resulting plate sinkage profile is much more pronounced for the sandy loam than for the dry sand, with a significant increase in the pressure required for a given depth of penetration as the speed of penetration is increased from 1mm/s to 50mm/s. As with the dry sand, the effect of penetration speed is not consistent across the range of speeds considered, with a substantial increase in the apparent strength of the soil between 1 and 50mm/s, followed by a gradual reduction in the soil's resistance to penetration as the rate of loading increases beyond 50mm/s.

The relationship between penetration speed and sinkage for a given pressure is illustrated in Figure 4.16. In contrast to the variation observed for dry sand, an initial increase in penetration speed results in a sharp reduction in sinkage for the sandy loam. As the speed of penetration is increased above 50mm/s, a very gradual increase in sinkage is observed, with no plateau in sinkage observed over the range of penetration speeds considered.

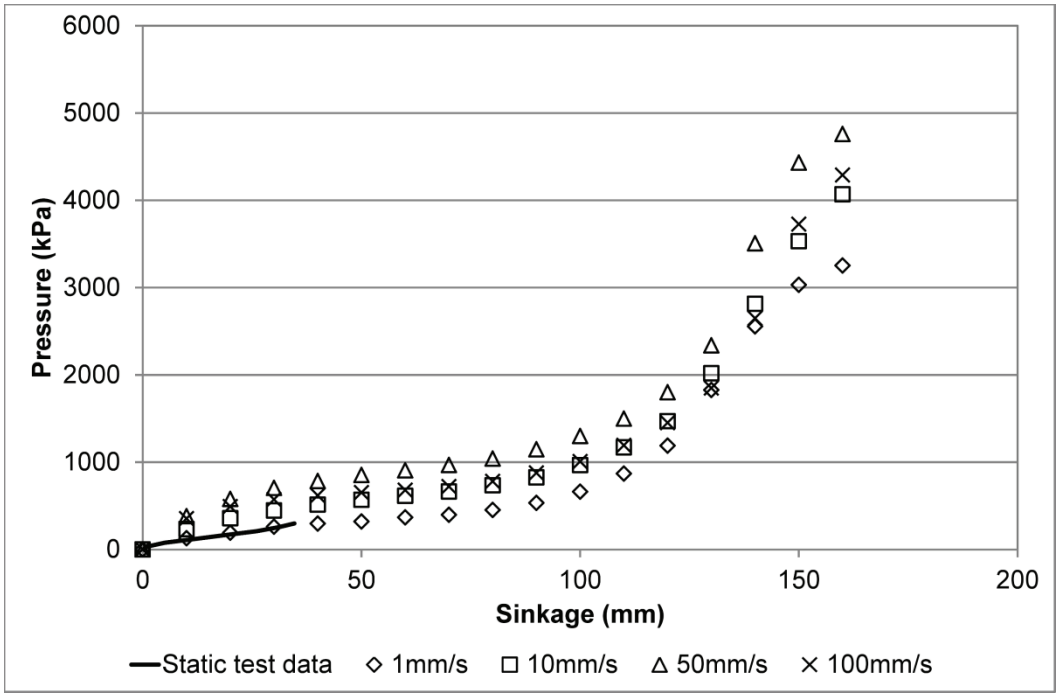

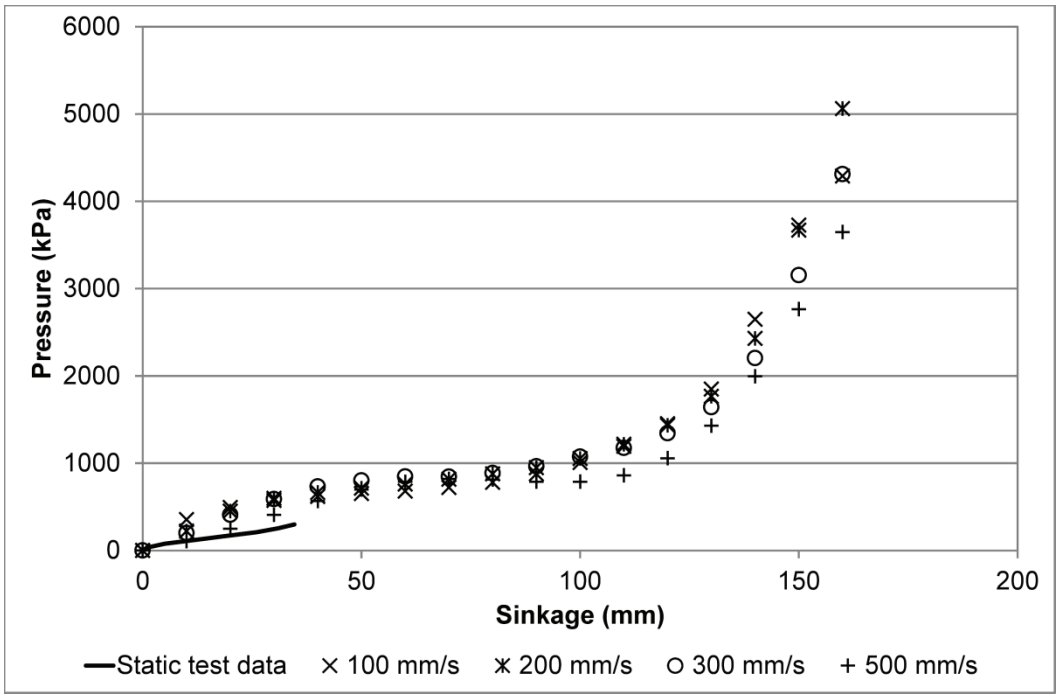

Figure 4.14: Experimental dynamic plate sinkage data for sandy loam, illustrating effect of plate velocity on resulting plate sinkage profile for sinkage depths of up to 160mm

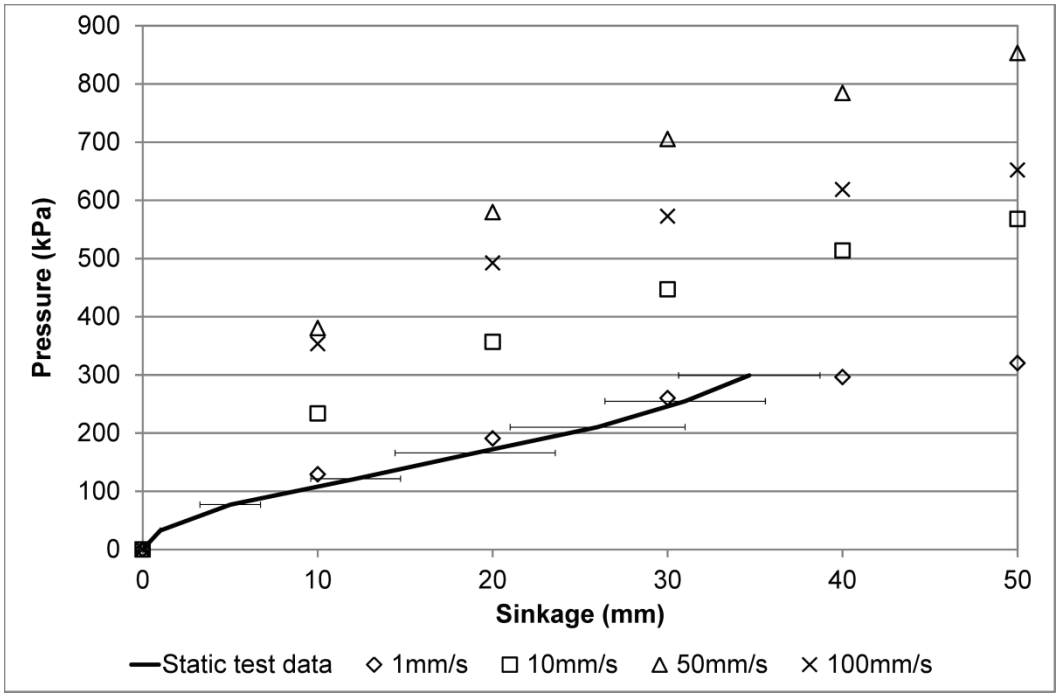

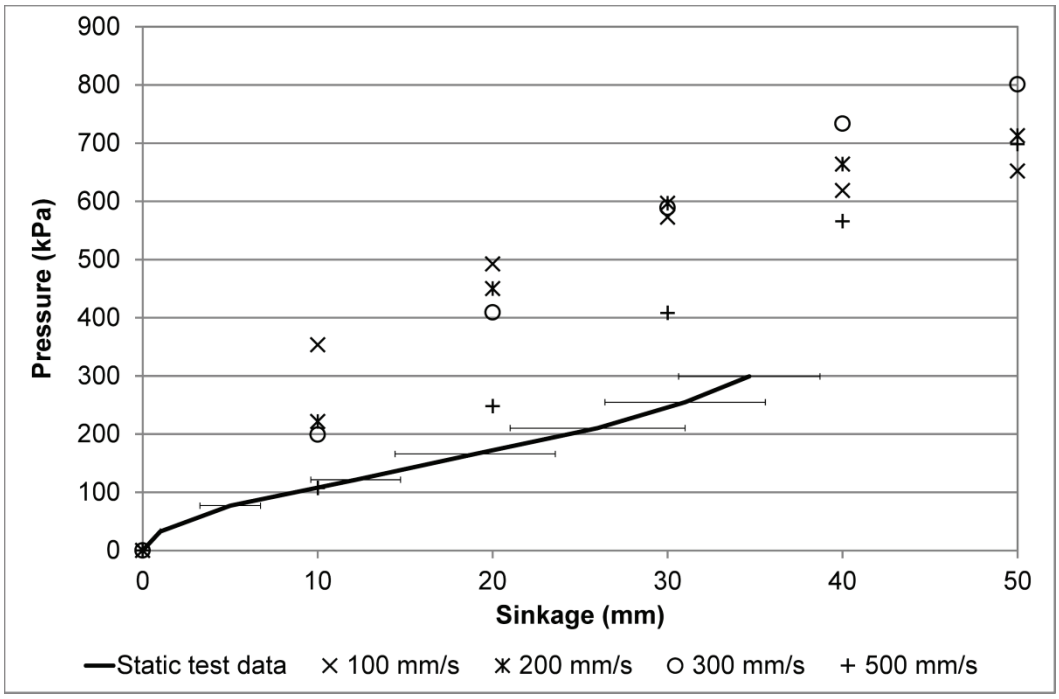

Figure 4.15: Experimental dynamic plate sinkage data for sandy loam, illustrating effect of plate velocity on resulting plate sinkage profile for sinkage depths of up to 50mm (error bars indicate standard deviation for static test data)

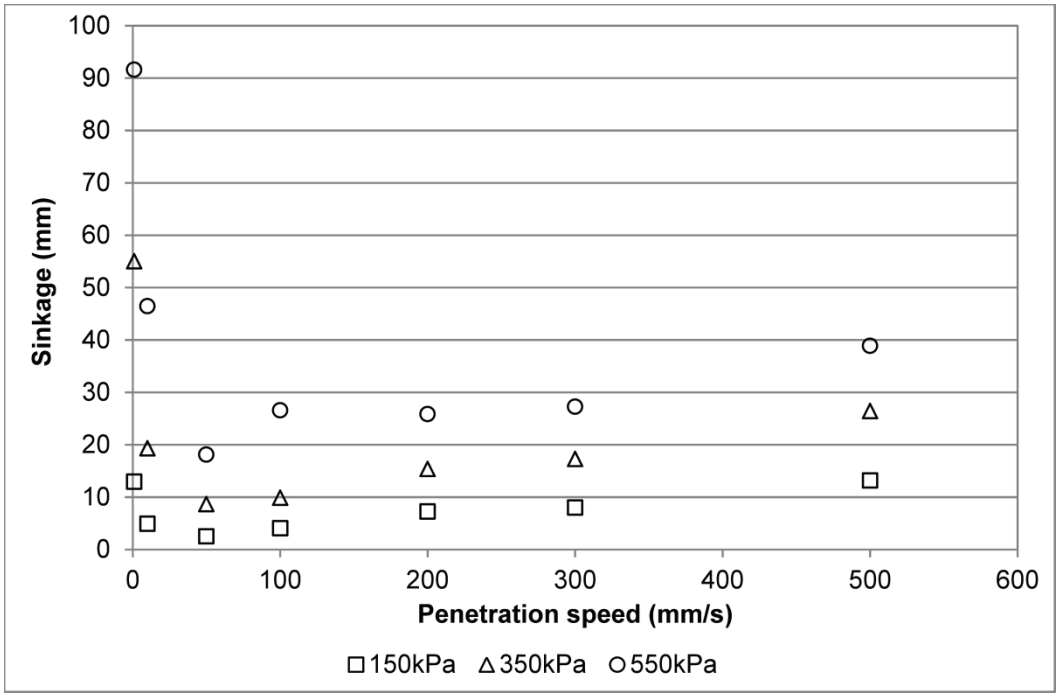

Figure 4.16: Effect of plate penetration speed on depth of sinkage for a given ground pressure

For the dry sand, it was observed that after an initial increase in sinkage between 1 and 50mm/s, the sand recovered much of its resistance to penetration, and that the variation in sinkage was mostly within the variability associated with static plate sinkage tests. In the case of the sandy loam, the initial variation in sinkage with penetration speed is more pronounced, with a significant reduction in sinkage at low loading rates. As the rate of penetration is increased further, from 50mm/s to 500mm/s, the apparent strength of the soil gradually reduces, with a corresponding increase in sinkage. Unlike the dry sand, where the level of sinkage at 500mm/s was generally within 20% of that observed at 1mm/s, the level of sinkage observed at the highest penetration rate (500mm/s) in the sandy loam is less than half of that recorded at 1mm/s for pressures above 250kPa.

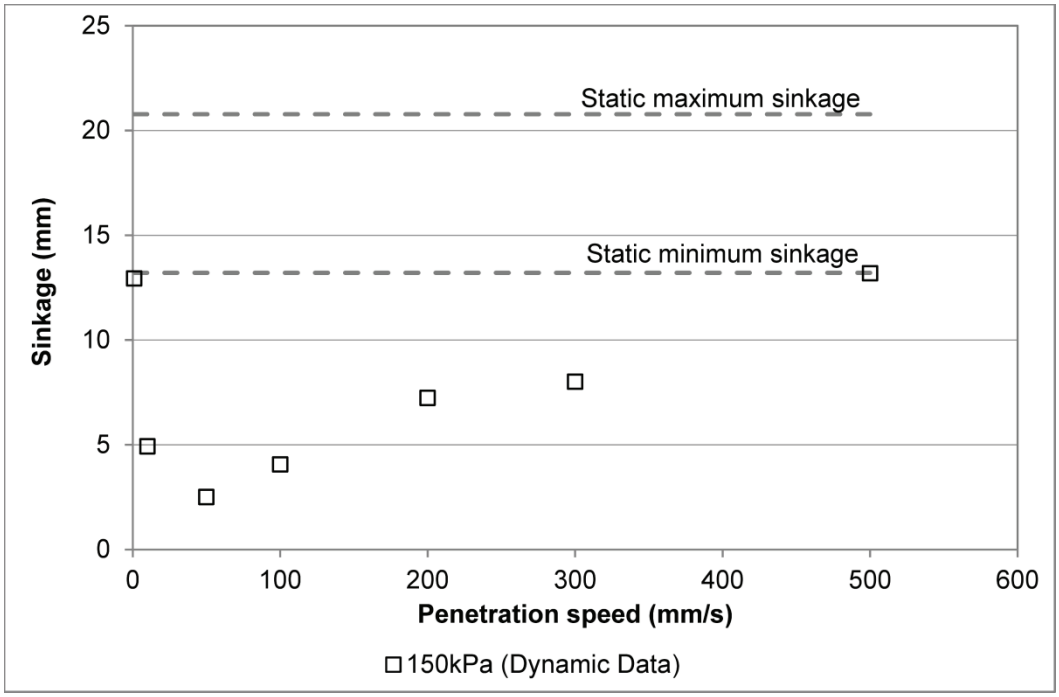

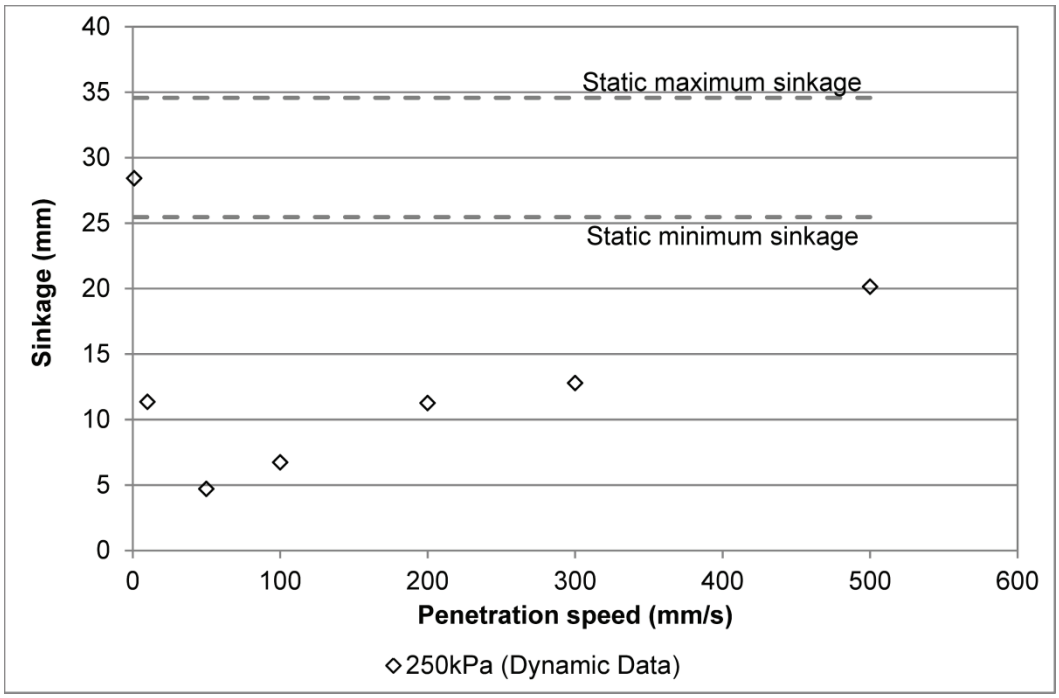

Figure 4.17: Comparisons of dynamic plate sinkage data against static test results for applied pressures of 150kPa (top) and 250kPa (bottom) in dry sand

4.2.2 Implications of loading rate effects on mobility modelling

As demonstrated by the dynamic plate sinkage results presented above, the rate at which the load is applied to the plate can affect the pressure-sinkage profiles obtained. To assess the implications of the observed rate sensitivity on the development of an FE-based mobility prediction tool, an analysis was undertaken to relate vehicle translational velocity to the loading rate of the soil. Considering only the in-plane, vertical deformation of the soil, and taking Bekker's model as an example, rolling resistance can be related to the level of wheel sinkage as follows:

$$R = \int_0^{z_0} bp\,\partial z = \frac{bkz_0^{\,n+1}}{(n+1)} \qquad \textit{Equation 4.1}$$

To assess the effect of loading rate on rolling resistance, the soil parameters k and n were first determined for each loading rate in both dry sand and sandy loam soils (Table 4.1). From this data, Bekker's equation for sinkage (Equation 4.2) was used to calculate the level of sinkage for a series of arbitrary wheel loads between 5 and 15kN. Finally, Equation 4.1 was used to calculate the variation in rolling resistance, assuming a wheel of unit width.

$$Z_0^{\,n+1/2} = \frac{3W}{bk\sqrt{D}(3-n)} \qquad \textit{Equation 4.2}$$

Having calculated the effect of vertical loading rate on rolling resistance, it was then possible to relate the vertical loading rate of the soil to the translational speed of the vehicle. This was achieved by considering the geometry of a rigid wheel interacting with deformable terrain, assuming a given sinkage / entry angle, as illustrated in Figure 4.18.

From Figure 4.18, the average vertical speed of a point on the wheel's circumference between initial contact with the soil and bottom dead centre can be calculated from the translational velocity of the wheel as follows:

$$v_Z = \frac{v_X * (1 - Cos\theta)}{Sin\theta} \qquad \textit{Equation 4.3}$$

Rearranging the terms in Equation 4.3 allows the vehicle's translational speed to be related to the average vertical loading rate of the soil. Figure 4.19 and Figure 4.20 illustrate the predicted relationship between vehicle translational velocity and rolling resistance for a towed wheel, 600mm in diameter operating on dry sand and sandy loam soil, respectively. It should be noted that the above relationship between vehicle translational velocity and the vertical loading rate (Equation 4.3) is dependent upon the entry angle of the wheel, θ, and therefore on the level of sinkage. As a result, the relationship between vehicle translational speed and rolling resistance is also influenced by the applied wheel load.

The results of the experimental plate velocity study indicate that the rate of loading (and therefore the vehicle's translational speed) influences the level of sinkage observed in both dry sand and sandy loam soils. The effect is much less pronounced in dry sand, with the observed variation in sinkage / rolling resistance generally being within the expected variability of static or quasi-static test data. For the sandy loam soil, the variation in sinkage / rolling resistance between quasi-static (1mm/s) and relatively low-rate dynamic tests (>10mm/s) is much larger, suggesting that mobility models based on static or quasi-static test data may significantly over-estimate the level of motion resistance, even for low vehicle translational speeds.

Table 4.1: Bernstein pressure-sinkage parameters derived from dynamic plate sinkage results (sinkage in mm, pressure in kPa)

Loading rate	**Soil type**			
	Dry sand (up to 150mm sinkage)		**Sandy loam (up to 50mm sinkage)**	
	k	n	k	n
Static	6.08	0.81	290	0.60
1 mm/s	0.55	1.29	36	0.56
10 mm/s	2.83	0.86	71	0.54
50 mm/s	3.12	0.82	136	0.47
100 mm/s	1.39	1.02	161	0.36
200 mm/s	1.53	1.02	67	0.62
300 mm/s	0.57	1.25	38	0.79
500 mm/s	0.41	1.30	9	1.12

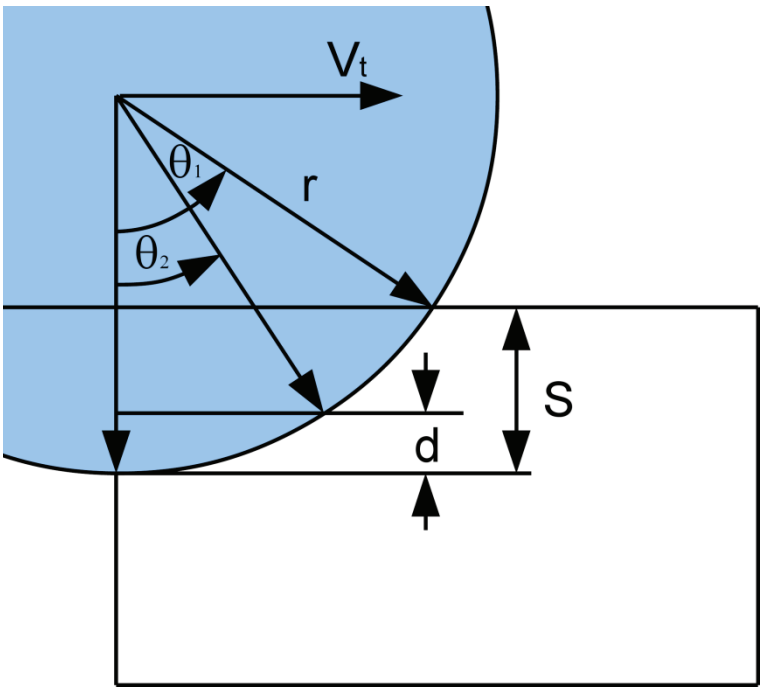

Figure 4.18: Geometry of rigid wheel interacting with deformable terrain for calculation of vertical sinkage rate as a function of translational speed

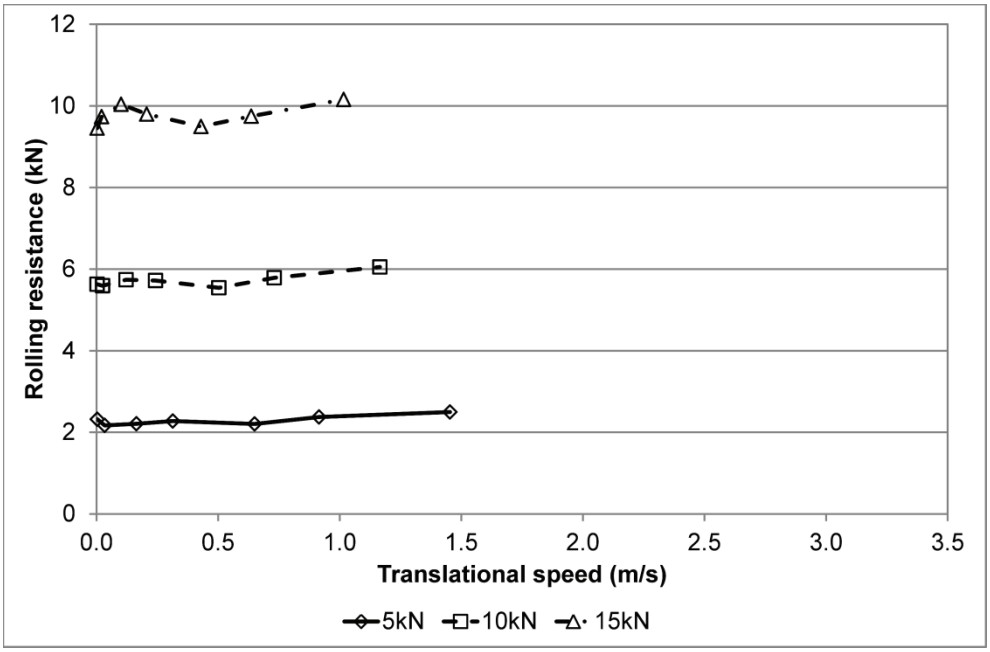

Figure 4.19: Calculated influence of vehicle translational speed on rolling resistance for a towed rigid wheel operating on dry sand under wheel loads of 5, 10 and 15kN, based on plate dynamic sinkage profiles obtained at sinkage rates of between 1 and 500mm/s

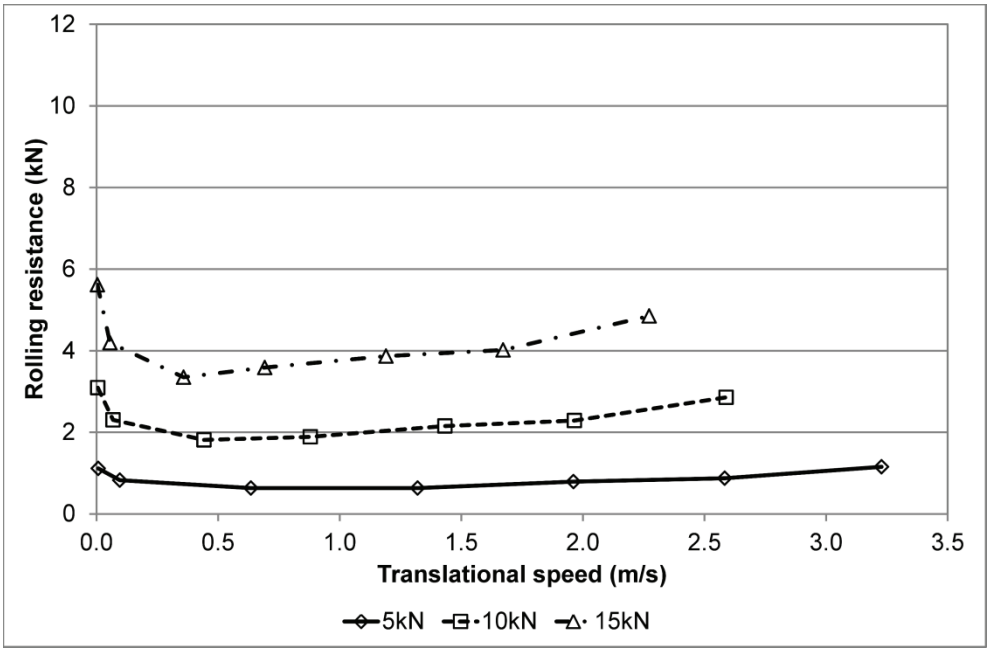

Figure 4.20: Calculated influence of vehicle translational speed on rolling resistance, for a towed wheel operating on sandy loam, based on dynamic plate sinkage profiles obtained at sinkage rates of between 1 and 500mm/s

Summaries of the main sources of rate effects within soils, including the influence of moisture content, are provided by Karafiath and Sobierajski (1974) and Grujicic et al. (2009). It is reported that the macroscopic deformation of the soil can be described in terms of contributions from two main sources:

- Deformation and fracture of the bonds between soil particles;
- Deformation and fracture of the constituent phases (solid soil particles, water and air).

For dry soils loaded at relatively low pressures, the response of the soil to applied loading is primarily controlled by the first of the above mechanisms. As the applied pressure is increased, and the soil approaches a fully compacted state, deformation and fracture of the solid soil particles begins to occur. While there may be a degree of strain rate sensitivity within the solid soil particles, rate effects are generally of secondary importance in terms of the macroscopic resistance of the soil to deformation.

As moisture is introduced, the macroscopic response of the soil to applied loading begins to be influenced by the time-dependent movement of water / air through the solid soil skeleton. As the rate of loading is increased, the liquid and gas phases become trapped within the solid soil skeleton, and will therefore contribute to the overall load carrying capacity of the soil as a whole.

Shmulevich, Mussel and Wolf (1998) provide a useful overview of previous studies on the rate dependency of soils. Interestingly, the study completed by Shmulevich et al., along with papers by Grahn (1991) and Pope (1971) all indicate that the resistance to penetration continues to increase across a much wider range of speeds than suggested by the experimental study reported above. From dynamic plate sinkage tests in sandy loam soil, Grahn proposed the following modification to Bernstein's pressure sinkage relationship, accounting for the effect of penetration speed:

$$P = kz^n \dot{z}^m \qquad \textit{Equation 4.4}$$

Using the above relationship to relate rolling resistance to vehicle translational speed results in a steep initial reduction in rolling resistance as speed is

increased from a quasi-static condition, followed by a more gradual reduction at higher translational speeds, as illustrated in Figure 4.21.

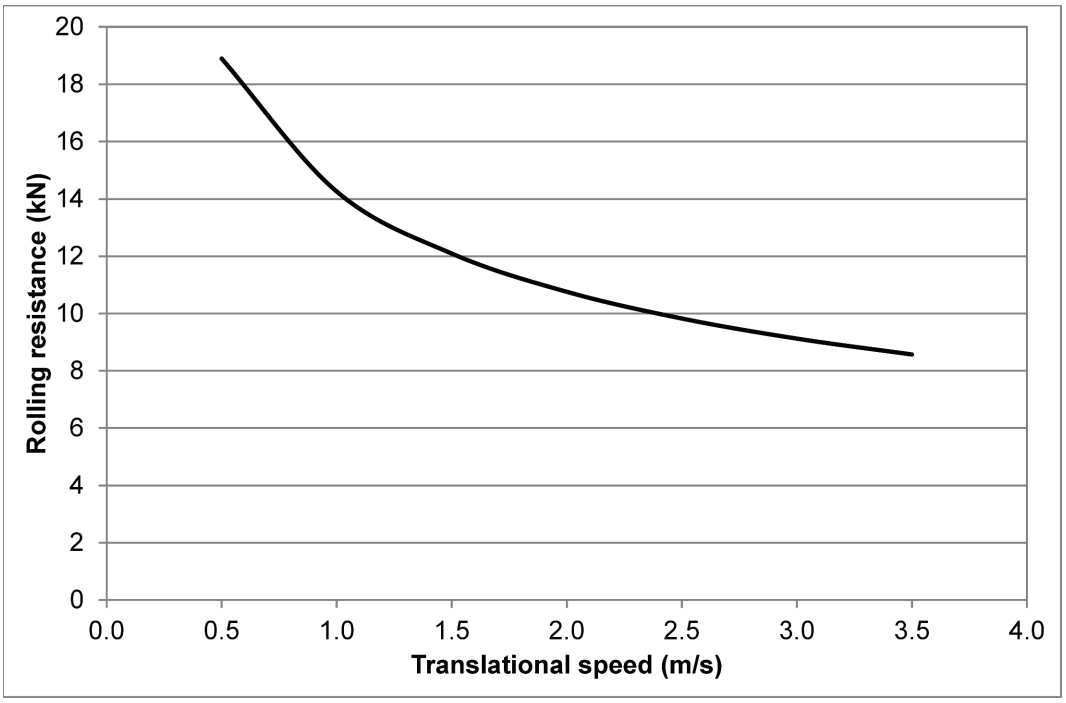

Figure 4.21: Relationship between rolling resistance and vehicle translational speed, as reported by Grahn (1991)

4.2.3 Dynamic plate sinkage models

To investigate the sources of the observed loading rate sensitivity, and the ability of FE mobility models to incorporate loading rate effects, the plate sinkage model described above was used to run a series of simulations at different rates of penetration. The penetration rates used in the modelling study were based upon those used for the experimental tests, covering penetration rates of between 10 and 500mm/s. The simulations focussed on the sandy loam soil, since the observed influence of plate sinkage speed on the soil's resistance to penetration was much greater for the sandy loam than for the dry sand.

4.2.3.1 Influence of simulation timestep

The plate sinkage simulations run in LS-DYNA used explicit time integration, with the timestep for the simulation calculated based on the Courant stability criterion:

$$\Delta t_{\min} = \frac{l}{\sqrt{\frac{E*(1-\nu)}{(1+\nu)*(1-2\nu)*\rho}}} \qquad \textit{Equation 4.5}$$

Since the timestep determined by LS-DYNA is based on the critical dimensions and material properties of the elements within the simulation, the default timestep is independent of the rate of deformation. For coarse meshed simulations involving large, rapid deformations, the default timestep can result in instabilities caused by the large displacement of the penetrator per timestep. A timestep safety factor is employed to address instabilities related to the default timestep being too large; by default, the timestep safety factor is set to 0.9, but this can be overridden by the user as required.

To investigate the influence of the explicit simulation timestep and the relative penetration rate, dynamic plate sinkage simulations were run using two differing approaches. In the first, the default timestep safety factor was used, such that the plate displacement per timestep increased as a function of penetration speed. In the second, the timestep was reduced to maintain a constant plate displacement per timestep. Table 4.2 compares the differences in timestep and plate displacement per timestep using these two methods.

Table 4.2: Comparison of plate displacement per timestep for sinkage speeds of between 10 and 500mm/s using constant timestep and constant displacement per timestep methods

	Constant timestep			Constant displacement per timestep		
Plate speed	**Timestep safety factor**	**Timestep**	**Displacement / timestep**	**Timestep safety factor**	**Timestep**	**Displacement / timestep**
(mm/s)	-	(ms)	(mm)	-	(ms)	(mm)
10	0.600	2.09E-2	2.09E-4	0.600	2.09E-2	2.09E-4
50	0.600	2.09E-2	1.05E-3	0.120	4.19E-3	2.09E-4
100	0.600	2.09E-2	2.09E-3	0.060	2.09E-3	2.09E-4
200	0.600	2.09E-2	4.19E-3	0.030	1.05E-3	2.09E-4
300	0.600	2.09E-2	6.28E-3	0.020	6.98E-4	2.09E-4
500	0.600	2.09E-2	1.05E-2	0.012	4.19E-4	2.09E-4

4.2.3.2 Dynamic plate sinkage model results

Figure 4.22 and Figure 4.23 illustrate the results obtained from the dynamic plate sinkage simulations, using both the constant displacement per timestep approach and the more conventional constant timestep method. The results of the models indicate that the predicted plate sinkage profile obtained from the model is sensitive to the rate of deformation in terms of the displacement per simulation timestep, but not in terms of the displacement per unit time. For a given mesh resolution, therefore, the timestep safety factor must be reduced as the speed of the plate is increased to prevent numerical errors which may affect the accuracy of the results obtained.

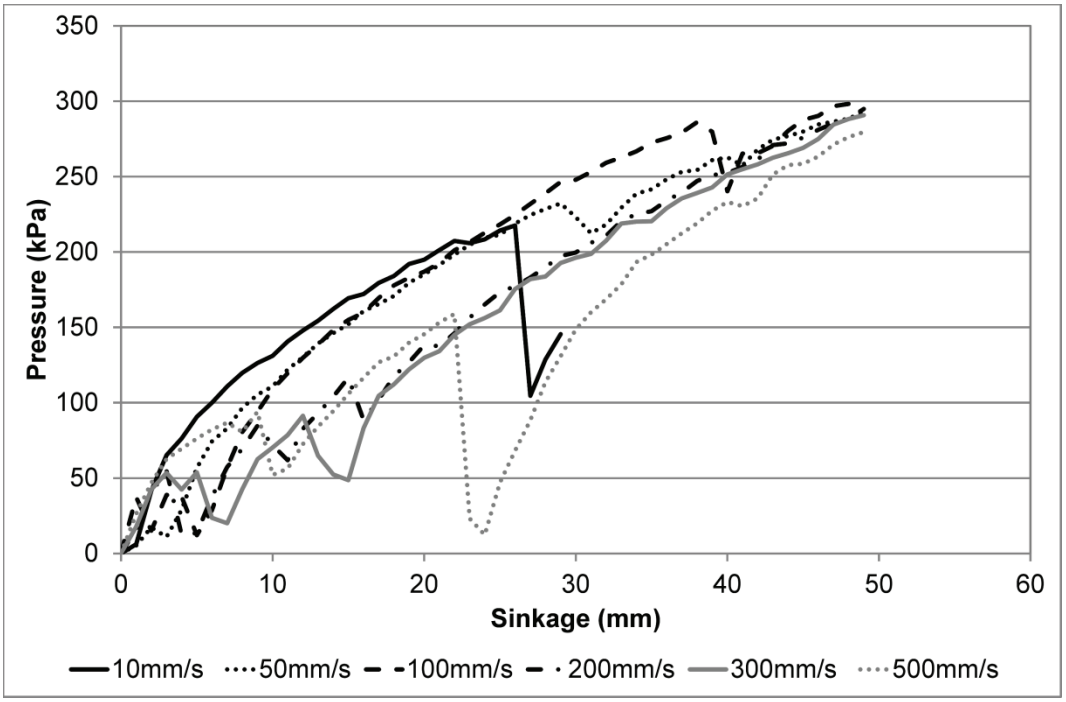

Figure 4.22: Effect of plate velocity on predicted plate sinkage profile for sandy loam soil using constant simulation timestep

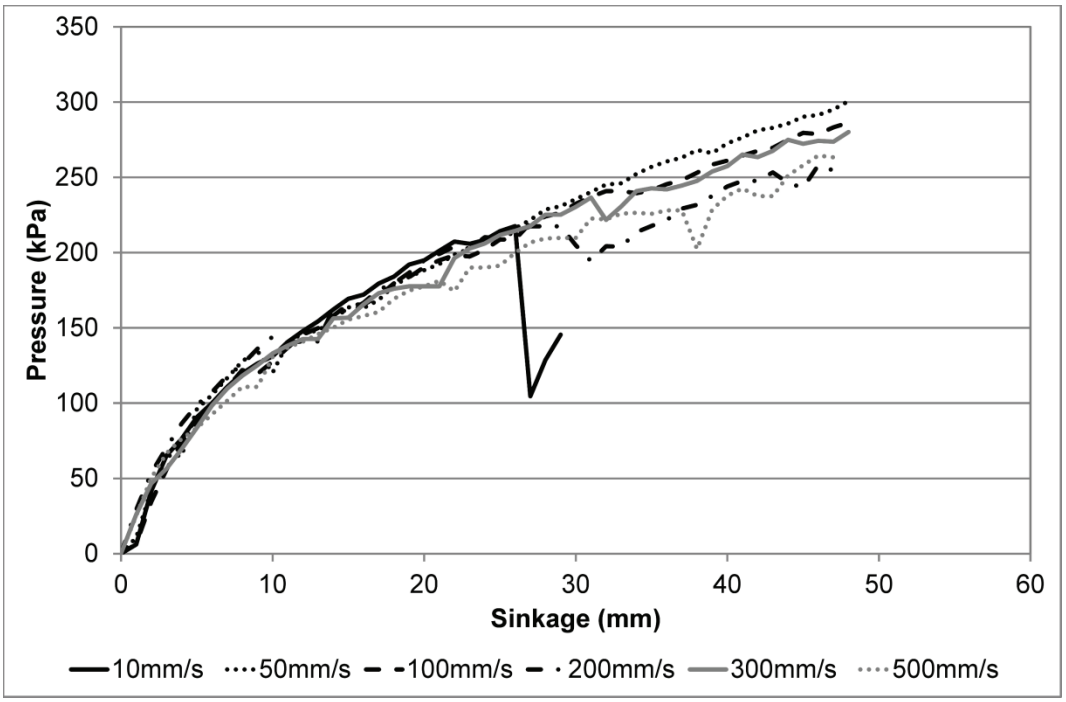

Figure 4.23: Effect of plate velocity on predicted plate sinkage profile for sandy loam using constant displacement per timestep

4.3 Alternative material models

Given the dependency of the sandy loam's resistance to penetration on the rate of loading, alternatives to the MAT_SOIL_AND_FOAM material model were considered. Reviewing the material models identified in Section 3.3 once more, with the added criteria of strain rate sensitivity, resulted in only two applicable material models:

- MAT_PSEUDO_TENSOR
- MAT_FHWA

MAT_PSEUDO_TENSOR is similar to MAT_SOIL_AND_FOAM, in that the material's response to loading is primarily described in terms of a pressure-volume curve and a shear failure surface. Like the MAT_SOIL_AND_FOAM model, the pressure volume envelope is described using a piecewise curve, although MAT_PSEUDO_TENSOR also allows variations in bulk unloading modulus to be specified as a function of volumetric strain. The shear failure surface in the MAT_PSEUDO_TENSOR model can be defined in one of two ways: in the first, the variation in shear strength with confinement is described as a simple piecewise curve, while the second method uses a pressure dependent shear failure surface of the form:

$$SD = \sigma_1 - \sigma_3 = a_0 + \frac{p}{a_1 + a_2 p} \qquad \textit{Equation 4.6}$$

Strain rate effects in MAT_PSEUDO_TENSOR are accounted for by the use of a strain rate multiplier curve, defining the increase in yield strength (σ_1 - σ_3) as a function of strain rate (ms^{-1}). Given that the yield surface as a whole is scaled while pressure dependency remains constant, this approach allows control over the soil's cohesive response as a function of strain rate.

MAT_FHWA is a more recent introduction to LS-DYNA, having been implemented in v970 of the software in 2002. An extensive set of documentation for the model is provided by the US Federal Highway Agency (Lewis, 2004; Reid et al., 2004), which reviews the intended applications of the model, its development and an evaluation of the model's performance and

accuracy from users at the Midwest Road Safety Facility. MAT_FHWA is potentially more widely applicable and more representative of physical soils than the other soil models available in LS-DYNA, as it includes terms to model the effects of moisture, strain hardening, strain softening and strain rate sensitivity. Strain rate effects within MAT_FHWA are implemented using a viscoplastic update algorithm, which interpolates between the elastic trial stress and inviscid stress on the plasticity surface:

$$\bar{\sigma}_{vp} = (1-\varsigma)\bar{\sigma} + \varsigma\bar{\sigma}_{trial}$$

$$\varsigma = \frac{1}{\left(\frac{\Delta t}{\eta}\right)+1} \qquad \textit{Equation 4.7}$$

$$\eta = \left(\frac{\gamma}{\dot{\varepsilon}}\right)^{\frac{n-1}{n}}$$

While the ability to represent strain rate effects is included within the MAT_FHWA model, no guidance is provided on the physical or analytical methods used to derive the parameters used (γ and n). Setting the parameter γ to zero deactivates any strain rate dependency within the material model. The developers state that strain rate sensitivity may not be needed for the soil model's intended application (modelling of vehicle impacts into roadside safety equipment), and offer little justification for the viscoplastic update algorithm used. Somewhat worryingly, the introduction to the material's theory manual entry includes a statement that only one set of material property data was available to support the development of the model, and that much of the model is therefore based on the "*general behaviour of cohesionless soils*".

Given the breadth and flexibility of the model, a much larger set of input parameters are required to define the soil, and this currently represents one of the main drawbacks of the MAT_FHWA model. The evaluation manual, which details an assessment of the material model conducted by users at the Midwest Roadside Safety Facility (Reid et al., 2004), concludes that for many of the soil parameters, the methods required to derive input values from physical test data

are undefined. As such, parameter studies are required in order to identify the most appropriate values to obtain the desired behaviour.

4.3.1 Dynamic characterisation of soils

The main difficulty in defining strain rate sensitivity in soil material models, regardless of the modelling approach used, is the availability of dynamic soil characterisation data for intermediate strain rates. Most of the work reported in the literature to assess the effect of strain rate on soil properties has either focussed on relatively low strain rates (10^{-8} to 10^{-4} s^{-1}) for civil engineering applications or on the very high strain rates associated with mine blast and ballistic impacts (10^{3} to 10^{5} s^{-1}).

Using a crude first approximation by considering a confined compression test on a linear elastic soil, the strain rate in the soil will be linearly related to the plate penetration speed. For penetration speeds of between 1 and 500mm/s, which correspond to translational speeds of up to 2.7m/s (6mph), the strain rate in the confined elastic soil sample will vary between 10^{-3} and 1 s^{-1}. These orders of magnitude values for strain rates during tyre / soil interaction are broadly in agreement with those determined by Karafiath and Sobierajski (1974) for 9.00-14 tyres operating at translational speeds of between 0.15 and 1.52m/s. In Karafiath and Sobierajski's study, an attempt is also made to relate indirect measurements of strain rate effects, based on cone index values for different rates of penetration, to the Mohr-Coulomb soil properties required for mobility prediction. Two key difficulties are encountered using this approach: firstly, indirect property measurements such as cone index or plate sinkage profiles are dependent on both cohesive and frictional soil behaviour, such that the individual contributions from cohesive and frictional effects cannot be readily identified; secondly, strain and strain rate will vary throughout the soil sample over time.

For the characterisation of soils at intermediate strain rates (10^{-3} to 10^{3} s^{-1}), a relatively small number of studies have been completed, but have focussed on direct shear testing. Zeng and Yao (1991), for example, used a modified direct

shear box apparatus with a hydraulic loading mechanism to characterise clay and loam soils at shear strain rates of between 5 and $30s^{-1}$. Matchett and Smith (1985) used a similar approach, while Stafford and Tanner (1983) employed an annular shear device loaded by an electric motor drive system to test a clay and a sandy loam. The split Hopkinson pressure bar (SHPB) has also been used to dynamically load direct shear box tests to allow characterisation of soil properties under higher rate loading (Muro and O'Brien, 2004).

Both Zeng and Yao and Stafford and Tanner concluded that cohesion could be directly related to the logarithm of the deformation rate, while friction angle was independent of the rate of loading. The findings of these studies therefore suggested a simple yield surface scaling approach, as used by the MAT_PSEUDO_TENSOR material model, would be appropriate for the addition of rate sensitivity to an FE mobility prediction tool.

4.3.2 Strain rate effects in MAT_PSEUDO_TENSOR

Given the lack of intermediate strain rate property data available for the soils under investigation, an attempt was made to calibrate the load curve for yield strength scaling in MAT_PSEUDO_TENSOR against the experimental dynamic plate sinkage profiles presented above. As before, parameterisation of the MAT_PSEUDO_TENSOR material model focussed on the sandy loam soil, since the variation in the soil's resistance to penetration with loading rate was much greater for the sandy loam than for the dry sand.

Using a similar approach to that presented in Chapter 3, the material model input deck for MAT_PSEUDO_TENSOR was populated to describe the soil's response to shear loading. Response to hydrostatic loads was described using a tabulated compaction equation of state, which also permitted the variation in bulk unloading modulus to be described as a function of pressure. As with the MAT_SOIL_AND_FOAM material model used previously, yield surface parameters can either be obtained by curve fitting Equation 4.6 to experimental triaxial / shear box data or by direct calculation. In the pseudo tensor material model, the parameter a_2 defines the non-linearity of the yield surface, so when

using direct calculation from Mohr-Coulomb parameters, a_2 should be set to zero.

$$\tau = \frac{\sigma_1 - \sigma_3}{2} = \frac{1}{2}\left(a_0 + \frac{p}{a_1}\right) \quad \text{Equation 4.8}$$

$$c + ptan\varphi = \frac{1}{2}\left(a_0 + \frac{p}{a_1}\right) \quad \text{Equation 4.9}$$

$$a_0 = 2c \quad \text{Equation 4.10}$$

$$a_1 = \frac{1}{2tan\varphi} \quad \text{Equation 4.11}$$

The yield surface parameters obtained through curve fitting and direct calculation from direct shear box tests on the sandy loam are compared in Table 4.3. The input cards for the pseudo tensor material model and tabulated compaction equation of state are presented below:

```
*MAT_PSEUDO_TENSOR_TITLE
SANDY_LOAM_SOIL
$#     mid        ro         g        pr
         1 1.4700E-6  0.001120  0.300000
$#    sigf        a0        a1        a2       a0f       a1f        b1       per
     0.000    [See Table 4.3]      0.000     0.000     0.000     0.000
$#      er       prr      sigy      etan       lcp       lcr
     0.000     0.000     0.000     0.000   XXXXXXX         0
$#      x1        x2        x3        x4        x5        x6        x7        x8
     0.000     0.000     0.000     0.000     0.000     0.000     0.000     0.000
$#      x9       x10       x11       x12       x13       x14       x15       x16
     0.000     0.000     0.000     0.000     0.000     0.000     0.000     0.000
$#     ys1       ys2       ys3       ys4       ys5       ys6       ys7       ys8
     0.000     0.000     0.000     0.000     0.000     0.000     0.000     0.000
$#     ys9      ys10      ys11      ys12      ys13      ys14      ys15      ys16
     0.000     0.000     0.000     0.000     0.000     0.000     0.000     0.000


*EOS_TABULATED_COMPACTION_TITLE
SANDY_LOAM_SOIL
$#   eosid      gama        e0        vo
         1     0.000     0.000     0.000
$#           ev1             ev2             ev3             ev4             ev5
          0.000      -0.0202000      -0.0408200      -0.0618800      -0.0833800
$#           ev6             ev7             ev8             ev9            ev10
     -0.1054000      -0.1508000      -0.1985000      -0.2485000      -0.6300000
$#            c1              c2              c3              c4              c5
          0.000  1.2170000e-005  2.5170000e-005  4.0330000e-005  5.8000001e-005
$#            c6              c7              c8              c9             c10
  8.0500002e-005  1.4370000e-004  2.3629999e-004  3.7940001e-004       0.0028310
$#            t1              t2              t3              t4              t5
          0.000           0.000           0.000           0.000           0.000
$#            t6              t7              t8              t9             t10
          0.000           0.000           0.000           0.000           0.000
$#            k1              k2              k3              k4              k5
       0.0037788       0.0039288       0.0040957       0.0042990       0.0045490
$#            k6              k7              k8              k9             k10
       0.0048890       0.0059850       0.0080490       0.0127240       0.0140000
```

Table 4.3: Comparison of MAT_PSEUDO_TENSOR yield surface parameters obtained through curve fitting and direct calculation from direct shear box test data on sandy loam

Parameter	Curve fitting	Direct calculation
a_0	6.73×10^{-6}	5.33×10^{-6}
a_1	7.68×10^{-1}	7.89×10^{-1}
a_2	-1.985	0

The effect of strain rate on the soil's response to loading is described using a scaling factor curve, which is referenced in the MAT_PSEUDO_TENSOR input card as LCP. In the absence of laboratory characterisation data across a range of strain rates, the dynamic plate sinkage models using MAT_SOIL_AND_FOAM were interrogated to estimate the strain rate in the soil around the plate as a function of the plate's sinkage speed. The results of this investigation are presented in Figure 4.24, below, and suggest an approximately linear relationship between sinkage speed and strain rate.

Having related strain rate to plate sinkage speed, it was then necessary to estimate the variation in the soil's strength as a function of strain rate. To achieve this, the results of the dynamic plate sinkage tests on sandy loam were processed to determine the mean pressure scaling factor for each plate sinkage speed, relative to the baseline value for a speed of 1mm/s. This produced the scaling factors shown in Table 4.4 for plate sinkage speeds of between 1 and 500mm/s.

It should be recognised at this stage that the approach outlined above is a necessary approximation. As highlighted by Karafiath and Sobierajski (1974), the strain rate experienced by the soil during a dynamic plate sinkage test will vary as a function of both position and time. As a result, the concept of a characteristic strain rate that can be directly related to plate penetration speed represents a simplification of actual loading conditions experienced by the soil sample. Even using relatively well-controlled laboratory characterisation techniques, both Matchett and Smith (1985) and Stafford and Tanner (1983)

recognised the potential difficultly in relating the shear box's deformation rate (in m/s) to the strain rate experienced at the failure surface within the soil sample.

When defining the strain rate multiplier curve in LS-DYNA, it is also necessary to consider how the curve is defined and how LS-DYNA interprets the data supplied. For strain rates falling between the data points supplied by the user, LS-DYNA uses linear interpolation to determine the relevant strain rate multiplier value. Due to the relatively rapid rise in apparent soil strength with loading rates between 1 and 50mm/s and the limited data available, large changes in gradient occur at each of the supplied data points, which can lead to numerical noise and instability.

To reduce the likelihood of instabilities, the strength multiplier curve for the sandy loam soil was initially simplified to allow a smoothed function to be fitted to the experimental scaling data (Table 4.4). Given the limited number of data points available, particularly for sinkage speeds below 50mm/s, the selection of a function for curve fitting was somewhat arbitrary, and a generalised logistic function (Equation 4.12) was selected on the basis that it would be possible to smoothly capture the relatively rapid increase in apparent soil strength between sinkage rates of 1mm/s and 50mm/s, followed by a plateau region (Figure 4.25).

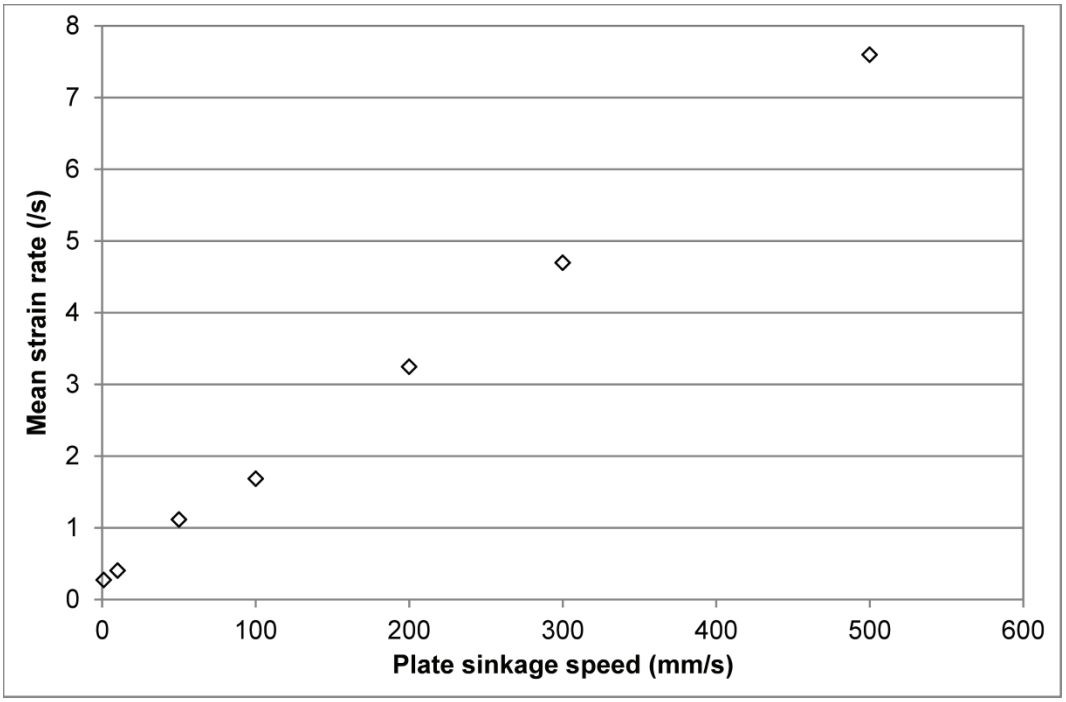

Figure 4.24: Relationship between plate sinkage speed and mean strain rate in soil around plate

Table 4.4: Plate sinkage profile scaling factors for plate sinkage speeds of between 1 and 500mm/s in sandy loam

Sinkage speed	Estimated mean strain rate	Strength scaling factor	Simplified scaling factor
(mm/s)	(s^{-1})	-	-
1	0.27	1.00	1.00
10	0.40	1.81	1.81
50	1.12	2.87	2.87
100	1.68	2.30	2.87
200	3.25	2.04	2.87
300	4.70	2.02	2.02
500	7.60	1.41	1.41

$$SF = A + \frac{K - A}{\left(1 + Qe^{-B(\dot{\varepsilon} - M)}\right)^{1/v}} \qquad \textit{Equation 4.12}$$

Table 4.5: Generalised logistic function (Equation 4.12) parameters used to describe the relationship between strain rate and yield strength scaling factor for sandy loam soil

Parameter	Value	Parameter	Value
A	1.000	K	2.871
B	3.924×10^{4}	v	0.587
Q	1.129	M	3.903×10^{-4}

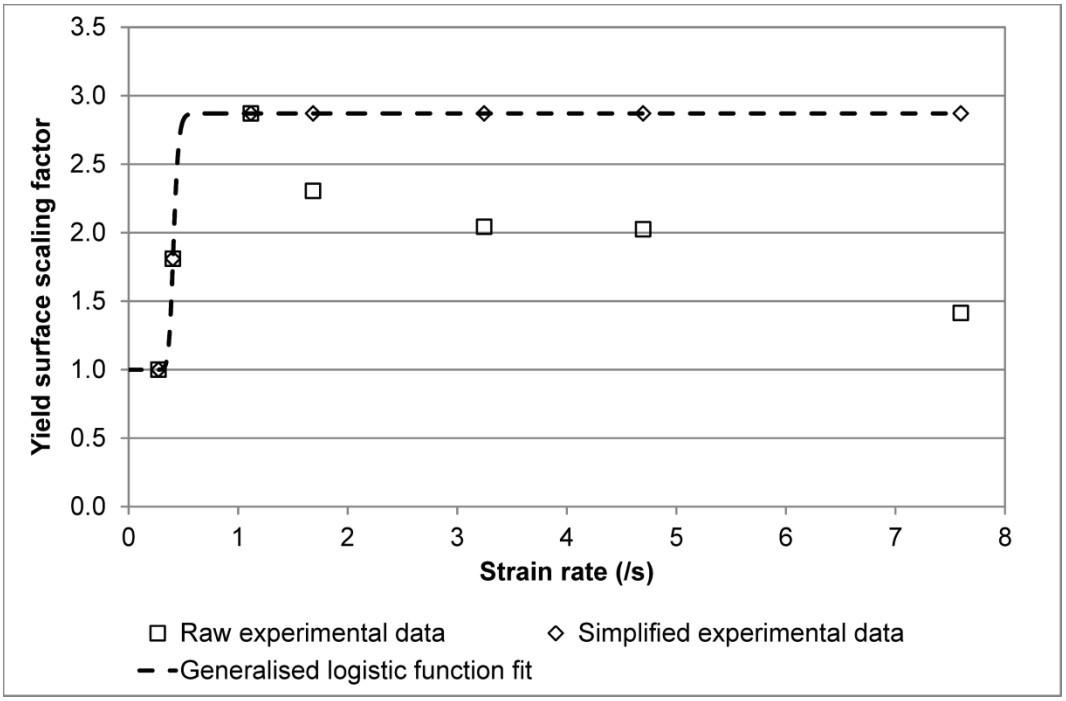

Figure 4.25: Comparison of default linear interpolation between experimental data points and generalised logistic function to represent the transition between quasi-static and high strain rate properties in sandy loam soil

4.3.3 MAT_PSEUDO_TENSOR results

To assess the performance of the MAT_PSEUDO_TENSOR material model, the dynamic plate sinkage models were run again using the revised model for sandy loam soil and a constant displacement per timestep condition. The initial results obtained are illustrated in Figure 4.26, which demonstrates the dependence of the predicted plate sinkage profile on the rate of plate displacement.

To allow easier comparison against experimental results, the scaling factors used as inputs to the material model were plotted against the scaling factors obtained from the dynamic plate sinkage models. This comparison, illustrated in Figure 4.27, indicated that the effect of plate speed on the predicted plate sinkage profile was overestimated by the initial pseudo tensor model. The dynamic plate sinkage simulations were therefore re-run using the revised scaling factors provided in Table 4.6 in an effort to improve the accuracy of the predicted plate sinkage profiles over the range of plate sinkage speeds considered. The results of the dynamic plate sinkage simulations run with the revised strain rate scaling factors are presented in Figure 4.28 and Figure 4.29.

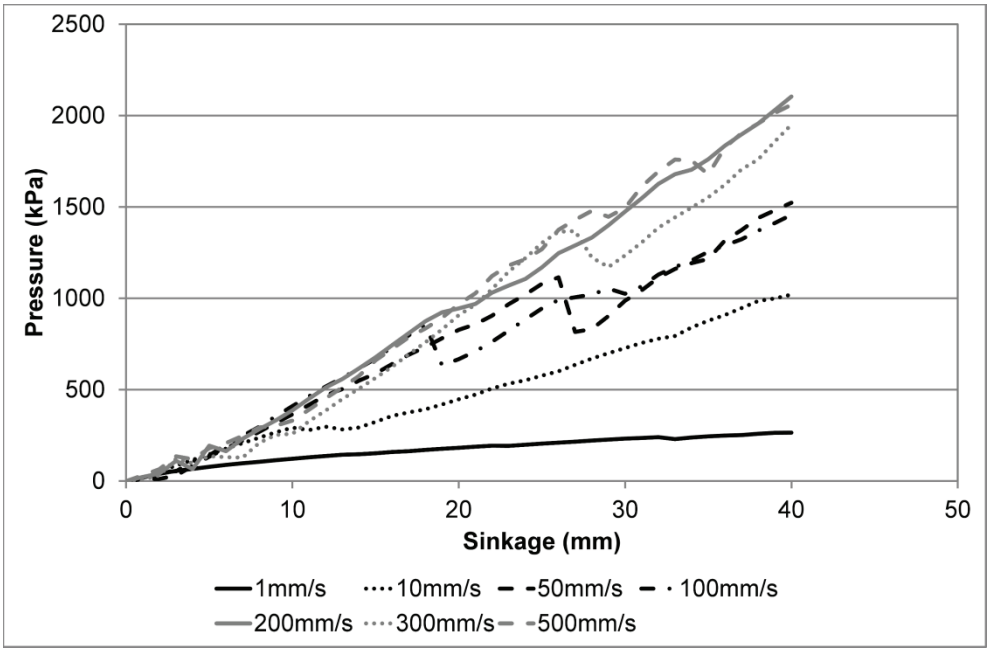

Figure 4.26: Dynamic plate sinkage simulation results obtained using MAT_PSEUDO_TENSOR to represent sandy loam soil, demonstrating sensitivity of model to the rate of plate displacement using scaling factors presented in Table 4.4

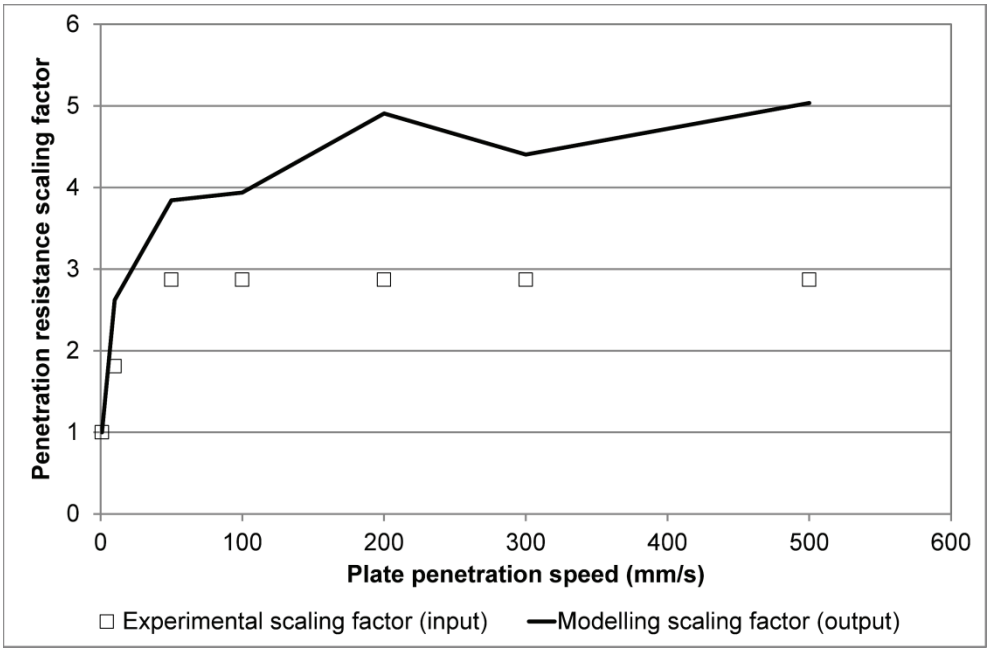

Figure 4.27: Comparison of yield strength scaling factors (Table 4.4), used as input data to the MAT_PSEUDO_TENSOR material model, against plate sinkage profile scaling factors obtained from dynamic plate sinkage simulations

Table 4.6: Revised plate sinkage profile scaling factors for plate sinkage speeds of between 1 and 500mm/s in sandy loam

Sinkage speed	Estimated mean strain rate	Original simplified scaling factor	Revised strength scaling factor
(mm/s)	(s^{-1})	-	-
1	0.27	1.00	1.00
10	0.40	1.81	1.08
50	1.12	2.87	1.71
100	1.68	2.87	1.71
200	3.25	2.87	1.71
300	4.70	2.02	1.71
500	7.60	1.41	1.71

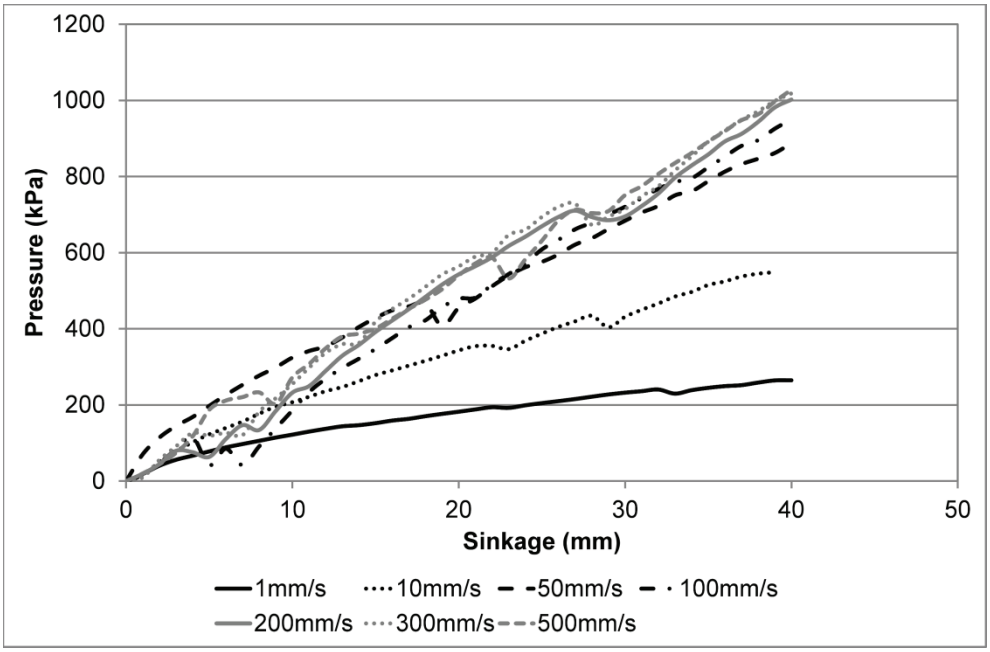

Figure 4.28: Dynamic plate sinkage simulation results obtained using MAT_PSEUDO_TENSOR to represent sandy loam soil, demonstrating sensitivity of model to the rate of plate displacement using scaling factors presented in Table 4.6

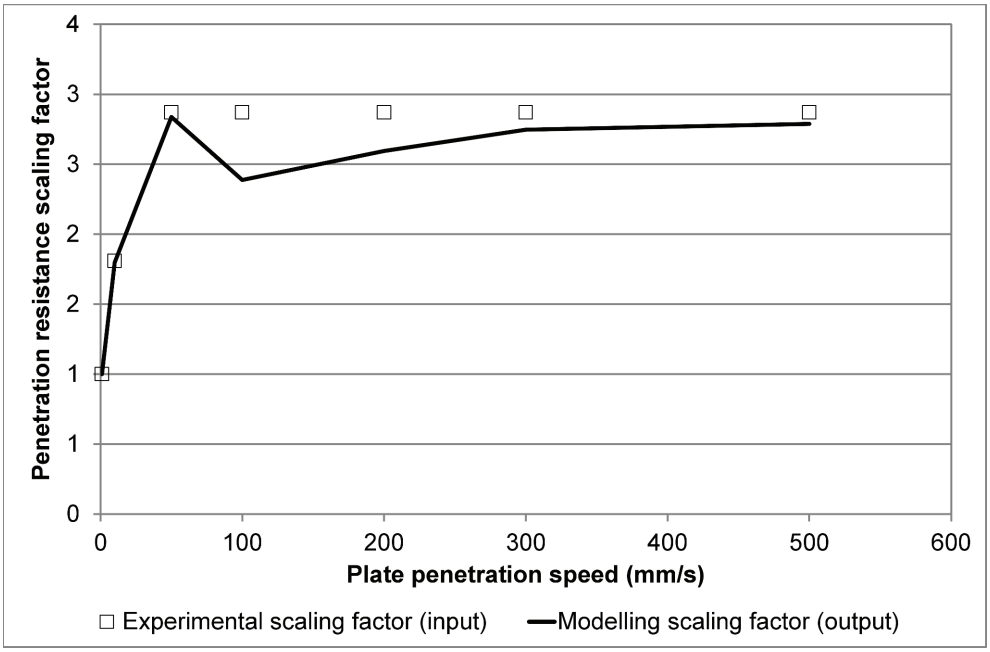

Figure 4.29: Comparison of yield strength scaling factors (Table 4.6), used as input data to the MAT_PSEUDO_TENSOR material model, against plate sinkage profile scaling factors obtained from dynamic plate sinkage simulations

The results presented above demonstrate the ability to replicate the rate dependent response of moisture containing sandy loam within FE simulations of machine-soil interaction. The procedure used, with strain rate dependence of the soil's yield surface calibrated against dynamic plate sinkage results, is less than ideal, but does provide a means of incorporating rate dependence in the absence of dynamic laboratory test data.

Comparing Figures 4.26 and 4.28, and 4.27 and 4.29, the agreement between the dynamic experimental and modelling results is still not perfect, but the initial overestimation of the soil's resistance to penetration has, for the most part, been addressed by the use of the revised yield surface scaling factors presented in Table 4.6. Making a detailed comparison between model predictions and experimental results is complicated by an increased level of noise in the results of the dynamic plate sinkage simulations, with occasional sharp fluctuations in the contact force between the plate and soil. Reviewing the animation files associated with the dynamic simulations, these drops appear

to be associated with the relative softness of the soil and, in some cases, leakage of the soil beyond the surface of the plate mesh.

4.4 Summary

The work reported above has investigated the methods used to represent naturally occurring soils within FE simulations for the prediction of off-road vehicle mobility. The main findings of this work can be summarised as follows:

- The plate sinkage profiles predicted using FE simulations are very dependent on the yield surface parameters provided by the user. As discussed in Chapter 3, yield surface parameters determined in the laboratory will in turn depend on the test methods used to obtain them. It is therefore necessary to assess the accuracy of any soil material model in predicting in-situ soil behaviour prior to use in more complex simulations.

  For the sandy soils investigated in the current study, the yield surface parameters derived from direct shear box test data produced much better agreement with experimental static or quasi-static plate sinkage profiles than those derived from triaxial tests. For the dry sand, using a fine mesh, yield surface parameters derived from triaxial tests produced a mean percentage error of between 70 and 88%, compared to a mean percentage error of between 5 and 7% using shear box data.

- The use of an Euler solver has been investigated, as a means of addressing the instabilities reported by previous researchers when simulating the behaviour of ‘cohesionless’ soils (Hambleton, 2010). The results obtained indicate that, using a coarse mesh for both the dry sand and sandy loam soils, an Euler solver produces a lower mean percentage error than an equivalent Lagrange solution. The improvement in accuracy was most pronounced for the dry sand, most likely due to the fluid-like nature of the soil in the unconfined condition and the need for increased hourglass control coefficients in the Lagrange

simulations. As the mesh is refined, the two solution methods converge to produce broadly similar results, although quantitative comparison is complicated by a large amount of noise in some of the modelling results.

- Dynamic plate sinkage tests have shown that the apparent strength of both dry sand and sandy loam is dependent on the speed of penetration. For dry sand, with a moisture content of less than 1%, the influence of plate penetration speed on the apparent strength of the soil is limited, with the plate sinkage profiles for penetration speeds of between 1mm/s and 500mm/s being within the range of a series of static test results.

  For sandy loam soil, the variation in apparent strength with loading rate is much more pronounced, with a large increase in the soil's resistance to penetration as the plate penetration rate is increased from 1mm/s to 50mm/s; the mean pressure required for a sinkage of 25mm, for example, is 227kPa at 1mm/s and 655kPa at 50mm/s. The increased sensitivity of the sandy loam soil to loading rate is most likely due to the increased moisture content (14%) compared to the dry sand: as the rate of loading increases, pore water pressure provides a greater contribution to the macro-scale strength of the soil.

- Many of the existing mobility modelling methods, discussed in Chapter 2, assume that soil properties are independent of the vehicle's translational speed, and their accuracy will therefore be dependent on the loading rate used to characterise the soil's response. To assess the potential impact of rate dependency on model accuracy, an analysis has been completed using Bekker's semi-empirical model for the rolling resistance of a rigid wheel.

  As an example, for a 600mm diameter rigid wheel operating on a sandy loam soil with a moisture content of 14%, under the action of a wheel load of 20kN, static plate sinkage results predict a rolling resistance of 3.14kN. Using dynamic plate sinkage results for a penetration speed of 10mm/s, equivalent to a translational speed of 0.07m/s, the predicted rolling resistance reduces to just 2.30kN. At 50mm/s, the predicted rolling

resistance reduces further to 1.81kN. A frequent assumption used in many of the previous analytical and numerical modelling studies of wheel / soil interaction is that, providing the translational speed of the vehicle is low enough, rate effects may be ignored. The findings of the current study, however, indicate that rate effects should be considered, even for translational speeds as low as 0.1m/s (0.2mph).

- Due to the potential variation in soil strength as a function of loading rate, FE-based mobility prediction tools require soil material models that are capable of incorporating loading rate effects. The need to characterise soils under a range of loading rates introduces additional cost and complexity, not least of which is the difficulty in defining the actual strain rate experienced by the soil sample. Under the current study, in the absence of dynamic laboratory test data for the sandy loam under investigation, an iterative process has been used to calibrate the MAT_PSEUDO_TENSOR material model in LS-DYNA against dynamic plate sinkage profiles obtained for sinkage speeds of between 1 and 500mm/s.

Chapter 5: Rigid wheel interaction

From the literature review in Chapter 2, some of the complexities involved in tyre / soil interaction modelling, regardless of the methods used, can be summarised as follows:

- dynamic variations in wheel load, translational velocity and rotational velocity;
- non-linear soil and tyre properties;
- three-dimensional soil displacement and deformation;
- contact between two deformable bodies.

As with empirical and analytical modelling methods, an FE analysis of wheel terrain interaction can be greatly simplified by removing at least some of the above sources of complexity from the initial problem statement. One common approach is the assumption that an appreciable difference in stiffness exists between the two contacting bodies, permitting either the wheel or terrain to be represented as a rigid body without significantly affecting the accuracy of the results obtained. In the case of pneumatic tyres operating at low inflation pressures, the problem is frequently simplified by describing the surface on which the tyre operates as rigid, while pneumatic tyres operating at their usual road-going pressure on deformable terrains are often represented by a rigid wheel. Alternative methods to simplifying the problem include assuming plane strain conditions (representing an infinitely wide wheel with no out of plane soil deformation), the assumption of linear elasticity, or the use of a constant wheel load, translational speed or rotational speed.

In the case of analytical and numerical mobility prediction models, which aim to provide a detailed representation of the physical processes involved, the ability to accurately describe the displacements and stress distributions across the contact interface between tyre and soil is crucial. Since the off-road mobility of wheeled and tracked vehicles can also be limited by failure within the soil body beneath the wheel, the deformations and stress distributions within the soil beneath the wheel should also be accurately represented.

As an initial assessment of the Euler FE approach to off-road mobility prediction, a simplified wheel / soil interaction model was constructed, representing rigid wheels of varying diameter, wheel load and translational velocity interacting with dry sand. The variations in rolling resistance as a function of wheel diameter and load were compared against those predicted by existing empirical and semi-empirical methods, while the predicted levels of sinkage and soil deformation were compared against experimental data.

While the use of an Eulerian solver for the soil body demonstrated some advantages over more traditional Lagrangian methods in the plate sinkage study discussed in Chapter 4, the differences in the extent and distribution of soil deformation between the plate sinkage test and the interaction with a towed wheel meant that a comparison between the two solution methods for wheel / soil interaction would be useful in assessing the potential benefits of an Eulerian approach to mobility prediction.

5.1 Problem definition

To aid comparison between modelling results and experimental data, the FE model used was based on the test rig used for the experimental testing described later in this chapter. A 5,000mm long soil bin was defined, 500mm wide and filled to a depth of 250mm with dry sand. The width of the rigid wheel was equal to that of the soil bin to prevent out of plane displacement of the soil. The rigid wheel was towed at a constant translational speed across the dry sand under the action of a constant vertical load.

The effect of wheel diameter, load and translational speed were investigated using a combination of modelling and experimental testing. A wide range of wheel diameters, loads and translational speeds were modelled, with a smaller number of experimental tests completed for selected conditions. The test matrix for the rigid wheel study is provided in Table 5.1, with X indicating the conditions considered during the modelling and experimental studies.

Table 5.1: Test matrix for rigid wheel interaction study

Treatment	Wheel diameter	Wheel load	Translational speed	Model	Experiment
1	400 mm	1.64 kN	0.1 m/s	X	
2	600 mm	0.46 kN	0.1 m/s	X	
3		0.85 kN	0.1 m/s	X	
4		1.25 kN	0.1 m/s	X	
5		1.64 kN	0.1 m/s	X	X
6			0.2 m/s	X	X
7			0.4 m/s	X	
8			0.8 m/s	X	
9		2.03 kN	0.1 m/s	X	
10		2.42 kN	0.1 m/s	X	
11	800 mm	1.64 kN	0.2 m/s	X	
12	1000 mm	1.64 kN	0.1 m/s	X	X

5.2 Experimental study

To provide data for model assessment, an experimental study was completed to determine the vertical soil displacements occurring beneath steel wheels towed across dry sand. The experimental study was completed using the small scale rolling / soil flow rig, located at Cranfield University. The rig (Figure 5.1) consisted of a 350 x 500 x 2500mm soil bin, filled to a depth of 250mm with dry sand. The width of the rigid wheels used was equal to that of the soil bin (500mm), with the aim of preventing out of plane deformation around the edges of the wheel. This meant that the displacement of the soil beneath the wheel could be directly observed through an inspection window, which was located midway along the length of the soil bin.

The rigid wheels were housed within a box section frame, which was in turn connected to a linear drive system, using linear bearings at the connection between the drive system and frame to allow unrestrained vertical motion of the wheel. Additional mass could be applied to the box section frame, which permitted control over wheel load.

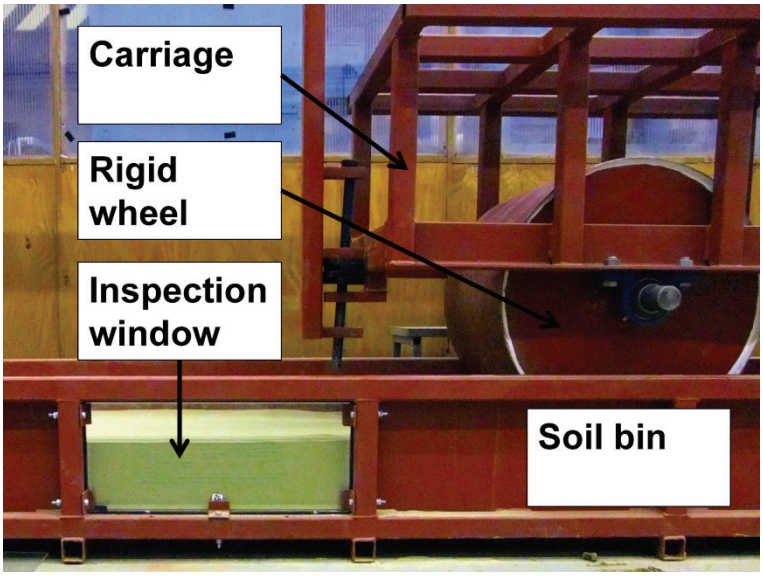

Figure 5.1: Overview of the Cranfield small scale rolling / soil flow rig

Prior to each run, the sand within the central section of the soil bin was manually prepared. The sand was first excavated from the region adjacent to the inspection window, before being gradually replaced in a series of thin layers. The soil was skimmed level after each layer had been deposited, and a line of coloured sand positioned adjacent to the inspection window before the next layer was added. This soil preparation process resulted in alternating horizontal layers of coloured and uncoloured sand, as illustrated in Figure 5.2. During each run, a series of digital photographs were taken, which could then be post processed to determine the vertical displacement of the coloured sand layers and the surface of the sand during interaction with the rigid wheel.

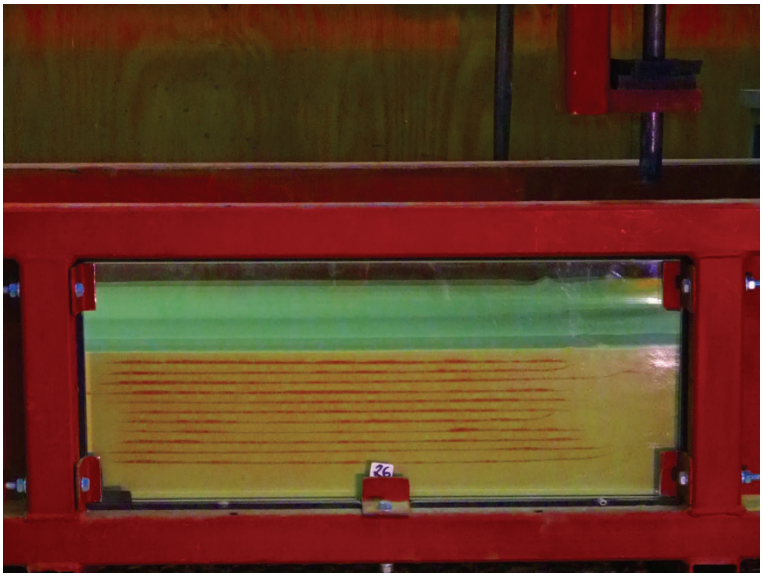

Figure 5.2: Inspection window in soil flow rig, illustrating alternating layers of coloured and uncoloured sand used to track vertical displacement during wheel / soil interaction

Post processing of the digital photographs taken during each run was completed using the open source GNU Image Manipulation Program (GIMP) and the OOoDigitizer extension to OpenOffice.org's Calc. The photographs were first processed in GIMP to increase the contrast between the coloured sand layers and the surrounding material and to overlay a grid of known spacing. Use of an overlaid grid ensured that the horizontal position of the vertical displacement measurements were consistent between the disturbed and undisturbed soil.

The OOoDigitizer extension in OpenOffice.org's Calc was then used to determine the vertical position of the soil surface and coloured soil layers both before and during wheel / soil interaction, given the known dimensions of the inspection window. For a number of experimental runs, it was not possible to directly measure the position of the wheel / soil interface due to leakage of sand between the wheel and the observation window. To address this, it was necessary to superimpose a circle of known size onto the digital photograph to identify the position of the wheel / soil interface (Figure 5.3). The leakage of

sand between the wheel and inspection window also affected the observed level of soil deformation in the first 20 – 30mm beneath the wheel.

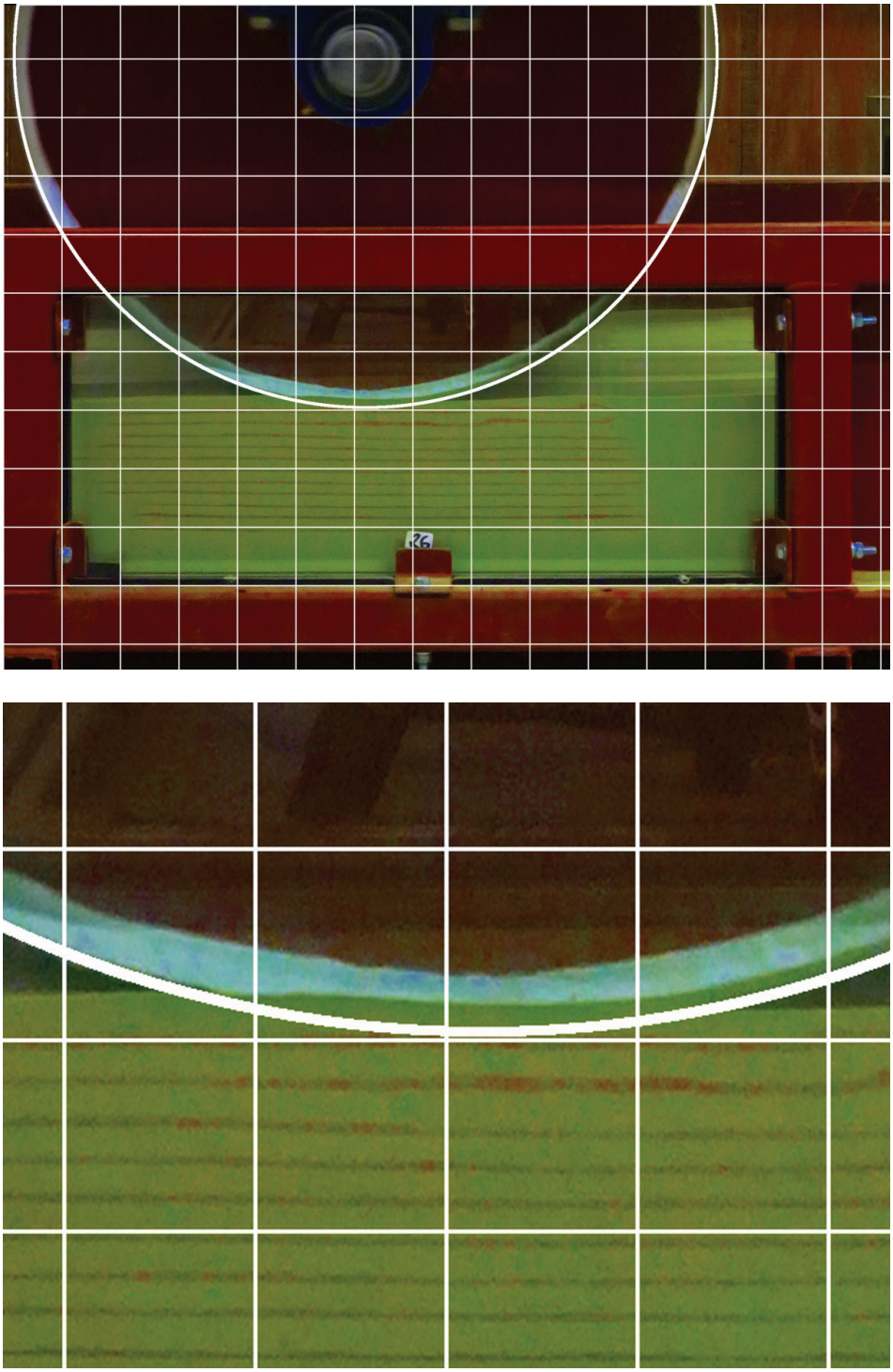

Figure 5.3: Post processed digital photograph from rigid wheel interaction study, illustrating leakage of sand between wheel and inspection window of soil bin

Having taken measurements at known horizontal distances from the centreline of the wheel, it was possible to calculate the arithmetic mean displacements for a series of experimental runs, which simplified comparison of results for different combinations of wheel diameter, load and speed.

5.2.1 Experimental results

Three replicates were completed for each experimental combination of wheel diameter, load and speed. Using the grid overlay approach presented above, the initial y and z coordinates were consistent between experimental runs, which then permitted the arithmetic mean vertical displacements of the soil to be calculated at each location. This averaging process is illustrated in Figure 5.4 for a small number of experimental data points.

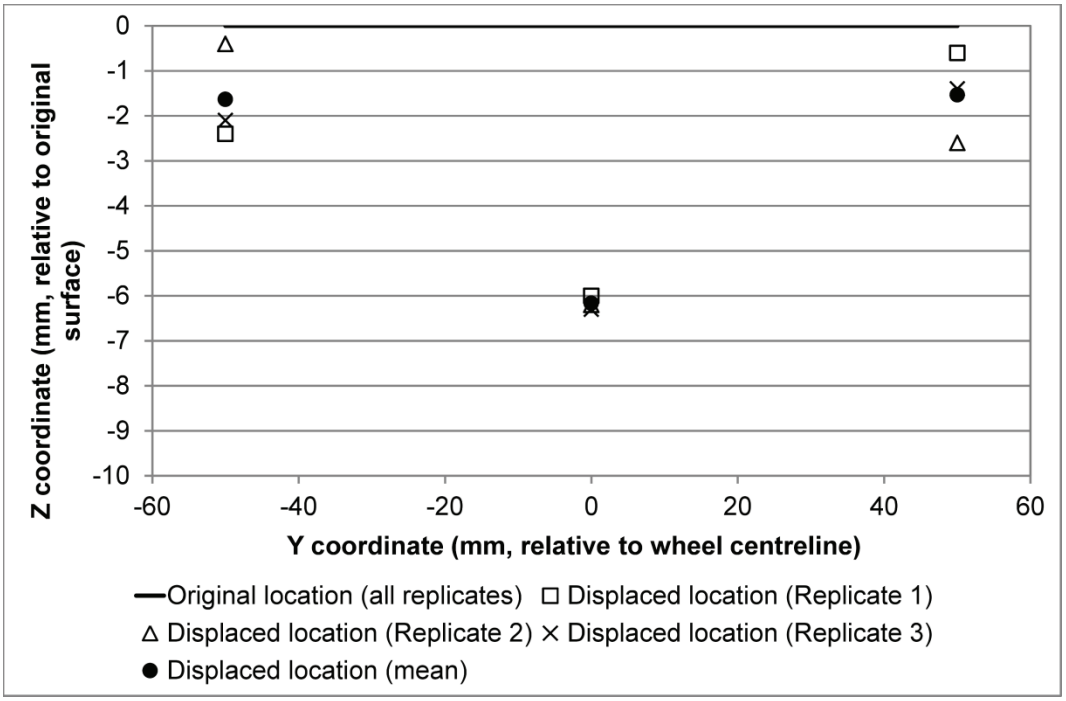

Figure 5.4: Example plot illustrating averaging process applied to experimental soil displacement data for comparison with numerical modelling results

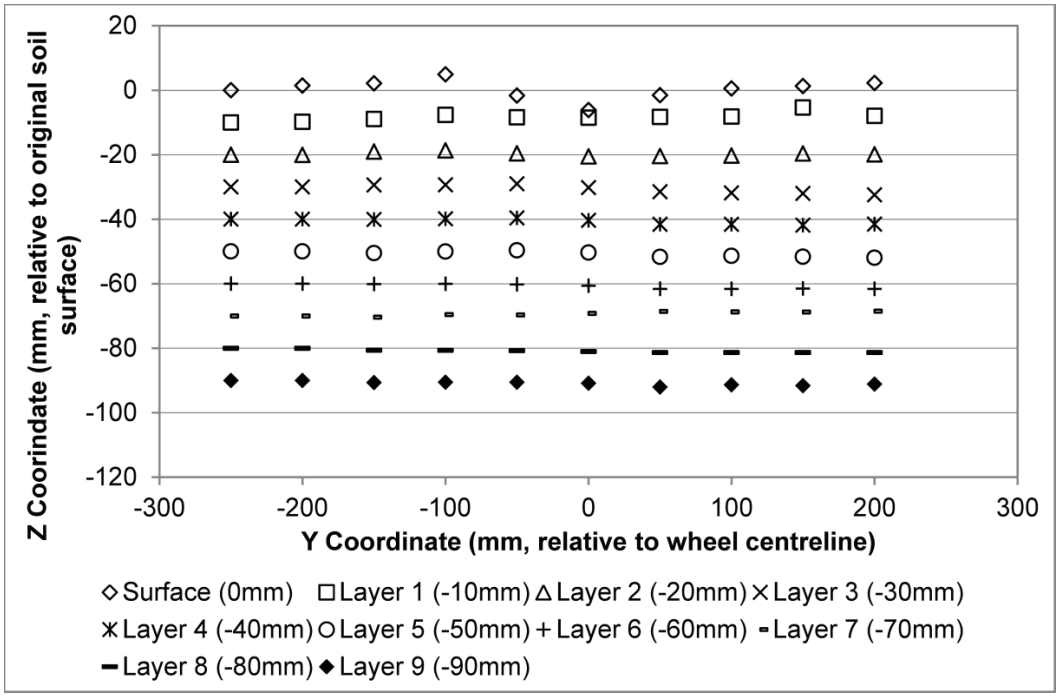

Figure 5.5: Experimental soil deformation plot for 600mm diameter rigid wheel towed across dry sand at 0.1m/s under wheel load of 1.64kN (direction of travel from right to left)

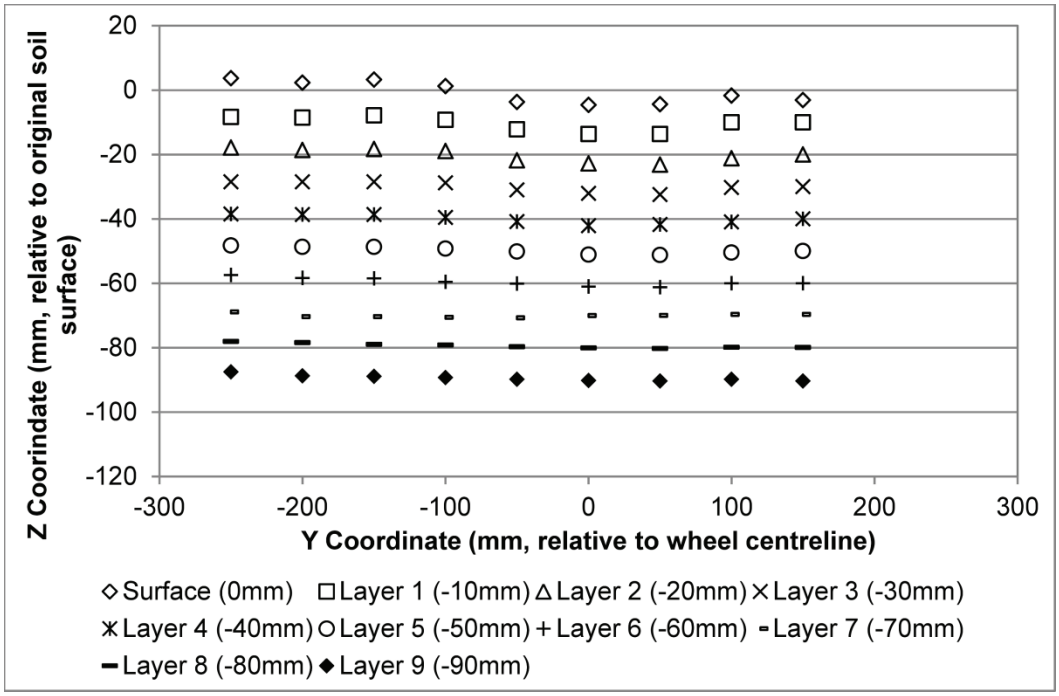

Figure 5.6: Experimental soil deformation plot for 1,000mm diameter rigid wheel towed across dry sand at 0.1m/s under wheel load of 1.64kN (direction of travel from right to left)

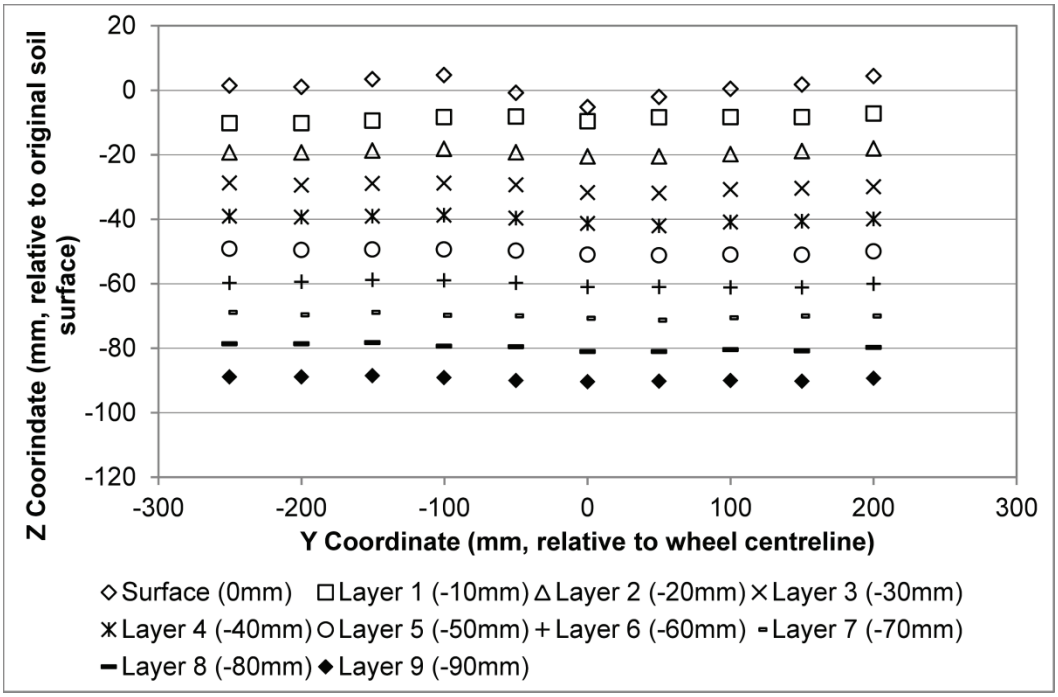

Figure 5.7: Experimental soil deformation plot for 600mm diameter rigid wheel towed across dry sand at 0.2m/s under wheel load of 1.64kN (direction of travel from right to left)

5.3 Modelling study

The models used during the numerical modelling study are illustrated in Figure 5.8. Given that the width of the rigid wheel was equal to that of the soil bin, and that out of plane deformation was therefore prevented, it was not necessary to model the full width of the soil bin. A series of coarse mesh simulations were run, however, gradually reducing the width of the soil bin model to ensure that artificially reducing the width of the soil bin in this manner, to represent a thin slice of the physical soil bin, did not affect the results obtained. The results of this short study, completed using both Euler and Lagrange solvers, are summarised in Table 5.2, below.

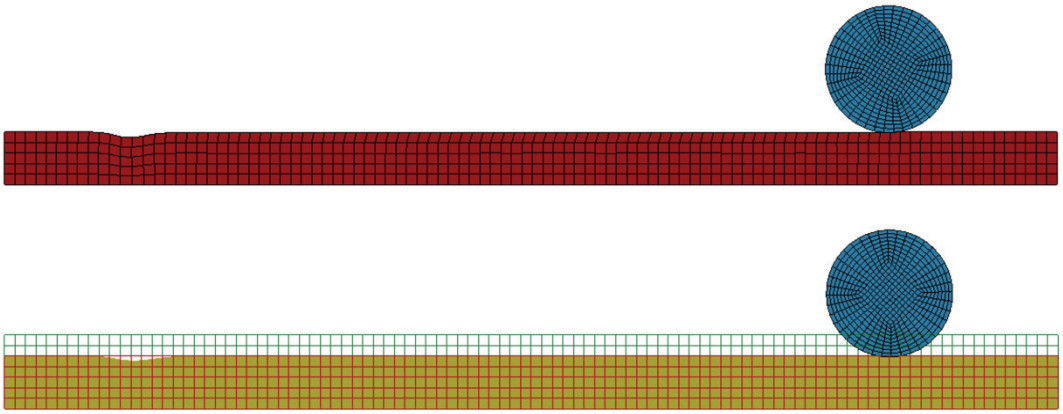

Figure 5.8: Lagrange (top) and Euler (bottom) rigid wheel interaction models

Having assessed the impact of model width on the predicted level of rolling resistance, a short mesh resolution study was completed, the results of which are summarised in Table 5.3. As with the plate sinkage model, the results obtained using the Euler solver were found to be more consistent over the range of mesh resolutions studied, although it was also necessary to identify whether or not this modelling approach was consistently producing the right answer. The levels of dynamic sinkage predicted by the Lagrange and Eulerian FE models were therefore compared against experimental results in an effort to identify the most appropriate solver to take forward.

5.3.1 Comparison with experimental results

To assess the relative performance of the Lagrange and Euler methods in predicting the deformation of the soil beneath a rigid wheel, the experimental data points were plotted to visualise the relationship between vertical displacement and depth directly beneath the centre of the wheel. Soil displacement data could then be extracted from the FE models and plotted alongside the experimental data for comparison.

Table 5.2: Results of modelling study to assess the effect of FE model width on the prediction of rolling resistance

Solver	Cell size	Model width	Wheel load	Load / unit width	Rolling resistance	Resistance / unit width	Rolling resistance coefficient
	mm	mm	N	N / mm	N	N / mm	%
Lagrange	50	500	1639	3.278	66	0.132	4.03
		250	819	3.278	33	0.133	4.06
		100	327	3.274	14	0.140	4.27
Euler	50	500	1639	3.278	118	0.236	7.20
		250	819	3.278	58	0.234	7.13
		100	327	3.274	23	0.227	6.93

Table 5.3: Results of modelling study to assess the effect of FE mesh resolution on the prediction of rolling resistance

Solver	Cell size	Model width	Wheel load	Load / unit width	Rolling resistance	Resistance / unit width	Rolling resistance coefficient
	mm	mm	N	N / mm	N	N / mm	%
Lagrange	50.0	100	327	3.274	14	0.140	4.27
	25.0	100	328	3.276	15	0.154	4.70
	12.5	100	328	3.276	21	0.209	6.39
Euler	50.0	100	327	3.274	23	0.227	6.93
	25.0	100	328	3.275	21	0.214	6.52
	12.5	100	328	3.275	22	0.216	6.60

Figure 5.9 compares experimental and modelling data for the vertical displacement of sand beneath a 600mm towed rigid wheel, operating under a wheel load of 1.64kN at 0.1m/s. As shown, reasonably good agreement was obtained at depths greater than 30mm, regardless of the modelling approach used. At the lowest mesh resolution, using 50mm cells, the Euler simulation method is less accurate than the Lagrange approach. As element size is reduced, however, the two methods converge to produce very similar results.

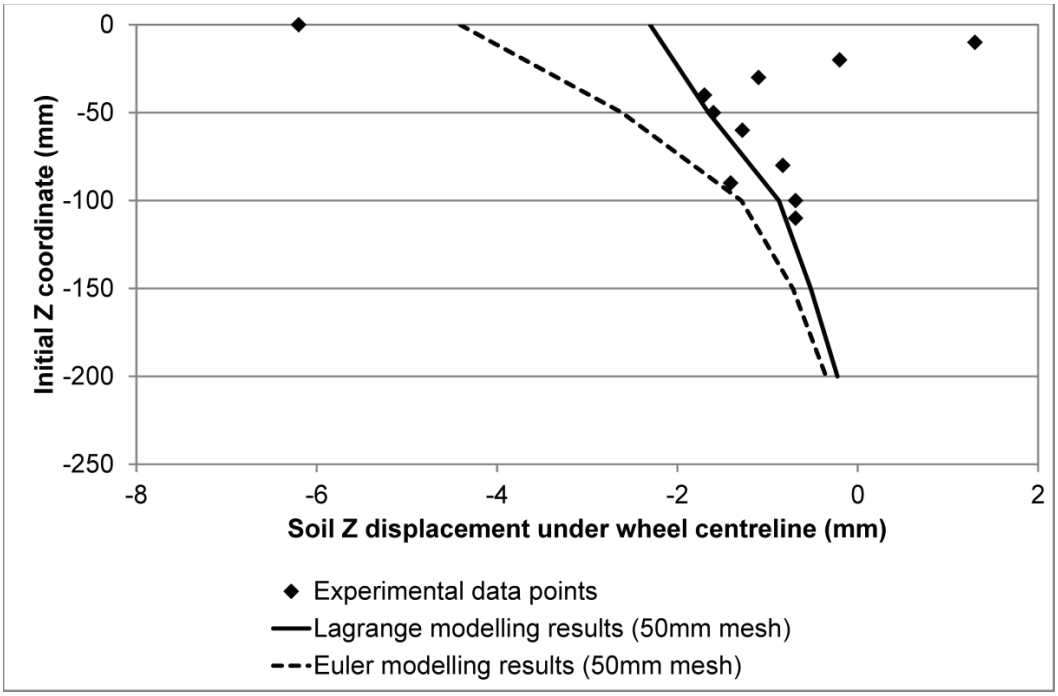

Figure 5.9: Comparison of experimental and modelling data for the vertical displacement of sand beneath a 600mm diameter towed rigid wheel operating under a wheel load of 1.64kN and translational speed of 0.1m/s

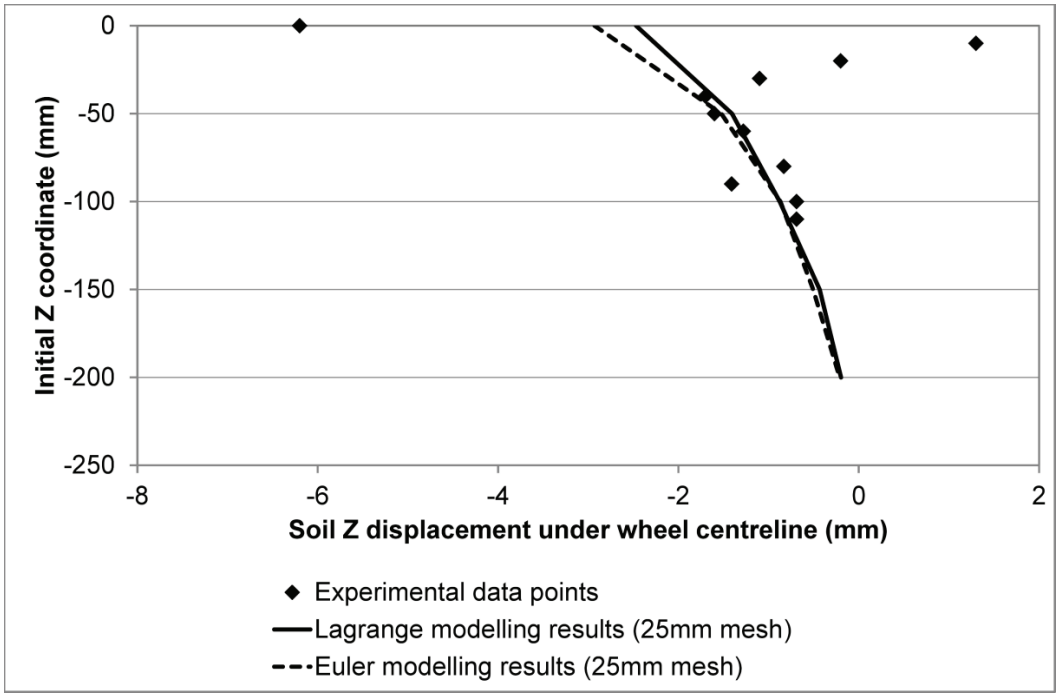

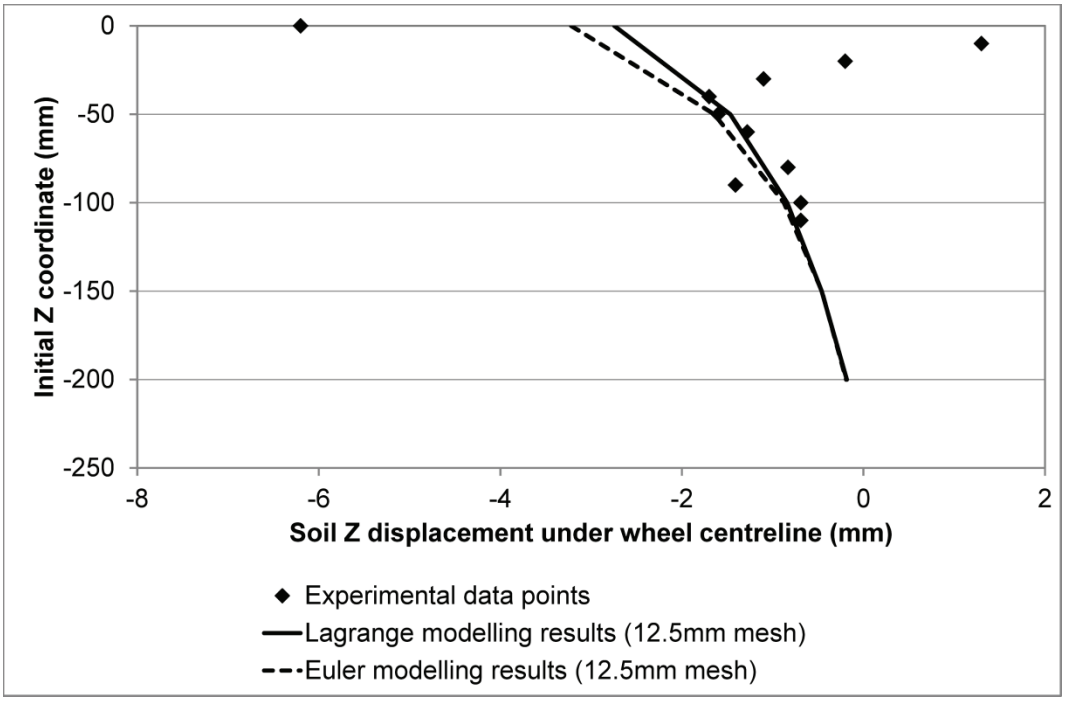

Figure 5.9 (continued): Comparison of experimental and modelling data for the vertical displacement of sand beneath a 600mm diameter towed rigid wheel operating under a wheel load of 1.64kN and translational speed of 0.1m/s

While the FE models produced good agreement beyond a soil depth of 40mm, the predicted vertical soil displacements in the upper layers (initial z coordinates of 0 to 30mm) differ significantly from the experimentally measured values. This can be explained by experimental measurement errors in this region, caused by the leakage of sand between the wheel and the observation window in the experimental rig. This leakage of sand at the wheel / observation window interface led to an *observed* positive vertical displacement in the uppermost layers of soil, despite the fact that, in reality, the soil beneath the wheel will have experienced a negative vertical displacement due to the applied wheel load. The experimental results show a gradual transition to the expected level of negative vertical displacement at a depth of 40mm.

In post-processing the experimental results, the vertical displacement of the soil surface (with an initial z coordinate of 0mm) was determined based on the known shape of the contact patch, rather than the observed position of the soil surface. Greater confidence can therefore be placed in the experimentally measured displacement of the soil's surface, compared to the measurements at depths of between 10 and 30mm. The difference between the predicted soil surface displacements and the experimentally measured value suggest that the level of compaction in the uppermost layer of soil is not correctly represented by the soil material model. The absolute difference between the experimental and numerical soil surface displacements, however, is small (3mm).

Based on the results obtained for the baseline condition of a 600mm diameter wheel operating under a wheel load of 167kg at 0.1mm/s, no significant difference in accuracy was found between the Lagrange and Euler solution methods using a mesh size of 25mm. Euler simulations were therefore run at this resolution for the remaining experimental treatments, the results of which are provided in Figure 5.10 and Figure 5.11.

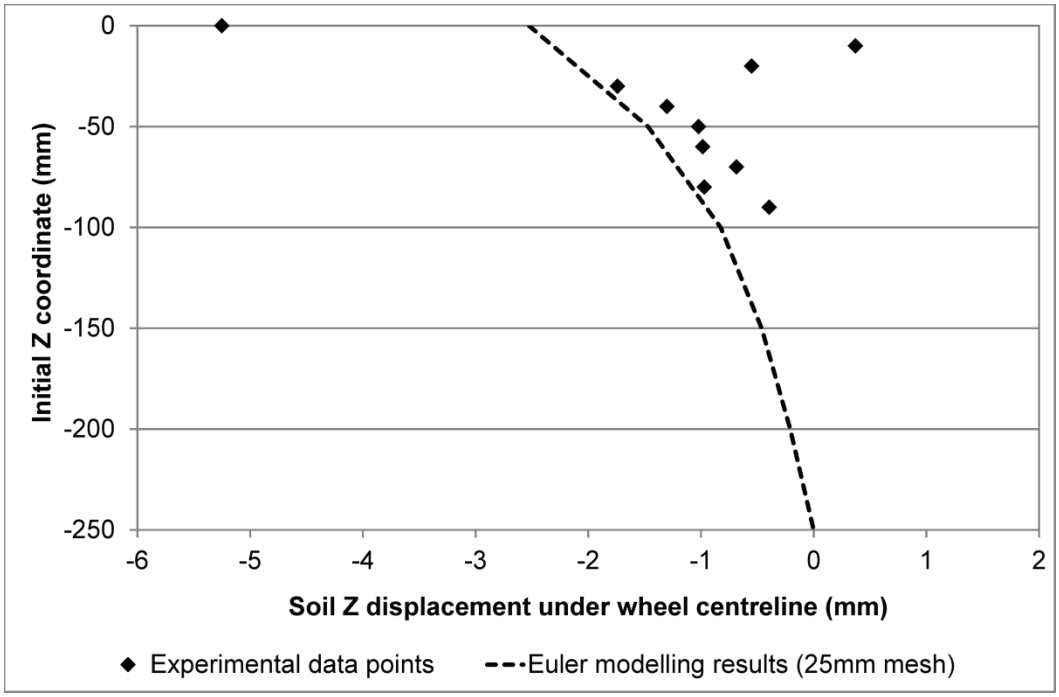

Figure 5.10: Comparison of experimental and modelling data for the vertical displacement of sand beneath a 600mm diameter towed rigid wheel operating under a wheel load of 1.64kN and translational speed of 0.2m/s

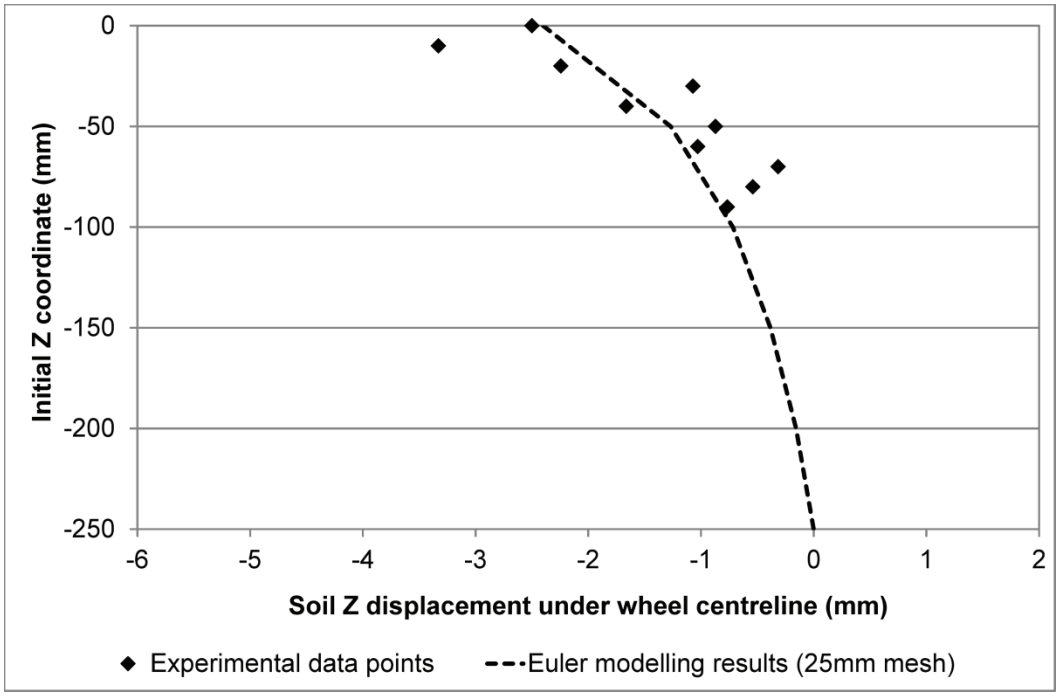

Figure 5.11: Comparison of experimental and modelling data for the vertical displacement of sand beneath a 1000mm diameter towed rigid wheel operating under a wheel load of 1.64kN and translational speed of 0.1m/s

The above study highlighted the potential difficulties in obtaining reliable experimental measurements for comparison with numerical models, even under relatively well-controlled laboratory conditions. From a qualitative comparison, the results obtained show reasonably good agreement between modelling predictions and experimental data for the conditions considered. It must be acknowledged, however, that for the range of variables considered during the experimental study, the variation in the soil's vertical displacement is very small (Figure 5.12). It is therefore difficult to quantitatively assess the model's accuracy in predicting the influence of variables such as wheel diameter and wheel load.

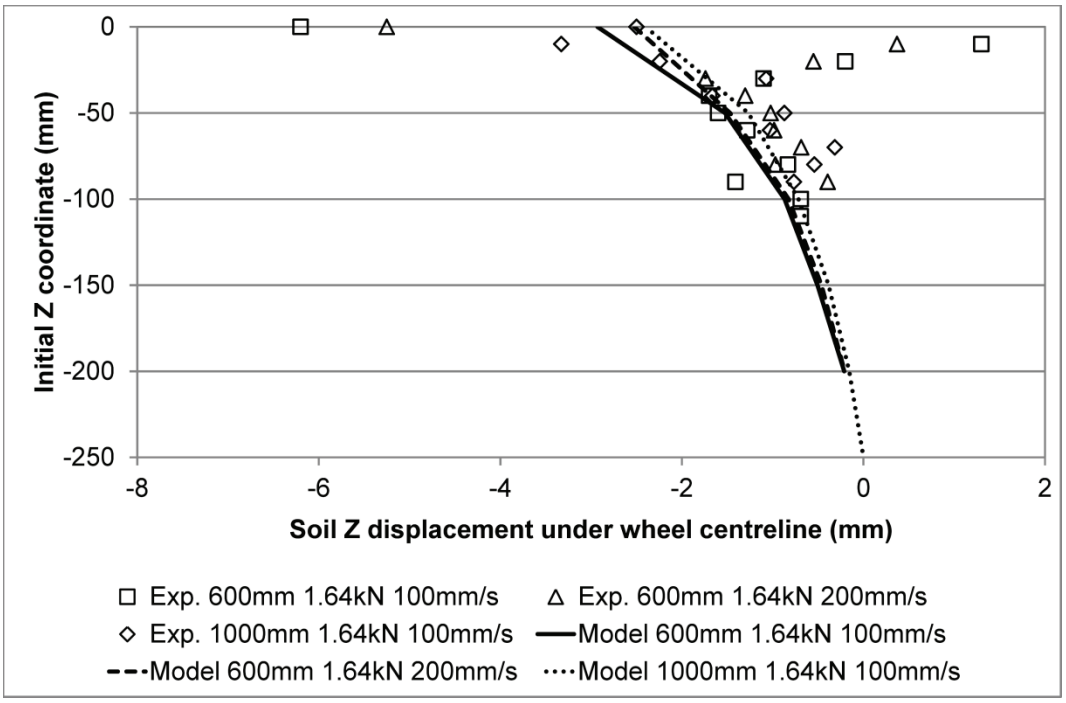

Figure 5.12: Comparison of experimental and modelling data for the vertical displacement of sand beneath towed rigid wheels of varying diameter and translational speed operating under a wheel load of 1.64kN

5.3.2 Comparison with existing models

In an effort to quantitatively assess the predicted influence of diameter and vertical load on the performance of a towed rigid wheel, FE modelling results were compared against existing mobility models. As a result of the simplifications made during the rigid wheel interaction study, with towed rigid wheels operating at constant wheel load and translational speed in the absence of out of plane deformation, it was possible to compare the predicted effects of wheel diameter and wheel load on rolling resistance against the mobility prediction models proposed by Bekker, Gee-Clough and Freitag (Chapter 2). This provided an additional check on the FE model's ability to describe the effects of wheel diameter and wheel load on rolling resistance for a rigid wheel operating on dry sand.

5.3.2.1 Effect of wheel diameter

From Gee-Clough (1978), the coefficient of rolling resistance for rigid wheels is related not only to wheel diameter, but also to the level of sinkage. For shallow sinkage, Gee-Clough derives the following expression for the coefficient of rolling resistance per unit width:

$$C_{RR} = \sqrt{\frac{z_0}{D}} \qquad \textit{Equation 5.1}$$

A similar relationship between wheel diameter, sinkage and rolling resistance is derived by Bekker (1956):

$$C_{RR} = \sqrt{\frac{z_0}{D}} * \frac{3}{(n+1)*(3-n)} \qquad \textit{Equation 5.2}$$

The relationship between rolling resistance coefficient and wheel diameter predicted using the Eulerian FE model was determined by running a series of simulations for rigid wheels 400, 600, 800 and 1000mm in diameter, with all other variables within the simulation held constant. The results of these simulations are presented in Figure 5.13, and show very good agreement with the relationships proposed by Bekker and Gee-Clough.

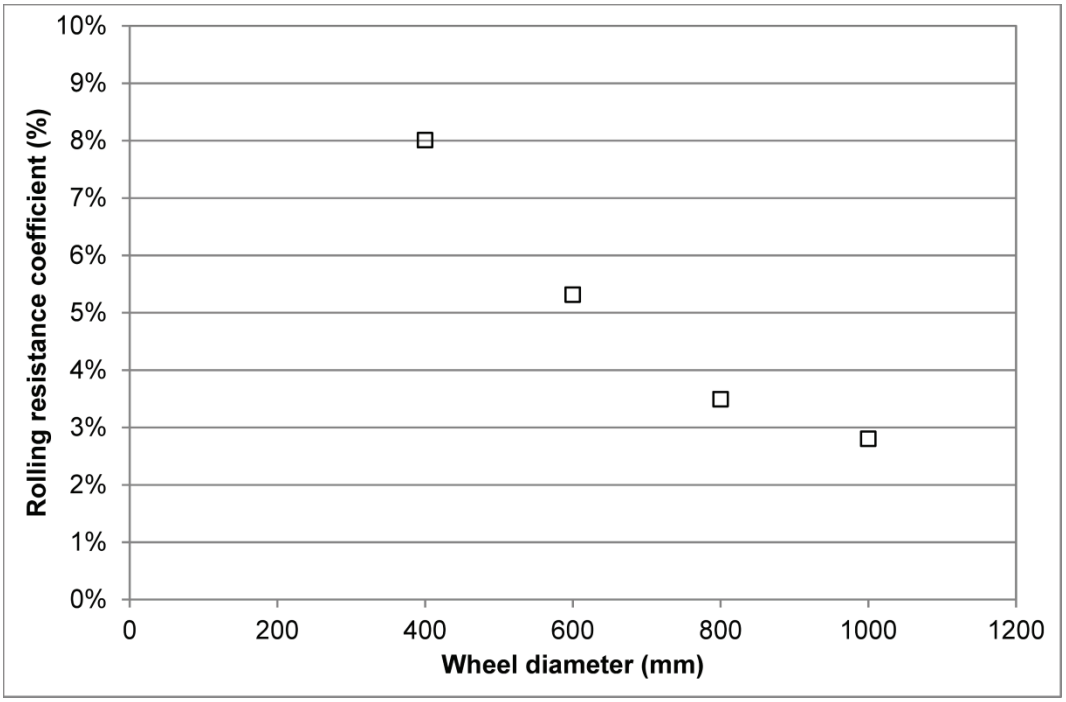

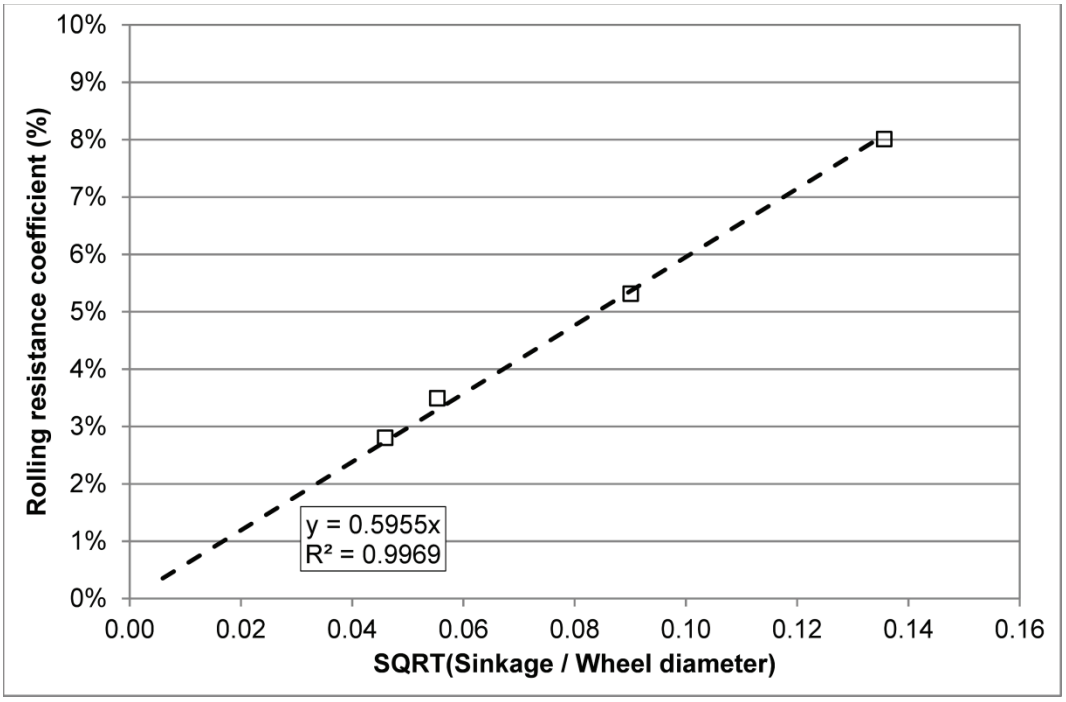

Figure 5.13: Effect of wheel diameter on coefficient of rolling resistance for towed rigid wheels operating on dry sand under a constant load

5.3.2.2 Effect of wheel load

The effect of wheel load on rolling resistance for a towed rigid wheel was considered by both Frietag (1962) and Bekker (1956). From experimental trials of rigid wheels operating on sand, Freitag derived the following expression for rolling resistance:

$$\frac{RD}{b} = K\left(\frac{W}{b}\right)^{3/2} \qquad \textit{Equation 5.3}$$

For a fixed soil type and wheel diameter, rolling resistance per unit width will vary as a function of wheel width. It is interesting to note that, in this case, rolling resistance is a non-linear function of wheel load, and that the rolling resistance coefficient will therefore also depend on the applied wheel load.

$$R \propto W^{3/2} \qquad \textit{Equation 5.4}$$

From Bekker's analysis of rolling resistance for a rigid wheel, rolling resistance is a function of both wheel load and the soil's sinkage exponent, n:

$$R = \frac{bk}{(n+1)}\left[\frac{3W}{bk\sqrt{D}(3-n)}\right]^{\frac{2n+2}{2n+1}} \qquad \textit{Equation 5.5}$$

To assess the FE model's ability to predict the effect of wheel load on rolling resistance, a series of models where run using a 600mm rigid wheel with applied wheel loads of 0.46, 0.85, 1.25, 1.64. 2.03 and 2.42kN, with the predicted effect of wheel load compared against Freitag and Bekker's analyses in Figure 5.14. For the purposes of the current comparison using Equation 5.5, initial constants for the Bernstein pressure sinkage equation (Equation 2.21) were derived from static plate sinkage tests (see Table 4.1).

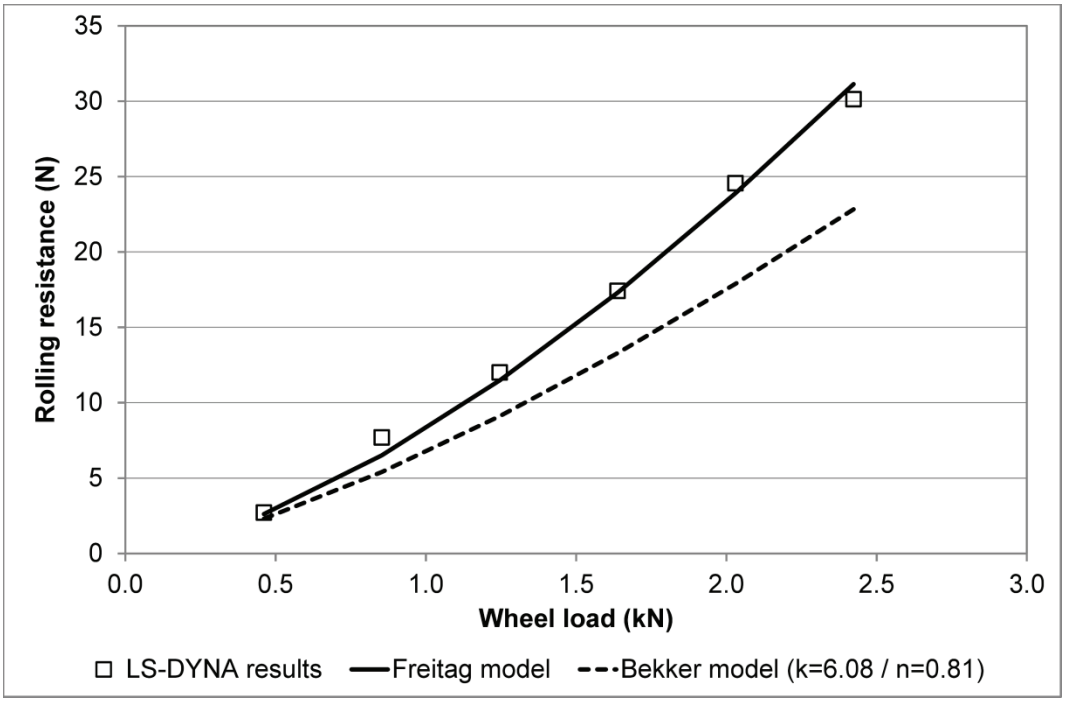

Figure 5.14: Comparison of FE modelling results against the relationships proposed by Freitag and Bekker between rolling resistance and applied wheel load

The results of the FE models show very good agreement with Freitag's model for the effect of wheel load, which is understandable given that Freitag's equation for rolling resistance was based on experimental trials undertaken on dry sand. Bekker's semi-empirical approach is more general in its application, with soil properties represented in terms of the sinkage modulus, k, and exponent, n. This allows Bekker's model to be applied to a wider range of soils, but its accuracy is dependent on the soil properties specified by the user.

Using the quasi-static plate sinkage test data reported in Chapter 4, the influence of wheel load on rolling resistance is underestimated, with a mean percentage error of 24% across the range of wheel loads considered. To evaluate the impact of the Bernstein model parameters, k and n, on the predicted level of rolling resistance, the vertical soil loading rate was estimated from the sinkage levels predicted by the FE models. Using Equation 4.3, the vertical loading rates experienced by the soil were first calculated as being

between 6 and 9mm/s, depending on the wheel load applied. Bernstein sinkage parameters derived from dynamic plate sinkage tests at 10mm/s were then substituted into Bekker's model for rolling resistance, which reduced the mean percentage error to 7% (Figure 5.15).

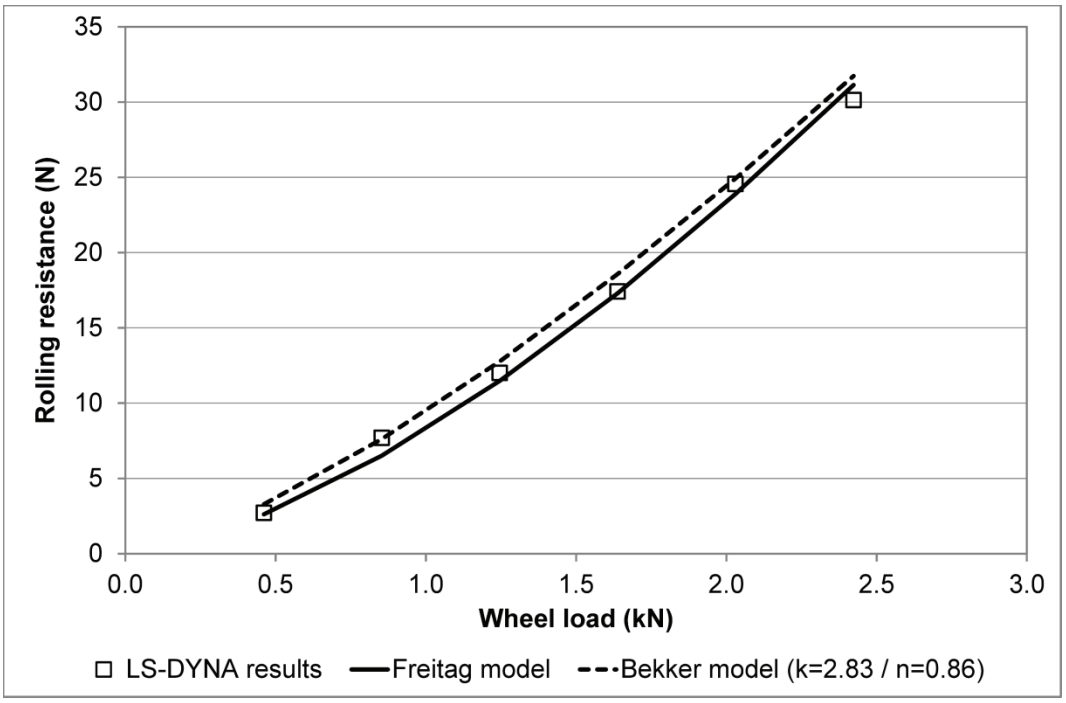

Figure 5.15: Revised comparison of FE modelling results against the relationships proposed by Freitag and Bekker between rolling resistance and applied wheel load

5.4 Stress distributions beneath a towed rigid wheel

For mobility models to be truly predictive, the normal and tangential stress distributions along the wheel / soil interface must be accurately represented. A number of previous studies have investigated the stress distributions beneath towed rigid wheels, using both experimental and analytical methods, while some of the early FE mobility models used the findings of these experimental and analytical studies as inputs to predict soil deformation. Three of the most commonly referenced papers in this area are those by Onafecko and Reece (1967) and Wong and Reece (1966 and 1967b).

One of the key findings of the experimental work reported by Onafecko and Reece was the existence of a transition point on the wheel / soil interface, located ahead of the wheel's centreline for a towed wheel, where the tangential stress changes sign from positive (opposite in direction to the wheel's rotation) to negative. In terms of soil deformation beneath the wheel, the transition point corresponds to the boundary between two failure zones in the soil, with soil in front of the transition point moving forwards and upwards to form a bow wave in front of the wheel. The soil behind the transition point, meanwhile, moves backwards. For a towed rigid wheel, the transition point is also the location of the maximum radial stress.

As shown in Figure 5.16, both the Lagrange and Euler solution methods predict the location of the peak vertical stress just ahead of the wheel's centreline, as would be expected for a towed rigid wheel. Figure 5.17 then provides a comparison of the predicted shear stress distributions, which illustrate the presence of a transition point corresponding with the peak vertical stress. The use of vertical stress and horizontal shear stress is recognised as an approximation, but can be justified in this case due to the relatively short contact interface and the low level of sinkage, relative to the wheel's diameter. Both modelling methods, therefore, show good qualitative agreement with previous studies on the distribution of normal and tangential stresses along the interface between soil and a towed rigid wheel.

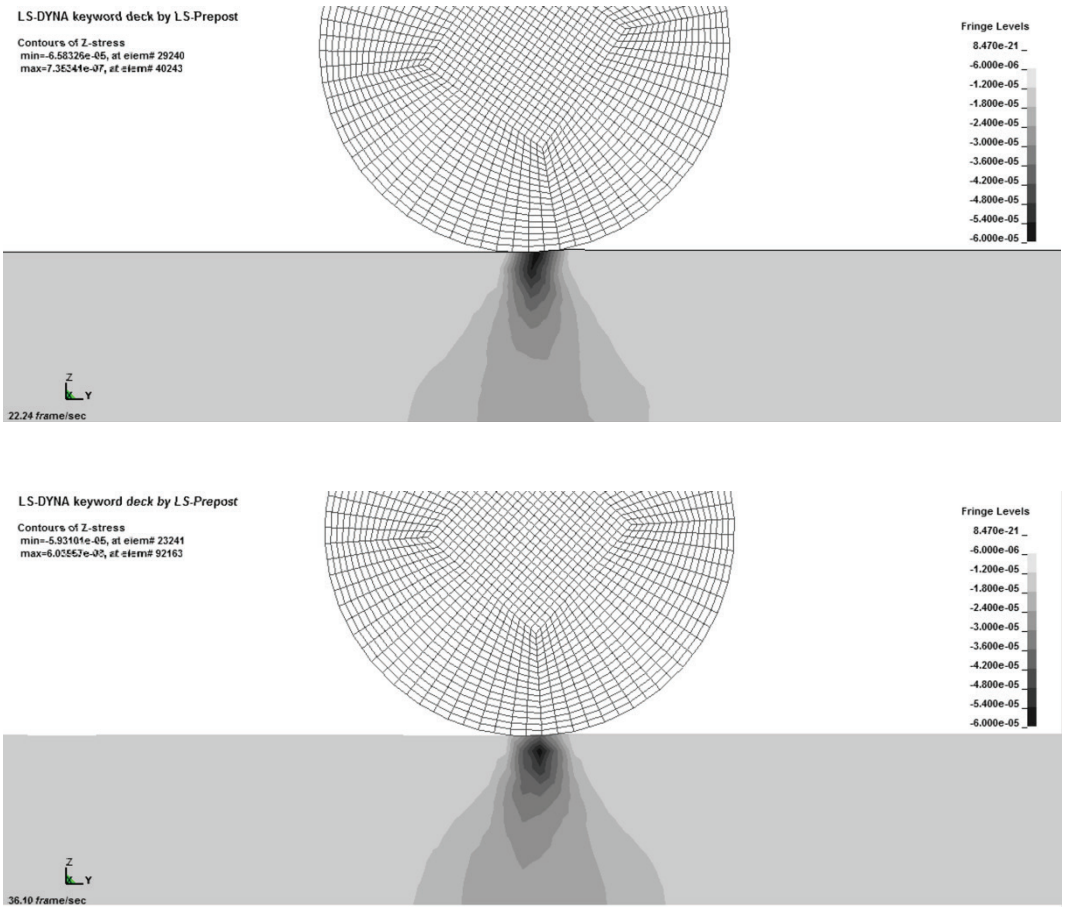

Figure 5.16: Comparison of vertical stress distributions beneath a towed rigid wheel, as predicted using Lagrange (top) and Euler (bottom) solvers in LS-DYNA

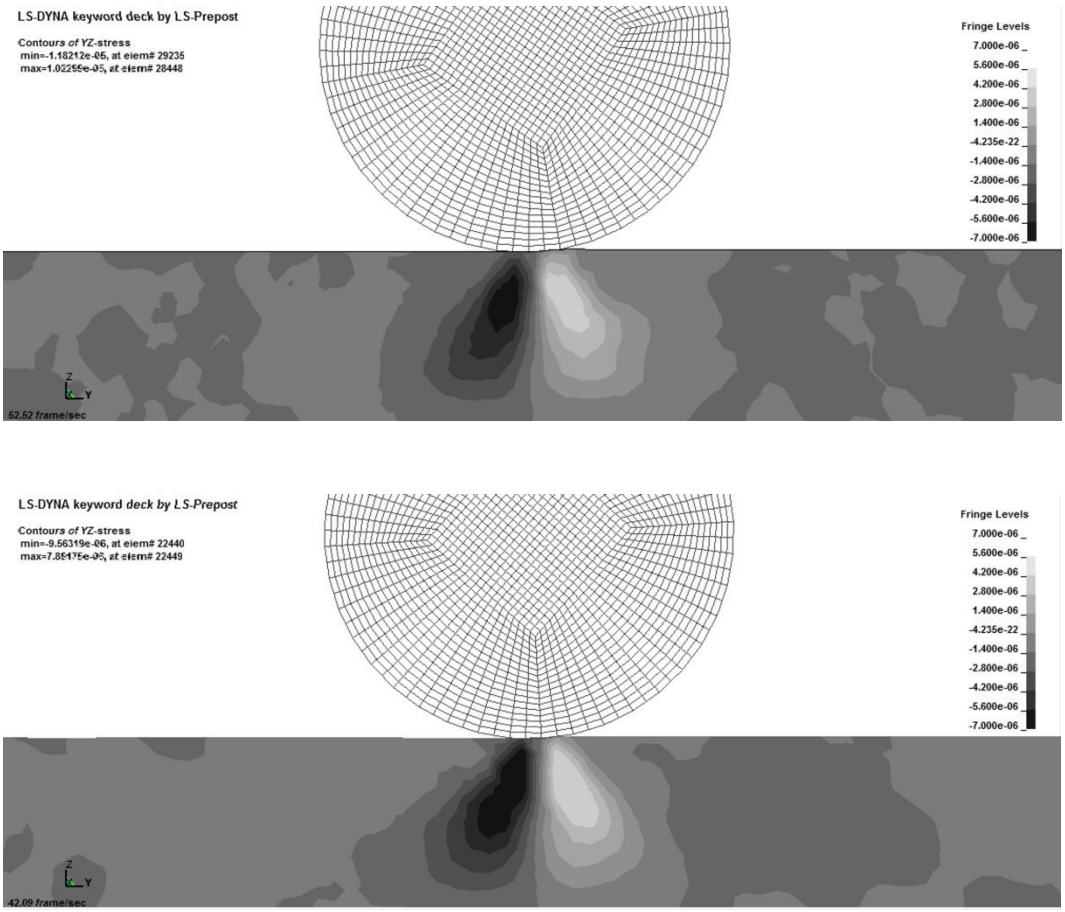

Figure 5.17: Comparison of shear stress distributions beneath a towed rigid wheel, as predicted using Lagrange (top) and Euler (bottom) solvers in LS-DYNA

5.5 Summary

The aim of the work reported in this chapter was to provide a preliminary assessment of an FE mobility prediction tool in LS-DYNA, in terms of the ability of the model to predict soil displacements, rolling resistance and normal / tangential stress distributions for a towed rigid wheel operating on dry sand. Restricting the analysis to a rigid wheel operating under plane strain conditions not only simplified the FE analysis, but also permitted a comparison of FE results against both experimental data and existing empirical, semi-empirical and analytical models.

The soil displacements predicted by the LS-DYNA model demonstrated good qualitative agreement with experimental results. A full quantitative comparison between model and experimental data, to assess the predicted influence of variables such as wheel diameter, was not feasible due to the relatively small variations in soil displacement between treatments and the limited resolution of the experimental method. To supplement the limited set of experimental data, a comparison was made between the rolling resistance values predicted by LS-DYNA against empirical and semi-empirical models. The predicted influences of wheel diameter and wheel load on rolling resistance were compared, with excellent agreement between FE modelling results and the relationships derived by Bekker, Freitag and Gee-Clough.

Finally, a qualitative evaluation of the predicted normal and tangential stress distributions acting at the wheel / soil interface was undertaken. FE modelling results were compared against benchmark experimental and analytical studies in this area, with LS-DYNA results showing good agreement with the stress distributions reported in the literature.

Chapter 6: Tyre model development

The soil modelling approach discussed above focussed on the ability to relate off-road vehicle mobility to terrain characteristics. In order to relate mobility parameters such as rolling resistance and drawbar pull to vehicle characteristics, the behaviour of the vehicle's tyres must be accurately represented. This chapter discusses the development and validation of efficient pneumatic tyre models for off-road mobility simulations.

6.1 Physical tyre construction

The earliest tyres were intended to improve the strength and wear characteristics of wooden wheels, and consisted of an iron or steel band applied around the circumference of the wheel. During the 19th and early 20th centuries, flexible rubber and pneumatic tyres were developed, which helped to overcome both passenger discomfort and the resistance to motion caused by obstacles such as bumps and pot holes (National Highway Traffic Safety Administration, 2006).

For off-road mobility, the development of pneumatic tyres also permitted a degree of control over contact patch dimensions; by reducing the inflation pressure of the tyre, the flexibility of the tyre is increased, leading to an increase in contact patch area and an associated reduction in ground pressure for a given wheel load. This increase in contact patch area can improve off-road mobility in two ways: for both towed and driven wheels, a reduction in vertical contact pressure reduces the level of wheel sinkage and rolling resistance, while an increase in contact area means that a greater force (thrust) can be generated before shear failure occurs at the wheel / soil interface.

For a simple inflated torus contacting a rigid surface, a reduction in inflation pressure produces an increase in both the length and width of the contact patch. While an increase in contact patch area can be beneficial in reducing rolling resistance and increasing gross tractive force, this improvement in performance will be offset to an extent by any increase in width since the

resistance to motion presented by soil compaction and bulldozing is directly related to wheel width. Modern pneumatic tyres are therefore designed to ensure that, as inflation pressure is reduced, the contact patch increases in length with a negligible increase in width. The construction of a typical radial ply tyre is shown in Figure 6.1, which illustrates the different components used.

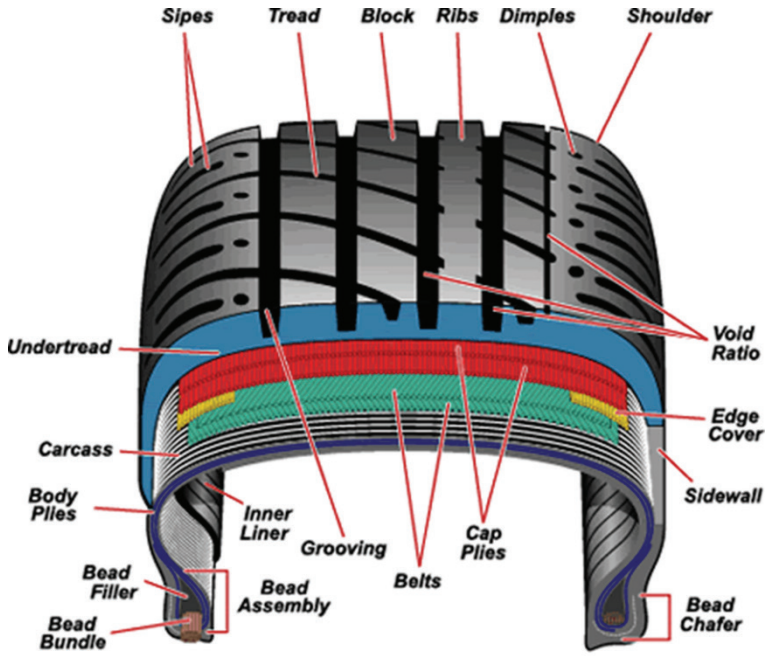

Figure 6.1: Typical construction of a radial tyre (source: yokohama-online.com, accessed 7th January 2012)

The construction and function of each of the main tyre components are discussed below:

- Tread – the tread is a thick band of rubber on the outer circumference of the tyre that that comes into contact with the terrain. For the majority of tyres, the tread contains a tread pattern, which is a geometric arrangement of grooves, lugs and voids designed to provide traction while channelling water and mud from the centre to the edges of the

contact patch. The rubber compound used is intended to balance traction requirements with wear resistance.

- Belt – the belt is a thin band located on the inner surface of the tread, which provides support to the tread and helps to regulate contact with the terrain. The belt has a composite construction, with layers of closely-spaced steel cords sandwiched between layers of rubber, and runs around the circumference of the tyre as shown in Figure 6.1. In addition to providing support to the tread, the belt helps to resist longitudinal stresses and cornering forces. The individual layers of steel cords are arranged a slight angle to the centreline of the tyre, typically 15 – 25°, with the angle of the cords affecting the ride and handling characteristics of the tyre.

- Sidewall – the sidewall of the tyre is a non-reinforced rubber section that connects the tread and the bead of the tyre and protects the inner plies from abrasion and environmental degradation.

- Ply – the plies of the tyre are steel or polymer fabric reinforced rubber layers which line the inner surface of the tyre. Due to the high in-plane stiffness of the steel or fabric relative to that of the surrounding rubber, the plies prevent significant dimensional changes from occurring as a result of internal pressurisation. The plies, in combination with the sidewall and inflation pressure, provide much of the tyre's resistance to applied loads. The plies, which pass from one side of the tyre to the other, also transmit torque from the driven wheel rim to the tread; their orientation can have a significant effect on the performance of the tyre as a whole, and is therefore one of the main ways in which tyres are classified.

- Bead – finally, the beads are bands of steel reinforced rubber which make contact with the rim on which the tyre is mounted. The beads on

either side of the tyre sit tightly against the rim under the action of the inflation pressure to prevent leakage of air from the tyre and to ensure that the tyre does not rotate relative to the rim.

6.2 Tyre model construction

The tyre models developed to date may generally be separated into the large, highly detailed tyre models used by tyre manufacturers and the simplified tyre models that are used as part of larger scale, full vehicle analyses. The use of detailed FE models, which explicitly represent the physical construction of a pneumatic tyre, has typically focussed on improving on-road performance, where the main contribution to rolling resistance comes from deformation of the tyre itself. For on-road tyres, the ability to identify even small improvements in tyre performance is desirable given the number of miles travelled and the corresponding reduction in fuel consumption.

In recent years, there has been increasing interest in the development of efficient tyre models that accurately capture the mechanical characteristics of the physical tyre to applied loading while reducing computational effort. The main focus for their development has been for use in vehicle crash and road safety simulations, such as those associated with kerb impacts (Shiraishi, 2002) and tyre blowout (Orengo et al., 2003), although the use of efficient tyre models has also been demonstrated for vehicle turn analysis (Fukushima and Shimonishi, 2004).

For the tyre / soil interaction problem considered here, the expected dimensions of the model dictated the use of an efficient tyre model which captured the response of the tyre to applied loads while minimising run time. To this end, a generic tyre model was used, based on the approach reported by Reid et al. (2006). To demonstrate the generic nature of the tyre modelling approach and assess the ability of the tyre / soil interaction model to quantify the effects of tyre geometry and inflation pressure, models were developed for Michelin XZL 445 / 65 R 22.5 and Goodyear G90 7.5 R 16 tyres.

The four basic components of the generic tyre model are illustrated in Figure 6.2. The sidewall was represented using fully integrated shell elements and, as shown, split into eight individual parts to allow the thickness of the sidewall to be varied across the width of the tyre. The tread band was represented using constant stress solid elements and, due to the coarse mesh used, it was not possible to explicitly represent the tread pattern. A blank tread band was therefore specified, with the impact of this simplification assessed as part of the experimental work to validate the tyre / soil interaction model, discussed in Chapter 7 of this thesis.

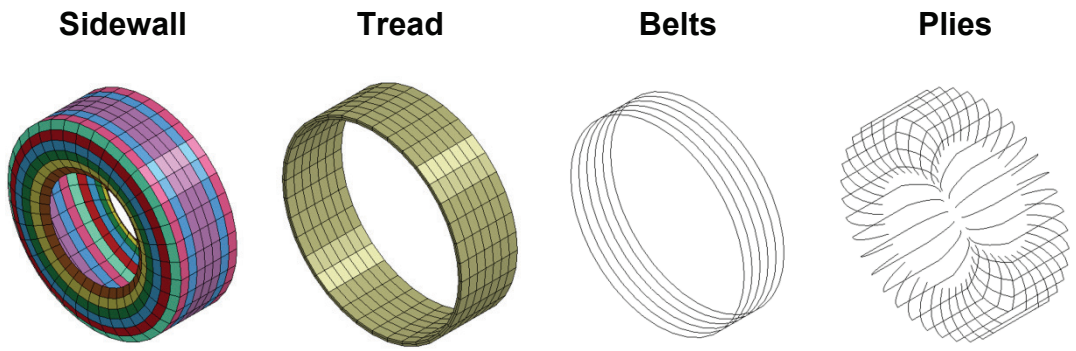

Figure 6.2: Components of a generic model for pneumatic tyres

The complex arrangement of belt and ply reinforcements within the physical tyre was described using a simplified arrangement of beam elements. Both the belt and ply reinforcements were represented using Belytschko-Schwer resultant beam elements, where the response of the beam is described primarily in terms of its bending stiffness, and the parallel axis theorem could be used to reduce the large number of physical reinforcing cables to a much smaller number of beam elements. Each beam element therefore represents a large array of physical reinforcements.

Considering the steel belts of the Goodyear G90 7.5 R 16 tyre as an example, the belts in the physical tyre consist of three layers of steel cables, with each cable containing four individual wires (Figure 6.3). Assuming a regular arrangement of cables, the ply layer can be broken down into a number of

repeating unit cells, with each beam element in the simplified tyre model representing one unit cell of cables, as illustrated in Figure 6.4. Using this approach significantly reduces the number of elements required to describe the complex arrangement of reinforcements within the tyre while capturing their contribution to the tyre's overall response to applied loads.

The materials within the tyre models were represented using a combination of simple linear elastic material models for tyre reinforcements and hyperelastic Mooney-Rivlin material models for rubber components. The material property data used for each component within the tyre models was obtained from a previous study by Erashin (2003), and is summarised in Table 6.1.

6.3 Tyre model validation

As discussed above, the use of pneumatic tyres provides users with a degree of control over contact patch area through changes in inflation pressure. Given the potential impact of tyre inflation pressure on mobility, it was necessary to validate the Michelin XZL 445 / 65 R 22.5 and Goodyear G90 7.50 R 16 tyre models against experimental tyre characterisation data across a wide range of inflation pressures.

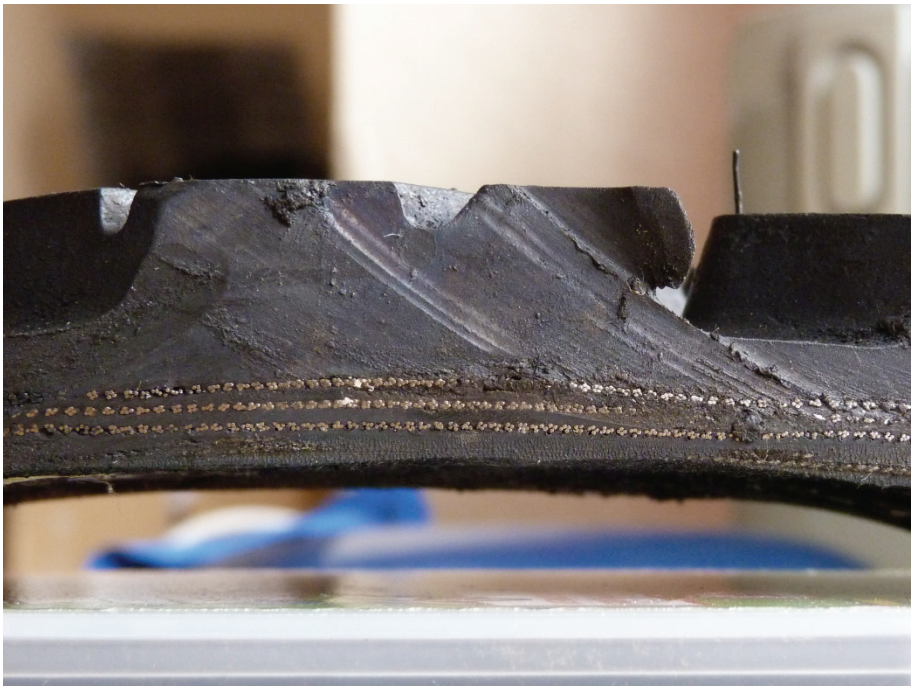

Figure 6.3: Cross section of Goodyear G90 7.50 R 16 tyre illustrating arrangement of steel belt reinforcements

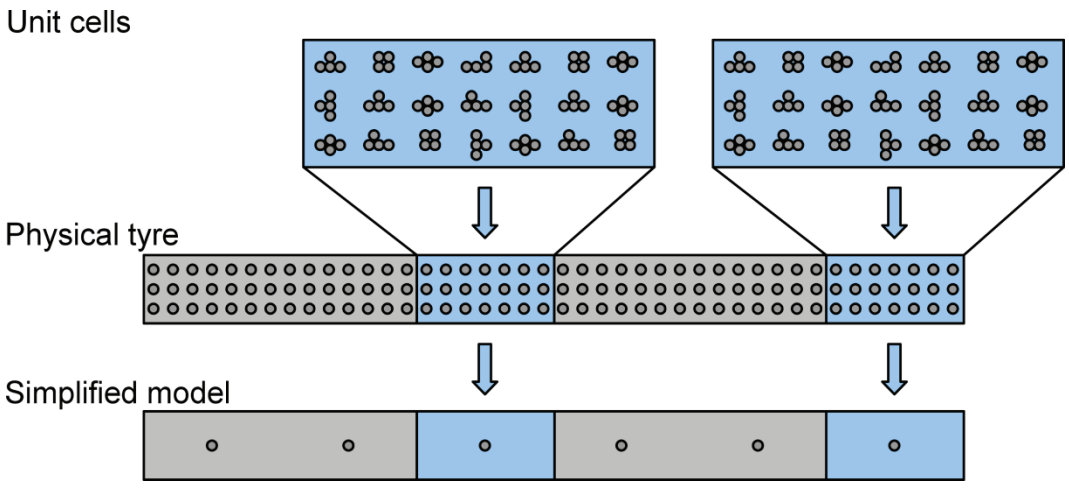

Figure 6.4: Unit cell approach used to model complex arrangement of belt and ply reinforcements

Table 6.1: Material property data used in tyre model (Ersahin, 2003)

	Michelin XZL 445 / 65 R 22.5	**Goodyear G90 7.50 R 16**
Sidewall	Rubber MAT_MOONEY_RIVLIN ρ: 1.25 x 10^{-6} kg.m^{-3} C_{10}: 171.8 kPa C_1: 830.3 kPa ν: 0.495	Rubber MAT_MOONEY_RIVLIN ρ: 1.25 x 10^{-6} kg.m^{-3} C_{10}: 171.8 kPa C_1: 830.3 kPa ν: 0.495
Tread	Rubber MAT_MOONEY_RIVLIN ρ: 1.25 x 10^{-6} kg.m^{-3} C_{10}: 806.1 kPa C_1: 1,805 kPa ν: 0.495	Rubber MAT_MOONEY_RIVLIN ρ: 1.25 x 10^{-6} kg.m^{-3} C_{10}: 806.1 kPa C_1: 1,805 kPa ν: 0.495
Belts	Steel MAT_ELASTIC ρ: 7.90 x 10^{-6} kg.m^{-3} E: 200 MPa ν: 0.30	Steel MAT_ELASTIC ρ: 7.90 x 10^{-6} kg.m^{-3} E: 200 MPa ν: 0.30
Plies	Steel MAT_ELASTIC ρ: 7.90 x 10^{-6} kg.m^{-3} E: 200 MPa ν: 0.30	Polyester MAT_ELASTIC ρ: 1.39 x 10^{-6} kg.m^{-3} E: 3.97 GPa ν: 0.30

6.3.1 Load deflection

The compliance of pneumatic tyres is commonly assessed in terms of the deflection occurring under varying levels of applied vertical load. During a load-deflection test, the tyre is brought into contact with a rigid surface; the test may be either load or deflection controlled, with the relationship between load and tyre deflection recorded throughout to obtain a curve for each inflation pressure tested.

In the case of the Michelin XZL 445 / 65 R 22.5 tyre, load deflection data was obtained from the manufacturer for tyre pressures of between 100 and 1100kPa. Data on the Michelin website (Michelin Americas Truck Tires, accessed 29th October 2011) indicates standard operating pressures of between 520 and 830kPa for this tyre, depending on the expected axle load. For comparison against the supplied load-deflection data, load deflection simulations were run for the Michelin XZL 445 / 65 R 22.5 tyre at inflation pressures of 100, 200, 400, 600 and 800 kPa. These inflation pressures covered the range used during the experimental test programme described in Chapter 7.

Within the load deflection model, the tyre is first inflated to the desired pressure over a period of two seconds. The simulation is run under a displacement controlled condition, with a prescribed displacement boundary condition applied to the centre of the wheel over a period of eight seconds, as this ensured that the desired level of deflection was achieved without the need to estimate the maximum load required for each pressure. The force required to cause the deflection was then recorded at both the contact interface between the tyre and rigid surface and at the wheel centre.

The effect of inflation pressure on the deformed shape of the Michelin XZL tyre model, for a constant load of 2,000kg, is illustrated in Figure 6.5. Figure 6.6 provides a comparison between the load-deflection data provided by Michelin and the predicted load-deflection curves obtained from the model. As shown, reasonably good agreement was achieved between the predicted and manufacturer-supplied load deflection data across a wide range of inflation

pressures. The error associated with the predicted load deflection response was greatest at low inflation pressures, with a mean absolute percentage error of 17 and 18% for inflation pressures of 200 and 100kPa. For higher inflation pressures, of between 400 and 800kPa, better agreement was achieved, with mean absolute percentage errors of between 2 and 8%.

As discussed in the literature review, rolling resistance on a rigid surface is dominated by hysteresis energy losses within the tyre. No unloading data was supplied for the Michelin XZL tyre and the unloading behaviour of the tyre model was therefore not assessed.

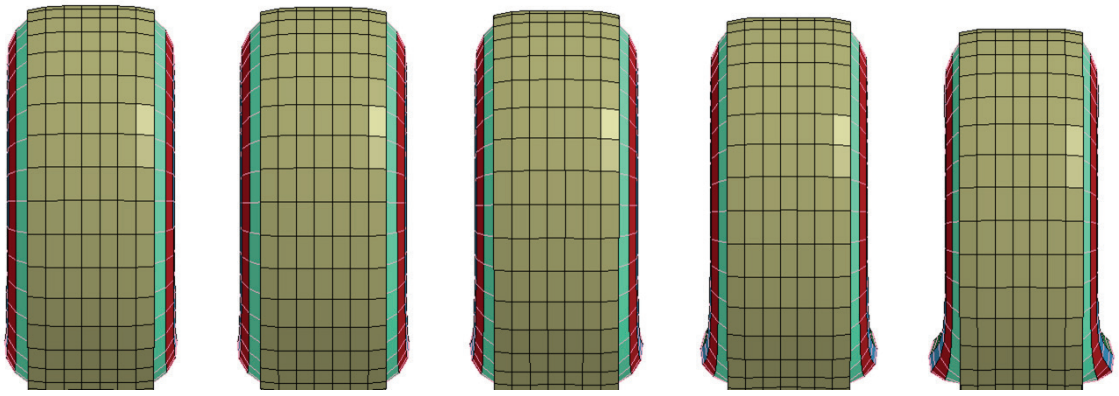

Figure 6.5: Effect of tyre inflation pressure on tyre deflection for a Michelin XZL 445 / 65 R 22.5 tyre model under a constant load of 20kN

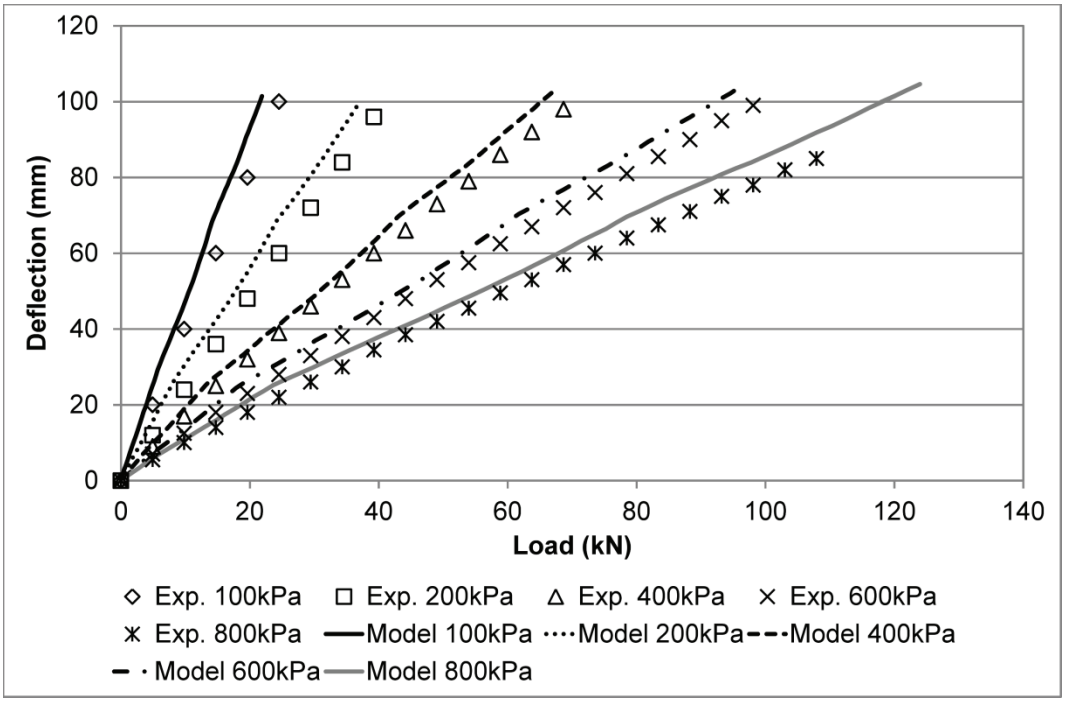

Figure 6.6: Comparison of FE modelling results against manufacturer supplied load-deflection data for a Michelin XZL 445 / 65 R 22.5 tyre interacting with a rigid surface

The Goodyear G90 7.50 R 16 tyre model was constructed in an almost identical manner to the Michelin XZL 445 / 65 R 22.5 tyre model, with the primary differences between the two being the diameter and aspect ratio, as illustrated in Figure 6.7. Unlike the 445 / 65 R 22.5 tyre, load-deflection data for was not available from the manufacturer, and experimental testing was undertaken to generate validation data for the tyre model. Load deflection data for the 7.50 R 16 tyre was obtained for inflation pressures of between 50 and 450kPa and loads of between 0 and 10kN.

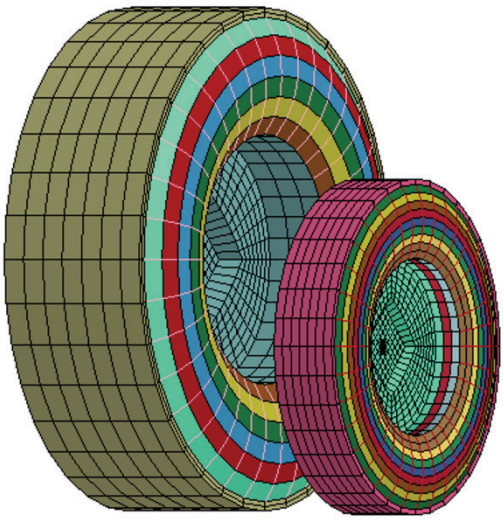

Figure 6.7: Visual comparison of Michelin XZL 445 / 65 R 22.5 (left) and Goodyear G90 7.50 R 16 (right) tyre models, illustrating differences in tyre diameter, width and section height

Initial simulations run using the Goodyear 7.50 R 16 tyre model indicated an overly stiff response from the model. To improve the model's accuracy, a physical tyre was sectioned to provide more detail on the construction of the tyre and the materials used. As discussed previously, the ply reinforcements act in combination with the inflation pressure to provide much of the tyre's resistance to applied loads, and initial investigations therefore focussed on this component. On investigation, it was found that the Goodyear G90 7.50 R 16 tyre uses textile cord plies, rather than the steel ply construction used in the larger Michelin XZL 445 / 65 R 22.5 tyre.

Material property data for polyester was therefore substituted into the Goodyear G90 7.50 R 16 tyre model and the load deflection models re-run to assess the effect of this change on the response of the tyre model to applied loads. As shown in Figure 6.8, this material change made a substantial difference to the behaviour of the tyre model, with the revised Goodyear 7.50 R 16 tyre model showing a good level of agreement with the experimentally derived load deflection data. As for the Michelin XZL tyre, the Goodyear G90 7.50 R 16 tyre model's accuracy was assessed in terms of the mean absolute percentage error

in load for a given deflection, with values of between 4 and 6% obtained for inflation pressures between 250 and 450kPa. For the lowest inflation pressures of 130 and 50kPa, the mean percentage errors increased to 14 and 23%, respectively.

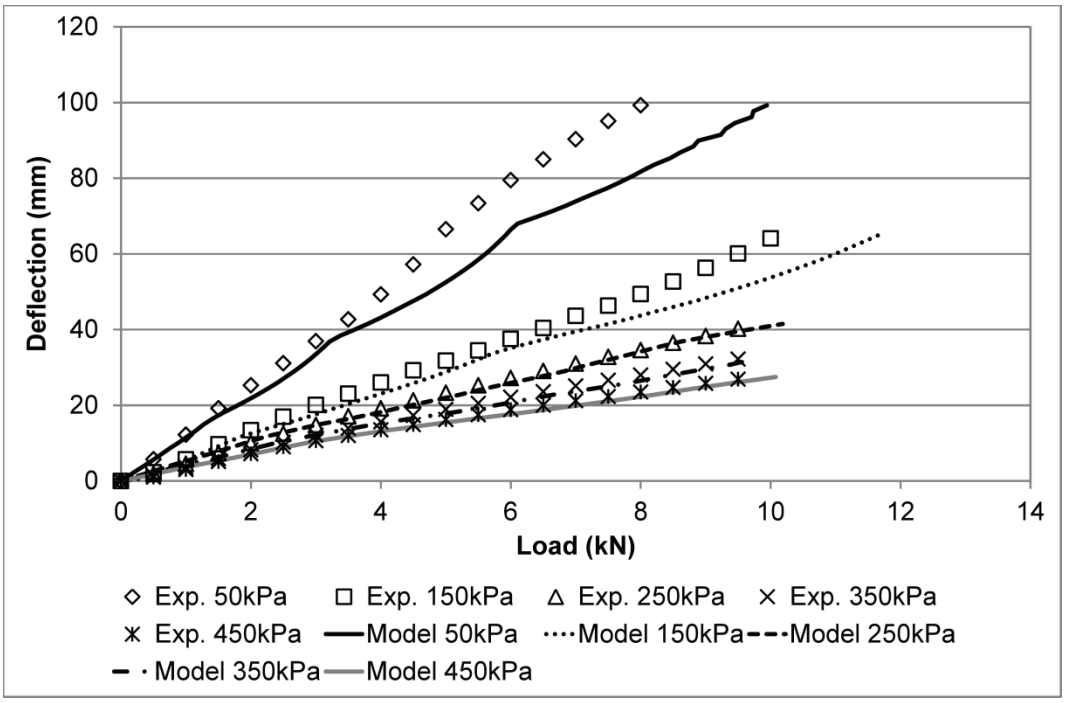

Figure 6.8: Comparison of FE modelling results against experimentally derived load-deflection data for a Goodyear G90 7.50 R 16 tyre interacting with a rigid surface

Since experimental data for the 7.50 R 16 tyre was generated through physical testing under the current study, it was possible to assess hysteresis during loading / unloading cycles. The effect of hysteresis within the physical tyre is clearly shown in Figure 6.9, where the loading and unloading curves form a loop, with less energy recovered during unloading than is required to deform the tyre as the load is applied. In the case of the FE tyre model, no hysteresis effects are included, with the unloading curve replicating the path followed during the initial loading stage. It would be expected, therefore, that the FE tyre models described above will under-predict rolling resistance on a rigid surface,

since no energy is consumed during the deformation of the model tyre. Rigid surface rolling resistance and the implications of a purely elastic tyre response are discussed further in Section 6.3.3.

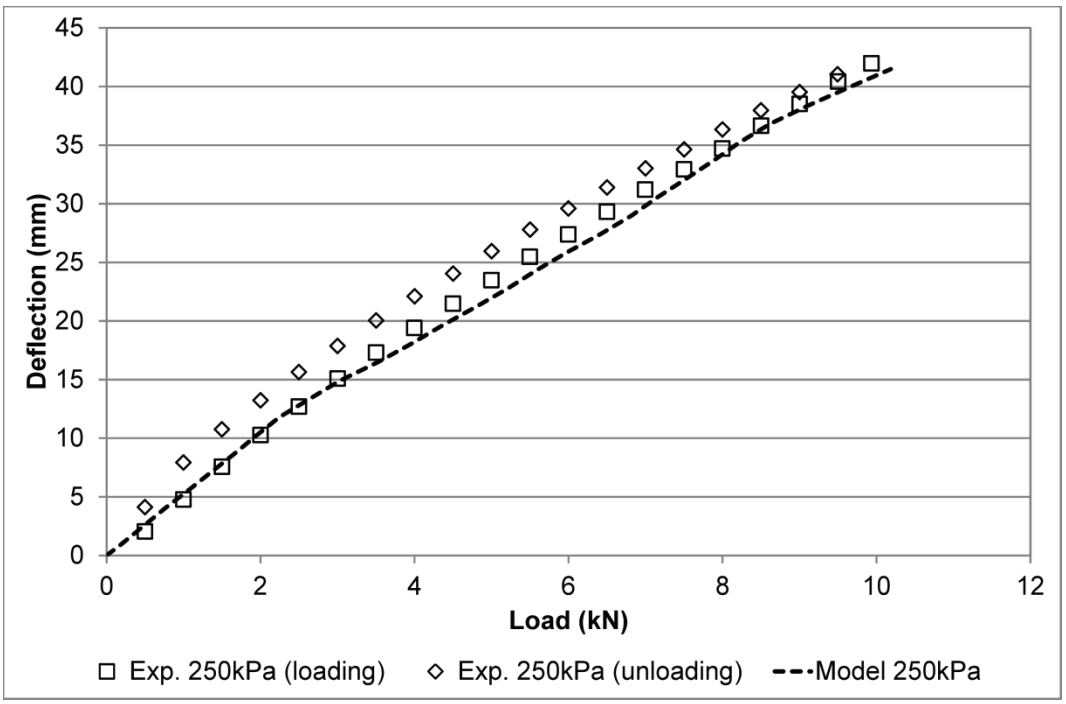

Figure 6.9: Comparison of FE modelling load deflection results against experimentally measured loading and unloading curves for a Goodyear G90 7.50 R 16 tyre at an inflation pressure of 250kPa

6.3.2 Contact patch dimensions

Modern off-road tyres are designed such that the contact patch increases in length as inflation pressure is reduced, without a significant increase in width. For off-road mobility prediction, the load deflection characteristic of the tyre model is only one aspect of its validation, and the effects of inflation pressure and load on contact patch dimensions must also be addressed.

To generate validation data, both the 445 / 65 R 22.5 and 7.50 R 16 tyres were subjected to physical testing to establish the relationship between the dimensions of the contact patch, the inflation pressure and the applied load.

Contact patch dimensions were determined by applying ink to the tread of the tyre, with paper positioned on a rigid surface to record the imprint of the tyre under the action of a specific combination of load and inflation pressure. After obtaining a series of prints of the contact patch, the prints were photographed and post-processed to produce plots of contact patch length, width and area against wheel load for each inflation pressure. The test matrix used for the contact patch study is provided in Table 6.2. Results obtained from the 445 / 65 R 22.5 and 7.50 R 16 tyre models are presented in terms of contact patch area in Figure 6.10 and Figure 6.11, respectively.

Table 6.2: Test matrix for validation of tyre model contact patch dimensions

Pressure	100 kPa	200 kPa	400 kPa	50 kPa	120 kPa	260 kPa	400 kPa
Load	Michelin XZL 445 / 65 R 22.5			Goodyear G90 7.50 R 16			
3.92 kN					X		
5.89 kN				X	X	X	X
7.85 kN				X	X	X	X
9.81 kN				X	X	X	
12.26 kN	X	X	X				
24.53 kN	X	X	X				
36.79 kN	X	X	X				
49.05 kN	X	X	X				

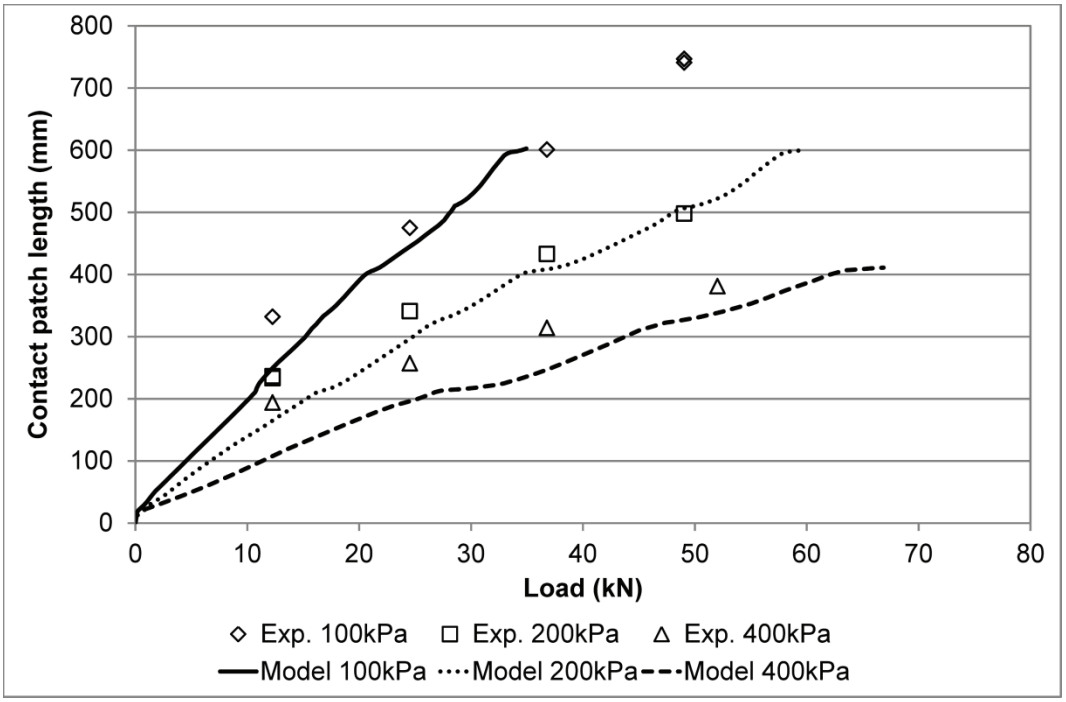

Figure 6.10: Comparison of predicted contact patch area as a function of wheel load and inflation pressure against experimental data for 445 / 65 R 22.5 tyre

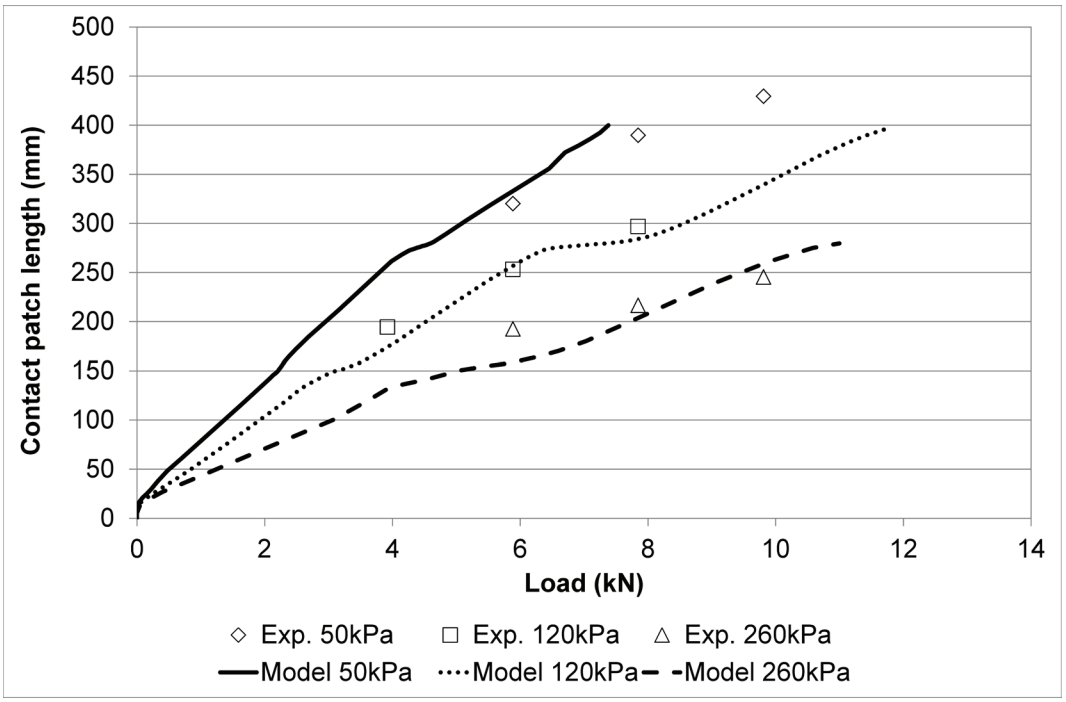

Figure 6.11: Comparison of predicted contact patch area as a function of wheel load and inflation pressure against experimental data for 7.50 R 16 tyre

The Goodyear G90 7.50 R 16 tyre model was found to display good agreement with the experimentally measured contact patch lengths, with mean percentage errors of between -7 and +9%, depending on the inflation pressure specified. For the larger 445 / 65 R 22.5 tyre, the agreement between experimentally measured and predicted contact patch lengths was poor by comparison, with mean percentage errors of between 13 and 48%. The difference in accuracy between the two tyre models is somewhat surprising, given their broadly similar accuracy in predicting vertical deflection, but reflects the difficulties experienced in attempting to reverse engineer FE models of specific physical tyres.

6.3.3 Rigid surface rolling resistance

Rigid surface rolling resistance values were measured for both tyres while operating on asphalt using different combinations of translational speed, inflation pressure and wheel load. The results of the experimental rolling resistance tests, each the average of at least three test runs, are provided in Table 6.3 and Table 6.4.

Table 6.3: Experimental rolling resistance test results for Michelin XZL 445 / 65 R 22.5 tyre operating on asphalt

Speed	Inflation pressure	Load	Rolling resistance	Rolling resistance coefficient
m/s	kPa	kN	kN	%
1.0	500	29.43	0.263	0.89
2.0	750	29.43	0.273	0.93
2.0	750	44.15	0.370	0.84
1.0	750	29.43	0.254	0.86

Table 6.4: Experimental rolling resistance test results for Goodyear G90 7.50 R 16 tyre operating on asphalt

Speed	Inflation pressure	Load	Rolling resistance	Rolling resistance coefficient
m/s	kPa	kN	kN	%
1.0	275	4.91	0.026	0.53
2.0	275	4.91	0.047	0.96
2.0	275	7.36	0.083	1.13
1.0	190	4.91	0.050	1.02

As discussed earlier in this chapter, the absence of hysteresis in the load-deflection response of the FE tyre models can adversely affect the prediction of rigid surface rolling resistance. For off-road mobility, the rolling resistance component due to tyre deformation forms a relatively small part of the total, but it was necessary to quantitatively assess the likely impact of this simplification on the model's ability to predict rolling resistance on deformable terrain. To achieve this, an example case was selected for simulation from the experimental tests reported above. The test case simulation represented a Goodyear G90 7.50 R 16, inflated to 275kPa, towed across a rigid surface at a translational speed of 1.0m/s and under a wheel load of 4.91kN. The simulation produced a rigid surface rolling resistance of 0.015kN (0.3% of the applied wheel load), compared to an experimentally measured value of 0.026kN (0.5%).

Off-road rolling resistance is dominated by soil deformation, with rolling resistance values typically in the region of 5 – 35% of the applied wheel load (Wong, 2001). While the observed difference between the predicted and experimental values for *rigid surface* rolling resistance is relatively large, therefore, the influence of this simplification on rolling resistance prediction for deformable terrain is expected to be low.

6.4 Summary

This chapter has addressed the extension of efficient tyre models, previously used by other researchers in road safety and vehicle handling analyses, to address the problem of off-road vehicle mobility. The construction of radial tyres has been reviewed, and used to inform the development of tyre models to represent Michelin XZL 445 / 65 R 22.5 and Goodyear G90 7.50 R 16 tyres in FE simulations.

Building on previous work in this area, and to specifically address off-road mobility modelling, the resulting tyre models have been assessed in terms of their vertical deflection and the contact patch length developed in response to applied wheel loads across a wide range of inflation pressures. The results obtained demonstrate reasonable agreement with experimentally measured load deflection curves for both tyres, with mean percentage errors of less than 20% for the majority of inflation pressures considered. In the case of the 445 / 65 R 22.5 tyre model the ability to predict vertical deflection did not translate to an accurate prediction of contact patch length, with the model under predicting contact patch length for a given level of applied load. The work completed has highlighted the potential difficulty in attempting to reverse engineer representative tyre models for specific physical tyres.

Chapter 7: Tyre / soil interaction modelling

The main aim of the research reported here has been to extend the VPG concept to address off-road mobility of wheeled vehicles, improving the accuracy and applicability of FE mobility prediction models to allow competing vehicle designs to be directly compared in a repeatable and objective manner. The culmination of the modelling work was therefore to use the soil and tyre models discussed in previous chapters to predict key mobility parameters, including the effects of soil type, tyre geometry, inflation pressure and translational speed. This chapter describes the models used to predict rolling resistance and drawbar pull – under both positive and negative slip conditions – including the experimental work undertaken to validate the modelling results obtained.

7.1 Rolling resistance

For towed wheels, off-road mobility is entirely defined by the rolling resistance, which quantifies the effort required to tow the wheel across a given terrain. Since rolling resistance is influenced by the vertical load acting on the tyre, rolling resistance is often discussed in terms of the rolling resistance coefficient, which is the absolute value of rolling resistance divided by the wheel load. For modern passenger tyres operating on a rigid surface, the coefficient of rolling resistance is typically between 0.7 and 1.4% (Transportation Research Board, 2006). Under the current study, rigid surface rolling resistance values for the Michelin XZL 445 / 65 R 22.5 and Goodyear G90 7.50 R 16 tyres were measured experimentally and found to be between 0.5 and 1.1% for the combinations of inflation pressure, wheel load and translational speed considered. For vehicles operating off-road, the rolling resistance coefficient is typically much larger than that for a rigid surface, and is dictated primarily by the deformation of the soil around the wheel.

7.1.1 Experimental testing

Validation data for the rolling resistance model was generated using a combination of single wheel, single axle and full vehicle testing. In each case, the wheels were towed across the relevant surface at a constant translational speed under the action of a constant wheel load. The force required to tow the wheel, axle or vehicle axle was recorded throughout.

For the Goodyear G90 7.50 R 16 tyre, the physical dimensions of the tyre and the wheel loads studied permitted the use of Cranfield's single wheel tester, while the size of the Michelin XZL 445 / 65 R 22.5 tyre necessitated the use of a specially constructed single axle test rig (Figure 7.1). Rolling resistance values for the 445 / 65 R 22.5 tyres were measured using an extended octagonal ring transducer (EORT), which was positioned at the front end of a long drawbar to minimise any load transfer effects. The design and use of EORTs as a means of measuring forces and moments is discussed in detail by O'Dogherty (1996).

Figure 7.1: Cranfield University single wheel tester (SWT), on left, used for testing of Goodyear G90 7.50 R 16 tyres and rolling resistance / negative slip test rig, on right, used for Michelin XLZ 445 / 65 R 22.5 tyres

For the full vehicle tests with the 445 / 65 R 22.5 tyre, EORTs were installed between the front axle of the four wheel drive test vehicle and suspension (Figure 7.2) to measure the vertical and horizontal forces acting on the axle.

This allowed the rolling resistance and vertical load acting on the front and rear axles to be separated out from the overall towing force while the complete vehicle was towed across the terrain under investigation. For the 7.50 R 16 tyres, full vehicle tests made use of individual wheel transducers to measure the horizontal and vertical forces at each wheel as a function of time. The experimental treatments completed, the methods used and the rolling resistance values obtained are summarised in Table 7.1.

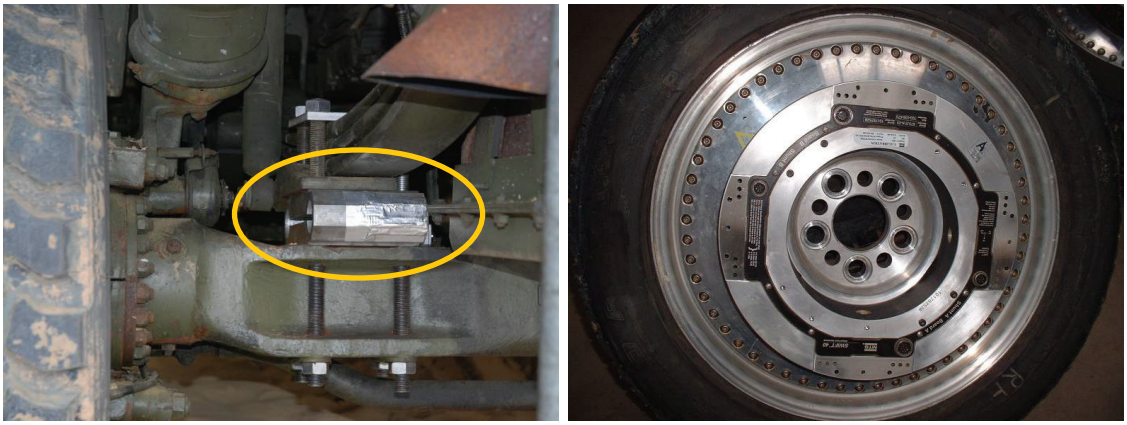

Figure 7.2: Instrumentation used to measure horizontal and vertical wheel forces for 445 / 65 R 22.5 tyres, using EORTs installed between the vehicle's front axle and suspension (left, highlighted), and for 7.50 R 16 tyres using individual wheel transducers (right)

The results of the experimental rolling resistance trials are plotted for the 445 / 65 R 22.5 and 7.50 R 16 tyres in Figure 7.3 and Figure 7.6, respectively. In an effort to address the variation in applied wheel load for the 7.50 R 16 tyre, the resistance to motion is presented in terms of the rolling resistance coefficients, rather than the absolute rolling resistance values. The experimental results indicate a marked decrease in rolling resistance for the 445 / 65 R 22.5 tyre, from 24% to 9%, as tyre inflation pressure is reduced from 300kPa to 100kPa on dry sand. This represents a large reduction in tyre inflation pressure from the standard on-road operating values recommended by the Michelin (520 – 830 kPa). Looking at the effect of translational speed for a constant inflation

pressure of 400kPa, rolling resistance initially increases as translational speed is increased from 0.2m/s to 0.5m/s, levelling off as translational speed is increased further to 1.0m/s (Figure 7.5). The apparent increase in rolling resistance with an increase in translational speed, from 32% at 0.2m/s to 39% at 0.5m/s, is surprising given the findings of dynamic plate sinkage tests on dry sand, which suggested no significant rate dependency.

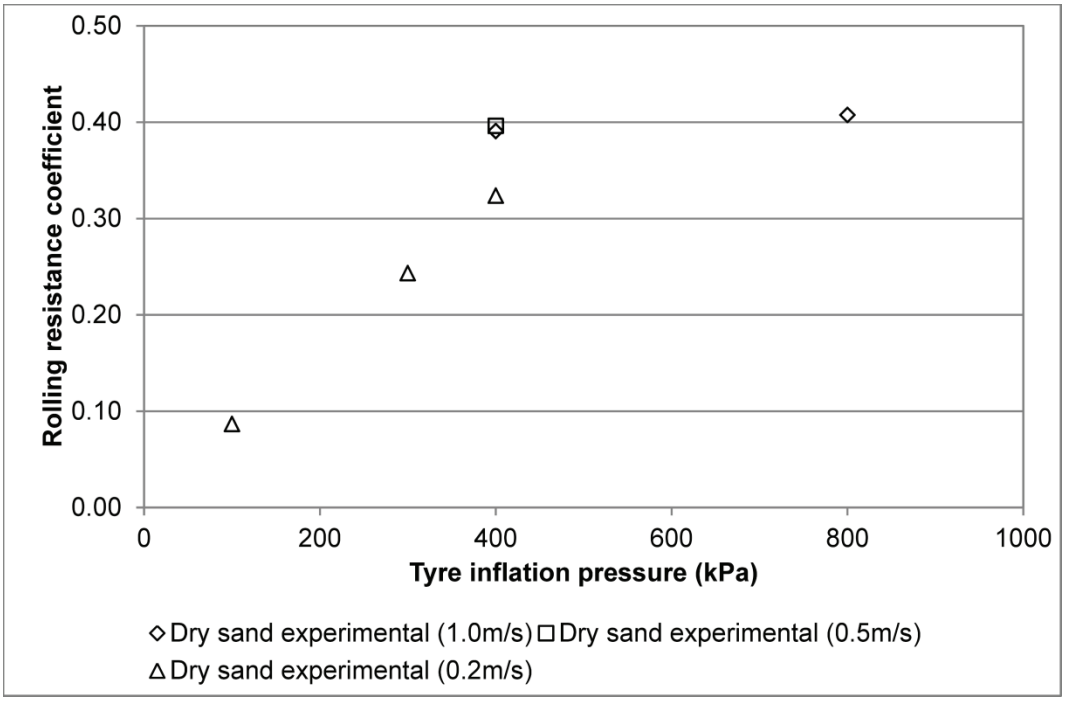

Figure 7.3: Experimental rolling resistance results for a towed Michelin XZL 445 / 65 R 22.5 tyre operating on dry sand

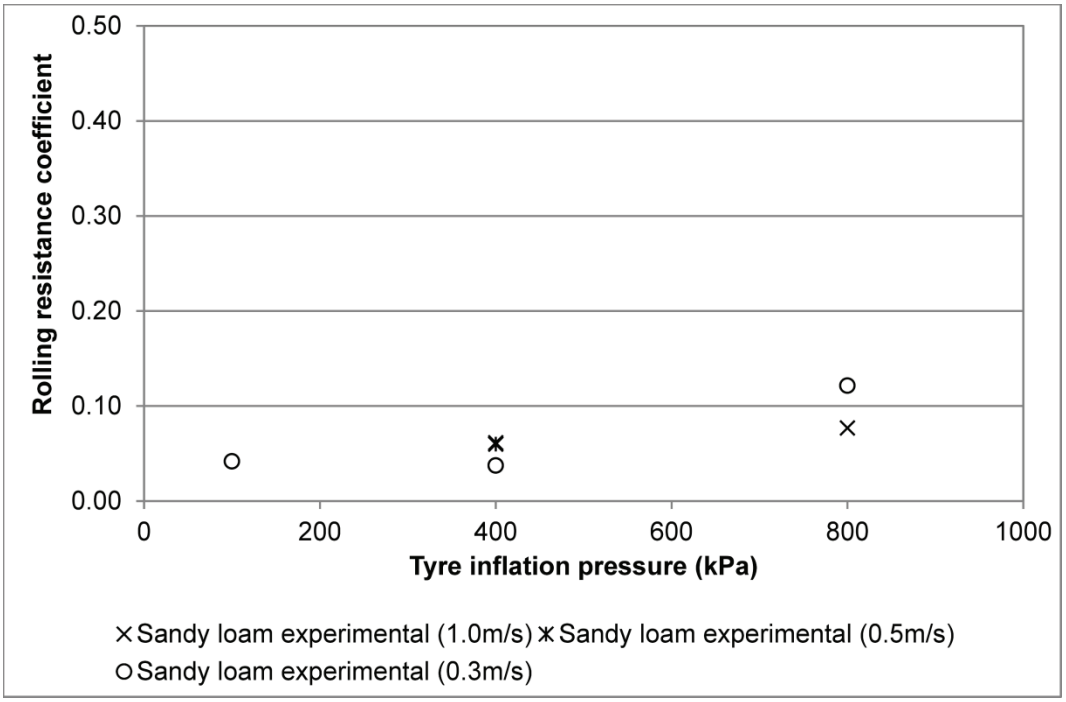

Figure 7.4: Experimental rolling resistance results for a towed Michelin XZL 445 / 65 R 22.5 tyre operating on sandy loam

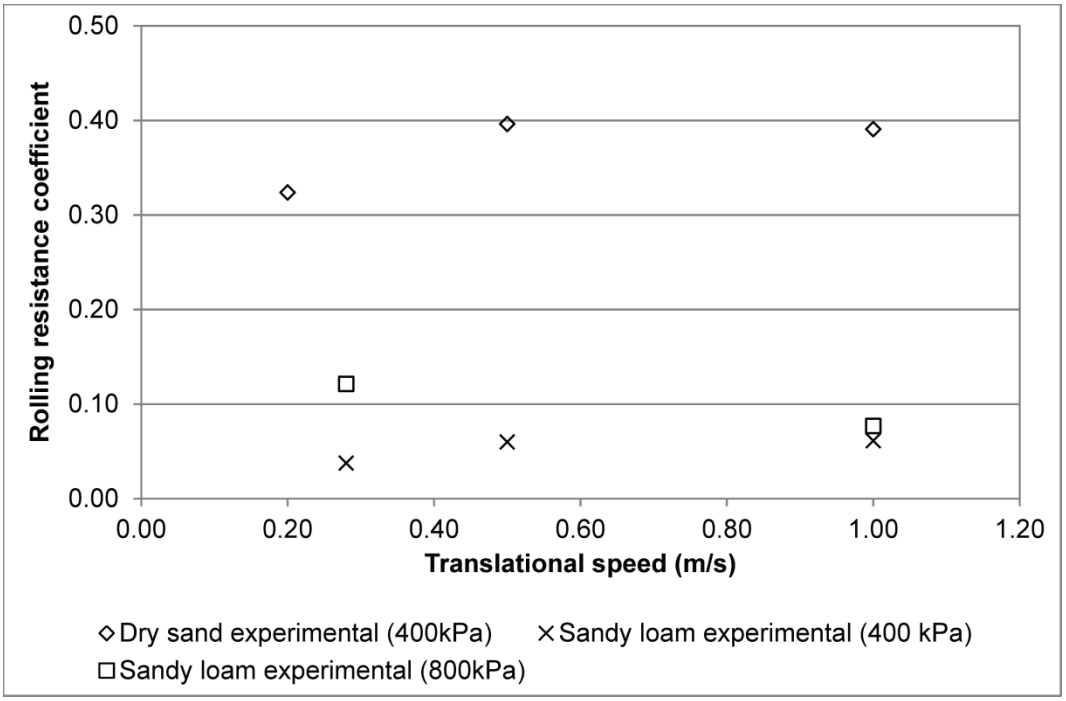

Figure 7.5: Effect of vehicle translational speed on rolling resistance for a towed Michelin XZL 445 / 65 R 22.5 tyre operating on dry sand and sandy loam soils

On the sandy loam soil, a similar relationship between rolling resistance and translational speed is observed for the 445 / 65 R 22.5 tyre when operating at an inflation pressure of 400kPa. Again, this appears to contradict the findings of the dynamic plate sinkage tests discussed in Chapter 4, which suggested a reduction in sinkage would accompany an increase in translational speed in the low speed range (<0.5m/s). At a higher inflation pressure of 800kPa the trend shown at 400kPa is reversed, with a reduction in rolling resistance coefficient from 12 to 8% as the vehicle's translational speed is increased from 0.3 to 1.0m/s.

Looking at Figure 7.5 from a slightly different perspective, an increase in inflation pressure has relatively little influence on the rolling resistance coefficient when operating on sandy loam soil at a translational speed of 1.0m/s. When operating at a translational speed of 0.3m/s, on the other hand, the effect of inflation pressure on rolling resistance coefficient is pronounced. At 0.3m/s, increasing the tyre inflation pressure from 400 to 800 kPa increases the rolling resistance coefficient from 4 to 12% while, at 1.0m/s, the rolling resistance coefficient increases from 6 to 8%.

For the sandy loam soil, the basic level of rolling resistance is much lower than that recorded for the dry sand, and the effect of tyre inflation pressure on rolling resistance is less prominent. Given the non-linear relationship between rolling resistance and inflation pressure on dry sand, the levels of rolling resistance for the two soils are broadly similar when operating at the lowest inflation pressure of 100kPa.

Caution should be exercised in comparing the Goodyear G90 7.50 R 16 results at low inflation pressures (50 and 130kPa) with those at higher inflation pressures (190 and 275kPa), since these data sets represent quite different experimental conditions with variations in both translational speed and wheel load. As discussed in Chapter 5, rolling resistance is a non-linear function of wheel load and, for this reason, the rolling resistance coefficient itself will vary as a function of the vertical load applied to the wheel. Focussing on the high inflation pressure regime, therefore, the influence of soil properties on rolling

resistance is similar to that observed for the larger 445 / 65 R 22.5 tyre, with the rolling coefficient on dry sand being between four and six times that measured on the sandy loam for inflation pressures of 190kPa and above (Figure 7.6). As with the 445 / 65 R 22.5 tyre, very low inflation pressures can produce a substantial reduction in rolling resistance, with a reduction from 130 to 50kPa reducing the rolling resistance coefficient from 27 to 17%.

As for the larger tyre, the level of rolling resistance when operating at standard on-road pressures is much lower on the sandy loam soil (8% at 190kPa) than on dry sand (45% at 190kPa). Limited data was obtained to assess the impact of translational speed on rolling resistance for the 7.50 R 16 tyre on sandy loam soil, although a reduction in translational speed from 1.0 to 0.5m/s produced an increase in rolling resistance coefficient from 8 to 10%.

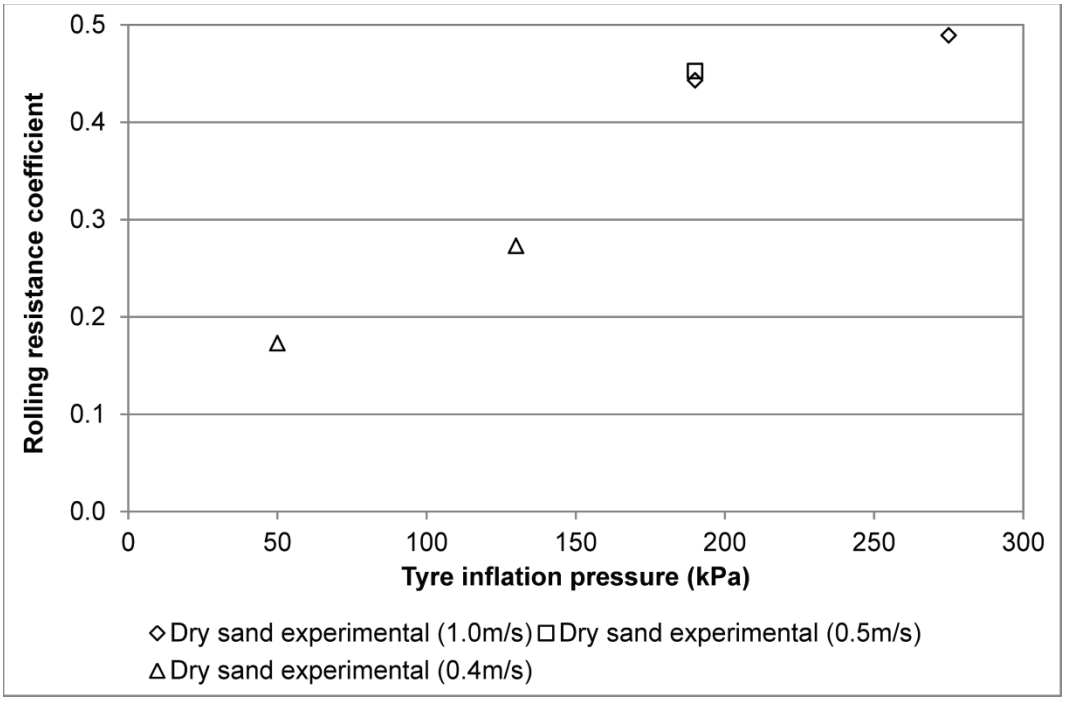

Figure 7.6: Experimental rolling resistance results for a towed Goodyear 7.50 R 16 tyre operating on dry sand

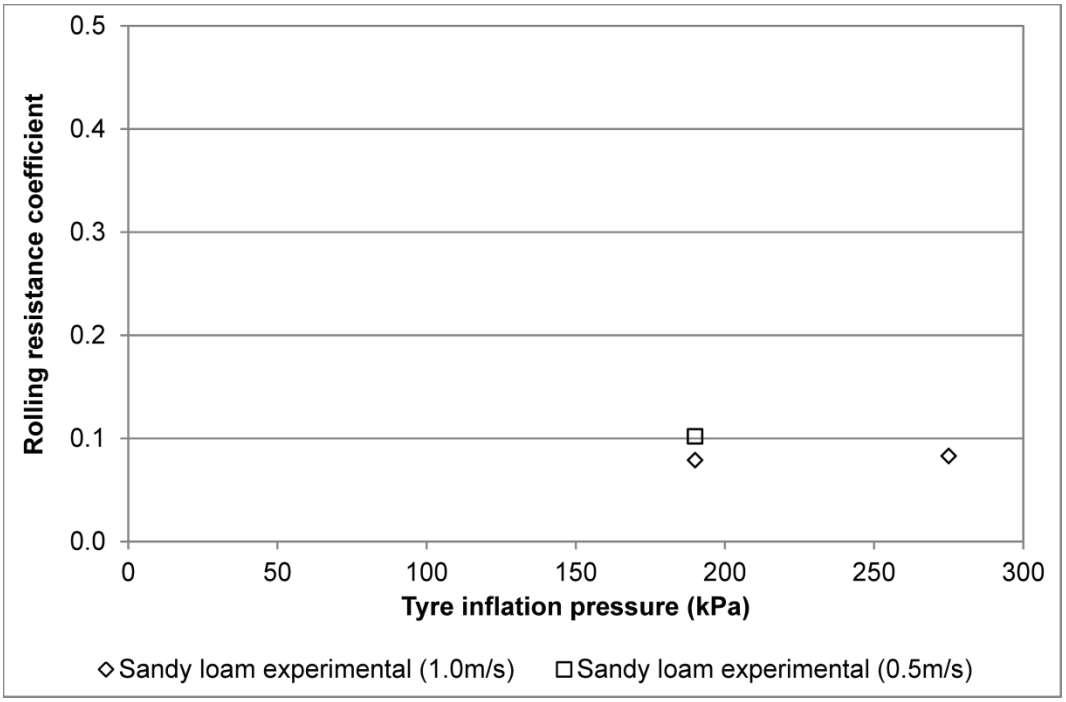

Figure 7.7: Experimental rolling resistance results for a towed Goodyear 7.50 R 16 tyre operating on dry sand

7.1.2 Model construction

To generate rolling resistance predictions for comparison with the experimental data presented above, a series of models were built to represent towed wheels operating within a virtual soil bin. Based on the results obtained for the plate sinkage and rigid wheel interaction models, an Eulerian approach was used to represent the soil within the soil bin, with fluid structure interaction used to define contact between the tyre and soil.

The soil bin was defined as a rectangular box, 1500mm wide and 500mm deep, with a 250mm high void region above the initial surface of the soil, into which the soil could flow (Figure 7.8). The length of the soil bin was varied depending on the translational speed of the wheel to minimise model runtime for low speed simulations. A prescribed vertical load was applied to the centre of the wheel, with inflation pressure specified as a distributed pressure loading on the inner surface of the tyre carcass. Finally, a prescribed translational velocity condition was used to tow the tyre across the surface of the soil.

Two different methods were available to measure and record interaction forces during the course of a simulation: by measuring the forces at the contact interface between the tyre and soil, or by recording the force required to generate the prescribed boundary condition used to move the wheel along the length of the soil bin. An example of the results obtained using these two methods is provided in Figure 7.9, which illustrates the differences in the longitudinal forces recorded. For the purposes of the current modelling study, the prescribed boundary condition force was used to measure the predicted level of rolling resistance, as this more closely replicated the experimental test procedure.

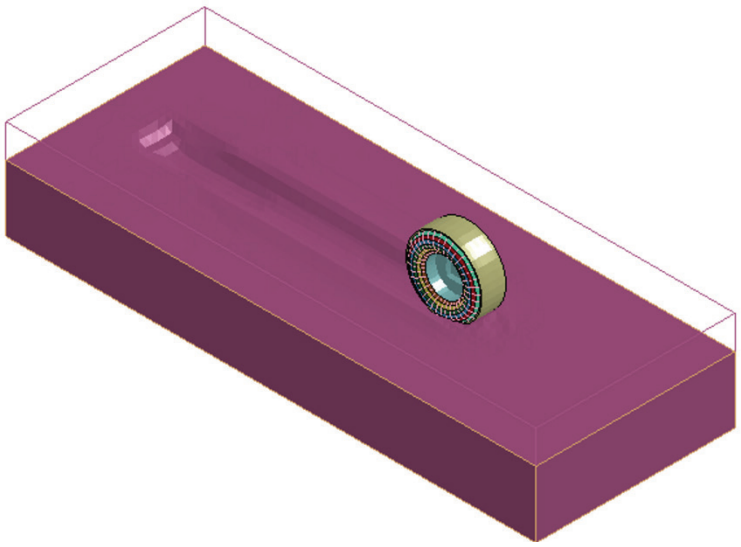

Figure 7.8: Overview of tyre / soil interaction model used to predict rolling resistance for a towed wheel operating on deformable terrain

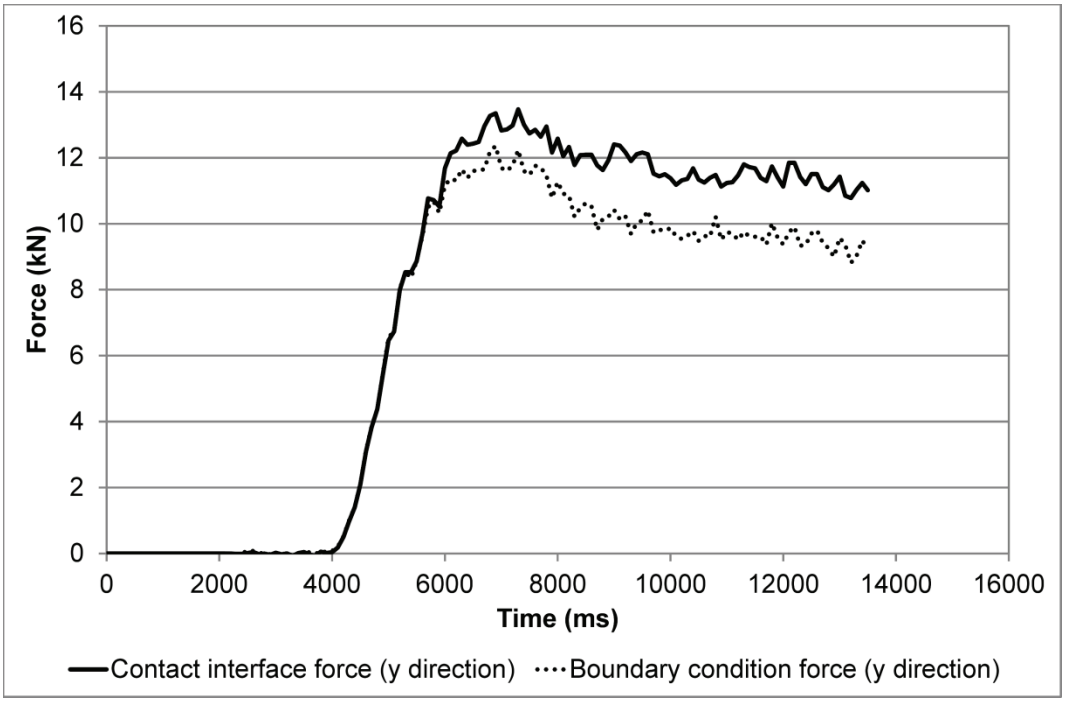

Figure 7.9: Comparison of the longitudinal forces recorded at the tyre / soil contact interface and at the wheel rim during rolling resistance simulation

7.1.3 Model accuracy assessment

Figure 7.10 provides a visual comparison of the experimental and numerical modelling results obtained for a towed Michelin XZL 445 / 65 R 22.5 tyre operating on dry sand under a constant wheel load of 29.43kN. The FE rolling resistance models were found to provide a good level of agreement with the experimental results, including the substantial reduction in rolling resistance occurring at very low inflation pressure. The increase in rolling resistance with an increase in translational speed, observed during the experimental study for an inflation pressure of 400kPa, was not replicated by the model, although this is largely to be expected due to the absence of rate effects within the dry sand material model.

The effect of translational speed and rate dependency within the soil material model was investigated in more detail for the 445 / 65 R 22.5 tyre operating on the moisture containing sandy loam (Figure 7.11). Modelling runs were completed at both high (1.0m/s) and low (0.3m/s) translational speed for the full

range of inflation pressures (100 – 800kPa). As shown, a good level of agreement with experimental results was again obtained, with the FE modelling results using a rate dependent soil model mostly bounding the experimentally obtained data. One exception to this was for an inflation pressure of 400kPa, where a reduction in translational speed produced a corresponding reduction in rolling resistance; this was to be expected, however, given that the soil model was set up to strengthen as the rate of loading is increased.

To assess the effect of rate dependency in the sandy loam soil model, additional modelling runs were completed with rate dependency in the pseudo tensor material model switched off (LCP set to zero). The results obtained demonstrate that, as suggested in Chapter 4, soil models based on static or quasi-static test data lead to significant over-predictions of rolling resistance.

In comparison to the results obtained using the 445 / 65 R 22.5 tyre model, relatively poor accuracy was achieved using the 7.50 R 16 tyre model with the predicted rolling resistance values being, on average, half of the experimentally measured value. A quantitative comparison between predicted and experimentally measured rolling resistance values is provided in Table 7.1.

Table 7.1: Quantitative comparison of modelling and experimental rolling resistance results

Tyre	**Soil**	**Inflation pressure**	**Trans. speed**	**Wheel load**	**Rolling resistance**	
					Exp.	**Model.**
445 / 65 R 22.5	Dry sand	800 kPa	1.0 m/s	29.43 kN	11.99 kN	12.15 kN
		400 kPa	1.0 m/s		11.50 kN	9.82 kN
			0.5m/s		11.66 kN	9.42 kN
			0.2 m/s		9.53 kN	9.60 kN
		300 kPa			7.16 kN	8.46 kN
		100 kPa			2.55 kN	2.88 kN
	Sandy loam	800 kPa	1.0 m/s		2.26 kN	1.99 kN
		400 kPa	1.0 m/s		1.80 kN	2.06 kN
			0.5m/s		1.76 kN	2.34 kN
		800 kPa	0.3 m/s		3.57 kN	3.74 kN
		400 kPa			1.10 kN	3.14 kN
		100 kPa			1.22 kN	2.00 kN
7.50 R 16	Dry sand	275 kPa	1.0 m/s	7.36 kN	3.60 kN	2.01 kN
		190 kPa			3.26 kN	1.38 kN
			0.5 m/s		3.33 kN	2.81 kN
		130 kPa	0.4 m/s	5.45 kN	1.54 kN	1.01 kN
		50 kPa	0.4 m/s	5.43 kN	0.91 kN	0.49 kN
	Sandy loam	275 kPa	1.0 m/s	7.36 kN	0.61 kN	0.28 kN
		190 kPa			0.58 kN	0.26 kN
			0.5 m/s		0.75 kN	0.27 kN

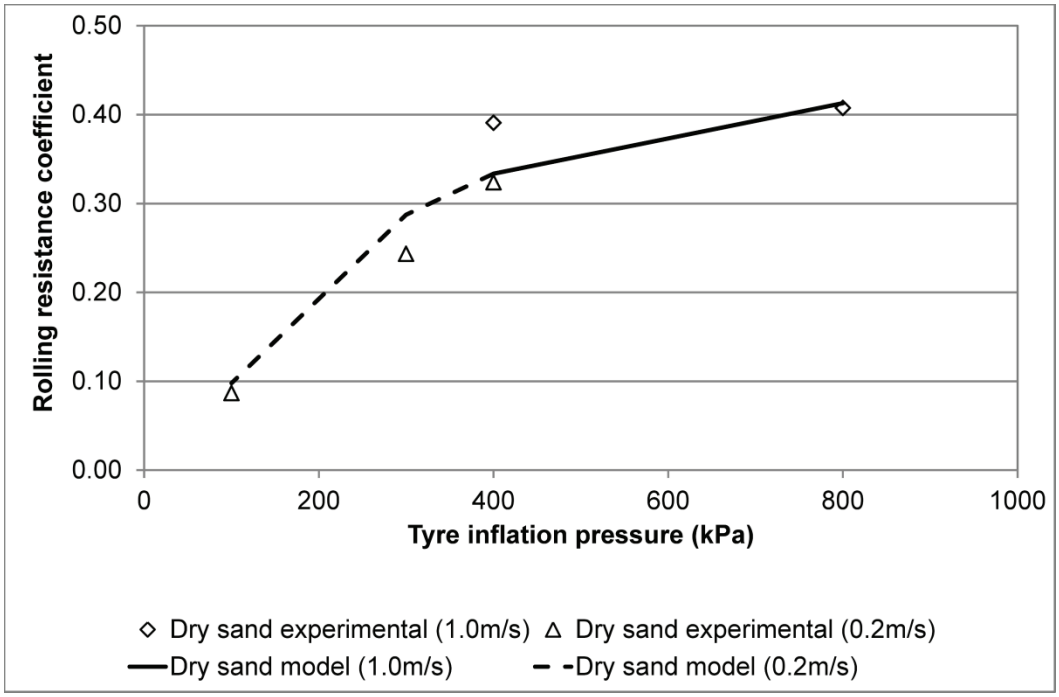

Figure 7.10: Comparison of experimental and FE modelling results obtained for 445 / 65 R 22.5 tyre operating on dry sand at inflation pressures between 100 and 800kPa

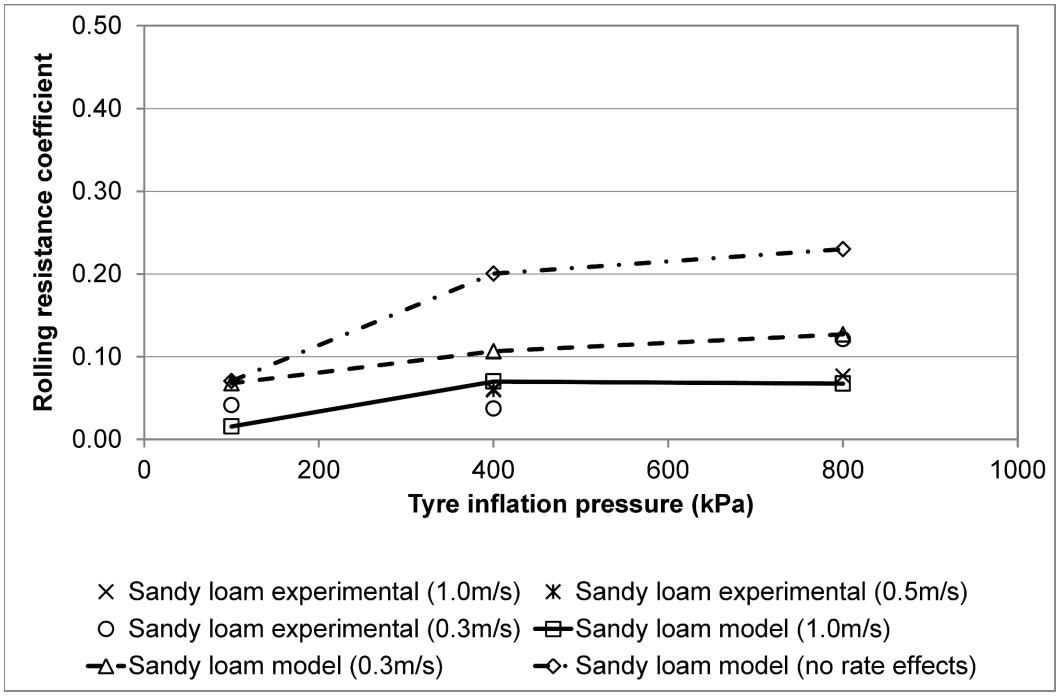

Figure 7.11: Comparison of experimental and FE modelling results obtained for 445 / 65 R 22.5 tyre operating on sandy loam at inflation pressures between 100 and 800kPa

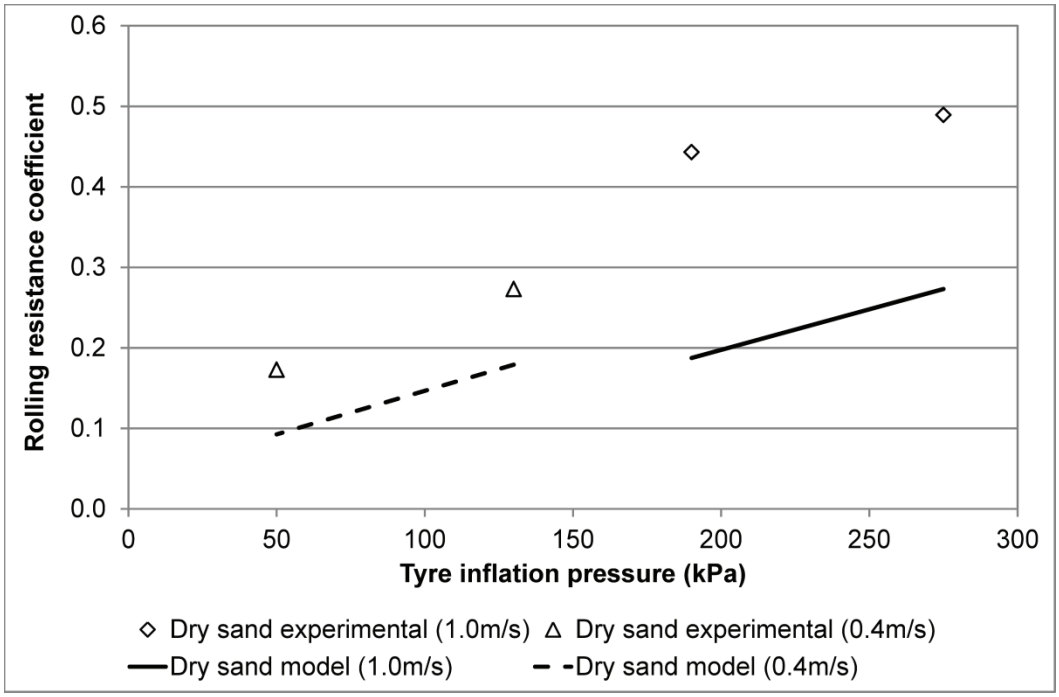

Figure 7.12: Comparison of experimental and FE modelling results obtained for 7.50 R 16 tyre operating on dry sand at inflation pressures between 50 and 275kPa

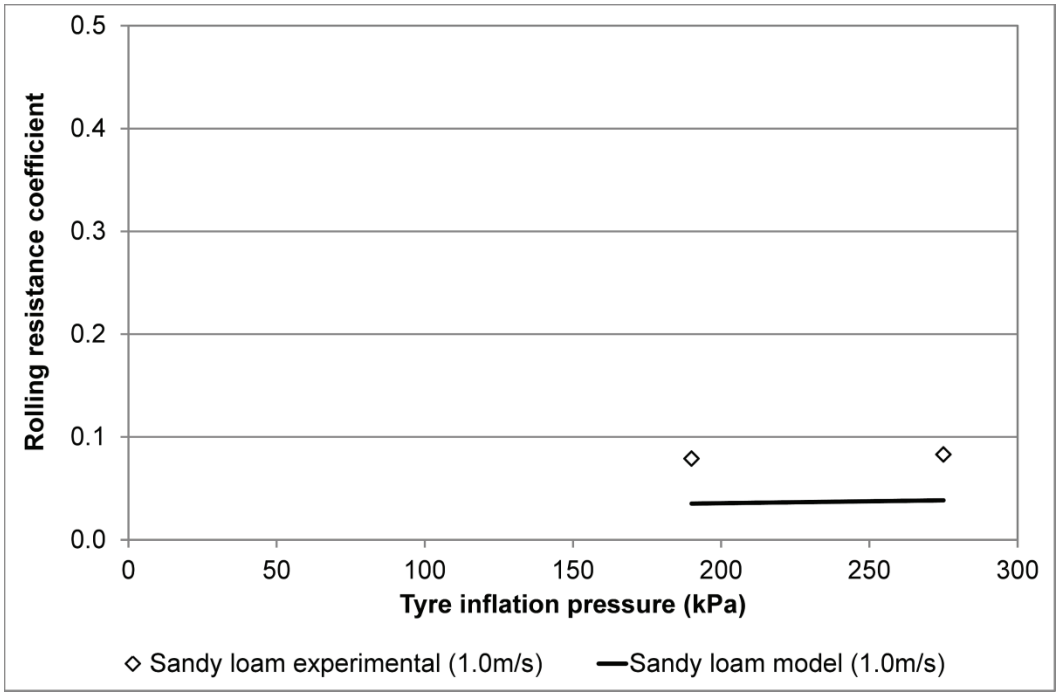

Figure 7.13: Comparison of experimental and FE modelling results obtained for 7.50 R 16 tyre operating on sandy loam at inflation pressures between 190 and 275kPa

7.2 Drawbar pull prediction

Rolling resistance provides a measure of the effort required to tow a free-rolling wheel across a given terrain. To measure the ability of wheeled vehicles to accelerate, climb gradients and pull loads, positive slip drawbar pull is also of interest, as it measures the net tractive force that can be generated by driven wheels. The ability of a vehicle to decelerate, meanwhile, can be quantified in terms of the negative slip drawbar pull. This of particular interest in the case of aircraft landing on unpaved airfields, as the level of negative slip drawbar pull that can be generated will influence the length of runway required for safe operation. As the current study has only addressed wheels travelling in a straight line, with no applied steering forces, the term 'slip' throughout relates to the longitudinal slip ratio (LSR), and should not be confused with lateral slip.

7.2.1 Experimental testing

As for the rolling resistance work discussed above, experimental testing was completed using a combination of single wheel, single axle and full vehicle testing. For the smaller 7.50 R 16 tyre, it was again possible to mount the tyre on Cranfield University's single wheel tester (SWT), which provided control over individual test parameters such as wheel load, translational speed and rotational speed. The single wheel tester was used for negative LSR drawbar pull testing, with full vehicle testing used to obtain positive LSR drawbar pull curves. For the larger 445 / 65 R 22.5 tyre, it was not possible to use the SWT for any of the drawbar pull tests, and the experimental work instead relied on single axle testing for negative LSR conditions and full vehicle testing for positive LSR.

In the negative LSR tests, the single wheel / axle was initially towed across the soil under study. Braking was then gradually applied to reduce the rotational speed of the wheels while the translational speed of the wheel was held constant. The force required to maintain the translational speed of the wheel across the surface was recorded as a measure of the negative LSR drawbar pull.

In the full vehicle tests for positive LSR, the vehicles under test were driven into the soil bin at a set translational speed. Once the vehicle had entered the soil bin, a constant throttle setting was maintained with the intention of achieving a constant rotational speed for the wheels, while a 'smart' winch applied a steadily increasing restraining force to the rear of the vehicle to gradually reduce the translational speed from the initial value to zero. In this manner, a range of positive LSR conditions were obtained, with the force required to decelerate the vehicle recorded as a measure of the positive LSR drawbar pull.

The results of the drawbar pull tests are generally presented in terms of the drawbar pull generated as a function of the wheel's LSR. For both tyres, the rotational speed of the wheel was monitored using wheel encoders which measured the rotational position of the wheel as a function of time. This, combined with data on the translational speed of the vehicle over the same period, allowed the force required to either pull (negative LSR) or restrain (positive LSR) the vehicle during the test to be presented as a function of slip. Given that the wheel can operate in either a driven or braked condition, drawbar pull is often presented in the form of a quad plot illustrating the transition between driven, self-propelled and braked conditions. Where the longitudinal slip ratio is zero, with the wheel's peripheral velocity equal to the translational velocity of the vehicle, the wheel is in a self-propelled condition with no applied force required to maintain the vehicle's current speed.

The results of the experimental drawbar pull tests are summarised in the following figures, which provide mean curves from at least three experimental replicates of each treatment.

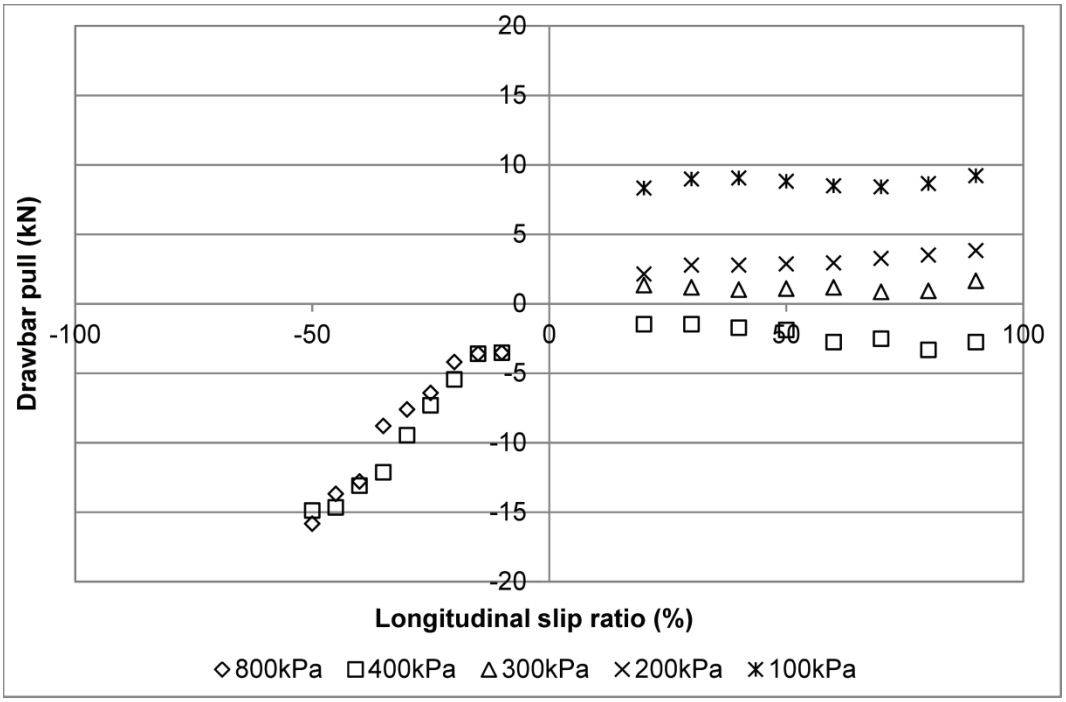

Figure 7.14: Summary plot showing effect of inflation pressure on drawbar pull for 445 / 65 R 22.5 tyres operating on dry sand with wheel load of 29.43kN

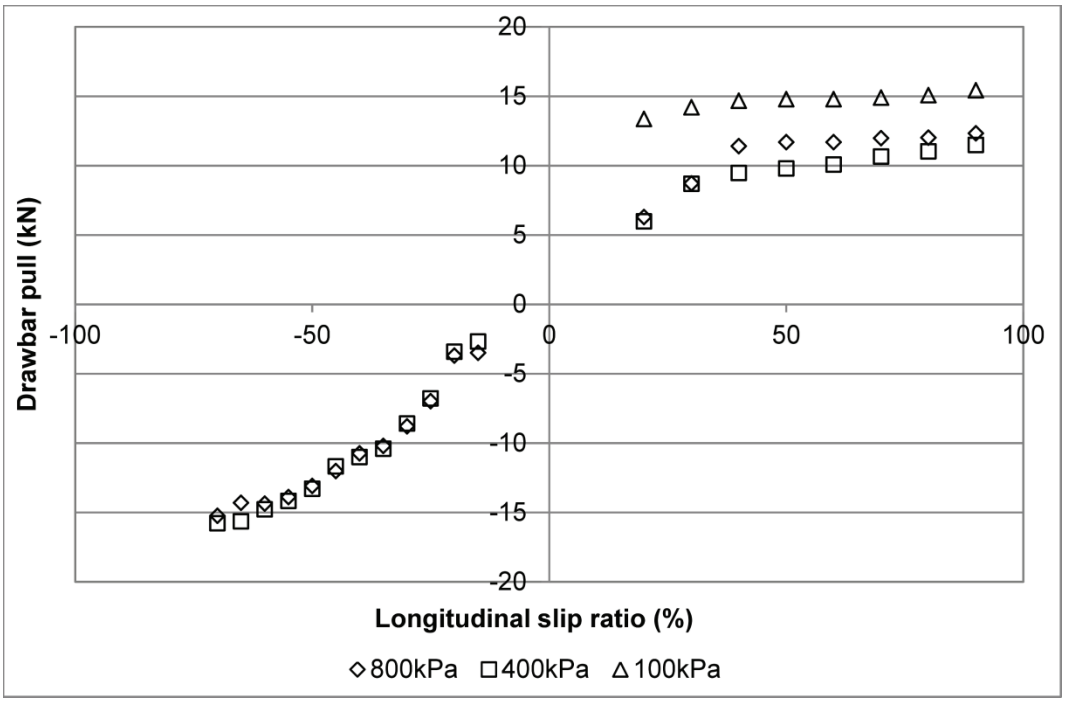

Figure 7.15: Summary plot showing effect of inflation pressure on drawbar pull for 445 / 65 R 22.5 tyres operating on sandy loam with wheel load of 29.43kN

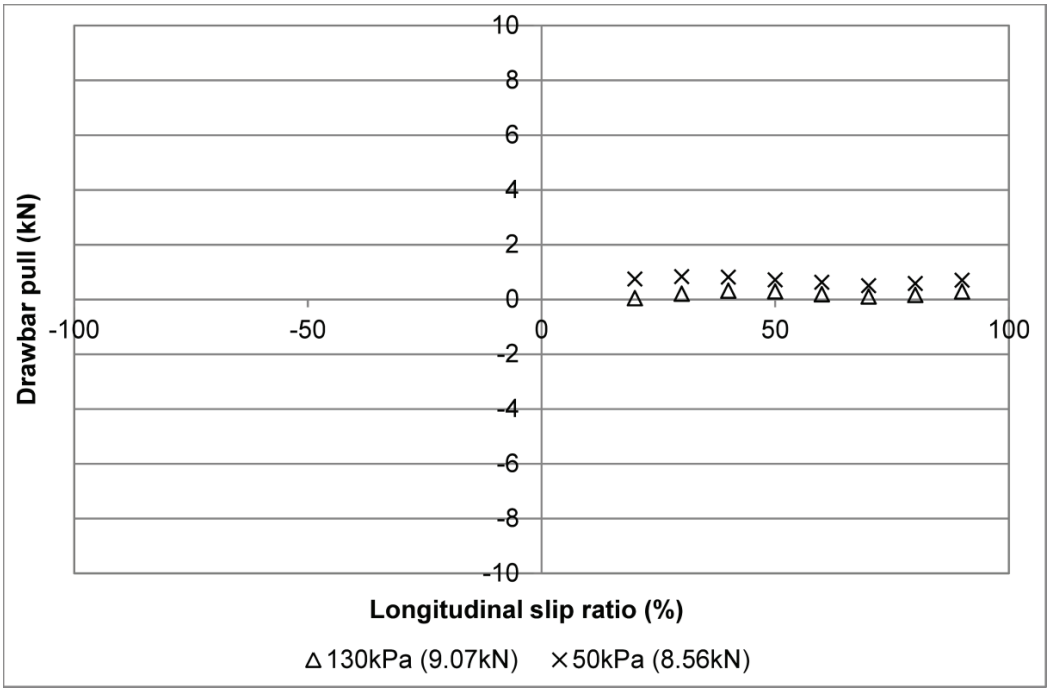

Figure 7.16: Summary plot showing effect of tyre inflation pressure on drawbar pull for 7.50 R 16 tyres operating on dry sand (note: wheel loads shown in brackets)

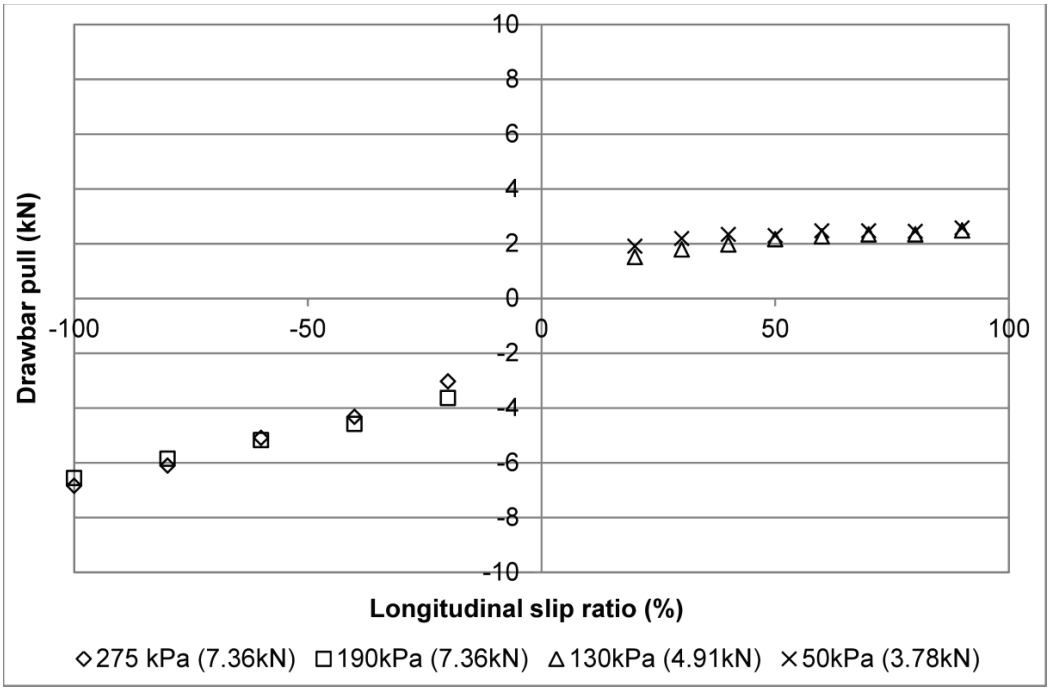

Figure 7.17: Summary plot showing effect of inflation pressure on drawbar pull for 7.50 R 16 tyres operating on sandy loam (note: wheel loads shown in brackets)

The experimental results indicate that, for both tyres operating on the dry sand, a large reduction in tyre inflation pressure is required to achieve any practical level of mobility. For the Michelin XZL 445 / 65 R 22.5 tyre operating at 400kPa (77% of the minimum road going value recommended by the manufacturer), a negative drawbar pull is obtained, indicating that additional work is required to pull the wheels across the soil bin. Further reducing the inflation pressure to 300kPa (58% of the recommended on-road pressure) results in the vehicle becoming mobile, but with a very low drawbar pull achieved compared to that observed on the sandy loam soil. The improvement in mobility with a reduction in tyre inflation pressure continues down to a pressure of 100kPa (19% of on-road value), where a substantial increase in drawbar pull is obtained, compared to that observed at 200kPa (38% of on-road pressure).

Similar behaviour is observed for the smaller Goodyear G90 7.50 R 16 tyre, with an inflation pressure of 130kPa (47% of the manufacturer's recommended on-road pressure) representing the threshold at which the vehicle just becomes mobile on dry sand. As the inflation pressure is further reduced to 50kPa (18% of the recommended on road pressure), the achievable drawbar pull increases, but remains low with a mean value of 0.69kN across the range of slip ratios measured.

For vehicles operating on sandy loam, the level of drawbar pull achieved for a given inflation pressure is higher than for vehicles operating on dry sand and, as a result, the influence of tyre inflation pressure is less pronounced. In the case of the 445 / 65 R 22.5 tyre, off-road mobility can be improved by reducing the tyre inflation pressure to as low as 100kPa, but the improvement in mobility is less notable than on dry sand. On the sandy loam, an increase in inflation pressure from 100 to 400kPa produces a 33% reduction in the mean drawbar pull whereas the vehicle becomes immobile on dry sand.

Comparing the performance of the two tyres, the drawbar pull achieved using the 7.50 R 16 tyre is much lower than that obtained using the 445 / 65 R 22.5, despite the larger tyre having a higher level of rolling resistance.

7.2.2 Influence of tyre tread

In the interests of efficiency, the tyre models introduced in Chapter 6 and used in the tyre / soil interaction simulations did not explicitly represent the tread pattern that was present on the physical tyres used in the experimental trials. To assess the potential impact of this simplification on the accuracy of the model, additional experimental runs were completed using specially modified tyres where the tread band had been removed. Pull slip profiles for the treaded and skimmed tyres were compared to quantify the contribution of the tyre tread to off-road mobility on both the dry sand and sandy loam soils. The results of the tyre tread comparison tests are presented graphically in Figures 7.18 to 7.21.

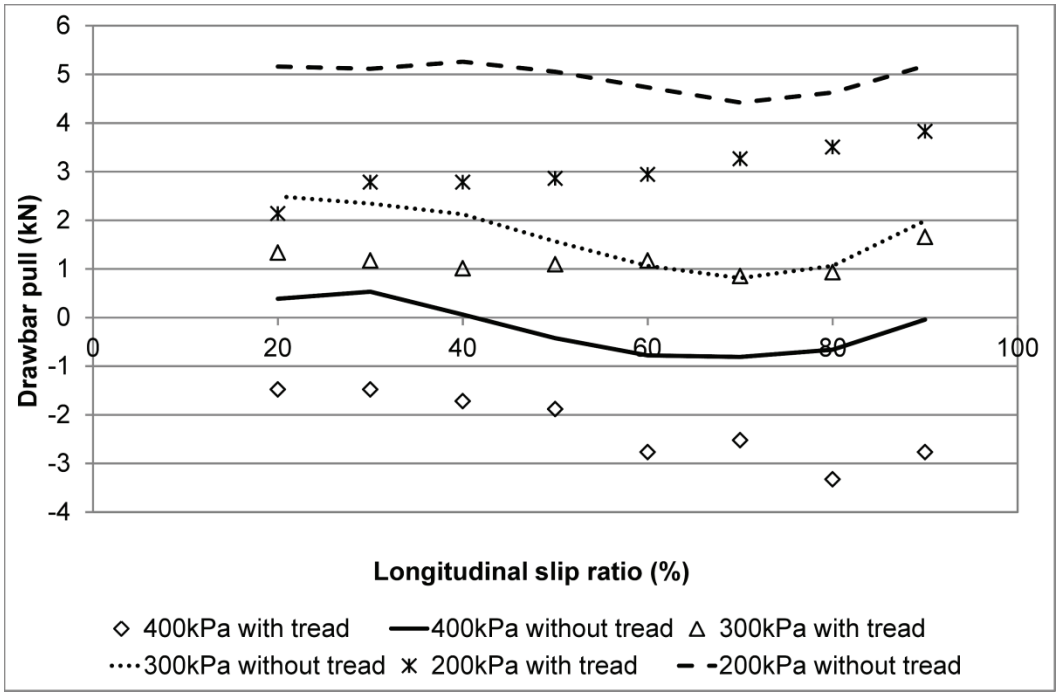

Figure 7.18: Effect of tyre tread pattern on drawbar pull for Michelin XZL 445 / 65 R 22.5 tyres operating at inflation pressures of between 200 and 400kPa on dry sand

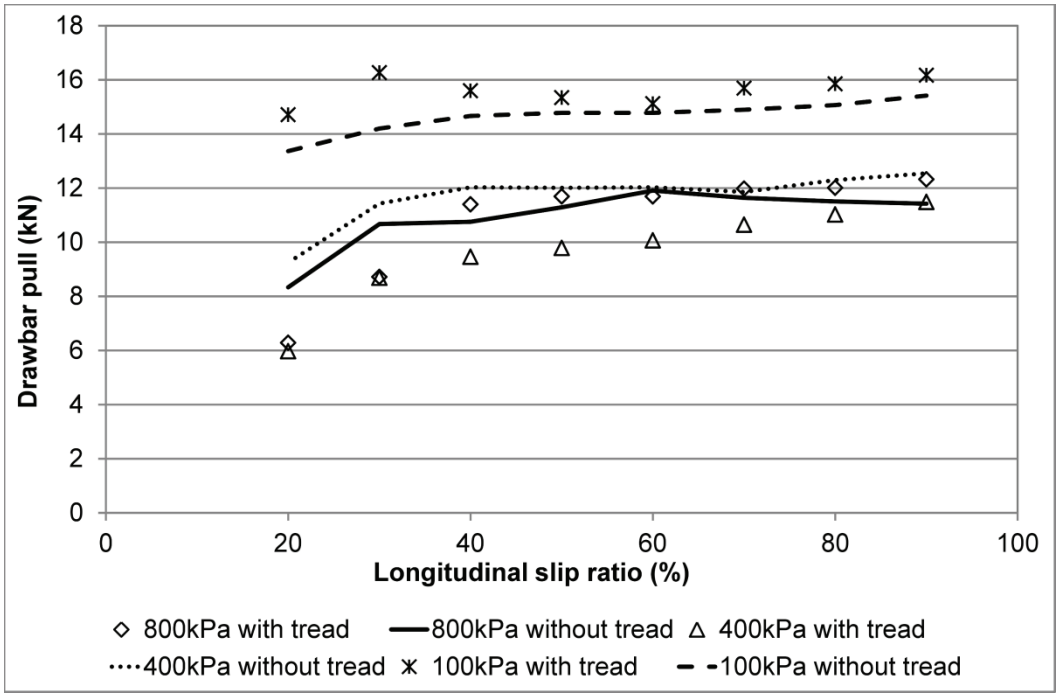

Figure 7.19: Effect of tyre tread pattern on drawbar pull for Michelin XZL 445 / 65 R 22.5 tyres operating at inflation pressures of between 100 and 800kPa on sandy loam

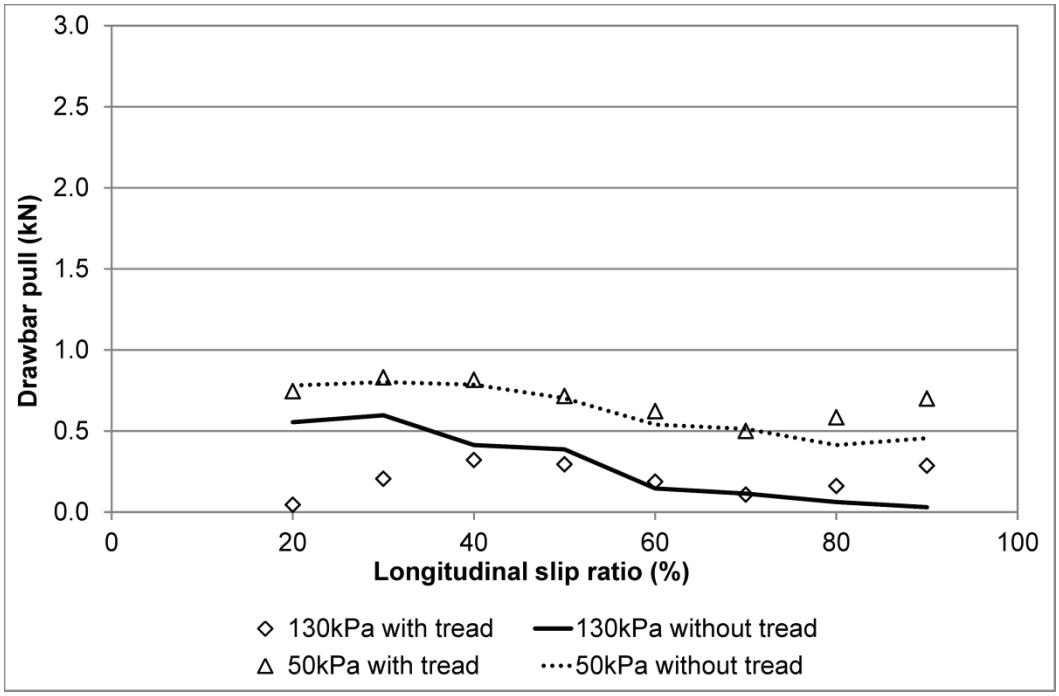

Figure 7.20: Effect of tyre tread pattern on drawbar pull for Goodyear G90 7.50 R 16 tyres operating at inflation pressures of between 130 and 50kPa on dry sand

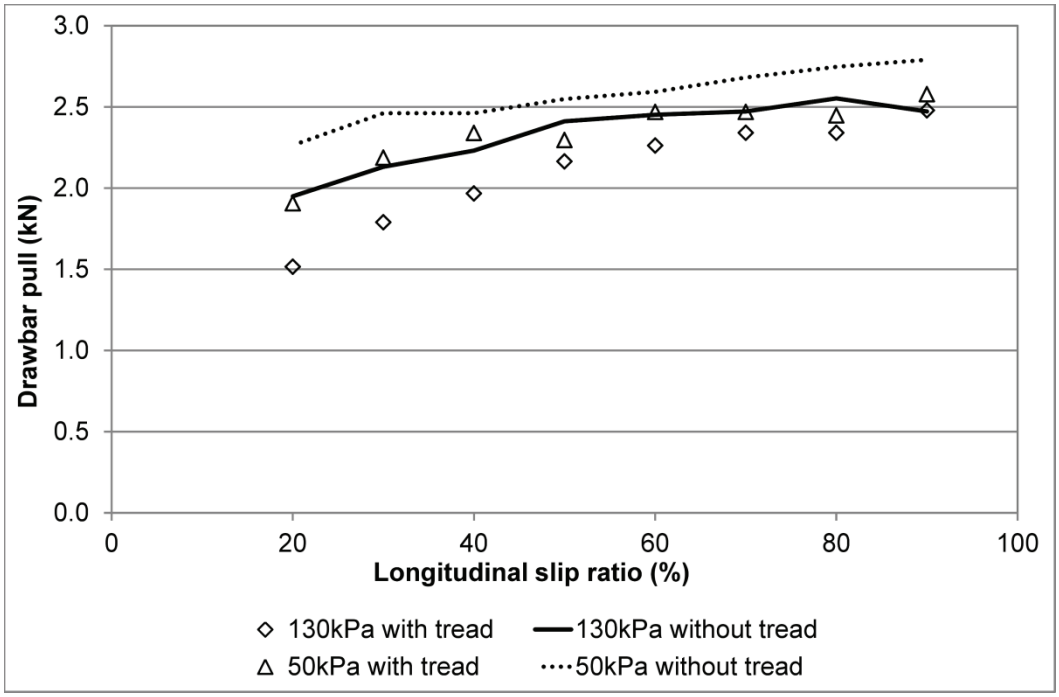

Figure 7.21: Effect of tyre tread pattern on drawbar pull for Goodyear G90 7.50 R 16 tyres operating at inflation pressures of between 130 and 50kPa on sandy loam

The results of the experimental trials to compare the performance of treaded and skimmed tyres are quantitatively assessed in Table 7.2. The effect of the tyre tread pattern on drawbar pull was quantified using an approach based on the mean absolute percentage error (MAPE), where the drawbar pull values achieved using skimmed tyres at specific levels of slip were compared against the baseline performance of the standard treaded tyres (Equation 7.1). Individual data points were compared against the arithmetic mean of the drawbar pull values obtained for the range of LSRs, rather than individual baseline values. This approach permitted the effect of tyre tread to be compared across the full range of LSRs, while smoothing out any large variations in performance due to the low drawbar pull values that were obtained using the standard treaded tyres.

The experimental results obtained show that, for the majority of the conditions studied, the absence of a tyre tread pattern results in an increase in the level drawbar pull achieved. The effect is more pronounced on the dry sand soil than

for the sandy loam. For both soils, the improvement in performance is greatest when operating at low levels of slip, with the percentage increase in drawbar pull reducing as the longitudinal slip ratio is increased.

In general, the presence of a tyre tread pattern reduced the level of achievable drawbar pull. This observation can largely be explained by the relatively controlled and uniform soil conditions used during the experimental tests, with no lubricating layers present on the surface of the soil bin. Where the condition of the soil's surface is the limiting factor in a vehicle's mobility, the presence of a tread pattern allows the tyre to penetrate the lubricating surface layer and improve traction by interacting with the main body of the soil. For very soft terrains, however, penetration of the soil's surface can reduce mobility by increasing the wheel's sinkage and, in this case, floatation of the tyre on the soil's surface is key to maintaining mobility. To this end, smooth floatation tyres are frequently used to improve mobility on dry desert sands.

$$MAPE = \frac{1}{n}\sum_{t=1}^{n}\frac{P_{t,skimmed} - P_{t,treaded}}{A} \qquad \textit{Equation 7.1}$$

$$A = \frac{1}{n}\sum_{t=1}^{n} P_{t,treaded}$$

As shown by the experimental results, the presence of tyre tread patterns can substantially influence off-road mobility for wheeled vehicles. A more detailed representation of the tyre's tread pattern would therefore be beneficial in improving the accuracy of FE mobility prediction tools. This improvement in accuracy would significantly increase the runtime of mobility prediction models using an explicit time integration scheme, however, as not only would a more detailed tread model entail a larger number of elements, but these smaller elements would most likely control the timestep of the simulation as a whole. An Eulerian representation of the soil, as used in the current study, could provide a novel solution to this problem, as inflow and outflow boundaries can

be used to minimise the volume of soil represented within a moving reference frame. This approach, while not addressing the reduction in simulation timestep, would substantially reduce the number of elements used to represent the soil within the simulation and would therefore minimise the number of calculations required per cycle. The potential benefit of a moving reference frame approach would also increase as a function of the vehicle's translational speed, as the required length of the simulated soil bin is directly related to translational speed.

Table 7.2: Quantitative assessment of the effect of tyre tread pattern on drawbar pull

Soil	Dry sand				Sandy loam				
Tyre	7.50 R 16		445 / 65 R 22.5		7.50 R 16		445 / 65 R 22.5		
Pressure	50	130	200	300	50	130	100	400	800
Slip	**Percentage change in mobility using skimmed tyres**								
20	+5	+254	+100	+100	+15	+21	+9	+34	+19
30	-4	+195	+77	+102	+12	+16	+13	+28	+18
40	-4	+46	+82	+96	+5	+13	+6	+27	-6
50	-2	+46	+73	+41	+11	+12	+4	+23	-4
60	-12	-21	+59	-10	+5	+9	+2	+20	+2
70	-2	+4	+38	-3	+9	+6	+5	+12	-3
80	-25	-49	+37	+11	+13	+10	+5	+13	-5
90	-35	-127	+45	+29	+9	0	+5	+11	-8
Mean	-12	+44	+64	+46	+10	+11	+6	+21	+2

7.2.3 Model construction

To predict drawbar pull, the rolling resistance model was modified to include a prescribed rotational velocity boundary condition, in addition to the prescribed translational velocity representing the forward speed of the vehicle. Independent control over the translational and rotational speed of the wheel allowed a range of slip conditions to be achieved for both positive and negative longitudinal slip ratios.

Based on the conditions used in the experimental trials, positive and negative LSRs were achieved in slightly different ways. For a negative LSR, the wheel was initially accelerated to a rotational speed that ensured the peripheral speed of the tyre's tread matched the translational speed of the wheel, resulting in an initially self-propelled condition. The rotational speed of the wheel was then gradually reduced while the translational speed was held constant, representing a braked wheel and producing a negative LSR. As for the rolling resistance models, the force required to produce the prescribed translational velocity boundary condition was monitored throughout the simulation to obtain a measure of the force required to drag the braked wheel across the soil. By varying the rotational speed of the wheel, a wide range of slip conditions could be achieved within a single simulation.

For positive slip, a slightly different approach was taken: from the initial self-propelled condition, the *translational* speed of the wheel was reduced while the rotational speed was held constant, resulting in a peripheral velocity at the contact patch that was higher than the translational speed of the wheel and producing a positive slip condition. The alternative to this approach would be to increase the rotational speed of the wheel from the self-propelled condition while holding the translational speed constant. While this approach is certainly possible within the modelling environment, it presents two main difficulties. Maintaining a constant translational speed throughout the drawbar pull simulation results in a large distance being travelled over the timeframe of the test, and this requires a larger soil domain with an associated increase in computational time. Secondly, in order to achieve high values of slip, the

rotational speed of the wheel must be increased significantly, which increases the likelihood of numerical errors within the model due to mesh distortion. This could be overcome by reducing the simulation timestep as the rotational speed of the wheel is increased, but again at the expense of an increase in model runtime. The latter difficulty is a purely modelling related issue, but the former affects both the modelling and physical test environments, since maintaining a constant translational speed throughout the duration of the test requires a greater length of prepared soil.

7.2.4 Model accuracy assessment

The accuracy of the modelling predictions for negative and positive slip conditions was initially qualitatively assessed using a series of quad plots for both the 445 65 R 22.5 and 7.50 R 16 tyres operating at a range of inflation pressures (Figures 7.22 to 7.25). To quantify the accuracy of the modelling predictions across the range of experimentally measured slip ratios, model output values for specific levels of slip were compared against the corresponding experimental results to obtain the error for each condition. A quantitative comparison of model accuracy is presented in Appendix E.

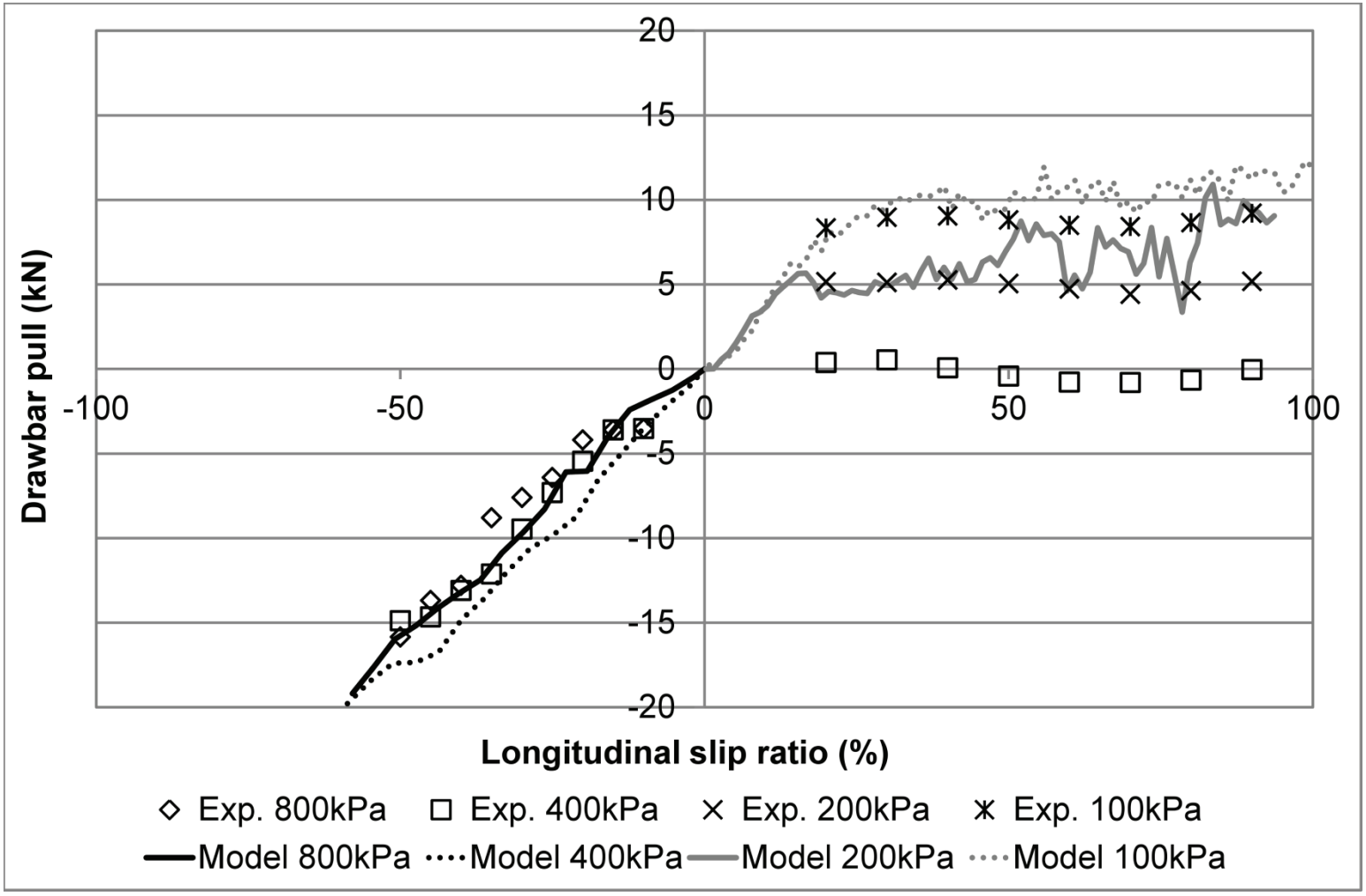

Figure 7.22: Comparison of experimental and FE modelling results for driven / braked 445 / 65 R 22.5 tyre operating on dry sand

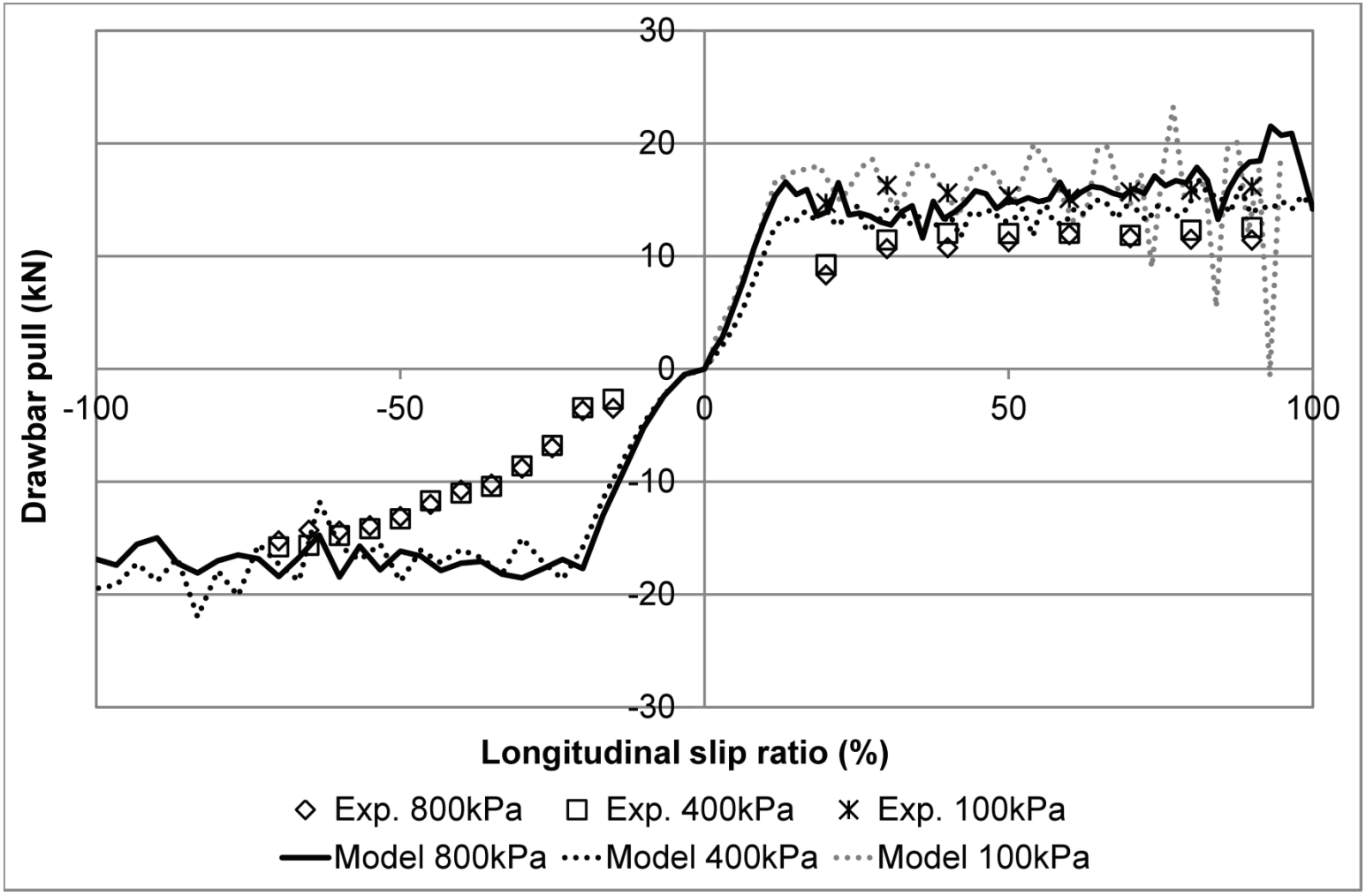

Figure 7.23: Comparison of experimental and FE modelling results for driven / braked 445 / 65 R 22.5 tyre operating on sandy loam

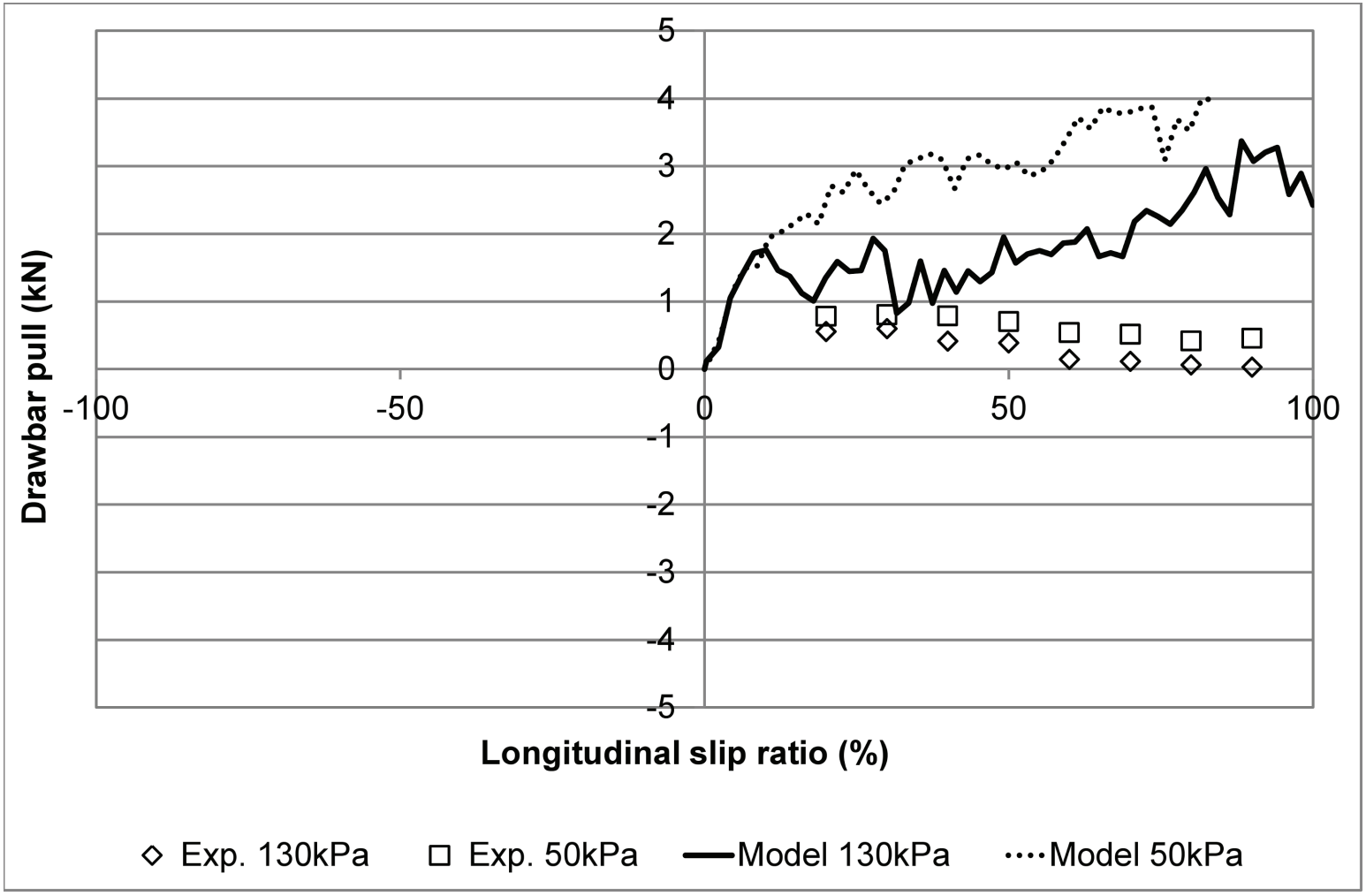

Figure 7.24: Comparison of experimental and FE modelling results for driven / braked 7.50 R 16 tyre operating on dry sand

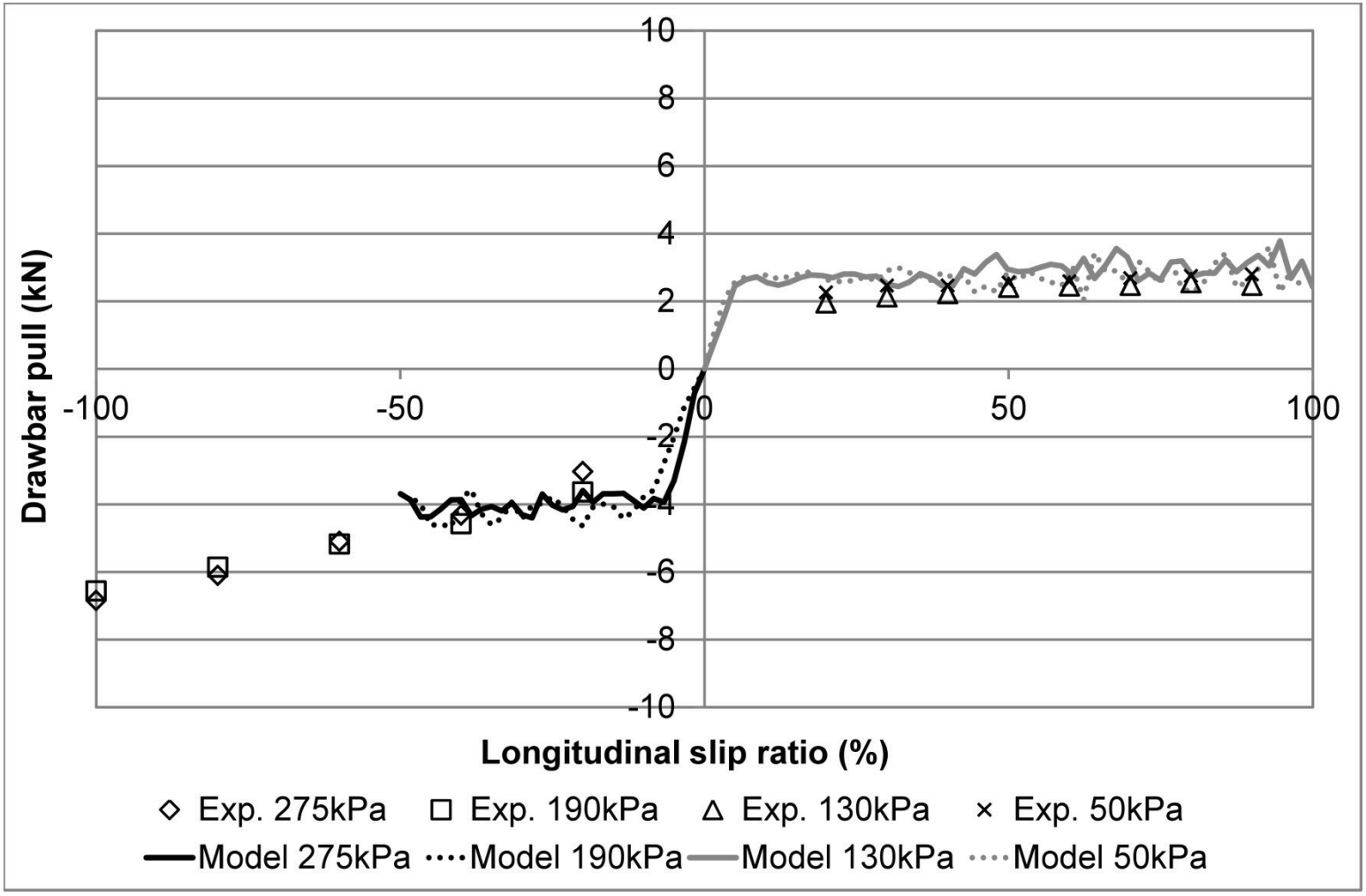

Figure 7.25: Comparison of experimental and FE modelling results for driven / braked 7.50 R 16 tyre operating on sandy loam

7.3 Summary

This chapter has demonstrated the use of an FE mobility prediction tool to obtain predictions of rolling resistance and drawbar pull for pneumatic tyres operating on dry sand and sandy loam soils. The combined experimental and numerical modelling work has addressed the influence of variables including soil type, tyre geometry, inflation pressure and vehicle translational speed.

The experimental results obtained for both towed and driven wheels have highlighted the potential benefits of operating at substantially reduced inflation pressures on soils with low levels of cohesion, such as the dry sand included in the current study. Since pneumatic tyres rely on inflation pressure to seal the tyre beads against the wheel rim and transmit torque from the wheel to the tyre soil interface, this finding indicates the importance of bead locks in assuring terrain accessibility. Given that operation at low inflation pressures can increase the rate of tyre wear, however, bead locks should generally be used in combination with a central tyre inflation system (CTIS) to strike a balance between mobility and durability. For the Michelin XZL 445 / 65 R 22.5 tyre operating on a firmer sandy loam soil, drawbar pull can again be increased by operating at very low inflation pressures, although the benefit over operation at standard inflation pressures is much less pronounced.

In Chapter 4, it was reported that the apparent strength of the sandy loam soil increased as a function of the rate of load application, with an analysis completed to assess the implications of this rate sensitivity on rolling resistance suggesting a reduction in rolling resistance as the rate of loading is increased. From the experimental rolling resistance results reported above, however, the effect of vehicle translational speed on rolling resistance is less clear than initially suggested: for 445 / 65 R 22.5 tyres operating at a constant inflation pressure, rolling resistance was observed to both increase and decrease with translational speed, depending on the inflation pressure considered. While previous studies by Pope (1971), Grahn (1991) and Shmulevich, Mussel and Wolf (1998) support the findings of Chapter 4, further study is required to confirm the source of the variability observed during the full scale trials.

An experimental study to assess the effect of tyre tread pattern on the level of achievable drawbar pull has shown that, under the test conditions studied, the presence of a tyre tread pattern reduces off-road mobility. Even for relatively well-controlled experimental tests, therefore, the absence of tyre tread pattern from the FE tyre model is a potential source of error and, for the soils and tyres studied here, could potentially lead to an over-prediction of off-road performance. The influence of tyre tread pattern means that it may be necessary to increase the level of detail within the FE tyre model, which would lead to an increase in simulation runtime given the explicit time integration method used.

For towed, driven and braked pneumatic tyres, the accuracy of an FE mobility prediction method has been assessed by comparison between numerical and experimental results. In the case of a towed Michelin XZL 445 / 65 R 22.5 tyre, rolling resistance values generated with the FE model show a good level of agreement with the experimental results, particularly on dry sand where a mean absolute percentage error of 11% was achieved. For sandy loam, a quantitative analysis is complicated by the rate dependency of the soil, although the high and low speed modelling predictions successfully bounded the majority of the experimental data points. As suggested by the dynamic plate sinkage results reported in Chapter 4, the failure to include rate effects within the soil material model leads to the over-prediction of rolling resistance, particularly at higher inflation pressures due to the accompanying increase in sinkage.

For the smaller Goodyear G90 7.50 R 16 tyre, the agreement between predicted and measured rolling resistance values was relatively poor, with the predicted value being approximately half that measured during experimental testing. This was found to be the case for both the dry sand and sandy loam soils, suggesting that the observed error was due to the tyre model, despite good agreement being achieved with rigid surface load-deflection and contact patch length data in Chapter 6.

A series of driven / braked wheel simulations have been completed to demonstrate the ability of the model to predict realistic levels of drawbar pull,

accounting for the influence of tyre geometry, soil type and inflation pressure. For the 7.50 R 16 tyre, the level of drawbar pull achievable on dry sand is significantly over-predicted by the model, possibly due to the under-prediction of rolling resistance for the 7.50 R 16 tyre. For the larger 445 / 65 R 22.5 tyre, the agreement between experimental and numerical results is better, with the requirement for very low inflation pressures replicated by the model, although the fidelity of the model around the threshold of immobilisation requires further investigation. In the full vehicle experimental trials, inertial effects permitted the vehicle to travel across the sand at 400kPa, even with a slightly negative drawbar pull, whereas the modelled tyre experienced unstable sinkage at this inflation pressure. On the sandy loam, the 445 / 65 R 22.5 tyre model displayed a tendency to over-predict drawbar pull at low values of slip, with better agreement was achieved as the level of slip increased towards the maximum level of drawbar pull.

The potential for variability in experimental results, even under relatively well controlled conditions, raises an interesting question regarding the validation of VPG mobility analysis tools. The aim of VPG mobility analysis is to provide a means of comparing and / or optimising vehicle designs while operating on a clearly-defined set of generic soils. In a VPG environment, therefore, a given vehicle operating on a given soil should produce the same results, regardless of how many times the model is run, whereas experimental trials will display some degree of variability, both between individual runs and between data sets. In comparing VPG results against experimental trials, a large experimental data set is required in order to fully quantify the expected range of results and to confirm whether or not the generalised model is representative of that range.

The experimental data set available for validation of the tyre / soil interaction models under the current study was limited, with no clearly defined baseline tests that could be used to benchmark different sets of trials against each other. As an example, rolling resistance results for the 445 / 65 R 22.5 tyre operating at 400kPa were obtained at translational speeds of 0.3, 0.5 and 1.0m/s, with rolling resistance values of 9.5kN, 11.7 and 11.5 kN, respectively. The 0.5 and 1.0m/s tests were undertaken during one set of trials, however, and the 0.3m/s

tests undertaken during a second set. From the test data available, it is not possible to categorically state whether this reduction in rolling resistance at 0.3m/s is due to natural variation between data sets or due to rate effects in the soil.

Chapter 8: Discussion

This chapter provides a summary of the work completed under the current study, highlighting the main contributions of the research. The key points covered are:

- Terrain characterisation methods;
- Development of efficient tyre models;
- Use of an Eulerian solution method as an alternative to Lagrange and discrete element methods;
- Validation of VPG model predictions.

8.1 Terrain characterisation for mobility analysis

In assessing the impact of soil conditions on the off-road mobility of wheeled vehicles, the ability to describe the soil's behaviour is a fundamental requirement. The literature survey discussed in Chapter 2 identified a number of existing methods for mobility prediction, with differing approaches to terrain characterisation used.

Soil characterisation methods can be divided into laboratory-based and in-situ tests. Laboratory-based characterisation of soils primarily focusses on the soil's resistance to compaction and shear stress using reconstituted soil samples. In-situ test methods, meanwhile, tend to focus on the force required to penetrate the soil to a particular level (for example, in plate sinkage and cone index tests), although the shear strength of the soil may also be assessed using methods such as the bevameter test proposed by Bekker. One of the main advantages of in-situ methods, other than speed, is the fact that the condition of the soil is largely undisturbed prior to the start of the test, whereas the process of obtaining and reconstituting soil samples for laboratory tests may mean that the condition of the laboratory sample is not fully representative of the undisturbed soil.

Within an FE-based VPG environment, the behaviour of the soil must be described in terms of discrete soil properties, such as cohesion and friction

angle, rather than a composite property such as the plate sinkage profile. Under the current study, therefore, the relationship between laboratory-derived soil properties and the in-situ response of soils has been investigated using FE models of the plate sinkage test.

8.1.1 The influence of yield surface parameters

To assess the impact of soil material model parameters on the ability to describe in-situ soils, both laboratory and in-situ test methods were applied to a dry sand (moisture content <1%) and a sandy loam with a moisture content of 14%. Hydrostatic, triaxial and direct shear box tests were completed on the two soils to obtain pressure-volume curves and shear failure surface parameters that could be used to describe the soil's response to applied loads within the FE models. It was found that the triaxial and direct shear box test methods produced markedly different Mohr-Coulomb shear failure surface parameters for the two soils. When used to derive failure surface parameters (a_0, a_1 and a_2) for the MAT_SOIL_AND_FOAM material model in LS-DYNA, this led to different input values, depending on the test method applied.

In the case of the dry sand, the primary difference between the two shear failure surfaces existed in the low confinement pressure (<100kPa) region, while significant differences in the position of the sandy loam failure surfaces extended across the full range of confinement pressures studied (up to 600kPa). The differences in shear failure surface parameters carried across to the predicted quasi-static plate sinkage profiles for the two soils, with the direct shear box test data resulting in a much lower mean percentage error than the triaxial test results, regardless of the mesh resolution used. Using the dry sand model with an Eulerian solution method and an intermediate mesh as an example, the triaxial test data produced a mean percentage error of 76%, reducing to 33% when direct shear box data was used as an input to the model. With a finer mesh, the mean percentage error reduced from 88% (with triaxial test data) to 7% (with direct shear box test data).

At this stage, it is unclear whether the observed differences in model accuracy are a direct result of the characterisation test method used, or due to differences in the range of confinement pressures in each test. Regardless, the results obtained from the quasi-static plate sinkage simulations highlight the importance of the low confinement pressure region in describing the in-situ response of soil to applied loading, and the need to accurately measure the soil's cohesion during soil characterisation work. The work reported here has also demonstrated the usefulness of in-situ tests, such as plate sinkage profiles, as a means of confirming that that the soil material model accurately represents the behaviour of the in-situ soil prior to undertaking more complex simulations.

8.1.2 Strain rate sensitivity of soils

A series of dynamic plate sinkage tests were completed to assess the influence of loading rate on the penetration resistance of both the dry sand and sandy loam soils. The results of the experimental study indicate that, for both soils, the apparent strength of the terrain is dependent on the rate of load application. In the case of the dry sand, moving from a static plate sinkage test to a low rate dynamic test (plate penetration speed less than 50mm/s) led to a reduction in the soil's resistance to penetration. As the rate of penetration was increased to 100mm/s and above, the soil's resistance to penetration recovered, with the force required to penetrate the soil to a given depth remaining broadly constant across the range of penetration speeds considered (up to 500mm/s). While this reduction in penetration resistance under low rate dynamic test conditions was consistent across a number of replicates, the variation in apparent soil strength was found to be within the spread of a set of plate sinkage profiles obtained from a series of static tests.

For the sandy loam, with a moisture content of approximately 14%, the effect of plate penetration speed on the soil's resistance to penetration was much more pronounced. Increasing the plate penetration speed from 1mm/s to 50mm/s, for example, led to a 265% increase in the mean force required to penetrate the sandy loam soil to a depth of 40mm. For a constant level of pressure applied to

the plate, therefore, the level of sinkage observed is significantly reduced as the rate of load application is increased: for a ground pressure of 250kPa, the sinkage observed at a loading rate of 50mm/s is reduced by 85%, compared to the level of sinkage observed in a conventional static plate sinkage test. From a review of relevant literature, the likely explanation for the observed rate dependency is the presence of moisture within the sandy loam soil (14% w/w): as the rate of load application is increased, the moisture becomes trapped within the surrounding soil skeleton, contributing to the total load that may be supported before shear failure occurs.

Since the level of rolling resistance experienced by a wheel operating on deformable terrain is closely related to the level of sinkage at which the wheel operates, this finding has major implications for the characterisation of soils, both within and outside of a VPG environment. A common assumption in existing mobility models is that strain rate and inertial effects within the soil may be ignored providing the vehicle moves sufficiently slowly across the terrain in question. An analysis as part of the current study, described fully in Chapter 4, indicated that the strain rate induced strengthening of the sandy loam soil may affect the level of observed sinkage, and hence rolling resistance, for translational speeds as low as 0.01m/s (0.022mph). For moisture containing soils, the soil properties derived from conventional static or quasi-static characterisation methods will not be representative of the dynamic properties exhibited during wheel / soil interaction.

While it is relatively straightforward to incorporate rate dependency of materials into an FE mobility model, accurate assessment of off-road mobility is still reliant on the availability of soil property data over the range of strain rates expected in practice. Under the current study, strain rate effects have been incorporated using strain rate scaling of the soil's shear failure surface. This approach was justified on the basis of the results obtained by both Stafford and Tanner (1983) and Zeng and Yao (1991), where dynamic shear test results for moisture-containing soils suggested a logarithmic relationship between loading rate and the soil's apparent cohesion, while the soil's friction angle was unaffected by the load of rate application.

In the absence of dynamic shear strength data for the sandy loam soil, dynamic plate sinkage profiles were used to estimate the effect of loading rate on soil strength, with an iterative approach required to calibrate modelling results against the available experimental data. While the modelling of naturally variable soils within a VPG environment inherently involves some degree of abstraction, this form of model calibration should be avoided if at all possible. Future work in this area should seek to characterise generic soils across a range of strain rates, with the aim of producing a small number of well-characterised soil models rather than a larger number of poorly characterised soils.

The influence of rate dependency in the sandy loam soil was further investigated and quantified using the tyre / soil interaction models described in Chapter 7. In the absence of strain rate sensitivity, the model predicted a rolling resistance coefficient of 23% for a 445 / 65 R 22.5 tyre operating on the sandy loam at an inflation pressure of 800kPa; including rate sensitivity reduced the predicted level of rolling resistance to 12% for a translational speed of 0.3m/s and 7% for a translational speed of 1.0m/s. The results obtained using the rate sensitive model for the sandy loam show very good agreement with experimental results, with rolling resistance coefficients of 8 and 12% for translational speeds of 0.5 and 0.3m/s, respectively.

8.1.3 Soil recovery

Validation of soil material models against hydrostatic test data for both dry sand and sandy loam soils highlighted another area for future development, addressing the non-linear unloading behaviour of soils within FE codes. While a number of the material models available in LS-DYNA are able to accurately represent the non-linear pressure-volume response of soils as hydrostatic loading is applied, unloading behaviour is simplified to a linear function of the bulk unloading modulus, K_{un}. The impact of this simplification is that the permanent soil compaction predicted by the model after passage of the wheel will be greater than that observed in reality.

This effect is exemplified by a comparison of the experimentally measured pressure-volume curve for the dry sand with that produced by a single element verification model (Figure 3.10). Loading the sand to a maximum pressure of 500kPa results in a permanent volumetric strain of 0.01 when the load is removed in experimental tests, whereas the linear unloading path followed by the material model leads to a permanent volumetric strain of 0.05. This difference in residual volumetric strain will ultimately limit the accuracy of an FE based mobility modelling approach in predicting multipass performance (including single passes by a vehicle with multiple axles).

8.2 Development of efficient tyre models

While the main focus of the research has been to improve the representation of generic soils within an FE based VPG environment, the use of efficient tyre models in mobility prediction has also been investigated.

Previous studies addressing efficient tyre models for full-vehicle analysis have focussed on vehicle dynamics and crash applications, where tyres operate at standard operational pressures. These studies have used a combination of beam, shell and solid elements to capture the load / deflection response of the tyre while minimising the number of elements required, but validation against experimental results has usually focussed on a single inflation pressure for a given tyre design. Since inflation pressure is a key variable in off-road mobility, the extension of efficient tyre models to accurately predict tyre deflection across a wide range of loads and pressures had to be addressed during the current study.

The results of the tyre modelling work reported in the body of this thesis have shown that the type of efficient tyre models developed for crash and on-road dynamics simulations can also be applied to off-road mobility analysis. Efficient tyre models, representing Michelin XZL 445 / 65 R 22.5 and Goodyear G90 7.50 R 16 tyres, have been developed and validated against experimentally determined load deflection data across a wide range of inflation pressures. For the 445 / 65 R 22.5 tyre, a good level of agreement was achieved using material

property, tyre geometry and construction data obtained from literature, with modelling results within 10% of the experimental load-deflection results supplied by Michelin for inflation pressures of 400kPa and above.

For the 7.50 R 16 tyre, it was necessary to section a physical tyre to obtain accurate geometry and construction data. Even with accurate geometry and construction data obtained from the sectioned tyre, the load-deflection results obtained using the 7.50 R 16 tyre model indicated significant error at inflation pressures below 150 kPa, with the deflection corresponding to a given wheel load underestimated by an average of 23% for a pressure of 50kPa. For inflation pressures above 250kPa, a much better level of agreement was achieved, with the tyre deflection results provided by the model within 6% of the experimental values measured for a given wheel load. The increased error observed at very low inflation pressure highlights a possible area for further study, since the work completed to assess the effect of tyre inflation pressure on off-road mobility (discussed in more detail below) has shown the potential benefits of very low inflation pressures in dry 'cohesionless' soils.

The work completed has highlighted the potential difficulties in the reverse engineering of FE models to represent particular tyres.

8.3 Prediction of mobility using fluid structure interaction

The idea of a VPG is based around the concept of a single, consistent vehicle model, which can then be subjected to a range of virtual assessment tests without the need to build bespoke vehicle models for each type of analysis. In keeping with this idea, it is desirable that the soil modelling approach within the VPG is consistent, regardless of the type of soil being considered. Previous research in this area has highlighted the difficulties that can be experienced in modelling low-cohesion or 'cohesionless' soils using a conventional Lagrange representation of the soil body (Hambleton, 2010), particularly at high levels of longitudinal slip ratio. Similarly, problems have been reported by some researchers when representing cohesive soils using a discrete element method (Nakashima et al., 2010). To address these issues, and to develop a more

widely applicable soil modelling approach for mobility prediction, the current study has focussed on the use of an Euler solution method within LS-DYNA, which permits large volumes of purely-cohesive, purely-frictional and mixed cohesive / frictional soils to be represented using a consistent approach.

A combined experimental and numerical modelling study has been completed to demonstrate the ability of this approach to predict rolling resistance and drawbar pull for two pneumatic tyres operating on dry sand and sandy loam soils, addressing the effects of soil type, tyre inflation pressure, tyre geometry and the translational speed of the vehicle. While not currently able to fully capture the detail of vehicle performance (for example drawbar pull at low slip on sandy loam), the general trends and relative levels of tyre performance on the two soils show good quantitative agreement with the experimental data set, with coefficients of determination of 0.93 and 0.86 for rolling resistance and drawbar pull predictions, respectively (Figure 8.1).

The experimental study also addressed the effect of tyre tread pattern on drawbar pull, with the results indicating that the presence of a tread pattern can significantly alter the level of tractive force developed. For the soils included, where no lubricating surface layer was present, the presence of a tread pattern tended to reduce the level of drawbar pull achieved. The increase in drawbar pull using skimmed tyres was most notable for the dry sand, with a mean increase in drawbar pull of 51% across the four treatments completed. For accurate mobility prediction, therefore, FE tyre models should include an explicit representation of the tread pattern, even in the case of ‘homogenous’ soils.

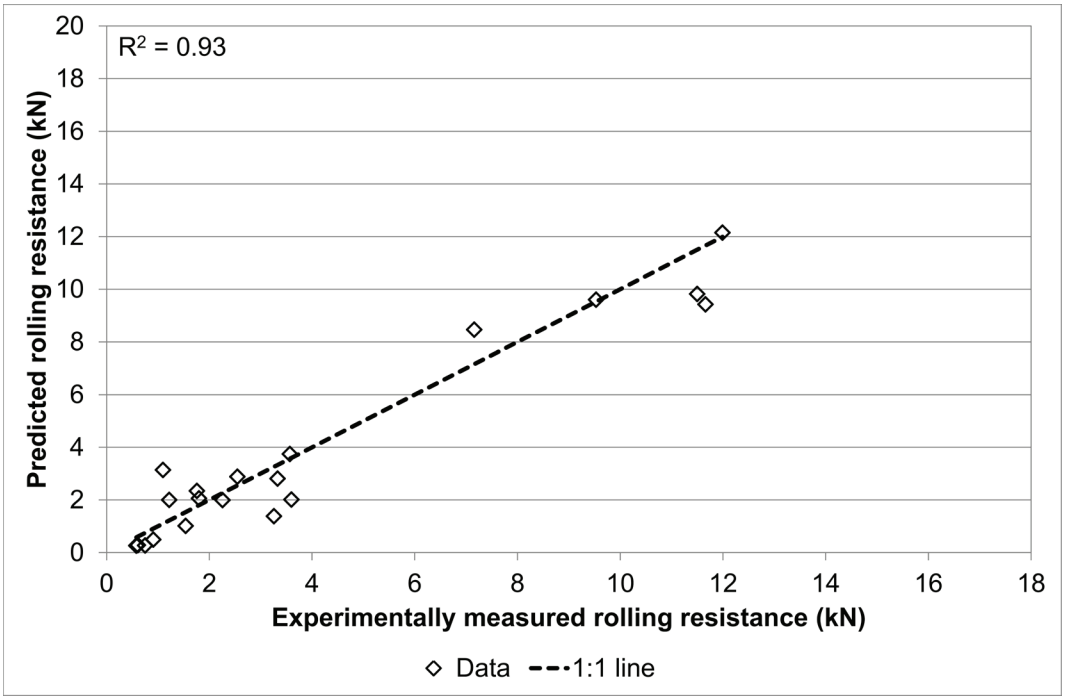

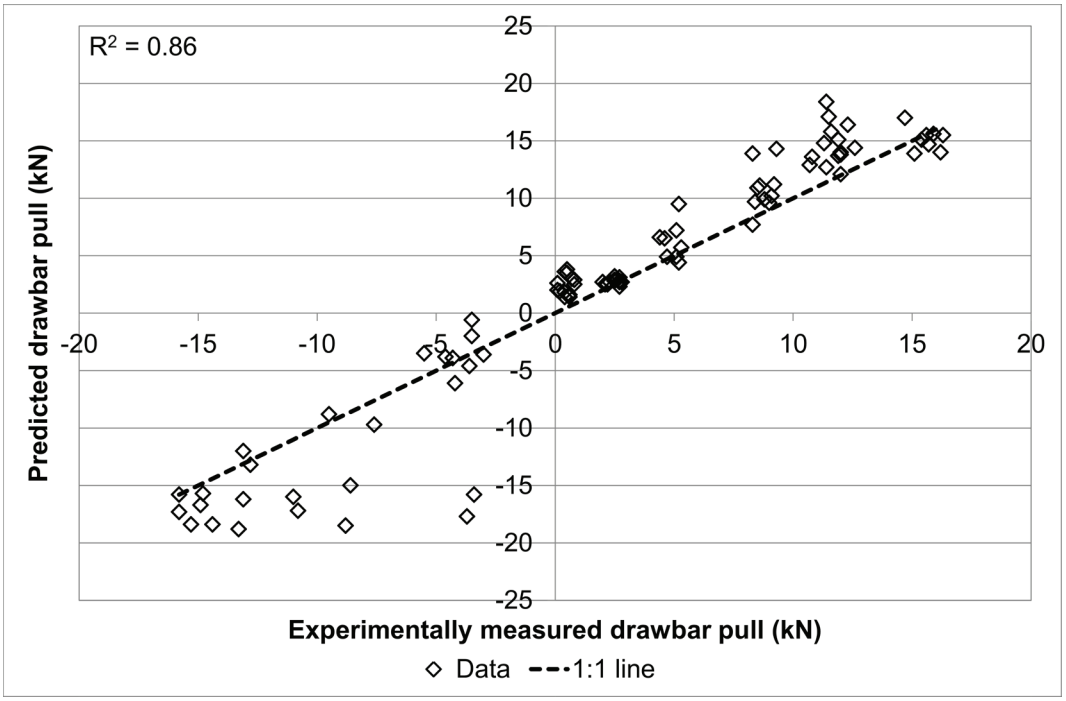

Figure 8.1: Correlation plots for predicted and experimentally measured values of rolling resistance and drawbar pull

The need to include tyre tread pattern points to another potential advantage of an Eulerian approach, when compared with traditional Lagrangian methods. Since advection effectively allows material to flow through the Euler mesh, it is possible to define a moving reference frame with soil flowing in at one end of the soil mesh and out at the other. Providing the rate of inflow and outflow are matched, a steady state condition could be established, representing the wheel moving with a fixed translational speed without the need to explicitly represent a large volume of soil. The advantages of this approach would be greatest for simulations involving high translational speeds, such as aircraft landing gear simulations, since the distance travelled over the duration of the simulated event is controlled by the mean translational speed.

8.4 Virtual proving ground validation

A fundamental issue regarding the development and implementation of a VPG mobility prediction methodology is the level of validation required before the approach is widely accepted as a useful design tool. The natural variability of in-situ soils means that comparison of model predictions against a small set of experimental results will, almost inevitably, show some level of disagreement between the predicted and measured values of rolling resistance and / or drawbar pull.

Using the plate sinkage test as a simple example, the results of the static plate sinkage tests presented in Chapter 3 indicate that the level of sinkage for a given load can vary by 18 – 20% from the mean sinkage value.

A key strand to validation of the VPG approach, therefore, is understanding the level of variability in experimental trials and ensuring that the model represents the average response of the soil. To fully validate the modelling approach, therefore, and to fully quantify the expected range of experimental results, a much larger data set is required, including a number of baseline tests completed on different test sites containing nominally the same soil.

Alternatively, if it is accepted that there will be some natural variability in experimental results, and that final design development and acceptance will be based on full scale experimental testing, the mobility modelling approach outlined in this thesis can be readily adopted as an engineering tool for comparative and optimisation studies. In this case, validation of the model as a whole is built on the smaller scale validation of individual components, rather than comparison against full scale vehicle test data.

Chapter 9: Conclusions and future directions

The purpose of the current study has been to investigate the prediction of off-road mobility within an FE-based VPG environment. Unlike traditional approaches to full vehicle analysis, where different modelling techniques are applied to address a range of specific scenarios (rigid body dynamics for ride and handling, FE for crash, rollover and blast analysis, and a combination of the two for durability analysis), the VPG concept is based around the central idea that a single vehicle model can be subjected to a range of loading conditions. The primary advantages of this approach are the ability to identify design modifications at a pre-tooling stage and the significantly reduced level of modelling effort required to generate vehicle models for each scenario, with an associated reduction in the number of modelling personnel required.

For mobility prediction, the main advantage of a VPG approach is the ability to directly compare the expected performance of different vehicle designs, removing the natural variability of large scale physical tests where soil properties are subject to both spatial and temporal changes. Soil properties within a VPG environment may be uniform across the volume of the modelled body of soil or varied throughout but, crucially, soil properties between vehicle runs will be consistent for each vehicle design.

The work reported here has focussed on extending the VPG concept to include the accurate prediction of off-road mobility, in terms of rolling resistance and drawbar pull for wheeled vehicles operating on soft soils. This has been achieved through the development of improved soil models – including strain rate effects due to the presence of moisture – the extension of efficient tyre models to capture the effects of variations in inflation pressure, and the combination of soil and tyre models to predict key measures of off-road mobility.

Chapters 3 and 4 addressed the development of improved soil models for use in explicit FE analysis, investigating the relationship between laboratory-based soil characterisation methods and the in-situ response of soils to dynamic loading. The effect of the soil model's shear failure surface on the baseline quasi-static response of the soil to applied loading has been investigated, along

with the effect of loading rate on the apparent strength of the soil, through the development of soil material models for dry sand and sandy loam soils. For mobility prediction, which is an inherently dynamic problem, it is important to ensure that any strain rate sensitivity of the soil is captured as well as including inertial effects. The degree of strain rate sensitivity will be affected by the soil type, the moisture content and the extent of any pre-compaction, but strain rate effects may be observed even at relatively low loading rates, and this means that strain rate sensitivity in the soil should be considered even in low speed simulations (less than 0.1m/s). Given the possible influence of strain rate on the soil's apparent strength, conventional static or low rate plate sinkage / cone index tests (at less than 10mm/s) cannot be used to accurately predict mobility parameters such as rolling resistance and drawbar pull.

In Chapter 5, the ability of the proposed modelling approach to predict soil deformation beneath a towed rigid wheel was assessed, including a comparison against both experimental results and existing theory regarding the radial and tangential stresses acting along the wheel / soil interface. Assessing the accuracy of the proposed methods in predicting soil displacements and the stresses along the wheel / soil interface not only provides confidence in the accuracy of the approach, but also supports the idea that FE simulations have a role to play, in conjunction with controlled experiments, in improving our understanding of the physical processes involved in off-road mobility.

Efficient tyre models were introduced in Chapters 6 and 7, aiming to accurately capture the behaviour of pneumatic tyres across a wide range of inflation pressures while minimising the level of computational effort required. These tyre models were then combined with the previously derived soil material models to predict rolling resistance and drawbar pull for two pneumatic tyre designs operating on soft soils. The resulting models have been used to investigate the relationships between tyre geometry, inflation pressure, vehicle speed and soil type on off-road mobility. The use of an Eulerian solution method to represent the soil in the current study has extended the range of soils that can be accurately represented within FE-based mobility analyses, allowing

a consistent modelling approach to be employed regardless of the soil type under consideration.

The results of the tyre / soil interaction modelling work have highlighted the potential benefits of operating at very low inflation pressures on dry, 'cohesionless' soils. As an example, the 445 / 65 R 22.5 tyre studied displayed a sharp increase in tractive performance on dry sand as the inflation pressure was reduced from 200 to 100 kPa, where a pressure of 100kPa represents an 80% reduction compared to the manufacturer's recommended inflation pressure for the wheel load used (520 kPa). Given the role of tyre inflation pressure in maintaining contact between the tyre and the wheel rim, the results obtained highlight the importance of bead locks in maximising terrain accessibility, and CTIS in balancing the need for increased mobility against tyre life.

9.1 Future directions

At each stage of the study, numerical modelling results have been compared against experimental results to assess the accuracy of the proposed modelling approach. Of equal importance, comparison against experimental results has helped to identify the current limits of FE-based mobility prediction, as well as areas for future research. Further research in the following areas would help to increase the applicability and accuracy of FE-based mobility prediction:

- Dynamic soil characterisation at intermediate strain rates

  It has been demonstrated under the current study that the response of a moisture-containing sandy loam soil to applied loading is dependent upon the rate at which the load is applied. Conventional practice in FE modelling of soils is to derive input data for material models from static or quasi-static test data. Given the dynamic nature of wheel / soil interaction and the possible rate dependency of certain soils, soil characterisation for dynamic FE analysis should be extended to include soil properties at 'intermediate' strain rates (10^{-3} to $10^{+3}s^{-1}$).

While a number of previous studies have investigated the rate dependency of soils through dynamic shear box testing, these have acknowledged difficulties in relating the strain rate experienced by the failing soil to the displacement rate of the apparatus. Further work is required to define and standardise dynamic test procedures for soil, ideally producing shear failure surfaces at a range of strain rates. This data can then be used to define more accurate soil models within dynamic FE analysis codes.

- Moving reference frames for high speed mobility analysis

The work reported here, in common with previous studies, has employed on a fixed reference frame, where the wheel moves across a soil bin of finite dimensions. Using this approach, model runtime is dictated by the translational speed of the wheel, since, for a fixed duration, a larger volume of soil must be represented. The Euler solution method presented here, in addition to providing a better representation of 'cohesionless' soils, enables the use of a moving reference frame centred around the wheel, rather than the soil. A similar approach has previously been used to model hydroplaning, with a Lagrangian tyre model interacting with an Eulerian fluid (Toshihiko and Masataka, 2000). By adopting a moving reference frame, the link between translational speed and model runtime is broken, which permits accurate and efficient simulation of high speed wheel soil interactions, such as aircraft operations on natural surfaces.

References

Abu-Hamdeh, N.H., and Reeder, R.C., 2003. *A non-linear 3D finite element analysis of the soil forces acting on a disk plow*. Soil and tillage research, 74, p. 115 – 124.

Anthony, D.A., 2007. *The horse, the wheel, and language: how Bronze-age riders from the Eurasian steppes shaped the modern world*. Princeton University Press. p. 67.

Asliani, F., Yatheendar, M., Visitainer, R.H., Rohweder, D.S., and de Alda, J.L., 1994. *Simulation of proving ground events for heavy truck cabs using ADAMS, MSC/NASTRAN and P/FATIGUE*. MSC world users conference proceedings.

Baladi, G.Y., and Rohani, B., 1984. *Development of a soil wheel interaction model.* Proceedings of the eighth international conference of International Society for Terrain Vehicle Systems (ISTVS), Cambridge, UK.

Bekker, M.G., 1956. *Theory of land locomotion (the mechanics of vehicle mobility)*. University of Michigan Press, Ann Arbor, 1956

Bekker, M.G., 1976. *Recent developments in evaluation of terrain vehicle systems.* In Vol. 2 of Wong, J.Y., and Bekker, M.G., Terrain vehicle systems analysis lecture notes, Carleton University.

Bragov, A.M., Lomunov, A.K., Sergeichev, I.V., Tsembelis, K., and Proud, W.G., 2008. *Determination of physicomechanical properties of soft soils from medium to high strain rates*. International journal of impact engineering, 35, p. 967 – 976.

Brixius, W.W., 1987. *Traction prediction equations for bias ply tires*. American Society of Agricultural Engineers, Paper No. 87-1622.

Chiroux, R.C., Foster Jr, W.A., Johnson, C.E., Shoop, S.A. and Raper, R.L., 2005. *Three dimensional finite element analysis of soil interaction with*

a rigid wheel. Applied mathematics and computation, 162 (2005), p. 707-722.

Choi, G.S. and Kim, H.K., 2000. *Vehicle dynamic simulation using a non-linear finite element simulation programme (LS-DYNA)*. 6th international LS-DYNA conference, Detroit.

Chung, T.J. and Lee, J.K., 1975. *Dynamics of viscoelastoplastic soil under a moving wheel*. Journal of Terramechanics, 12 (1), p. 15 – 31.

Ciobotaru, T., 2009. *Semi-empiric algorithm for assessment of the vehicle mobility*. Leonardo electronic journal of practices and technologies, 15, p. 19 – 30.

Crossley, C. P., Kibiwot, V.N., Reynolds, A.J. and Rickson, R.J., 2001. *Rut formation and rolling resistance on earth roads.* Journal of agricultural engineering research, 78(1), p. 99 – 107.

Edara, R., Shih, S., Tamini, N., Palmer, T., and Tang, A., 2008. *18 wheel truck dynamic and durability analysis using virtual proving ground*. 10th international LS-DYNA users conference, Detroit.

Elwaleed, A.K., Yahya, A., Zohadie, M., Ahmad, D. and Kheiralla, A.F., 2006. *Net traction ratio prediction for high-lug agricultural tyre*. Journal of Terramechanics, 43, p. 119 – 139.

Ersahin, M.A., 2003. *Finite element analysis of cornering characteristics of rotating tires.* PhD thesis, Middle East Technical University, Ankara.

Fasanella, E.L., Lyle, K.H. and Jackson, K.E., 2009. *Developing soil models for dynamic impact simulations*. NASA Langley Research Center, Report No. LF99-7733.

Fervers, C.W., 2004. *Improved FEM simulation model for tire soil interaction*. Journal of Terramechanics, 41, p. 87 – 100.

Foster, W.A., Johnson, C.E., Raper, R.L., and Shoop, S.A., 1995. *Soil deformation and stress analysis under a rolling wheel.* Proceedings of

the 5th North American ISTVS conference / workshop, Saskatoon, 194 – 203.

Freitag, D.R., 1962. *The performance of transport wheels in sand*. Auburn University.

Freitag, D.R., 1965. *A dimensional analysis of the performance of pneumatic tyres on soft soils.* USAE Waterways Experiment Station, technical report number 3-688.

Fukushima, T., Shimonishi, H., Hayashi, K. and Shiraishi, M., 2003. *Simulation of a vehicle running on to a curb by using tire and vehicle FE models.* 4th European LS-DYNA users conference, Ulm.

Fukushima, T., and Shimonishi, H., 2004. *Vehicle turn simulation using FE tyre model*. Proceedings of the 3rd German LS-DYNA forum. http://www.dynamore.de/documents/papers/forum2004/, accessed 29th October 2011.

Gee-Clough, D., 1978. *The effect of wheel width on the rolling resistance of rigid wheels in sand.* Journal of Terramechanics, 15, (4), p. 161 - 184

Gee-Clough, D., 1980. *Selection of tyre sizes for agricultural vehicles*. Journal of agricultural engineering research, 25(3), p. 261 – 278.

Gill, W.R., 1968. *Soil dynamics in tillage and traction*. Agriculture handbook No. 316, Agricultural research service, United States department of agriculture.

Grahn, M., 1991. *Prediction of sinkage and rolling resistance for off the road vehicles considering penetration velocity*. Journal of terramechanics, 28 (4), p. 339 – 347.

Grujicic, M., He, T., Pandurangan, B., Bell, W.C., Cheeseman, B.A., Roy, W.N., Skaggs, R.R., 2009. *Development, parameterization, and validation of a visco-plastic material model for sand with different levels of water saturation.* Proceedings of the institution of mechanical engineers, Part L: Journal of Materials Design and Applications, 223 (2), p. 63 – 81.

Hambleton, J., 2006. *Modeling test rolling in clay*. MSc thesis, University of Minnesota.

Hambleton, J., 2010. *Plastic analysis of processes involving material-object interaction*. PhD thesis, University of Minnesota.

Hetherington, J.G. and Littleton, I., 1978. *The rolling resistance of towed, rigid wheels in sand.* Journal of terramechanics, 15(2), p. 95 – 105.

Janosi, Z., and Hanamoto., B, 1961. *An analysis of the drawbar pull vs. slip relationship for track laying vehicles*. Land locomotion laboratory technical report, No. RR-47.

Janosi, Z., and Hanamoto., B, 1961. *The analytical determination of drawbar pull as a function of slip, for tracked vehicles in deformable soils.* Proceedings of the 1st International Conference Mech. Soil-Vehicle Systems, Turin, Italy.

Karafiath, L.L., and Sobierajski, F.S., 1974. *Effect of speed on tire soil interaction and development of towed pneumatic tire soil model.* Grumman Aerospace Corporation Technical Report 11997 (LL151).

Karafiath, L.L., and Nowartzki, E.A., 1978. *Soil mechanics for off-road vehicle engineering.* Transtech Publications, p. 355 – 427.

Larminie, J.C., 1992. *Modifications to the mean maximum pressure system*. Journal of Terramechanics, 29 (2), p. 239 – 255.

Lee, C.R., Kim, J.W., Hallquist, J.O., Zhang, Y. and Farahani, A., 1997. *Validation of a FEA tire model for vehicle dynamic analysis and full vehicle real time proving ground simulations.* SAE paper number 971100.

Lewis, B.A., 2004. *Manual for LS-DYNA soil material model 147*. Federal Highway Administration, Report No. FHWA-HRT-04-095.

Liu, C.H., and Wong, J.Y., 1996. *Numerical simulations of tire-soil interaction based on critical state soil mechanics*. Journal of terramechanics, 33 (5), p. 209 – 221.

Livermore Software Technology Corporation, USA. *LS-DYNA user documentation.* http://www.lstc.com.

Maclaurin, B., 2007. *Comparing the NRMM (VCI), MMP and VLCI traction models.* Journal of terramechanics, 44 (1), p. 43 – 51.

MacNeal, R.H., and Harder, R.L., 1985. *A proposed set of problems to test finite element accuracy.* Finite elements in analysis and design, 1, p. 3 – 20.

Matchett, A.J., and Smith, G.R., 1985. *The dynamic characteristics of particulate systems in a shear box.* Powder technology, 41, p. 11 – 21.

McAllister, M., 1983. *Reduction in the rolling resistance of tyres for trailed agricultural machinery.* Journal of agricultural engineering research, 28, p. 127 – 137.

Meyer M.P., Ehrlich I.R., Sloss D., Murphy Jr N.R., Wismer R.D., Czako T., 1977. *International society for terrain vehicle systems standards.* Journal of Terramechanics, 14(3), p. 153 – 82.

Michelin Americas Truck Tires XZL wide base page. http://www.michelintruck.com, accessed 29th October 2011

Micklethwaite, E.W.E., 1944. *Soil mechanics in relation to fighting vehicles.* Military college of science, Chertsey.

Muro, T. and O'Brien, J., 2004. *Terramechanics – land locomotion mechanics.* Tokyo: A.A. Balkema Publishers.

Nakashima, H. and Oida, A., 2004. *Algorithm and implementation of soil-tire contact analysis code based on dynamic FE-DE method*. Journal of terramechanics, Vol. 41, 127 – 137.

Nakashima, H., Fujii, H., Oida, A., Momozu, M., Kanamori, H., Aoki, S., Yokoyama, T., Shimizu, H., Miyasaka, J. and Ohdoi, K., 2010. *Discrete element method analysis of single wheel performance for a*

small lunar rover on sloped terrain. Journal of Terramechanics, 2010, 47 (5), p. 307 – 321.

O'Dogherty, M.J., 1996. *The design of octagonal ring dynamometers*. Journal of agricultural engineering research, 63 (1), p. 9 – 18.

Obermayr, M., Dressler, K., Vrettos, C., and Eberhard, P., 2011. *Prediction of draft forces in cohesionless soil with the discrete element method.* Journal of terramechanics, 48, p. 347 – 358.

Okello, J.A., 1992. *Prediction of the force distribution between the soil and a pneumatic wheel.* Journal of agricultural engineering research, 51, p. 249 – 262.

Onafeko, O., and Reece, A.R., 1967. *Soil stresses and deformations beneath rigid wheels.* Journal of Terremechanics, 4 (1), p. 59 – 80.

Onafeko, O., 1969. *Analysis of the rolling resistance losses of wheels operating on deformable terrain.* Journal of agricultural engineering research, 14 (2), p. 176 – 182.

Orengo, F., Ray, M.H. and Plaxico, C.A., 2003. *Modeling tire blow-out in roadside hardware simulations using LS-DYNA.* Proceedings of 2003 ASME International Mechanical Engineering Congress & Exposition, November 2003.

Perumpral, J.V., Liljedahl, J.B. and Perloff, W.H., 1971. *A numerical method for predicting the stress distribution and soil deformation under a tractor wheel.* Journal of Terramechanics, 8 (1), p. 9 – 22.

Plackett, C.W., 1985. *A review of force prediction methods for off-road wheels.* Journal of agricultural engineering research, 31, p. 1 – 29.

Pope, R.G., 1971. *The effect of wheel speed on rolling resistance.* Journal of terramechanics, 8 (1), p. 51 – 58.

Priddy, J.D. and Willoughby, W.E., 2006. *Clarification of vehicle cone index with reference to mean maximum pressure.* Journal of terramechanics, 43 (2), p. 85 – 96.

Qun Y., Sunrong, G. and Guyuan, Y., 1987. *On the modelling of tyre soil systems.* Proceedings of the 9th international conference of the International Society for Terrain Vehicle Systems (ISTVS), Barcelona.

Rashidi, M., Keyhani, A., and Tabatabaeefar, 2006. *Multiplate penetration tests to predict soil pressure-sinkage behaviour under rectangular region*. International journal of agriculture and biology, 1, p. 5 – 9.

Reid, J.D., Coon, B.A., Lewis, B.A., Sutherland, S.H. and Murray, Y.D., 2004. *Evaluation of LS-DYNA soil material model 147.* Federal Highway Administration, Report No. FHWA-HRT-04-094.

Reid, J.D., Boesch, D.A. and Beilenberg, R.W., 2006. *Detailed tyre modelling for crash applications.* ICrash 2006, Athens, Greece, July 2006.

Rowland, D., 1972. *Tracked vehicle ground pressure and its effect on soft ground performance.* Proceedings of the 4th International Society for Terrain Vehicle Systems (ISTVS) conference, Stockholm, p. 353 – 384.

Schwer, L., 2001. *Laboratory tests for characterizing geomaterials.* www.schwer.net/SECS/LaboratoryTestsArticle.pdf, accessed 20th December 2011.

Senatore, C., and Sandu, C., 2011. *Torque distribution influence on tractive efficiency and mobility of off-road wheel vehicles.* Journal of terramechanics, 48, p. 372 – 383.

Shiraishi, M., 2002. *Developing FE tire model library for durability and crash simulations.* 7th International LS-DYNA users conference, Detroit.

Shmulevich, I., Mussel, U., and Wolf, D., 1998. *The effect of velocity on rigid wheel performance.* Journal of terramechanics, 35, p. 189 – 207.

Shmulevich, I., 2010. *State of the art modelling of soil-tillage interaction using discrete element method.* Soil and tillage research, 111, p. 41 – 53.

Stafford, J.V., and Tanner, D.W., 1983a. *Effect of rate on soil shear strength and soil-metal friction. I. Shear strength.* Soil and tillage research, 3, p. 245 – 260.

Stafford, J.V., and Tanner, D.W., 1983b. *Effect of rate on soil shear strength and soil-metal friction. II. Soil-metal friction*. Soil and tillage research, 3, p. 321 – 330.

Tang, A., Tamini, N., and Yang, D., 2000. *Virtual proving ground – a CAE tool for automotive durability, ride and handling and NVH applications*. 6th international LS-DYNA conference, Detroit.

Tiwari, V.K., Pandey, K.P., and Pranav, P.K., 2010. *A review on traction prediction equations. Journal of terramechanics*, 47, p. 191 – 199.

Tonuk, E., 1998. *Computer simulation of dynamic behaviour of pneumatic tires.* PhD thesis, Middle East Technical University, Ankara.

Transportation research board, 2006. *Tyres and passenger vehicle fuel economy.* Special report 286. http://onlinepubs.trb.org/onlinepubs/sr/sr286.pdf, accessed 29th October 2011

Turnage, G.W., 1972. *Tyre selection and performance prediction for off-road wheeled vehicle operations.* Proceedings of the fourth international conference on soil terrain-vehicle systems, Stockholm.

Toshihiko, O., and Masataka, K., 2000. *Hydroplaning simulation using MSC.Dytran*. 2nd MSC worldwide automotive conference. http://www.mscsoftware.com, accessed 18 January 2012.

United Kingdom Ministry of Defence, 2000. *Guide to the common technical requirements for military logistic vehicles and towed equipment*. Defence standard 23-06, Issue 3.

Upadhyaya, S.K., Wulfsohn, D. and Jubbal, G., 1989. *Traction prediction equations for radial ply tyres.* Journal of terrmechanics, 26 (2), p. 149 – 175.

Upadhyaya, S.K., and Wulfsohn, D., 1993. *Traction prediction using soil parameters obtained with an instrumented analog device.* Journal of terramechanics, 30 (2), p. 85 – 100.

Upadhyaya, S.K., Sime, M., Raghuwanshi, N. and Adler, B, 1997. *Semi-empirical traction predictions based on relevant soil parameters.* Journal of terramechanics, 34 (3), p. 141 – 154.

Willis, B.M.D, Barrett, F.M. and Shaw, G.J., 1965, *An investigation into rolling resistance theories for towed rigid wheels*. Journal of terramechanics, 2(1), p. 24-53

Wismer, R.D., and Luth, H.J., 1974. *Off-road traction prediction for wheeled vehicles.* Transactions of the American Society of Agricultural and Biological Engineers, 17 (1), p. 8 – 10.

Wong, J., and Reece, A.R., 1967. *Prediction of rigid wheel performance based on the analysis of soil-wheel stresses.* Part II. Performance of driven rigid wheels. Journal of terramechanics, 4 (1), p. 81 – 98.

Wong, J., and Reece, A.R., 1967. *Prediction of rigid wheel performance based on the analysis of soil-wheel stresses.* Part II. Performance of towed rigid wheels. Journal of terramechanics, 4 (2), p. 7 – 25.

Wong, J., 1984. *On the study of wheel soil interaction*. Journal of terramechanics, 21 (2), p. 117 – 131.

Wong, J., 1989. *Terramechanics of off-road vehicles*. Elsevier, p. 214 – 241.

Wong, J., 2001. *Theory of ground vehicles*. John Wiley and Sons.

Wong, J., 2011. *Predicting the performance of rigid rover wheels on extraterrestrial surfaces based on tests obtained on earth.* Journal of Terramechanics, 49, p. 49 – 61.

Yong, R.N. and Fattah, E.A., 1976. *Prediction of wheel soil interaction and performance using the finite element method.* Journal of terramechanics, 13 (4), p. 227 – 240.

Yong, R.N., Fattah, E.A. and Boonsinsuk, P., 1978. *Analysis and prediction of tyre soil interaction and performance using finite elements.* Journal of terramechanics, 15 (1), p. 43 – 63.

Zeng, D., and Yao, Y., 1991. *Investigation on the relationship between soil shear strength and shear rate.* Journal of terramechanics, 28 (1), p. 1 – 10.

Appendices

Appendix A LS-DYNA element formulation verification

Unlike other codes such as ABAQUS and ANSYS, no formal verification manual is provided for LS-DYNA, with the user responsible for verifying the accuracy of his or her own results. Discussions with Livermore Software Technology Corporation (LSTC) instead pointed to the use of an LS-DYNA examples manual (LSTC, 2005) as a form of verification. Due to the lack of relevant verification examples for LS-DYNA, a short study was undertaken to verify the results obtained, based on comparable examples obtained from the ABAQUS and ANSYS verification manuals (ABAQUS Inc., 2004; ANSYS Inc., 2009).

A.1 Cantilever beam

This problem, originally proposed by MacNeal and Harder (1984), can be used to assess the accuracy of one-dimensional beam, two-dimensional shell and three-dimensional solid elements subjected to axial tension and bending loads. A straight cantilever beam is defined (Figure A.1), with various loads applied to the free end. The displacement of the cantilever beam's free end in the direction of load application is then used to assess the accuracy of the FE solution.

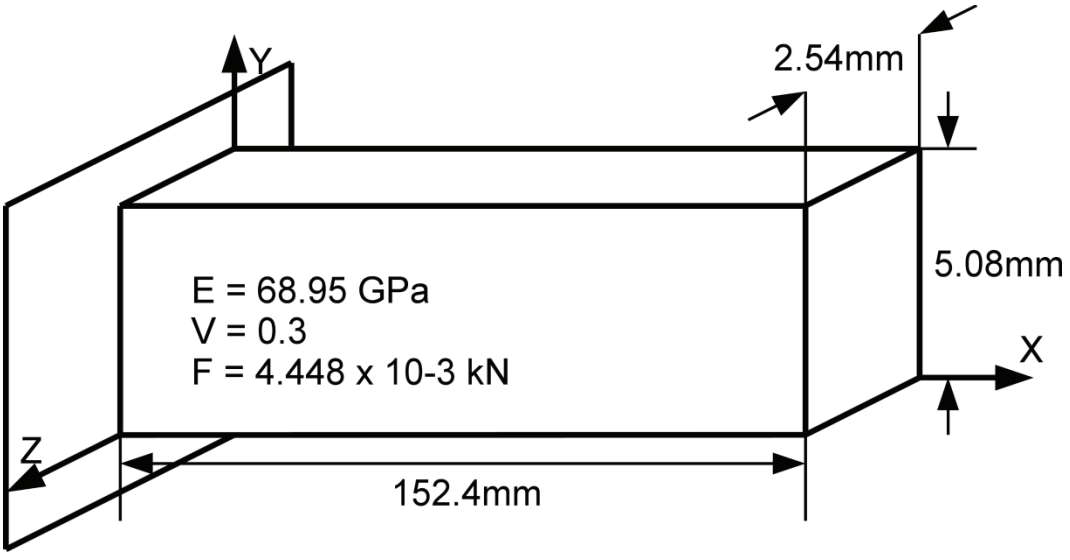

Figure A.1: Definition of cantilever beam verification problem

This verification problem is useful in confirming the accuracy of the various element formulations used within the pneumatic tyre model, which consists of beam, shell and solid elements. The results obtained using LS-DYNA are compared against analytical results reported by MacNeal and Harder inTable A.1. Beam element simulations made use of Type 2 Belytschko-Schwer resultant beam elements, while the shell and solid element simulations used Type 16 fully integrated shells and Type 2 fully integrated selectively reduced solid elements, respectively. For the shell and solid element simulations, three integration points where used through the thickness of the beam.

Table A.1: Results comparison for cantilever beam verification problem

Loading condition	**Theory**	**Beam elements**		**Shell elements**		**Solid elements**	
	Disp.	**Disp.**	**Error**	**Disp.**	**Error**	**Disp.**	**Error**
	mm	**mm**	**%**	**mm**	**%**	**mm**	**%**
Extension	7.62 x 10^{-4}	7.48 x 10^{-4}	-1.9	7.63 x 10^{-4}	+0.1	7.63 x 10^{-4}	+0.1
In plane shear	2.75	2.75	0.0	2.74	-0.1	2.85	+3.8
Out of plane shear	11.0	10.9	-0.8	11.0	+0.4	10.2	-6.9

A.2 Pressure loading

Given that the mobility of pneumatic tyres on soft soil is strongly dependent on the relative stiffness of the tyre and terrain, and that the stiffness of the tyre is in turn dependent on inflation pressure, verification problems were constructed to assess the accuracy of LS-DYNA in describing the effect of internal inflation pressure on material stresses and expansion of two different thin-walled pressure vessels.

A.2.1 Thin pressurised sphere

A thin walled sphere subjected to internal pressurisation was simulated, with verification based on the tangential stress and radial expansion values predicted by LS-DYNA. Both shell and solid element elements are used within the pneumatic tyre model, and models were therefore constructed using both element types. The input parameters for the model are summarised in Table A.2, while the results of the LS-DYNA simulations are compared against an analytical solution in Table A.3.

Table A.2: Summary of main input parameters for internally pressurized thin-walled sphere verification problem

Internal radius	370 mm
Outer radius	380 mm
Modulus	68.95 GPa
Poisson's ratio	0.3
Internal pressure	500 kPa

Table A.3: Results comparison for internally pressurized thin-walled sphere verification problem

	Theory	Shell elements		Solid elements	
	Result	Result	Error	Result	Error
Stress	9,127 kPa	9,315 kPa	+2.1%	8922	-2.2%
Radial expansion	0.0357 mm	0.0355	-0.6%	0.0336	-4.2%

A.2.2 Inflated torus

In addition to the thin walled sphere described above, a thin walled torus subjected to internal pressurisation was simulated, with verification again based on the stress and expansion values predicted by LS-DYNA. The primary input parameters for the inflated torus model are summarised in Table A.4, while the

results of the LS-DYNA simulations are compared against an analytical solution in Table A.5.

Table A.4: Summary of main input parameters for internally pressurized thin-walled sphere verification problem

Centreline radius	575 mm
Hoop radius	289.25 mm
Thickness	10 mm
Modulus	68.95 GPa
Poisson's ratio	0.3
Internal pressure	500 kPa

Table A.5: Results comparison for internally pressurized thin-walled torus verification problem (analytical solution from Fryer and Harvey, 1998)

	Theory	Shell elements		Solid elements	
	Result	Result	Error	Result	Error
σ_1	1.45×10^{-2}	1.44×10^{-2}	-0.2%	1.25×10^{-2}	-13.24%
σ_2	7.23×10^{-3}	7.27×10^{-3}	+0.5%	7.19×10^{-3}	-0.54%

A.3 Composite material verification

The approach used to represent reinforcements within the tyre, using beam elements with shared nodes (Chapter 6), was recognised as being a potential source of error, since the volume of the reinforcing material is not subtracted from the volume of the matrix. To assess the accuracy of this superposition approach to modelling composite materials, spread sheet calculations were first used to determine in plane and bending stiffness values for a composite component using the conventional rule of mixtures / laminate theory approach and a superposition method intended to replicate the representation of tyre reinforcement materials in LS-DYNA. The assessment was based on a cross

section of the cantilever beam defined above, as this would permit modified cantilever beam models models to be run in LS-DYNA to confirm the results of the spreadsheet based calculations. Within the composite beam's cross section, a regular arrangement of cylindrical reinforcements is defined, as illustrated in Figure A.2. The spacing between the reinforcing fibres is held constant, while the radius of the fibres can be varied to assess the impact of fibre volume fraction on the accuracy of the superposition approach.

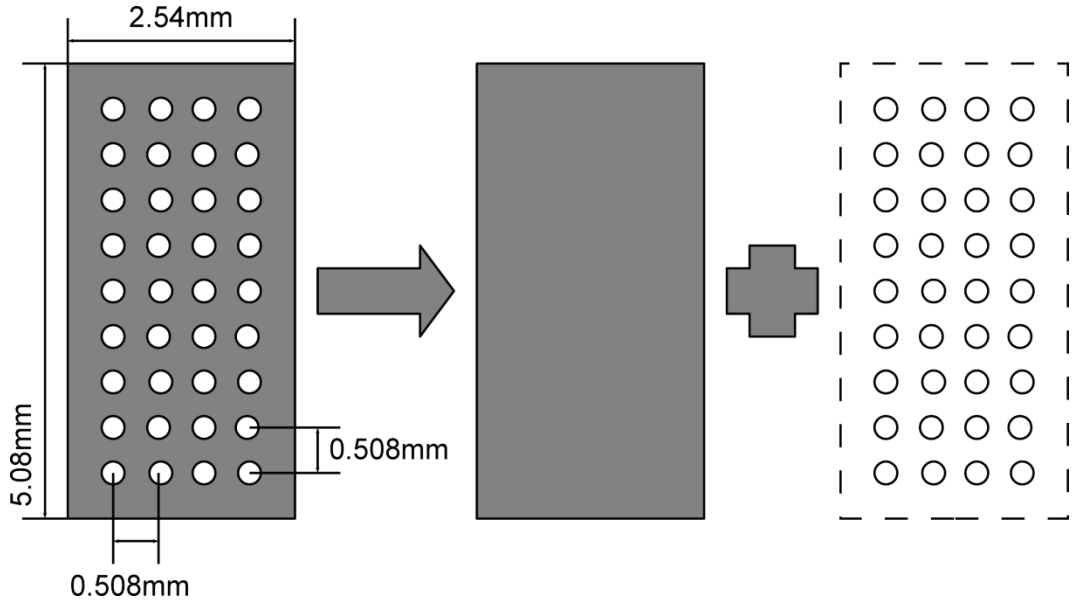

Figure A.2: Composite material cross section used to assess the impact of a superposition modelling approach on accuracy of in plane and bending stiffness

A.3.1 In plane modulus, fibre direction

For a unidirectional composite loaded in the fibre direction, the influence of reinforcements on the in plane stiffness of the material can be determined using the rule of mixtures as follows:

$$E_{11} = E_f \frac{V_f}{V_c} + E_m \left(1 - \frac{V_f}{V_c}\right) \qquad \textit{Equation A.1}$$

Using the superposition approach, the effective in plane stiffness of the composite in the direction of fibre reinforcement can be calculated in much the same manner, but the cross sectional area of the matrix is equal to that of the composite as a whole:

$$E_{11} = E_f \frac{V_f}{V_c} + E_m \qquad \textit{Equation A.2}$$

The effect of the superposition method is therefore to overestimate the in plane stiffness of the composite in the direction of reinforcement. The impact of this overestimation does, however, depend on relative stiffness of the two components. The impact of constituent material properties on the accuracy of the superposition method is illustrated in Figures A.3, A.4 and A.5 for steel reinforced rubber, nylon reinforced rubber and glass reinforced epoxy materials, respectively. As shown, the error associated with the superposition method is minimal for loading in the fibre direction providing the Young's modulus of the reinforcing material is significantly larger than that of the matrix material.

A.3.2 In plane modulus, matrix direction

For loading perpendicular to the fibre direction, the effect of superposition on accuracy is more pronounced. Since the one-dimensional beam elements representing the reinforcements are suspended within the matrix material with no interconnectivity between beams, they do not contribute to the transverse stiffness of the composite. By setting V_m equal to one in the following equation, it becomes evident that, when using a superposition approach for composites with stiff fibres in a compliant matrix, the modulus in the matrix direction is essentially equal to the modulus of the matrix alone.

$$E_{22} = \frac{E_f E_m}{V_m E_f + V_f E_m} \qquad \textit{Equation A.3}$$

For stiff fibres in a compliant matrix, a superposition approach to composite material modelling under-predicts the in plane, matrix direction stiffness of the composite lamina. It is possible, therefore, that the ability of the tyre model to transmit torque from the wheel rim to the tyre tread may be affected by the use of this modelling approach.

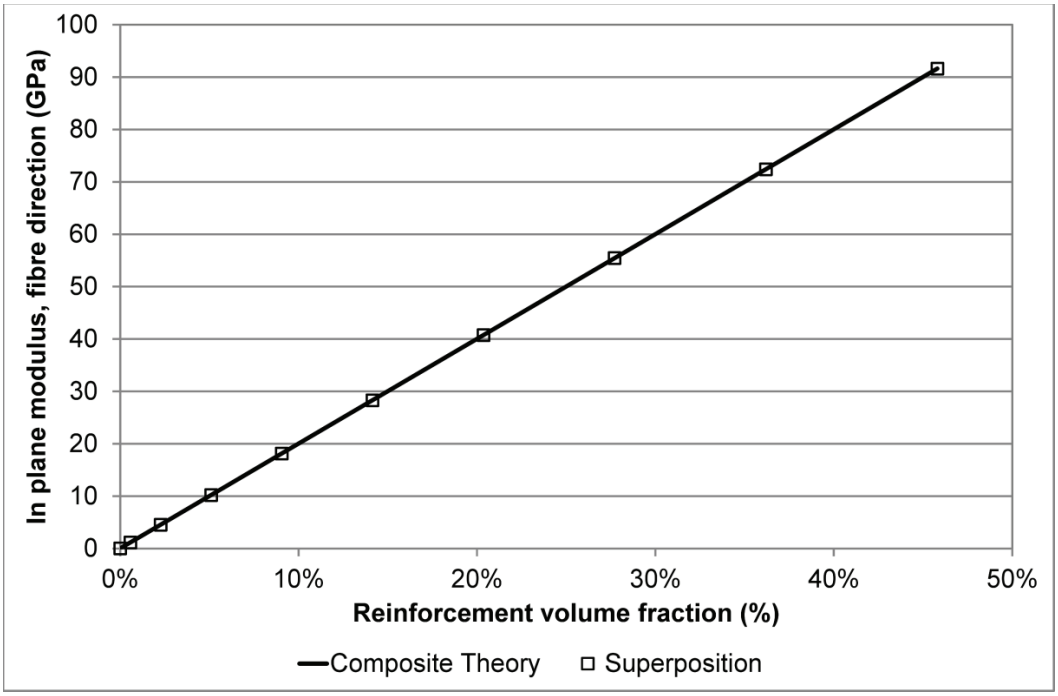

Figure A.3: Comparison of in plane modulus, in fibre direction, obtained using rule of mixtures and superposition for a continuous steel (200 GPa) fibre reinforced rubber (0.03 GPa) matrix

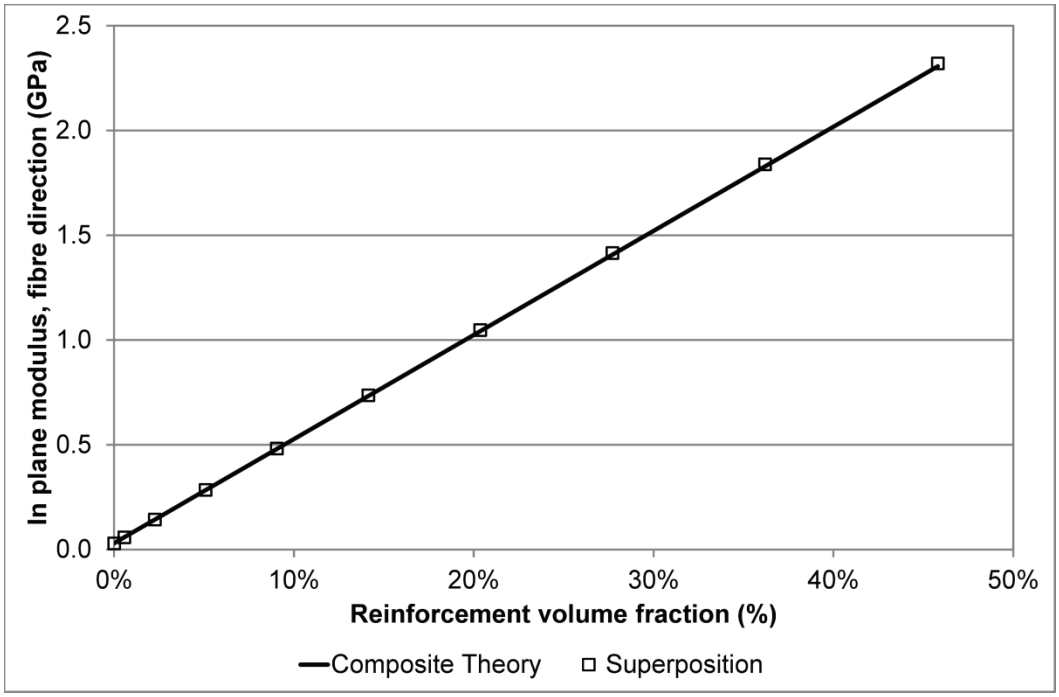

Figure A.4: Comparison of in plane modulus, in fibre direction, obtained using rule of mixtures and superposition for a continuous nylon (5 GPa) fibre reinforced rubber (0.03 GPa) matrix

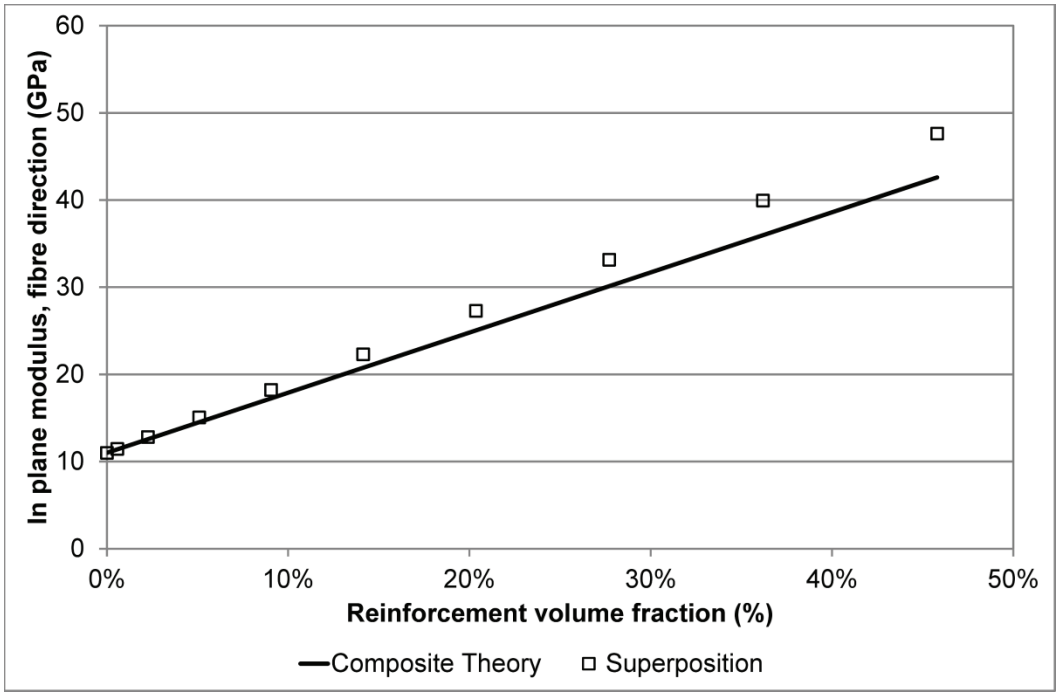

Figure A.5: Comparison of in plane modulus, in fibre direction, obtained using rule of mixtures and superposition for a continuous glass fibre (80 GPa) reinforced epoxy (11 GPa) matrix

A.3.3 Bending stiffness

Given that tyre deformation on a rigid or semi-rigid surface involves bending of both the belt and ply reinforcement layers within the tyre carcass, a spread sheet-based study was also undertaken to assess the accuracy of a superposition approach in representing the bending stiffness of the composite cross section. Again, the cantilever beam cross section described above was used as the base geometry for the study, with reinforcement diameter varying to produce different levels of reinforcement.

Using beam theory to calculate the bending stiffness of the composite cantilever beam, the second moment of area remains constant, due to the constant external dimensions of the composite beam, with the effective Young's modulus of the beam varying due to the different levels of reinforcement present. In contrast, the superposition approach requires the use of the parallel axis theorem to calculate the effective bending stiffness of the reinforcing fibre array, with the bending stiffness of the fibres changing as fibre diameter is increased. Combining this varying second moment of area with the constant value for the baseline rubber beam leads to a non-linear variation in bending stiffness as a function of fibre volume fraction (Figure A.6).

The superposition approach may over-predict the bending stiffness of the reinforced layers of the tyre carcass, leading to lower levels of tyre deflection for a given wheel load. The degree of over-prediction varies as a function of fibre volume fraction, however, and, for low levels of reinforcement, the error caused by the use of a superposition approach is relatively low.

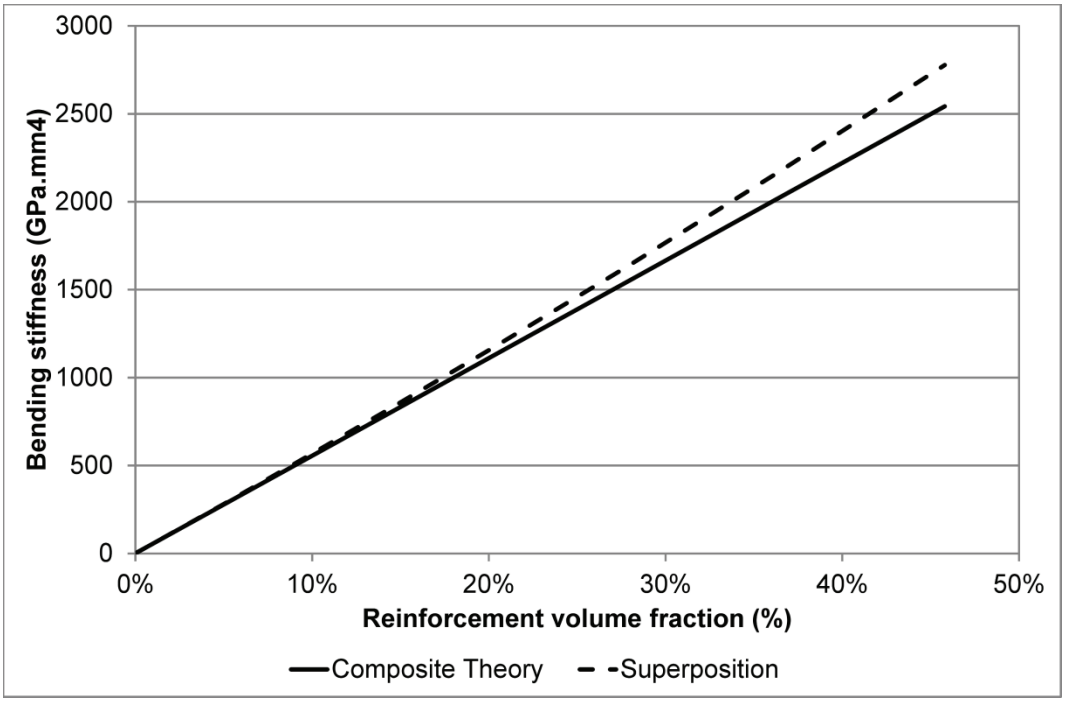

Figure A.6: Calculated variation in bending stiffness as a function of fibre volume fraction for a steel fibre reinforced rubber matrix composite

Appendix B LS-DYNA soil material models

Mat 5: soil and foam

*MAT_SOIL_AND_FOAM is based on the work of Kreig (1972), and describes the soil's volumetric response to compression using a piecewise pressure-volume curve. The deviatoric response of the soil is represented using a non-linear shear failure surface:

$$\sigma_1 - \sigma_3 = \sqrt{3\left(a_0 + a_1 P + a_2 P^2\right)}$$

Where σ_1 and σ_3 represent the axial and lateral stresses for a triaxial loading condition, and P represents the mean stress in the sample. A tensile cut off value can also be specified, which limits the stress that can be supported in tension.

This material model is implemented for Lagrangian solids, multi-material ALE solids, and SPH elements.

Mat 14: soil and foam with failure

The basic material model used is identical to that described above for Mat 5, with the exception that once tensile cut off stress is reached in an element, the material fails and is no longer able to support tensile loading.

This material model is also implemented for Lagrangian solids, multi-material ALE solids and SPH elements, although the multi-material ALE solid implementation has not been formally validated by LSTC.

Mat 16: pseudo tensor

This material model is primarily intended to represent reinforced concrete, with separate input parameters addressing a primary and a reinforcement material. With the reinforcement material undefined, however, it may also be used to represent materials that undergo volumetric compaction with a pressure dependent yield surface. Two "response modes" are available, with the first

based on a tabulated description of yield stress as a function of confinement pressure and the second based on a yield versus pressure curve of the form:

$$\sigma_y = a_0 + \frac{P}{a_1 + a_2 P}$$

The model must be used with a tabulated compaction equation of state, which describes the hydrostatic behaviour of the soil. There are two potential advantages of this model when compared against materials 5 and 14: the first is that the bulk unloading modulus can be varied as a function of volumetric strain, while the second is the ability to scale the tabulated yield stress versus pressure curve as a function of strain rate. Although this model does provide the ability to describe bulk unloading modulus as a function of volumetric strain, a linear unloading stage is assumed.

This material model is implemented for Lagrangian solids, multi-material ALE solids and SPH elements. The multi-material ALE solid implementation has not been formally validated by LSTC.

Mat 25: geologic cap model

This material model is described in terms of three interconnected failure surfaces, defined as in terms of the applied confinement pressure. The surfaces describing the soil's pressure hardening and tensile failure characteristics are defined in a similar manner to the shear failure surfaces discussed above, while the third 'cap' surface is defined at high levels of confining pressure. The presence of the cap surface accounts for the fact that plastic deformation of the soil may occur under purely hydrostatic loading conditions, where the extent of volumetric compaction is controlled by an additional hardening law.

This material model is implemented for Lagrangian solids and SPH elements, but cannot be used with multi-material ALE solids.

Mat 72: concrete damage

This material model is a development of the pseudo tensor model (Mat 16) discussed previously, with the addition of a damage function to describe softening of the material after initial failure.

This material model is implemented for Lagrangian solids and SPH elements, but cannot be used with multi-material ALE solids.

Mat 78: soil concrete

Material model 78 is similar in nature to Mat 5, being based around one load curve describing the pressure-volume response of the soil and a second load curve describing the soil's yield stress as a function of confinement pressure. A strain based damage / failure criterion can also be used.

This material model is implemented for Lagrangian and multi-material ALE solids. The multi-material ALE solid implementation has not been formally validated by LSTC.

Mat 79: hysteretic soil

In this material model, the soil's pressure hardening behaviour is described in much the same manner as Mat 5, with the pressure dependence of the soil's shear failure surface described using the following expression:

$$\sigma_1 - \sigma_3 = \sqrt{3\left(a_0 + a_1 p + a_2 p^2\right)}$$

The volumetric response of the soil is described using pressure sensitive elastic moduli:

$$K = \frac{K_0\left(p - p_0\right)^b}{\left(p_{ref} - p_0\right)^b}$$

The pressure-volume relationship for the soil can therefore be written as:

$$p = \left[-K_0 \ln\left(V\right)\right]^{\frac{1}{1-b}}$$

Where K is the current bulk modulus value, K_0 the bulk modulus at the reference pressure (p_{ref}), p_0 is the cut off pressure for tensile failure, and b is the exponent which describes the sensitivity of the moduli to changes in pressure. Hysteretic behaviour is obtained by internally separating the soil into as many as ten layers of elasto-perfectly plastic material, each with its own elastic modulii and yield stress. Hysteresis in each element is therefore generated by the internally defined layers yielding at different times.

This material model is implemented for Lagrangian solids, multi-material ALE solids and SPH elements, although the multi-material ALE solid implementation has not been formally validated by LSTC.

Mat 145: Schwer Murray cap model

The material model developed by Schwer and Murray (1994) represents an extension of Mat 25 (geologic cap model), with the addition of viscoplasticity to represent rate effects and a damage mechanics approach to model strain softening.

This material model is implemented for Lagrangian solids and SPH elements.

Mat 147: FHWA soil

This material model was developed by Lewis (2004) for the Federal Highways Agency (FHWA) for application to roadbase soils. The effect of confinement pressure on yield stress is accounted for using a modified Mohr Coulomb failure surface, with viscoplasticity used to represent strain rate effects. The effect of moisture content on the soil's mechanical response is also included.

This material model is implemented for Lagrangian solids, multi-material ALE solids and SPH elements, but the multi-material ALE solid implementation has not been formally validated by LSTC.

Mat 147N: FHWA soil Nebraska

This material model is a version of the basic Mat 147 FHWA soil model, with pre-determined material parameters based on experiments undertaken at University of Nebraska.

Mat 173: Mohr Coulomb

This material model, introduced in Release 3 of LS-DYNA v971, provides a linear shear failure surface, based on the well-known Mohr-Coulomb model for pressure dependent shear strength:

$$\tau = c + p \tan \phi$$

A dilation angle can also be defined, describing the change in volumetric strain associated with an increment in shear strain. Volumetric response to hydrostatic pressure is linear and defined by the elastic shear modulus and Poisson's ratio values provided by the user.

The Mohr-Coulomb material model is only implemented for Lagrangian solids.

Mat 192: Soil brick

The soil brick material model was specifically developed by ARUP for modelling of over-consolidated clay. This material model is only implemented for lagrangian solids.

Mat 193: Drucker Prager

This material model, again developed by ARUP, may be regarded as a modified version of the Mohr-Coulomb material model described above, with the addition of a shape parameter to smooth the sharp corners of the three-dimensional Mohr-Coulomb failure surface.

This material model is only implemented for Lagrangian solids.

Appendix C Soil characterisation data

In developing material models for soils, it is necessary to complete a number of replicates of each test to assess the level of natural variability in the soil. When using soil test data to develop deterministic material models for use in finite element analysis, therefore, the experimental data must be averaged. The tables presented below provide a quantitative comparison between the averaged response represented in the model with experimental data obtained from a series of hydrostatic laboratory characterisation tests on dry sand. Table C.1 provides a comparison between experimental and averaged response during loading, while Table C.2 provides a comparison during unloading.

Table C.1: Comparison of experimental pressure values with arithmetic mean used to describe hydrostatic loading response in LS-DYNA

Vol. strain	Radial pressure (kPa)					
	Rep.1	Rep. 2	Rep. 3	Rep. 4	Exp. Mean	Std. Deviation
0.00	0	0	0	0	0	0.0
0.01	14	14	13	15	14	1.0
0.02	32	35	29	37	33	3.6
0.03	55	64	52	68	60	7.5
0.04	86	102	84	109	95	12.5
0.05	124	152	123	162	140	20.0
0.06	170	212	161	230	193	33.1
0.07	234	281	211	301	257	41.7
0.08	295	365	283	387	332	51.3
0.09	373	460	363	477	418	58.7
0.10	450	564	453	586	513	71.9

Table C.2: Comparison of experimental pressure values with arithmetic mean used to describe hydrostatic unloading response in LS-DYNA

Volumetric strain	Hydrostatic pressure (kPa)					
	Rep.1	Rep. 2	Rep. 3	Rep. 4	Exp. Mean	Std. Deviation
0.10	450	564	453	586	513	71.9
0.09	327	435	323	460	386	71.6
0.08	241	330	236	350	289	59.3
0.07	167	240	162	252	205	47.2
0.06	107	164	107	171	137	35.1
0.05	67	104	65	108	86	23.3
0.04	36	60	33	64	48	16.1
0.03	14	28	12	30	21	9.4
0.02	1	7	2	7	4	3.1
0.01	0	0	0	0	0	0.0

Appendix D In-situ soil characterisation data

The tables presented in this appendix supplement the plots provided in Chapter 4, providing quantitative data from static experimental plate sinkage tests and a quantitative comparison between this experimental data and the modelling predictions made using a finite element model of the plate sinkage test.

Table D.1: Experimental plate sinkage test data

	Dry sand			Sandy loam		
Vertical pressure	**Mean sinkage**	**Standard deviation**		**Mean sinkage**	**Standard deviation**	
		Absolute	**Relative**		**Absolute**	**Relative**
kPa	mm	mm	%	mm	%	%
0	0	0	-	0	0	-
33	5	2.5	54	1	0.0	0
77	32	3.1	9	5	1.7	35
121	66	8.1	12	12	2.6	21
166	98	15.9	16	19	4.6	24
210	128	24.6	19	26	5.0	19
255	157	26.5	17	31	4.6	15
299	188	31.5	17	35	4.0	12

Table D.2: Comparison of predicted sinkage results against experimental means for Lagrange plate sinkage simulations in dry sand, using yield surface parameters derived from triaxial tests

	Experiment	Lagrange dry sand model with triaxial yield surface					
Pressure	Sinkage	Coarse mesh		Intermediate mesh		Fine mesh	
		Sinkage	Error	Sinkage	Error	Sinkage	Error
kPa	mm	mm	%	mm	%	mm	%
0	0	0	-	0	-	0	-
33	5	1.5	-68	2.5	-47	3.7	-21
77	32	2.8	-91	3.6	-89	7.1	-78
122	66	4.9	-93	5.5	-92	7.7	-88
166	98	6.2	-94	6.4	-94	8.3	-92
210	128	7.4	-94	7.1	-94	11.0	-91
255	157	8.6	-95	8.2	-95	11.8	-92
299	188	9.9	-95	9.7	-95	22.8	-88
Mean percentage error (0 – 166kPa)		-87 %		-80 %		-70 %	

Table D.3: Comparison of predicted sinkage results against experimental means for Lagrange plate sinkage simulations in dry sand, using yield surface parameters derived from shear box tests

	Experiment	Lagrange dry sand model with shear box yield surface					
Pressure	Sinkage	Coarse mesh		Intermediate mesh		Fine mesh	
		Sinkage	Error	Sinkage	Error	Sinkage	Error
kPa	mm	mm	%	mm	%	mm	%
0	0	0	-	0	-	0	-
33	5	2.0	-58	2.3	-50	7.5	+60
77	32	5.5	-83	15.6	-52	30.9	-4
122	66	11.5	-82	30.8	-53	41.9	-36
166	98	26.1	-73	40.3	-59	61	-38
210	128	35.1	-73	56.3	-56	Run terminated	
255	157	49.2	-69	79.2	-50	Run terminated	
299	188	80.6	-57	97.2	-48	Run terminated	
Mean percentage error (0 – 166kPa)		-74 %		-53 %		-5 %	

Table D.4: Comparison of predicted sinkage results against experimental means for Euler plate sinkage simulations in dry sand, using yield surface parameters derived from triaxial tests

	Experiment	Euler dry sand model with triaxial yield surface					
Pressure	Sinkage	Coarse mesh		Intermediate mesh		Fine mesh	
		Sinkage	Error	Sinkage	Error	Sinkage	Error
kPa	mm	mm	%	mm	%	mm	%
0	0	0	-	0	-	0	-
33	5	0.6	-87	2.9	-37	0.7	-84
77	32	1.4	-96	5.4	-83	5.0	-85
122	66	2.0	-97	6.0	-91	5.7	-91
166	98	2.9	-97	7.0	-93	6.6	-93
210	128	4.2	-97	7.8	-94	9.0	-93
255	157	9.0	-94	8.7	-94	10.1	-94
299	188	10.1	-95	9.7	-95	11.8	-94
Mean percentage error (0 – 166kPa)		-94 %		-76 %		-88 %	

Table D.5: Comparison of predicted sinkage results against experimental means for Euler plate sinkage simulations in dry sand, using yield surface parameters derived from shear box tests

	Experiment	Euler dry sand model with shear box yield surface					
Pressure	Sinkage	Coarse mesh		Intermediate mesh		Fine mesh	
		Sinkage	Error	Sinkage	Error	Sinkage	Error
kPa	mm	mm	%	mm	%	mm	%
0	0	0	-	0	-	0	-
33	5	1.9	-60	2.5	-48	2.2	-54
77	32	13.0	-60	25.6	-21	43.6	+35
122	66	29.2	-56	47.4	-28	64.3	-2
166	98	50.8	-48	65.6	-33	90.7	-8
210	128	67.4	-48	89.9	-30	105.3	-18
255	157	81.3	-48	110.9	-29	Run terminated	
299	188	94.4	-50	125.3	-33	Run terminated	
Mean percentage error (0 – 166kPa)		-56 %		-33 %		-7 %	

Table D.6: Comparison of predicted sinkage results against experimental means for Lagrange plate sinkage simulations in sandy loam, using yield surface parameters derived from shear box tests

	Experiment	Lagrange sandy loam model with shear box yield surface					
Pressure	Sinkage	Coarse mesh		Intermediate mesh		Fine mesh	
		Sinkage	Error	Sinkage	Error	Sinkage	Error
kPa	mm	mm	%	mm	%	mm	%
0	0	0	-	0	-	0	-
33	1	1.3	+33	1.1	+13	3.0	+198
77	5	3.4	-32	4.3	-13	7.2	+44
122	12	7.8	-35	12.6	+5	13.1	+9
166	19	12.6	-34	19.5	+3	20.5	+8
210	26	19.3	-26	32.9	+26	Run terminated	
255	31	38.2	+23	Run terminated		Run terminated	
Mean percentage error (0 – 166kPa)		-17 %		+2 %		+65 %	

Table D.7: Comparison of predicted sinkage results against experimental means for Euler plate sinkage simulations in sandy loam, using yield surface parameters derived from shear box tests

	Experiment	Euler sandy loam model with shear box yield surface					
Pressure	Sinkage	Coarse mesh		Intermediate mesh		Fine mesh	
		Sinkage	Error	Sinkage	Error	Sinkage	Error
kPa	mm	mm	%	mm	%	mm	%
0	0	0	-	0	-	0	-
33	1	1.1	+13	0.9	-14	1.2	+23
77	5	3.0	-40	3.0	-40	3.7	-25
122	12	12.0	0	8.9	-26	12.1	+1
166	19	24.3	+28	16.5	-13	17.9	-6
210	26	Run terminated		25.3	-3	29.3	+13
255	31	Run terminated		36.4	+17	38.9	+26
Mean percentage error (0 – 166kPa)		0 %		-23 %		+2%	

Appendix E Quantitative comparison of interaction model

The tables provided in this appendix provide a qualitative comparison between experimental drawbar pull test data and finite element modelling results for driven pneumatic tyres operating on dry sand and sandy loam soils.

Table E.1: Quantitative comparison of experimental and FE modelling results for positive slip testing of a Michelin XZL 445 / 65 R 22.5 tyre operating on dry sand

Tyre	Michelin XZL 445 / 65 R 22.5					
Soil	Dry sand					
Translational speed	3.0m/s					
Wheel load	29.43 kN		29.43 kN		29.43 kN	
Inflation pressure	100kPa		200kPa		400kPa	
Slip (%)	**Drawbar pull (kN)**					
	Exp. (w/ tread)	**Model**	**Exp.**	**Model**	**Exp.**	**Model**
+20	8.3	7.7	5.2	4.4	0.4	Tyre experiences unstable sinkage, leading to error termination of model
+30	9.0	9.6	5.1	4.9	0.5	
+40	9.1	10.2	5.3	5.7	0.1	
+50	8.8	9.9	5.1	7.2	-0.4	
+60	8.5	10.9	4.7	4.9	-0.8	
+70	8.4	9.7	4.4	6.6	-0.8	
+80	8.6	11.1	4.6	6.5	-0.7	
+90	9.2	11.2	5.2	9.5	0.0	
Mean	8.7	10.0	4.9	6.2	-0.2	

Table E.2: Quantitative comparison of experimental and FE modelling results for negative slip testing of a Michelin XZL 445 / 65 R 22.5 tyre operating on dry sand

Tyre	Michelin XZL 445 / 65 R 22.5			
Soil	Dry sand			
Translational speed	1.0m/s			
Wheel load	29.43 kN		29.43 kN	
Inflation pressure	400kPa		800kPa	
Slip (%)	**Drawbar pull (kN)**			
	Exp. (w/ tread)	**Model**	**Exp. (w/ tread)**	**Model**
-10	-3.5	-0.6	-3.5	-2.0
-20	-5.5	-3.5	-4.2	-6.1
-30	-9.5	-8.8	-7.6	-9.7
-40	-13.1	-12.0	-12.8	-13.2
-50	-14.9	-16.7	-15.8	-15.8
Mean	-9.3	-8.3	-8.8	-9.4

Table E.3: Quantitative comparison of experimental and FE modelling results for positive slip testing of a Michelin XZL 445 / 65 R 22.5 tyre operating on sandy loam

Tyre	Michelin XZL 445 / 65 R 22.5					
Soil	Sandy loam (14% moisture)					
Translational speed	3.0m/s					
Wheel load	29.43 kN		29.43 kN		29.43 kN	
Inflation pressure	100kPa		400kPa		800kPa	
Slip (%)	**Drawbar pull (kN)**					
	Exp.	**Model**	**Exp.**	**Model**	**Exp.**	**Model**
+20	14.7	17.0	9.3	14.3	8.3	13.9
+30	16.3	15.5	11.4	12.7	10.7	12.9
+40	15.6	15.5	12.0	12.1	10.8	13.6
+50	15.4	15.1	12.0	13.8	11.3	14.8
+60	15.1	13.9	12.0	14.0	11.9	15.1
+70	15.7	14.7	11.9	13.7	11.6	15.8
+80	15.9	15.6	12.3	16.4	11.5	17.1
+90	16.2	14.0	12.6	14.4	11.4	18.4
Mean	15.6	15.2	11.7	13.9	10.9	15.2

Table E.4: Quantitative comparison of experimental and FE modelling results for negative slip testing of a Michelin XZL 445 / 65 R 22.5 tyre operating on sandy loam

Tyre	Michelin XZL 445 / 65 R 22.5			
Soil	Sandy loam (14% moisture)			
Translational speed	1.0m/s			
Wheel load	29.43 kN		29.43 kN	
Inflation pressure	400kPa		800kPa	
Slip (%)	**Drawbar pull (kN)**			
	Exp. (w/ tread)	**Model**	**Exp. (w/ tread)**	**Model**
-20	-3.4	-15.8	-3.7	-17.7
-30	-8.6	-15.0	-8.8	-18.5
-40	-11.0	-16.0	-10.8	-17.2
-50	-13.3	-18.8	-13.1	-16.2
-60	-14.8	-15.7	-14.4	-18.4
-70	-15.8	-17.3	-15.3	-18.4
Mean	-11.2	-16.4	-11.0	-17.7

Table E.5: Quantitative comparison of experimental and FE modelling results for positive slip testing of a Goodyear G90 7.50 R 16 tyre operating on dry sand

Tyre	Goodyear G90 7.50 R 16			
Soil	Dry sand			
Translational speed	3.0m/s			
Wheel load	8.56 kN		9.07 kN	
Inflation pressure	50 kPa		130 kPa	
Slip (%)	**Drawbar pull (kN)**			
	Exp.	**Model**	**Exp.**	**Model**
+20	0.8	1.4	0.6	1.4
+30	0.8	1.6	0.6	1.6
+40	0.8	1.4	0.4	1.4
+50	0.7	1.8	0.4	1.8
+60	0.5	1.9	0.2	1.9
+70	0.5	2.0	0.1	2.0
+80	0.4	2.6	0.1	2.6
Mean	0.6	2.0	0.3	1.8

Table E.6: Quantitative comparison of experimental and FE modelling results for positive slip testing of a Goodyear G90 7.50 R 16 tyre operating on sandy loam

Tyre	Goodyear G90 7.50 R 16			
Soil	Sandy loam (14% moisture)			
Translational speed	3.0m/s			
Wheel load	4.91 kN		3.78 kN	
Inflation pressure	50 kPa		130 kPa	
Slip (%)	**Drawbar pull (kN)**			
	Exp.	**Model**	**Exp.**	**Model**
+20	2.0	2.7	2.3	2.7
+30	2.1	2.5	2.5	2.9
+40	2.2	2.5	2.5	2.8
+50	2.5	2.9	2.5	2.8
+60	2.6	2.9	2.6	2.9
+70	2.7	3.1	2.7	2.7
+80	2.7	2.8	2.7	2.3
+90	2.5	3.2	2.8	2.7
Mean	2.4	2.8	2.6	2.7

Table E.7: Quantitative comparison of experimental and FE modelling results for negative slip testing of a Goodyear G90 7.50 R 16 tyre operating on sandy loam

Tyre	Goodyear G90 7.50 R 16			
Soil	Sandy loam (14% moisture)			
Translational speed	1.0m/s			
Wheel load	7.36 kN		7.36 kN	
Inflation pressure	190 kPa		275 kPa	
Slip (%)	**Drawbar pull (kN)**			
	Exp. (w/ tread)	**Model**	**Exp. (w/ tread)**	**Model**
-20	-3.6	-4.6	-3.0	-3.6
-40	-4.6	-3.8	-4.3	-3.9
Mean	-4.8	-4.2	-4.6	-3.8

Appendix F Hourglass parametric study

In early plate sinkage simulations to investigate the in-situ response of soft soils to applied loading, severe hourglass deformation of the soil mesh was observed (Figure F.1). Hourglass deformation can occur in single integration point solid and shell elements, and represents a non-physical, zero strain deformation of the element. Given that no strain is associated with the hourglass deformation of an element, no stress is generated in the material and no energy is consumed as the mesh deforms.

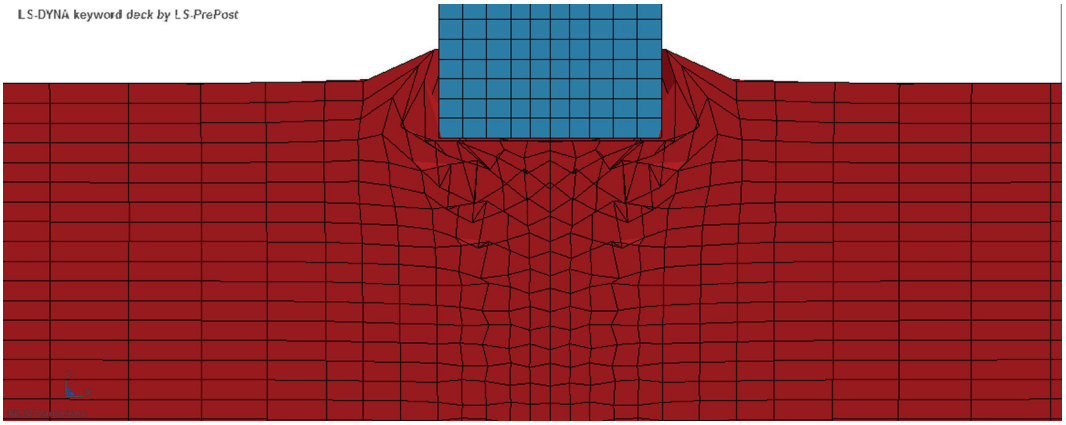

Figure F.1: Hourglass deformation modes in plate sinkage model

While no energy is consumed in the hourglass deformation process, the distorted elements caused by hourglassing can still lead to numerical errors, such as negative volumes, within a Lagrange solution scheme. Use of an Eulerian solver can help to address hourglassing, since an Eulerian mesh is effectively fixed in space with material flowing through it, but requires frequent advection cycles to prevent negative volume errors during the conventional Lagrangian portion of the calculation cycle.

As discussed in the main body of this thesis, hourglassing can be eliminated by the use of selectively reduced or full integrated elements. These element formulations, however, represent a significant increase in computational effort and can be unstable in simulations involving large deformations. If single

integration point elements are retained, then hourglass deformation can be reduced by the introduction of an hourglass control algorithm, which effectively damps the hourglass modes within the mesh, or by mesh refinement. Where an hourglass control algorithm is used, it is necessary to confirm that the energy input associated with the control of non-physical hourglass modes is small relative to the internal energy of each part in the simulation.

Two basic types of hourglass control are available to the user in LS-DYNA, in the form of either stiffness or viscous-based algorithms. Stiffness-based hourglass control is recommended for structural parts subjected to relatively low loading rates, while viscous-based control is recommended for high velocity impact simulations. For fluid parts, the damping associated with hourglass control can lead to overly stiff behaviour, and guidance from LSTC indicates that the default hourglass damping coefficient (0.1) should be reduced by several orders of magnitude for these materials.

F.1 Hourglass control in soft soil models

Having identified that some form of hourglass control would be required for the plate sinkage model discussed in Chapter 4, the available control methods where compared to determine whether or not hourglass modes could be successfully eliminated or reduced without artificially increasing the stiffness of the soil material model.

Firstly, a baseline simulation was run using fully integrated solid elements to represent the soil sample (Figure F.2). The results obtained highlighted the dependency of the model's output on the level of mesh refinement, with coarse and intermediate meshes producing broadly similar results, while the fine mesh produced a markedly different profile. All three simulations displayed some degree of instability in the soil mesh, as illustrated in Figure F.3.

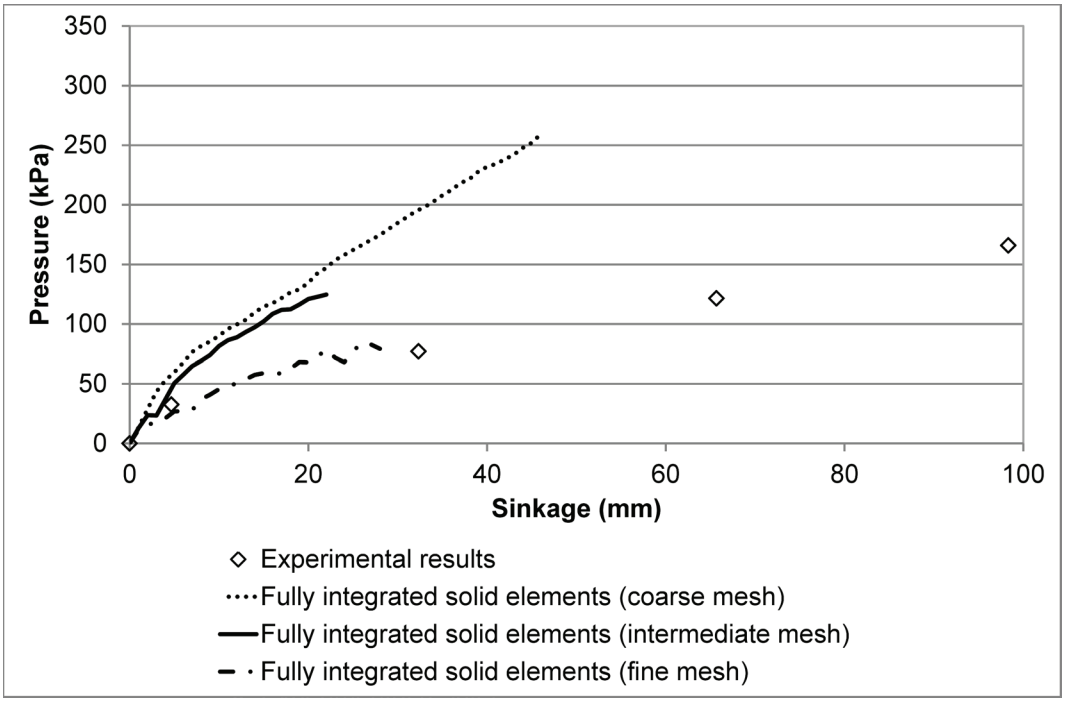

Figure F.2: Comparison of modelling and experimental results for quasi-static plate sinkage tests in dry sand, using fully integrated solid elements

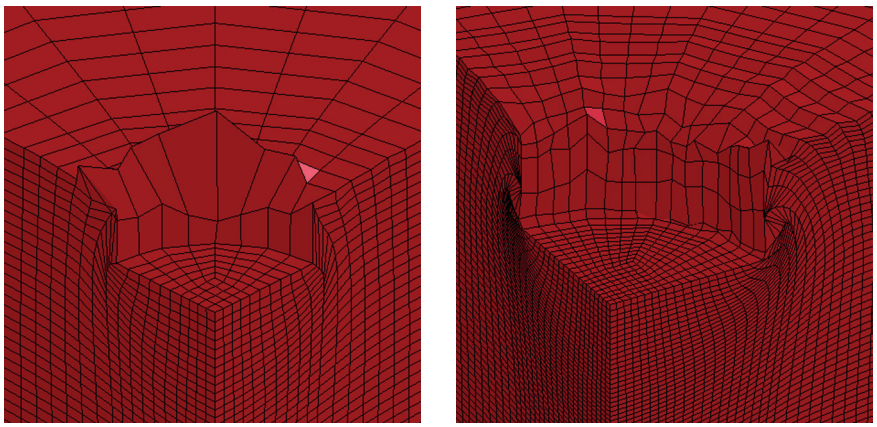

Figure F.3: Instabilities observed in fully integrated soil meshes, within quasi-static plate sinkage simulations, using 3.78mm (left) and 1.89mm (right) mesh sizes

A stiffness-based hourglass control algorithm, the 'Type 4' Flanagan-Belytschko stiffness form within LS-DYNA, was initially selected to investigate the effect of the hourglass control coefficient on the plate sinkage profile predicted by the model. A stiffness-based method was initially selected on the basis that the plate sinkage simulation represents a low velocity impact. A series of five simulations were run, increasing the hourglass control coefficient by an order of magnitude each time, from 5×10^{-6} to 5×10^{-2}. For the simulations using coefficients of 5×10^{-4} and below, severe hourglass deformation of the soil mesh occurred, resulting in negative volume errors that triggered termination of the modelling run. For higher hourglass coefficient values, hourglass deformation of the soil mesh was reduced but not eliminated, with the increased level of hourglass damping resulting in a stiffer soil response.

The main outcome of the short parametric study to assess the impact of hourglass control on soil model stability and accuracy was that, for 'cohesionless' soils, it would be desirable to use a significantly reduced level of hourglass damping, as the default levels of hourglass control in LS-DYNA produce an overly stiff response for these materials. The use of reduced hourglass control coefficients in Lagrange simulations is, however, limited by the severe levels of hourglass deformation that can occur, which lead to negative volume induced termination errors. For Lagrange simulations, therefore, hourglass control algorithms cannot be used in isolation and must be combined with mesh refinement. This will result in increased runtimes for Lagrange simulations involving 'cohesionless' soil.

Within an Eulerian solution scheme, the advection steps used to remap nodes to their original positions will help to minimise the impact of hourglass modes, and this permits the use of much lower hourglass control coefficients in Eulerian simulations without affecting their stability. Indeed, for ALE parts, the default hourglass coefficient value in LS-DYNA is 1×10^{-6}. Given that the frequency of advection steps can be controlled by the user, as part of the *CONTROL_ALE card, care must be taken to ensure that advection steps are frequent enough to prevent error termination due to negative volumes. Providing frequent advection steps are included in the simulation, the use of an Eulerian

representation of the soil will allow the use of a coarser mesh, which will in turn help to minimise model runtime for a given event duration.

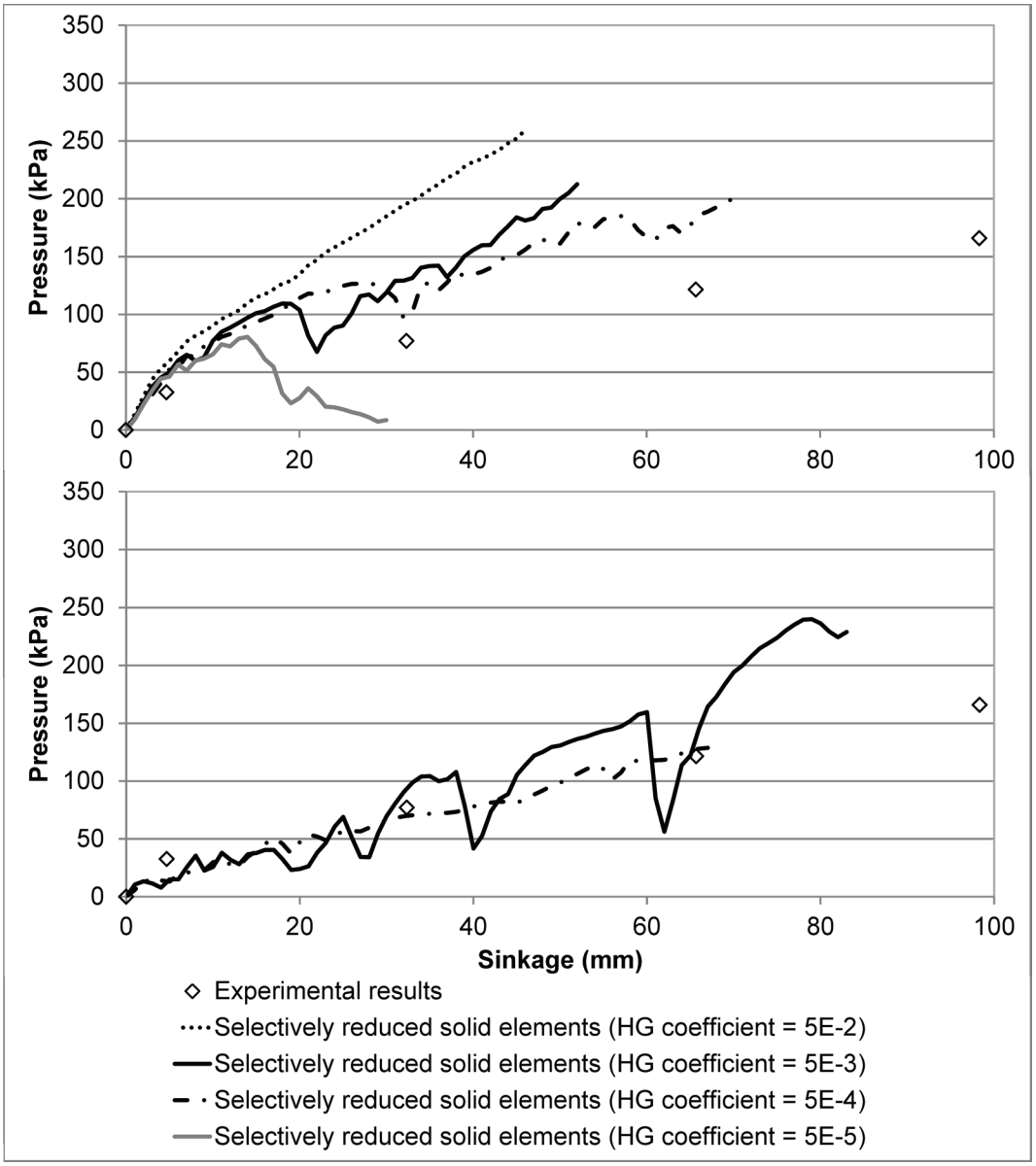

Figure F.4: Comparison of coarse (top) and fine (bottom) mesh modelling results quasi-static plate sinkage simulations in dry sand, using single integration point solid elements with stiffness-based (Type 4) hourglass control

Appendix G MAT_PSEUDO_TENSOR validation

Having identified MAT_PSEUDO_TENSOR as an alternative soil material model for the inclusion of rate effects in dynamic FE analysis, it was necessary to validate the response of the soil model against experimentally measured hydrostatic, trixaxial / direct shear box and static plate sinkage tests, as had previously been completed for the sandy loam model using MAT_SOIL_AND_FOAM. To this end, single element simulations of hydrostatic and triaxial tests were completed, along with simulations of quasi-static plate sinkage tests. The input deck used to describe the sandy loam soil within LS-DYNA is as follows:

```
*MAT_PSEUDO_TENSOR_TITLE
SANDY_LOAM_SOIL (14% moisture)
$#     mid        ro         g        pr
         1 1.4700E-6  0.001120  0.300000
$#    sigf        a0        a1        a2       a0f       a1f        b1       per
     0.000 6.7336E-6  0.767680  -1.95459     0.000     0.000     0.000     0.000
$#      er       prr      sigy      etan       lcp       lcr
     0.000     0.000     0.000     0.000         0         0
$#      x1        x2        x3        x4        x5        x6        x7        x8
     0.000     0.000     0.000     0.000     0.000     0.000     0.000     0.000
$#      x9       x10       x11       x12       x13       x14       x15       x16
     0.000     0.000     0.000     0.000     0.000     0.000     0.000     0.000
$#     ys1       ys2       ys3       ys4       ys5       ys6       ys7       ys8
     0.000     0.000     0.000     0.000     0.000     0.000     0.000     0.000
$#     ys9      ys10      ys11      ys12      ys13      ys14      ys15      ys16
     0.000     0.000     0.000     0.000     0.000     0.000     0.000     0.000
*EOS_TABULATED_COMPACTION_TITLE
SANDY_LOAM_SOIL
$#   eosid      gama        e0        vo
         1     0.000     0.000     0.000
$#           ev1             ev2             ev3             ev4             ev5
          0.000      -0.0202000      -0.0408200      -0.0618800      -0.0833800
$#           ev6             ev7             ev8             ev9            ev10
      -0.1054000      -0.1508000      -0.1985000      -0.2485000      -0.6300000
$#            c1              c2              c3              c4              c5
          0.000  1.2170000e-005  2.5170000e-005  4.0330000e-005  5.8000001e-005
$#            c6              c7              c8              c9             c10
  8.0500002e-005  1.4370000e-004  2.3629999e-004  3.7940001e-004       0.0028310
$#            t1              t2              t3              t4              t5
          0.000           0.000           0.000           0.000           0.000
$#            t6              t7              t8              t9             t10
          0.000           0.000           0.000           0.000           0.000
$#            k1              k2              k3              k4              k5
       0.0037788       0.0039288       0.0040957       0.0042990       0.0045490
$#            k6              k7              k8              k9             k10
       0.0048890       0.0059850       0.0080490       0.0127240       0.0140000
```

For the purposes of validation against the results of quasi-static or static characterisation tests, rate effects within the material model were deactivated by setting LCP equal to zero. The results of the work completed to validate the MAT_PSEUDO_TENSOR material model are presented in the following sections.

G.1 Hydrostatic validation

The output of the MAT_PSEUDO_TENSOR single element simulations under hydrostatic loading are visually compared against experimental test data in Figure G.1, and quantitatively compared in Table G.1.

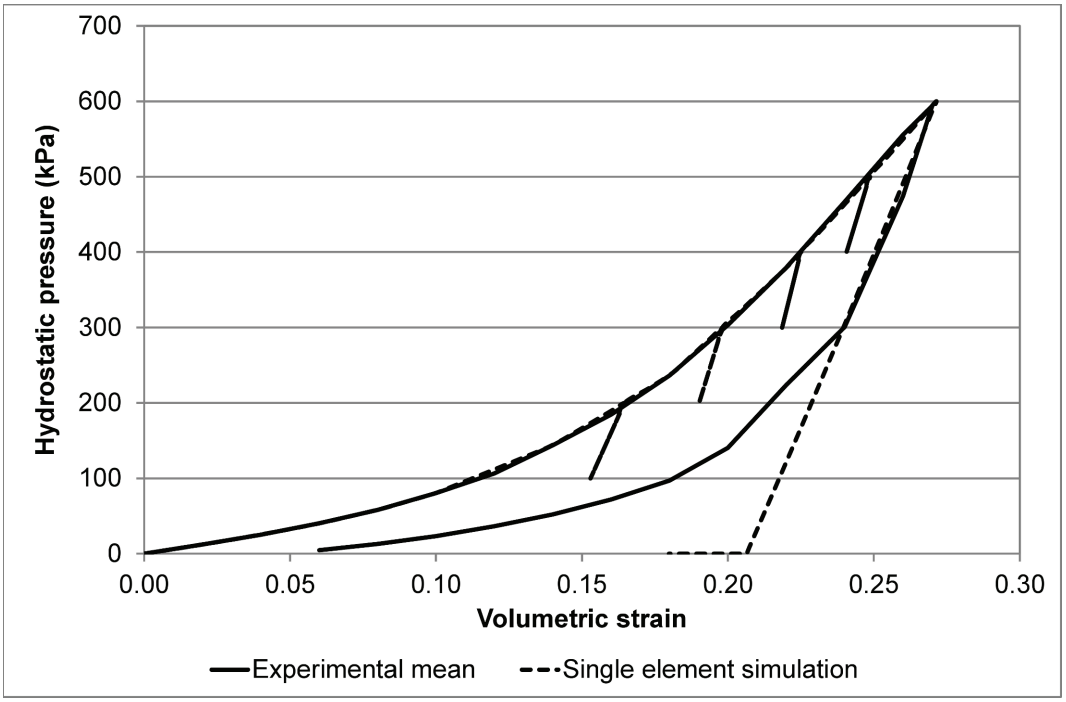

Figure G.1: Visual comparison of pressure-volume curve obtained from single element simulations with experimental hydrostatic data for sandy loam soil

Table G.1: Comparison of experimental mean and single element FE model results for hydrostatic loading of sandy loam

	Vol. Strain	Radial pressure (kPa)		
		Experimental		Single Element Model
		Mean	St. Dev.	
Loading	0.00	0	0.0	0.0
	0.04	25	0.8	26
	0.08	58	3.6	58
	0.12	107	11.7	112
	0.16	185	17.9	189
	0.20	303	47.5	307
	0.24	467	45.8	464
	0.27	594	6.5	594
Unloading	0.24	301	20.2	304
	0.20	140	13.3	0
	0.16	72	7.5	0
	0.12	36	4.0	0
	0.06	5	1.9	0

G.2 Shear failure surface

Given the influence of the test method used on the location of the shear failure surface, model output data was compared against the results of direct shear box testing only. The output of the MAT_PSEUDO_TENSOR single element simulations are visually compared against a directly calculated shear failure surface in Figure G.2, and quantitatively compared in Table G.2.

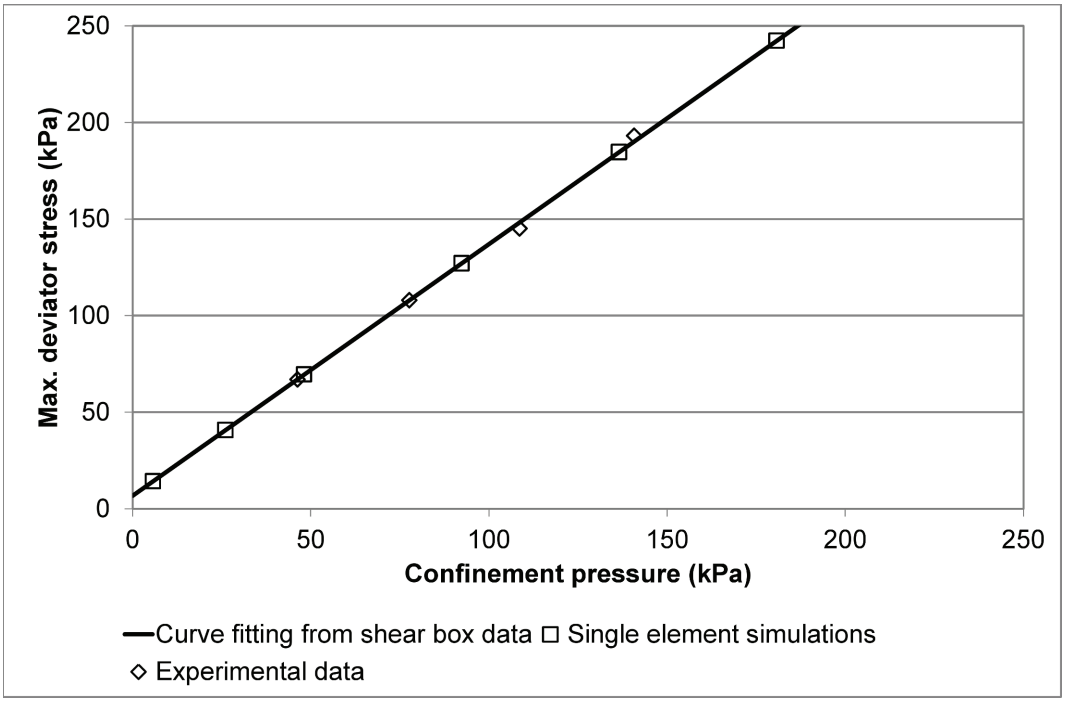

Figure G.2: Visual comparison of shear failure surface obtained from single element simulations with directly calculated yield surface

Table G.2: Quantitative comparison between experimental shear failure surface and single element simulation results for triaxial loading

Confinement pressure (kPa)	Maximum deviator stress (kPa)	
	Experimental	Single element model
46.3	67.0	67.0
77.7	108.0	107.9
108.6	145.1	149.5
140.8	193.2	193.2

G.3 Plate sinkage profile

To verify that the material model accurately described the response of the in-situ soil to applied loading, simulations of quasi-static plate sinkage tests were completed, as described in Chapter 4 of the main body of this thesis. The results of the plate sinkage simulations are compared against experimental plate sinkage profiles in Figure G.3 and Table G.3, below.

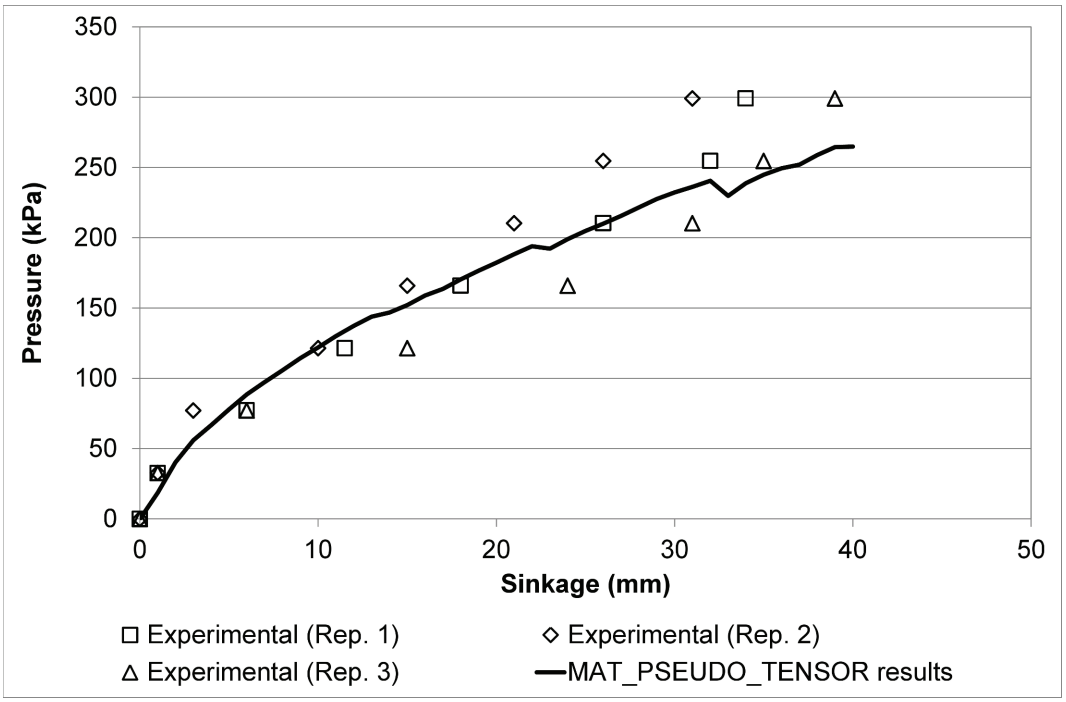

Figure G.3: Visual comparison of experimental static plate sinkage profiles against profile predicted by quasi-static Euler plate sinkage simulation

Table G.3: Comparison of predicted sinkage results against experimental means for Euler plate sinkage simulations in sandy loam, using yield surface parameters derived from direct shear box tests

	Experiment	Lagrange dry sand model with shear box yield surface	
Pressure	Sinkage	Sinkage	Error
kPa	mm	mm	%
0	0	0	-
33	1	1.0	0
77	5	5.0	0
122	12	10	-17
166	19	17.3	-9
210	26	26.0	0
255	31	37.1	+20
Mean percentage error (0 – 255kPa)		-1 %	